VNiVERSiDAD
Đ SALAMANCA

CAMPUS DE EXCELENCIA INTERNACIONAL

Doctoral Thesis

Out-of-Equilibrium Carrier Dynamics in Graphene and Graphene-based Devices for High-Performance Electronics

---

José Manuel Iglesias Pérez

May 2019

Facultad de Ciencias
VNiVERSiDAD
DE SALAMANCA

D. RAÚL RENGEL ESTÉVEZ, Profesor Titular de Electrónica del Departamento de Física Aplicada de la Universidad de Salamanca**,** y **Dª MARÍA JESÚS MARTÍN MARTÍNEZ**, Catedrática de Electrónica del Departamento de Física Aplicada de la Universidad de Salamanca,

CERTIFICAN:

Que la memoria de trabajo de investigación titulado “*Out-of-Equilibrium Carrier Dynamics in Graphene and Graphene-based Devices for High-Performance Electronics”* ha sido realizada por **D. JOSÉ MANUEL IGLESIAS PÉREZ** para optar al TÍTULO DE DOCTOR CON MENCIÓN INTERNACIONAL por la Universidad de Salamanca, bajo el marco del programa de doctorado **FÍSICA APLICADA Y TECNOLOGÍA**, y que ha sido desarrollada en su totalidad bajo la dirección de los directores de Tesis, en el Área de Electrónica del departamento de Física Aplicada, de la Universidad de Salamanca.

En Salamanca, a 2 de Mayo de 2019

Autor:

José Manuel Iglesias Pérez

Directores:

Raúl Rengel Estévez
María Jesús Martín Martínez

A mis padres,

y a Inés 👶

Agradecimientos/Acknowledgements

Llegar a terminar esta tesis es el fruto de un trabajo de más de cuatro años en el que han intervenido numerosas personas, a las cuales no puedo pasar sin agradecer debidamente su tiempo, dedicación, tutela o simplemente su apoyo y compañía.

En primer lugar a mis directores, Raúl y María Jesús. Por permitirme la oportunidad de adherirme a su grupo tras aquél trabajo fin de Carrera. Porque encontraron el equilibrio perfecto entre tutela y libertad a la hora de investigar, trabajar, y escribir. Con ellos siempre he visto mi trabajo reconocido a la vez que hacían crecer su calidad. También por su interés y predisposición a encaminar y apoyar mi futuro profesional. Además han sido un referente en cuanto a valores en el ámbito de la difusión de la ciencia y la tecnología, pues he presenciado de cerca no pocas horas de su trabajo dedicadas a la divulgación.

Ciertas partes de esta tesis no existirían sin el trabajo de algunas personas que con su tiempo, realizaron una contribución directa. La primera mención se la dedico a Íñigo J. Sola. Ha sido un ejemplo de tenacidad, paciencia, y buen hacer en el laboratorio, y le agradezco enormemente la formación que me ofreció en óptica experimental con motivo de mi preparación previa a la estancia. Lo que me lleva a Helder Crespo, no solo por acogerme su grupo de investigación durante mi estancia en instalaciones de la Universidad de Oporto, también por haberme hecho sentir cómodo desde el primer instante, permitiéndome gozar de una experiencia vital que recordaré siempre. A Óscar Zurrón y Luis Plaja, por su cálido trato y por permitirme experimentar con ellos un enriquecedor aprendizaje fruto de una colaboración multidisciplinar, agradecimiento que hago extensivo a Pablo Moreno. Asímismo, a Yahya Meziani por su ayuda con el manejo del Lock-in. Agradezco a nuestros compañeros de la Universidad Autónoma de Barcelona: David Jiménez, Pedro Feijoo y Fran Pasadas, tanto el enriquecimiento profesional fruto de nuestras colaboraciones, tanto el personal por su trato en las numerosas veces que hemos coincidido. A David López, por su asistencia técnica para la caracterización Raman de las muestras. A Ignacio Íñiguez, por su tiempo invertido con nosotros en el laboratorio de caracterización y las clases prácticas de iniciación con la mesa de puntas.

A todos los compañeros del área de Electrónica les tengo que agradecer haberme hecho sentir como en casa desde el primer día. Tras más de cuatro años compartiendo

espacios, la organización de dos congresos, y unas cuantas horas en las aulas, puedo decir que entre todos han sentado una marca difícil de batir en lo que se refiere a ambiente de trabajo y trato personal. A El Mokhtar y Elena Pascual, porque trabajar con vosotros ha sido una experiencia irrepetible.

A mis compañeros de laboratorio. Mike and Ana, you made my stay in Porto really unforgettable, and the long hours in the lab truly enjoyable. Your help with my tasks was very valuable, and I could never thank you enough for that. Llegados a este punto, Marta está deseando leer su nombre por aquí; gracias por tus horas en el laboratorio de óptica, y por todo lo que hemos aprendido el uno del otro, a pesar de ser tan distintos. El trabajo ligado a la realización de una tesis puede resultar realmente frustrarte en numerosas ocasiones. Sois muchos compañeros de departamento los que habéis contribuido a hacerlo más llevadero, bien de *paseito* por la montaña, de tapas en el trivial, o jugando al Seven Wonders... Gracias, Álex, Irene, Carlos, Julián, Rocío, Felipe, Laura, Aurora, Jose y Rosa.

Gracias también a los amigos que han soportado esos momentos de frustración con una cerveza de por medio; Elena, esta va especialmente por ti.

Es imposible no agradecer a mis padres... TODO. Desde la primera regañina, hasta la ayuda con las lecciones de historia, vuestro compromiso con la educación y la formación me ha puesto en el camino para hacer esta tesis realidad.

Finally, the realization of this thesis would have not been possible without the **financial founding** given by *Ministerio de Economía y Competitividad* (national government) and FEDER (European Regional Development Fund) via projects TEC2016-80839-P and TEC2013-42622-R, *Consejería de educación de la Junta de Castilla y León* (regional government) and FSE (European Social Fund) via PhD grant SA176-15, and *University of Salamanca* and its *Department of Applied Physics* via its stay grants for PhD students.

Abstract

With traditional semiconductor technology approaching the limits of scaling and chip integration, the discovery of graphene and its astonishing properties stood as a promising alternative for future electronics. In order to adequately put into context the possibilities of graphene, it is critical to investigate the microscopic properties of electronic transport in this material.

With this objective, a Monte Carlo simulator for graphene that includes the dynamics of electrons and holes, with especial focus on hot carrier phenomena, like hot phonons, Auger processes, and phonon-assisted generation and recombination mechanisms has been developed. The analysis of electronic transport at high fields allowed to quantify the relative impact that self heating and hot phonons have in the steady state drift velocity of the carriers and temperature. Linear sheet current behavior at high fields was found to be the result of free charge carriers created through impact ionization collisions.

Velocity fluctuation phenomena in graphene were studied employing various numerical methods aimed at the analysis of specific transient dynamics (under the application of switching or AC electric fields). The frequency-dependent noise temperature was obtained from the diffusivity an differential mobility, and the feasibility of generating high-order harmonics in graphene, was presented in terms of the detection bandwidth.

The potential of graphene for optoelectronic applications requires also a deep understanding of the ultrafast relaxation processes that carriers undergo after being exposed to light with an adequate wavelength. A thorough exploration of this process, with particular focus on the initial photoexcitation conditions, the effect of out-of-equilibrium phonons and the influence of an underlying substrate is presented, together with an experimental pump and probe differential transmission spectroscopy approach.

An initial version of a simulator of 2D material-based devices is presented, which allows to set the basis for future research in the field of Monte Carlo modeling of this kind of electronic devices.

Resumen

Con los límites tecnológicos de las tecnologías de semiconductores tradicionales alcanzando los límites de escalado y integración en chip, el descubrimiento del grafeno y sus impresionantes propiedades supuso una prometedora alternativa para el futuro de la electrónica. Para contextualizar adecuadamente las posibilidades del grafeno, la investigación de las propiedades micrsocópicas del transporte electrónico es una tarea crucial.

Con este objetivo, se ha desarrollado un simulador Monte Carlo para grafeno, que incluye la dinámica de electrones y huecos, con espacial atención a fenómenos de portadores calientes, como fonones fuera de equilibrio, procesos Auger o generación/recombinación asistida por fonones. El análisis del transporte electrónico a campos altos permitió cuantificar el impacto relativo del autocalentamiento y los fonones calientes sobre la velocidad de deriva en condiciones estacionarias y la temperatura del material. Además se observó un comportamiento lineal de la corriente debida a la ionización por impacto.

Se ha estudiado la fenomenología relacionada con fluctuaciones empleando diversos métodos numéricos orientados a condiciones transitorias particulares (saltos abruptos de campo o señales AC). La temperatura del ruido dependiente de la frecuencia se obtuvo a partir de la difusividad y movilidad diferencial los portadores, y la viabilidad de la generación de armónicos de orden alto en grafeno se presenta en términos del ancho de banda límite para su detección.

El potencial del grafeno para aplicaciones optoelectrónicas precisa de una comprensión detallada de los procesos de relajación ultrarrápida que sufren los portadores fotoexcitados con longitudes de onda apropiadas. Llevamos a cabo un examen exhaustivo de este proceso, con especial atención a las condiciones iniciales de fotoexcitación, el papel de los fonones calientes, y el efecto del sustrato.

Finalmente presentamos una versión inicial de simulador para dispositivos electrónicos basados en materiales 2D, que cimentará las líneas futuras de investigación en el campo del modelado Monte Carlo de estos dispositivos.

Contents

List of Figures

Nomenclature

Acronyms

SPP	Surface Polar phonons
AC	Alternate Current
Al_2O_3	Aluminium Oxide
AR	Auger Recombination
BJT	Bipolar Junction Transistor
BTE	Bolzman Transport Equation
CMOS	Complementary MOS
CVD	Chemical Vapor Deposition
DC	Direct Current
DFT	Density Functional Theory
DTS	Differential Transmission Spectroscopy
EMC	Ensemble Monte Carlo
FET	Field-Effect Transistor
FinFET	Fin-shaped FET
GaAs	Gallium Arsenide
GaN	Gallium Nitride
h-BN	Hexagonal Boron Nitride
HEMT	High-Electron-Mobility Transistor

HfO_2	Hafnium Oxide
HP	Hot Phonons
II	Impact Ionization
InP	Indium phosphide
LHS	Left-hand side
MLG	Monolayer Graphene
MOS	Metal-Oxide-Semiconductor
MOSFET	Metal-Oxide-Semiconductor Field-Effect Transistor
RF	Radio Frequency
RHS	Right-hand side
SH	Self-Heating
SiC	Silicon Carbide
SiNW	Silicon NanoWire
SiO_2	Silicon Oxide
SOI	Silicon on Insulator
TPSD	Transient Power Spectral Density

Constants

α	Fine-structure constant
ϵ_0	Vacuum permittivity
$\hbar$	Reduced Planck constant
e	Elementary charge
k_B	Boltzmann constant

Mathematical expressions

δ	Dirac delta
$\mathscr{F}$	Fermi-Dirac function

$\mathscr{F}_j$	Fermi integral of order j
Θ	Heaviside function
$\Im$	Imaginary part
$\Re$	Real part

Symbols

α_{def}	Defect parameter
$\mathit{\Omega}$	Normalized area
Δf_{th}	Threshold frequency
Δt	Monte Carlo temporal step
δv	Fluctuation
$\Delta(...)$	Functional for energy/momentum conservation in scattering probability
ϵ	Dielectric function
DoS	Density of states
ξ	Material Monte Carlo superparticle density of states equivalent
ε	Carrier energy
ε_F	Fermi Energy
ε_k	Carrier kinetic energy
PE	Device Monte Carlo electron/hole particle equivalent
Γ	Scattering probability
γ	Hopping energy
κ_0	Low-frequency relative permittivty
κ_∞	Optical-frequency relative permittivty
$\mathcal{F}$	Frolich coupling constant
$\mathcal{H}$	Scattering matrix element
$\mathcal{T}/\mathcal{T}_0$	Differential transmission measured signal

μ	Chemical potential
μ_{dif}	Differential mobility
$\mu_{\mathrm{e/h}}$	Electrons/holes quasi-Fermi levels
μ_{LF}	Carrier low-field mobility
μ_{dif}	Differential mobility
NP	Monte Carlo number of particles
ω	Angular frequency
ϕ	Electrostatic potential
Ψ_{max}	Maximum photocarrier occupation
ρ	Volumic charge
ρ_{Sg}	Graphene sheet resistivity
σ	Surface charge
σ_{Sg}	Graphene sheet conductivity
$\tau_{\mathrm{G/R}}$	Generation or recombination time
τ_{ν}	Phonon decay rate
$\mathbf{E}$	Electric field
$\mathbf{k}$	Carrier wavevector
$\mathbf{r}$	Position
$a_{\mathrm{c-c}}$	Carbon-Carbon interatomic distance
$C_{(\ldots)}$	Correlation function
D	Difussion coefficient
d_{VdW}	Separation of the 2D material sheet with the substrate
$D_{1/0}$	First/zeroth order deformation potential
f	Frequency
f_{max}	Maximum oscillation frequency

f_{T}	Cutoff frequency
$f_s(...)$	Distribution function in the sub-band s
$f_{e/h}(...)$	Distribution function of electrons/holes
g_s	Spin degeneracy
g_v	Valley degeneracy
K_v	Velocity reponse function
n	Electron density
N_{acc}	Accumulated generated or recombined carriers
n_{excit} / p_{excit}	Photoexcited electron/hole densities
$N_{\mathrm{G/R}}$	Number of carriers to generate/recombine
n_{imp}	Impurity concentration
n_{ν}	Number of phonons
N_c	Maximum number of particules in a **k**-space cell
p	Hole density
$P(... \rightarrow ...)$	Transition probability
$P_{\mathrm{int/sub}}$	Power transferred due to intrinsic/substrate mechanisms
$R_{\mathrm{sub/wafer/B}}$	Thermal resistance of the substrate/wafer/2D material interface
s	Sub-band
$S_{(...)}$	Spectral density
T_0	Ambient temperature
$T_{\mathrm{2D/g}}$	2D material/graphene temperature
T_{c}	Carrier temperature
$T_{\mathrm{e/h}}$	Electrons/holes temperatures
T_{n}	Noise temperature
T_{sub}	Substrate temperature

T_ν	Phonon temperature
v_F	description
v_m	m^{th} harmonic coefficient of the velocity response
$\langle ... \rangle$	Averaged value

Chapter 1

Introduction

The readers of this thesis are invited to look around and find the electronic devices at their reach. Most likely there is, at least, one smartphone. Maybe this thesis is being read on a computer or a tablet PC, and you are wearing a digital or smart watch. If you are in a living room, most certainly there is a TV and a hi-fi system. Electronic devices nowadays are everywhere: in transport access controls, electronic payment systems, GPS navigators... Even household appliances like microwaves or refrigerators not only rely on electronic controllers, now they can even be connected to the internet. All these ubiquitous devices are a result of an incessant push of the limits of science and technology.

The first irruption of a field-effect transistor (FET) dates back to October 1926, when J. E. Lilienfeld presented to the patent office a device *capable of controlling the electric flux between two terminals of a conducting solid by setting a third terminal between them* [1]. Later in 1933, he improved his invention by including an insulator layer between the modulation contact and the conducting material [2], what was later known as the MOSFET (Metal-Oxide-Semiconductor Field-Effect-Transistor). Fabrication of these devices was impossible at the time due to technical hindrances and scarce knowledge of semiconductor physics. As a result, electronics were based mainly on vacuum tubes, until a series of discoveries changed everything: in 1947, J. Bardeen and W. Brattain fabricated the first operative transistor based two point contacts on n-type Germanium [3]. Shortly after, W. Shockley perfected this idea and created the *Bipolar Junction Transistor* [4], BJT for which the three scientists won the Nobel prize. BJTs provided a more reliable, power efficient, and above all, smaller alternatives to vacuum tubes. From then on, the advances in the field were overwhelming. In 1954 the first commercial Silicon transistor is presented by Texas Instruments. Bell Labs developed the basic technological processes that made possible the realization of the integrated circuit by J. Kilby, from Texas Instruments in 1958. Just a few months later the basis of planar technology was settled by R. Noyce, paving the way to the development of complex integrated circuits.

It was in the following decade when the ideas of Lilienfeld could be finally put into practice: the first functional MOSFET was presented by D. Kahng and J. Atalla right on 1960 [5]. The CMOS (*Complementary Metal Oxide Semiconductor*) circuit was invented in 1963 by F. Wanlass and C. T. Sah [6], which was progressively adopted, replacing the n-MOS and BJT technology for most digital applications. The Silicon age –that lasts until today– had started. In 1965 G. Moore, co-founder of Intel, observed the evolution of the electronics technology and settled what is known as *Moore's Law*: every 18 months, the number of components per chip would double, as illustrated in figure 1.1. The industry took this observation as an objective. To accomplish this, every new generation of transistors were to halve its dimensions, the component count per chip had to be multiplied by a factor of four, and chip size had to be enlarged by 50% [7]. For a long time, this progression was only challenged by the need of creating more precise

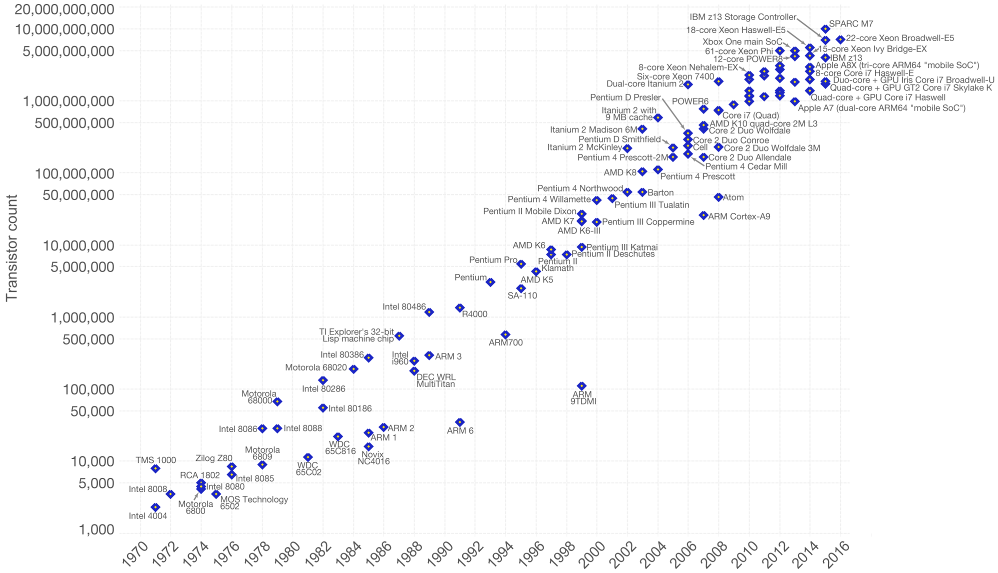

Figure 1.1: Graphic illustration of the Moore's Law from 1970 to 2016, showing the exponential growth of the transistor count.

technologies that could fulfill the circuit designer requirements. However, entering in the 21st century, the industry started facing new troubles as the device dimensions became smaller and smaller [8]: short-channel effects, parasitic elements, quantum effects, leakage currents, hot carrier phenomena, just to name some of them.

Therefore, further downscaling was not the only way to go anymore. New solutions had to be proposed and implemented in order to solve these issues, so that the future processors comply with Moore's Law. One of the earliest solutions was the *Silicon On Insulator* (SOI) [9, 10] technology, consisting on a very thin Silicon channel isolated from the substrate by means of a buried oxide, permitted MOSFETs to reach higher performances in digital and analog electronics. Strained Silicon technology [11] allowed enhancing the performance of the transistors by increasing the electron mobility. The use of high-κ dielectrics and metallic gates helped to overcome the need to escalate the SiO_2 oxide of the gate in proportion with the channel length [12], which lead to tunnel leakage currents through the insulator.

However, further downscaling at the end of 2000s proved that these solutions were not enough, and newer ones focusing on the transistor geometry, which supposed a deep re-thinking of the planar technology, were proposed. With the basic idea of incrementing the space in which the gate has control over the channel, new topologies such as Fin-FETs [13] came into play. In these transistors, the channel is shaped like a fin and sits on the wafer while surrounded by three sides by the gate, increasing the gate control, and reducing power consumption due to reduced power leakage to the die. Although processing techniques were compatible with FinFET geometries, it was not until 2011 when the industry finally managed to solve the issues related to their fabrication.

After being widespread implemented in today's commercial Silicon devices, prospects for the future suggest that further improvements will need to be done once the FinFET technology reach its limits. The most extreme extension of the previous idea are the Silicon nanowires (SiNW), where the channel is formed with thin wires of Silicon of a diameter in the 10 nm range. By surrounding them with an insulator, a gate-all-around transistor would be formed, increasing the electrostatic control of the channel and offering high $I_{\mathrm{on}}/I_{\mathrm{off}}$ ratios [14]. Another approach that allows a significant improvement in chip performance consists in the so-called 3D monolithic integration, where several on-die interconnected stacked layers of electronic components is built in the same chip, increasing the functionality and packaging density [15].

All these efforts have been related to what is known as *"more Moore"* scenario, considering Silicon as the cornerstone of the microelectronics (today, de facto, nanotelectronics) industry. However, other solutions have been also explored. An approach that has always been present in the quest to increase the performance, efficiency and scalability of transistors and other devices, is the search of new materials with properties that could outperform Silicon, and eventually replace it.

III-V compound semiconductors have been extensively studied for high-frequency RF devices [16], and proposed as future CMOS transistor channels [17–19]. Their higher electron mobilities and charge density allow transistors to operate at faster switching speed and lower power in comparison with Si. However, these alternatives have not yet irrupted in the mainstream binary logic semiconductor industry mainly because of two

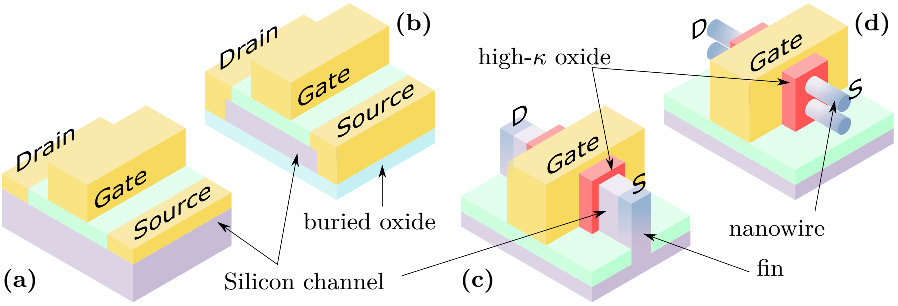

Figure 1.2: Various architectures devised to improve transistor performance: (a) primigenial planar MOSFET configuration, (b) Silicon on insulator (SOI), (c) FinFET, and (d) Silicon nanowire (SiNW) transistor.

reasons: these compound semiconductors do not have a native oxide with properties and growth simplicity able to challenge SiO2 [20]. Also, the disparity of electron and hole mobilities results in p-type FETs not being able to match the performances of the n-type counterparts, being this an essential requirement for CMOS [21]. Germanium, with around tree times the mobilities found in Silicon is in the spotlight for CMOS replacement [22–24], as the differences between hole and electron mobilities is not as large as in III-V compounds. On the other hand, n-type Germanium-based FETs are quite inferior to p-type, despite the higher electron mobility due to high resistances at the contact interfaces [25, 26]. Even though these materials have not yet made it, the thorough knowledge of these semiconductors have allowed its exploitation in a vast range of applications where Silicon would not perform so well, like high-frequency transistors for RF applications [27], optoelectronic emission and sensing [28], or THz detection [29], to cite some examples. Electronics beyond logic and memories is also an important part of the game.

A striking idea in the context of new materials, is the possibility to use two-dimensional crystals. Just attending to their topology, 2D materials suppose some advantages over 3D bulk semiconductors: with them, the thinnest possible channel would be accomplished, taking the gate control to the limit, thus reducing short-channel effects. Also, new device concepts can be feasible [30], and ultra-short scale lengths could be reached [13] guaranteed by the good scalability attributed to the two-dimensional nature.

In 2004, during one of their Friday after-work sessions in the University of Manchester, A. Geim and K. Novoselov managed to isolate a piece of a monoatomic layer of Carbon by successive exfoliation of graphite with Scotch® tape [31]. Although monoatomic layers had not been isolated up to then, this carbon allotrope had already been given the name of graphene [32]. Despite thinking that such crystalline form could not be stable some theoretical studies had already been carried out [33]. Since the discovery of the experimental procedure to obtain graphene, there has been an explosion of research around this material, that was not any more just an exotic academic idea, but had become a reality. The motivation for this outbreak of interest are its exciting and promising properties, like for example, being the strongest material ever tested, with a Young modulus of 1 TPa and tensile strength of 130 GPa [34], while being ultra light ($0.77\,\mathrm{mg/m^2}$). The relevance of this breakthrough was such that the lead the European Union to take the biggest research initiative with a budget of €1 billion, and A. Geim and K. Novoselov were awarded with the Nobel price in 2010.

As it regards this PhD thesis, our interest focuses mainly on the electronic and optical properties of graphene. Besides the advantages predicted for 2D materials in the field of electronic devices, graphene presents some additional properties that are very desirable, and emerge as a result of its band structure. The crystalline structure of graphene is

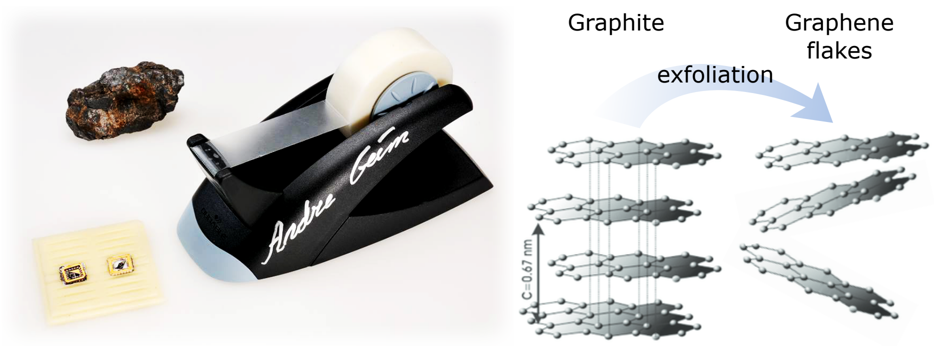

Figure 1.3: The Scotch® tape, a piece of graphite and some graphene samples as shown exhibited in the Nobel price museum. Graphite and graphene crystalline structures, and obtention of graphene by means of exfoliation.

based on an hexagonal arrangement of σ-bonded carbon atoms through sp^2 hybridization. This leaves available out-of-plane π^* and π orbitals that confer graphene the well known conical energy dispersion close to the Dirac points that makes electrons in graphene behave like massless particles. More technical details about the band structure are given in section 2.4.1.

Some of the properties that made graphene an interesting candidate for a potential use in electronics are its high mobilities, topping for suspended graphene samples, which reach over $250\,000\,\mathrm{cm^2V^{-1}s^{-1}}$ at room temperature [35]. However, for practical uses mechanical support is needed, and graphene is placed on top of a substrate. It has been found that the interaction with these substrates degrade the mobility, being found to be reduced to $40\,000\,\mathrm{cm^2\,V^{-1}s^{-1}}$ for graphene on Silicon oxide [36] (SiO_2) and to $50\,000\,\mathrm{cm^2\,V^{-1}s^{-1}}$ for graphene on hexagonal Boron nitride [37, 38] (h-BN) at room temperature. Still, it must be highlighted that these values are substantially higher than mobilities of Silicon ($1400\,\mathrm{cm^2\,V^{-1}s^{-1}}$ [39]) or Gallium arsenide ($8500\,\mathrm{cm^2\,V^{-1}s^{-1}}$ [40]). Also, electron saturation velocities are high, reaching up to $7 \times 10^7\,\mathrm{cm\,s^{-1}}$ [41, 42], again higher than those for Silicon and III-V compounds. Together with those high mobilities, under certain conditions mean free paths could reach the micrometric range [43, 44], allowing for its potential use as channel material for large area ballistic devices. These characteristics put graphene in the track for the realization of high-frequency electronics.

As it regards the realization of graphene devices, the first demonstration of a working graphene-based FET was done in 2007 by Lemme, Echtermeyer, Baus, and Kurz [45]. After it, improvements in the fabrication techniques have allowed to produce graphene-based FETs that reach threshold frequencies of ~430 GHz [46], and maximum operation frequencies of 200 GHz [47]. In the case of digital applications, despite the high graphene

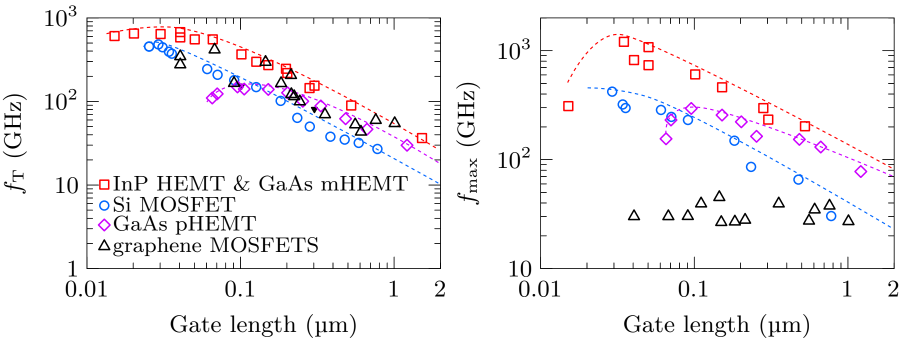

Figure 1.4: Cutoff frequency (f_T) and maximum oscillation frequency (f_{max}) figures of merit for transistor RF performance as a function of the gate length. Adapted from [51].

mobility, these RF figures of merit do not outperform yet those found in settled technology like InP or GaAs HEMTs [48, 49] and even Silicon MOSFETs [50], as it can be seen in figure 1.4. However, there is a fundamental problem with graphene transistors: the lack of a band gap does not allow them to completely switch off, which supposes a critical issue for logic circuits, where high I_{on}/I_{off} ratios are needed. While this is not a problem for RF applications, the use of graphene in amplifiers is hindered due to a lack of saturation region, which degrades the radio frequency performance. In this context, there is some uncertainty about the practical use of graphene FETs [51]. However, when taking into account other characteristics like its transparency, mechanical strength and flexibility, graphene becomes a reliable material for its use in flexible electronics [52, 53], being a potential replacement of the previously existing technology (Indium tin oxide).

As it regards the optical properties of graphene, it features a flat absorption of $\sim 2.3\%$, for a wide frequency spectrum from mid-infrared to the blue [54]. This absorption is low in absolute terms but extremely high if we account for its monoatomic thickness. Besides, the possibility to electrostatically change the Fermi level in graphene can alter its optical properties [55]. The high carrier mobility in graphene, combined with these characteristics are a perfect combination for optoelectronic applications [56], like saturable absorbers [57], or photodetectors [58–60].

Although graphene (at least in the device configurations explored up today) may not be the *"wonder material"* that was expected once to replace Silicon CMOS technology, it does not mean that it could be made useful under different paradigms. In the same way other semiconductors perform well where Silicon does not, graphene has already been found to be appropriate for certain uses where it could effectively replace or complement the current technology. Besides, the discovery of a stable two-dimensional material led to the use of similar processing techniques employed in graphene to other elements and compounds, originating a new huge research field in 2D materials. Now more than 1000 2D materials are under investigation [61], some of which are of more immediate interest in electronics [62–64]. The knowledge of their electronic behavior becomes mandatory in order to accomplish the future devices for which graphene and 2D materials are best suited: it should not be forgotten that graphene is still a new material that we need to know better, since an in-depth understanding of its electronic properties may open the path to new device architectures, radically different from those based on traditional semiconductors. In this context, physical models and simulation are an essential tool, since with them we can evaluate the feasibility and performance of such materials and devices, saving costs and providing a theoretical support to guide their technological development.

Objectives and structure of the thesis

For such purpose we concentrate in modeling and simulation with Monte Carlo methods, which offer a particle point of view of the carrier dynamics . Some authors have already developed Monte Carlo models for the study of graphene. In [65], [66] and [67] the high-field transport (saturation velocity) was analyzed in a bulk graphene framework. Within the same material context, the influence of a dielectric polar supporting substrates was studied in [68] and [69]. The impact of other extrinsic scattering sources on the electronic transport, including impurities and crystalline defects [70] has been investigated as well. Other topics like spin transport have also been approached from the Monte Carlo technique [71]. By means of a coupled Monte-Carlo and electromagnetic solver, in [72] the dynamic conductivity was obtained in a self-consistent manner. As it regards device modeling and simulation, in [73] the RF performance of graphene FETs was investigated, stressing the relevance of band-to-band tunneling in the output characteristics, and in [74] the influence of non-uniform impurity distribution along the channel length and supporting oxide thickness was studied.

The global aim of this thesis is to further deepen into the study of graphene electronic behavior, especially at the bulk material level and under strong out-of-equilibrium stationary and transient conditions. So, in our Monte Carlo model we will stress the relevant interactions required to correctly study the graphene properties in this kind of situations. In this context, the focus has been set in the following objectives:

- The development of a simulation tool that incorporates the most relevant physical processes that rule the carrier dynamics in graphene. Hot electron related phenomena must be stressed in order for the tool to be appropriate to fulfill the requirements to correctly tackle the forthcoming objectives.

- Investigate the electronic transport under the action of strong electric fields, and quantify how the particular effects that arise in this regime affect it. Perform characterization measurements of the conductivity of real samples.
- Study of the diffusivity and electronic noise phenomena under non-stationary regime, by employing the appropriate numerical methods. The intrinsic stochastic nature of Monte Carlo methods make them the ideal tool for this purpose.
- Comprehend the relaxation dynamics in photoexcited graphene attending to the optical excitation characteristics like wavelength and power, both from a theoretical framework by means of simulation, and also experimentally with time-resolved spectroscopy techniques.
- Create, over the base of the material simulator, a device simulator for 2D materials to evaluate the behavior of simple prototypes.

The thesis is organized as follows. In chapter 2 we will introduce the Monte Carlo method applied to the Boltzmann transport theory for electronic transport. The specific graphene aspects in the electron dynamics model will set the basis of the simulation tool that has been employed along the works done in this PhD. Chapter 3 explores the validity of the model in both low and high field regimes. Then, specific out-of-equilibrium phenomena, like Joule heating and impact ionization under steady high electric fields are analyzed. The stochastic nature of the Monte Carlo method is exploited in chapter 4: here we studied the frequency-dependent noise temperature, fluctuations under transient conditions, and the feasibility of high-order harmonic generation and extraction. Relaxation carrier dynamics of graphene after photoexcitation is investigated in chapter 5, with emphasis on the phenomena particularly relevant in those conditions, such as carrier multiplication or hot phonons. Also, we demonstrate the tunability of the carrier dynamics by means of the substrate choice. Chapter 6 introduces the work done for extending the simulation tool from the material towards the device level, and the preliminary results obtained. Finally, chapter 7 summarizes the main findings, and suggest future works that could be tackled in the field of graphene and other 2D materials for electronics.

Chapter 2

Monte Carlo transport model

The global objective of this chapter is to provide a thorough perspective of the modeling approach developed and employed in this thesis. With this purpose, first the Monte Carlo method is introduced in a general and brief fashion in section 2.1. Then, the section 2.2 presents the Boltzmann theory particularized for the case of electronic transport. Subsequently, the application of the Monte Carlo method to this Boltzmann transport framework is extensively detailed in section 2.2. Next, in section 2.4, the physical model that describes the interactions that govern the electron dynamics in graphene will be presented. In this PhD thesis, some work has been done in the context of device simulation. The features of the tool allowing the study of electronic devices, such as the geometric description of spatial constraints, an electrostatic resolution consistent with the charge redistribution, or boundary conditions will be presented in chapter 6.

2.1 Introduction to Monte Carlo methods

The Monte Carlo method, first devised and employed in the 1940s by scientists working in the development of nuclear weapons in Los Alamos, consists of a broad range of numerical and computational algorithms employed to approximate complex mathematical expressions. It is essentially based on the idea of using repeated random sampling to solve complex problems, even if they are deterministic [75]. Its name comes from the capital of the Principality of Monaco and the association of the games of chance played in its popular casino with the essence of the Monte Carlo method.

One illustrative example of using random sampling to solve a mathematical problem is the calculation of the number π. Imagine a circle (with radius d) and its circumscribed square (of side length $2d$) centered at the origin of a Cartesian space. The ratio of the circle and the square areas is $\pi/4$. We would sample a number N of points with random positions (x_i, y_i) within the $d \times d$ square area, and tell how many of them are inside the circle, N_c, that is, those that fulfill the condition $\sqrt{{x_i}^2 + {y_i}^2} < d$. As we know the relation of the two areas, we can obtain our result as $\pi = 4N_c/N$. Of course, the accuracy achieved strongly depends on the number of samples.

The Monte Carlo approach becomes particularly interesting for problems whose results rely on probability distributions that involve a large number of coupled degrees of freedom. For such reason it has been found useful in a wide number of areas in science and engineering [76]. Some of these cover dynamic liquids behavior [77], molecular dynamics of diverse types of materials and compounds [78], crystal synthesis and growth [79], quantum many-body problems [80] or even the study of radiative transfer and collision probability in astrophysics [81, 82], just to cite some. The main subject in this thesis, that is, the electronic transport at the mesoscopic scale in the diffusive regime, also lies among this kind of physics problems. In a semi-classical framework, charge transport can be described according to the Boltzmann theory [83], which is presented next.

2.2 The Boltzmann Transport theory

The theory was first introduced in 1872 by Ludwig Boltzmann [84] in an attempt to describe the statistical behavior of dilute gases in an state of non-equilibrium. Later on, this theory has given rise to the so called generalized kinetic models, usually composed of integro-differential mathematical expressions able to describe a wide range of phenomena in applied sciences [85]. The kinetic equation for the case of electron transport can be derived as follows [86]:

Let us assume that charge carriers can be characterized at an instant t by their position in the real space, $\mathbf{r}$, the energy sub-band, s, and its wavevector in the reciprocal space, $\mathbf{k}$. Then, we can describe the distribution function of particles as:

$$dN = \sum_s f_s(\mathbf{r}, \mathbf{k}, t) \frac{d\mathbf{r}\, d\mathbf{k}}{(2\pi)^D}, \tag{2.1}$$

where $\sum_s$ refers to the summation over the different sub-bands, $f_s(\mathbf{r}, \mathbf{k}, t)$ is the normalized instantaneous occupation function for each sub-band at the phase space $(\mathbf{r}, \mathbf{k})$, and D is the number of dimensions of the system. If we assume that the charge is conserved over time, the time derivative of the distribution function in the whole phase space must equal zero: $\dot{f}_s(\mathbf{r}, \mathbf{k}, t) = 0$. Such equality constitutes the Boltzmann Transport Equation (BTE), and in its expanded form reads

$$\sum_s \left(\frac{\partial}{\partial t} + \frac{\partial \mathbf{r}}{\partial t} \nabla_{\mathbf{r}} + \frac{\partial \mathbf{k}}{\partial t} \nabla_{\mathbf{k}} \right) f_s(\mathbf{r}, \mathbf{k}, t) = 0. \tag{2.2}$$

For every sub-band, three terms compose the equation. The first one –the time derivative– expresses the evolution of the distribution function for a given positionand wavevector.

The second term is related to the real space motion of the charge carriers due to their group velocity, $\mathbf{v}_s(\mathbf{k})$:

$$\frac{\partial \mathbf{r}}{\partial t} \nabla_{\mathbf{r}} = \mathbf{v}_s(\mathbf{k}) \nabla_{\mathbf{r}}. \tag{2.3}$$

The last one describes the change in momentum occupation due to the action of all the forces acting over the carrier:

$$\frac{\partial \mathbf{k}}{\partial t} \nabla_{\mathbf{k}} = \frac{1}{\hbar} \sum \mathbf{F}(\mathbf{r}, \mathbf{k}, t) \nabla_{\mathbf{k}} = \frac{1}{\hbar} \left[\mathbf{F}_{\mathcal{E}}(\mathbf{r}) \nabla_{\mathbf{k}} + \sum \mathbf{F}_i^{\mathrm{coll}}(\mathbf{r}, \mathbf{k}) \nabla_{\mathbf{k}} \right], \tag{2.4}$$

where $\mathbf{F}_{\mathcal{E}}(\mathbf{r}) = q[-\mathbf{E}(\mathbf{r}, t) + \mathbf{v}(\mathbf{k}) \times \mathbf{B}(\mathbf{r}, t)]$ is the electromagnetic force due to the local electric, $\mathbf{E}$, and magnetic, $\mathbf{B}$, fields applied externally to a carrier with charge q, and $\mathbf{F}_i^{\mathrm{coll}}$ is each of the forces due to intraband and interband collisions.

This general effect of the collision forces in the changes of population in the reciprocal space, can be statistically evaluated as a function of the accumulated effects of scattering probabilities [87]:

$$\begin{aligned}\frac{\mathbf{F}_i^{\text{coll}}(\mathbf{k},\mathbf{r})}{\hbar}\nabla_{\mathbf{k}} f_s(\mathbf{r},\mathbf{k},t) = \\ = -\sum_{s',\mathbf{k}'}\Big\{ f_s(\mathbf{r},\mathbf{k},t)P_i(s,\mathbf{k}\rightarrow s',\mathbf{k}')\left[1-f_{s'}(\mathbf{r},\mathbf{k}',t)\right] - \\ - f_s(\mathbf{r},\mathbf{k}',t)P_i(s',\mathbf{k}'\rightarrow s,\mathbf{k})\left[1-f_s(\mathbf{r},\mathbf{k},t)\right]\Big\},\end{aligned} \tag{2.5}$$

where $P_i(s,\mathbf{k}\rightarrow s,\mathbf{k}')$ expresses the probability that a charge carrier would suffer the action of a scattering mechanism that shifts its initial state from $\mathbf{k}$ in the s sub-band towards $\mathbf{k}'$ in the s' sub-band. Here, it is generally considered that the scattering forces provoke a change in momentum and energy that is almost instantaneous, and therefore do not produce an appreciable displacement in the real-space during the interaction.

Finally, we can rewrite the BTE as:

$$\left[\frac{\partial}{\partial t} + \mathbf{v}(\mathbf{k})\nabla_{\mathbf{r}} + \mathbf{F}_{\mathcal{E}}(\mathbf{r})\nabla_{\mathbf{k}}\right] f_s(\mathbf{r},\mathbf{k},t) = \left[\frac{\partial}{\partial t} f_s(\mathbf{r},\mathbf{k},t)\right]_{\text{coll}}, \tag{2.6}$$

where the term in the right-hand-side is called the collision term, that represents the statistical estimation of the forces due to all the considered scattering mechanisms as seen in equation (2.5). This is the base of the Monte Carlo method for electronic transport, which will be detailed in the following section.

2.2.1 Monte Carlo approach to the BTE

The Monte Carlo method allows to obtain the solution of the BTE from a microscopic perspective [88]. The main idea is to simulate the motion of individual carriers due to external fields through a periodic crystalline medium. The crystal provides the energy-momentum relation within the band structure theory and it is also responsible for part of the collisions.

There are two main approaches to tackle the BTE formalism within a Monte Carlo method:

- In the first one, a single particle is simulated for a time span that must be long enough to be able to obtain information of the whole electron gas according to the ergodicity principle. This is called the *single-particle Monte Carlo* [89] approach, and it allows obtaining the distribution function in stationary situations and when correlation between particles are not important.

- A more sophisticated option is called the *Ensemble Monte Carlo* (EMC) method, in which a large set of particles is simulated altogether [90], in order to account for the system distribution function. The main advantage of the EMC method is that it allows obtaining instantaneous distribution functions, thus being an appropriate method for the study of transient situations. Besides, the consideration of a large number of particles guarantees that correlations between them (i.e. electron-electron collisions and the effects of degeneracy) can be included in a straightforward manner in the simulation.

In this PhD thesis, an EMC simulator for graphene and other 2D materials of potential interest has been developed. Its possibilities have allowed the study of transport properties in stationary conditions, but also out-of-equilibrium transient phenomena. Also, the intrinsic stochastic nature of the method has permitted to determine some quantities related to fluctuations, such as the noise temperature or diffusion coefficients.

2.3 Ensemble Monte Carlo material simulator

Monte Carlo simulations for the study of electronic transport can be done at a device level (understanding a device as a system with limited dimensions and that depends on external boundary conditions, including contacts) or at the bulk material level. In this section, the Ensemble Monte Carlo method for material simulations will be explained.

The EMC material simulator describes the carrier dynamics in a conductive medium under the hypothesis that some quantities that could affect transport –such as temperature, carrier concentration, impurity density or local electric field– do not vary in space. In other words, it allows accessing the microscopic transport characteristics of a material. As a result of this main hypothesis, the BTE is solved only in the reciprocal (momentum) space, and therefore, after removing all the real-space dependencies, it reduces to:

$$\left[\frac{\partial}{\partial t} + \mathbf{F}_{\mathcal{E}} \nabla_{\mathbf{k}}\right] f_s(\mathbf{r}, \mathbf{k}, t) = \left[\frac{\partial}{\partial t} f_s(\mathbf{r}, \mathbf{k}, t)\right]_{\text{coll}} . \tag{2.7}$$

Although this is a simplification of the BTE, it is appropiate to explain the EMC paradigm.

The method consists on emulating the dynamics of a set of carriers inside the material, each one holding a representative part in the instantaneous distribution function $f_s(\mathbf{r}, \mathbf{k}, t)$. The rules that govern the simulation are the drag due to the external electromagnetic field forces, the energy-momentum dispersion, and the scattering mechanisms.

Time is divided in temporal steps of identical duration. Until the established ending time is reached in simulation, particles are moved during each time step. Carrier motion consist of a sequence of free flights interrupted by scattering mechanisms. Figure 2.1

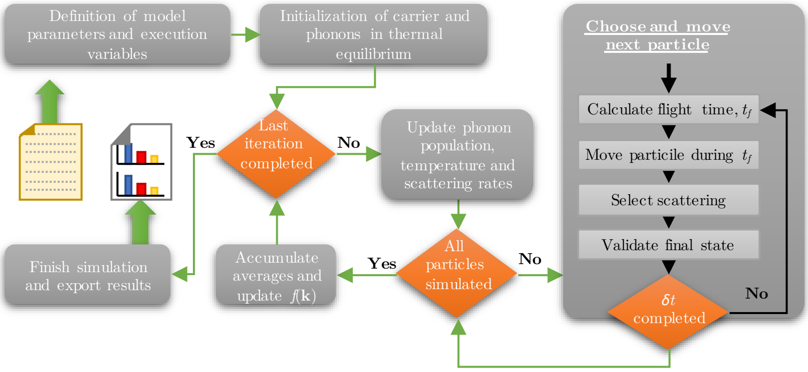

Figure 2.1: Flow diagram of the operation in an EMC simulator

illustrates the full simulation process as a flux diagram. The next subsections will explain the different steps that compose the simulation.

2.3.1 Free flight motion

The dragging effect from the electromagnetic forces has already been explained, since in the EMC approach it is treated semi-classically. For an infinitesimal time step, the carrier wavevector evolves obeying classical electrodynamics:

$$\frac{\partial \mathbf{k}}{\partial t} = \mathbf{F}_{\mathcal{E}} = \frac{q}{\hbar}[\mathbf{E} + \mathbf{v}(\mathbf{k}) \times \mathbf{B}]. \tag{2.8}$$

On its behalf, the influence of the crystal lattice manifests in two ways: the periodic arrangement of the atoms in the crystal gives place to the band structure. It establishes the energy-wavevector relation $\varepsilon_s(\mathbf{k})$, and therefore the way in which carriers gain energy from the action of the electromagnetic forces. This relation also implicitly determines the group velocity:

$$\mathbf{v}_s(\mathbf{k}) = \frac{1}{\hbar}\nabla_{\mathbf{k}}\varepsilon_s(\mathbf{k}). \tag{2.9}$$

Secondly, phonons related to collective lattice oscillations may provoke perturbations to the carrier motion, which can be introduced as scattering mechanisms. Additionally, the presence of a polar dielectric nearby the carriers, charged impurities, lattice defects, or even other carriers also participating in the transport process can be the source of further scattering mechanisms extrinsic to the crystal.

Dealing with such phenomena is a major issue in Monte Carlo simulations, where they are conceived as a set of instantaneous collision events which deviate the particle trajectory.

2.3.2 Scattering rates

Charge carriers in Monte Carlo simulations are considered to experiment *free flights* that are ruled by Newton's second law and are interrupted by scattering mechanisms, described in a quantum mechanics framework. As a consequence of these collisions, electrons and holes experience alterations in their trajectories, changes in their kinetic energy and even sub-band shifts. In the BTE, the effect of the scattering mechanisms is represented statistically in the collision integral as seen in equations (2.5) and (2.6).

$$\begin{aligned}\left[\frac{\partial}{\partial t} f_s(\mathbf{r},\mathbf{k},t)\right]_{\text{coll}} = -\sum_{i,s',\mathbf{k}'} \Big\{ f_s(\mathbf{r},\mathbf{k},t) P_i(s,\mathbf{k}\to s',\mathbf{k}')\left[1-f_{s'}(\mathbf{r},\mathbf{k}',t)\right] - \\ - f_{s'}(\mathbf{r},\mathbf{k}',t) P_i(s',\mathbf{k}'\to s,\mathbf{k})\left[1-f_s(\mathbf{r},\mathbf{k},t)\right]\Big\}. \qquad (2.10)\end{aligned}$$

Here, the change in the occupation of a particular wavevector $\mathbf{k}$ in the band s for a differential time is computed as the probability, for each scattering mechanism i, of taking a particle from any other state into $\mathbf{k}$ in the sub-band s (scattering-in process) minus the probability of leaving from such state to any other (scattering-out process). It has to be noted here that the multiplicative terms f stand for the present occupation, while the terms $[1-f]$, account for the probability that such states are not occupied, i.e., the Pauli exclusion principle. From the perspective of a free particle in Monte Carlo simulations, only the scattering-out terms are of relevance, as the scattering-in events would come as a result of scattering-out transitions involving particles with different initial states.

As a result, a Monte Carlo particle with wavevector $\mathbf{k}$ at the sub-band s experiences a probability to scatter

$$\Gamma_{\text{TOT}}(s,\mathbf{k}) = \sum_i \Gamma_i(s,\mathbf{k}), \qquad (2.11)$$

where Γ_i is the individual scattering probability of each interaction. These single probabilities are calculated as:

$$\Gamma_i(s,\mathbf{k}) = \sum_{s',\mathbf{k}'} P_i(s,\mathbf{k}\to s',\mathbf{k}'), \qquad (2.12)$$

where the already introduced quantity $P_i(s,\mathbf{k}\to s',\mathbf{k}')$ can be determined according to the Fermi's Golden rule [91, 88]:

$$P_i(s,\mathbf{k}\to s',\mathbf{k}') = \frac{2\pi}{\hbar}\left|\mathcal{H}^i_{s,\mathbf{k},s',\mathbf{k}'}\right|^2 \Delta(s,\mathbf{k},s',\mathbf{k}'), \qquad (2.13)$$

with $\mathcal{H}_{s,\mathbf{k},s',\mathbf{k}'}$ being the scattering matrix element for the transition from $s,\mathbf{k}$ to $s',\mathbf{k}'$, which depends on the particular scattering potential associated to each type of interaction. Putting equation (2.13) into equation (2.12) and transforming the summation in $\mathbf{k}$

to an integral in the 2D reciprocal space gives:

$$\Gamma_i(s,\mathbf{k}) = \sum_{s'} \frac{\mathit{\Omega}}{(2\pi)^2} \int_{\mathbf{k}'} \frac{2\pi}{\hbar} \left|\mathcal{H}^i_{s,\mathbf{k},s',\mathbf{k}'}\right|^2 \Delta(s,\mathbf{k},s',\mathbf{k}')\, d\mathbf{k}', \tag{2.14}$$

where $\mathit{\Omega}$ is the normalized area. Regarding the functional factor $\Delta(s,\mathbf{k},s',\mathbf{k}')$, it contains the restrictions over the final states, and depends on the type of interaction. In the case of elastic collisions, it reads:

$$\Delta_{\text{elastic}}(s,\mathbf{k},s,\mathbf{k}') = \delta(\varepsilon' - \varepsilon), \tag{2.15}$$

that ensures energy conservation. Here, we have introduce the shorthand for the energy associated to the sub-band and wavevector $\varepsilon_i = \varepsilon_{s_i}(\mathbf{k}_i)$. For short range, carrier-carrier collisions, which involve a second carrier with initial and final states $\mathbf{k}_2$ and $\mathbf{k}_2'$ in the sub-bands s_2 and s_2' respectively, an additional Dirac delta appears in order to preserve total momentum:

$$\Delta_{\text{c-c}}(s,\mathbf{k},s',\mathbf{k}',s_2,\mathbf{k}_2,s_2',\mathbf{k}_2') = \delta(\varepsilon+\varepsilon_2-\varepsilon'-\varepsilon_2')\delta(\mathbf{k}+\mathbf{k_2}-\mathbf{k}'-\mathbf{k_2}'). \tag{2.16}$$

As it concerns scattering with inelastic phonons[1],

$$\Delta_\nu(s,\mathbf{k},s',\mathbf{k}') = \left[n_\nu(\mathbf{q}) + \tfrac{1}{2} \pm \tfrac{1}{2}\right] \delta[\varepsilon' - \varepsilon \mp \hbar\omega_\nu(\mathbf{q})], \tag{2.17}$$

where ν identifies the phonon mode, $\mathbf{q} = \mathbf{k}' - \mathbf{k}$ is the exchange wavevector, $\pm\hbar\omega^\nu(\mathbf{q})$ is the energy shift of the electron[2] due to the absorption(+) or emission(−) of a phonon with the corresponding vibrational frequency at such wavevector, $\omega_\nu(\mathbf{q})$. The factors $n_\nu(\mathbf{q})$ and $n_\nu(\mathbf{q}) + 1$ are the annihilation and creation operators related to absorption and emission processes, respectively, with $n_\nu(\mathbf{q})$ being the phonon occupancy at $\mathbf{q}$. A thorough explanation on the calculation of this quantity will be given in section 2.3.5.

2.3.3 Free fllight duration

Now that, except for the scattering matrix elements that depend on the particular material and collision type, all the necessary basis to calculate the scattering probabilities have been presented, it must be explained how the duration of free flights is computed [88].

For any carrier in a particular state, its free flight duration is randomly determined in agreement with the total scattering probability associated to this initial state according to equation (2.11). So, the probability for an electron or hole of *not* undergoing a scattering mechanism during a time interval τ is $1 - \Gamma_{\text{TOT}}(s,\mathbf{k})\tau$. Therefore the probability that

---

[1] Here, it could apply to any inelastic scattering mechanism besides phonons, as, for example, plasmons, provided the right creation/annihilation operator is substituted.

[2] Note that a hole would experience opposite energy modifications.

a carrier moves though the reciprocal space for a time τ split in a large number of time intervals, n, is:

$$S_{\text{fly}}(\tau) = \prod_{j=1}^{n} \left[1 - \Gamma_{\text{TOT}}(s, \mathbf{k}_j)\frac{\tau}{n}\right], \tag{2.18}$$

being $\mathbf{k}_t$ the wavevector after having moved during a time interval t. Taking logarithms in equation (2.18), and provided that $\Gamma_{\text{TOT}}(s_j, \mathbf{k}_j)\tau/n \ll 1$, in the limit $n \to \infty$, we get:

$$S_{\text{fly}}(\tau) = \exp\left[-\int_0^{\tau} \Gamma_{\text{TOT}}(s, \mathbf{k}_{t'})\, dt'\right]. \tag{2.19}$$

Consequently, the probability per unit time that a carrier with initial wavevector $\mathbf{k}$ at the sub-band s freely flights during a time interval τ and then undergoes a collision is:

$$P_{\text{fly}}(\tau) = \Gamma_{\text{TOT}}(s, \mathbf{k}_{\tau}) \exp\left[-\int_0^{\tau} \Gamma_{\text{TOT}}(s, \mathbf{k}_{t'})\, dt'\right]. \tag{2.20}$$

In order to apply the Monte Carlo method to calculate these free flight times, with uniform distributions of $r \in [0, 1]$,

$$r = 1 - \exp\left[-\int_0^{\tau} \Gamma_{\text{TOT}}(s, \mathbf{k}_{t'})\, dt'\right]. \tag{2.21}$$

However, this equation would require complex inversions to obtain τ of an integral that is not analytically evaluable. To sort out this inconvenience, there exists a quite simple alternative called *self-scattering* [88], consisting of introducing a virtual scattering with a probability such that the total scattering rate, including self-scattering is a constant $\tilde{\Gamma}$ so $\Gamma_{\text{s/s}}(s, \mathbf{k}) = \tilde{\Gamma} - \Gamma_{\text{TOT}}(s, \mathbf{k})$, being $\Gamma_{\text{s/s}}(s, \mathbf{k})$ the self-scattering rate, added at the end of the scattering probabilities stack. In this way, equation (2.20) becomes:

$$P_{\text{fly}}(\tau) = \tilde{\Gamma} \exp(-\tilde{\Gamma}\tau). \tag{2.22}$$

Now, equation (2.20) can be evaluated and inverted, which results in free flights of duration

$$\tau_{\text{f}} = -\frac{\log(1 - r)}{\tilde{\Gamma}}. \tag{2.23}$$

The constant $\tilde{\Gamma}$ value is conveniently chosen according to the maximum Γ_{TOT} for the states in the range of interest. This technique introduces some penalty in computation time due to the introduction of a big number of fictitious events. There are some techniques that reduce this computation time. An efficient approach diminishes the value of $\tilde{\Gamma}$ along successive tries of calculating the free flight [92].

2.3.4 The scattering process

After performing a free flight motion under the previously described laws, the particle undergoes a scattering mechanism. A new random number, r, is calculated, and if

$r\tilde{\Gamma} > \Gamma_{\mathrm{TOT}}(s, \mathbf{k})$, then it means that the particle undergoes self-scattering: its state does not change, and a new free flight must be calculated. On the contrary case, the particle collides due to the mth scattering, which is selected paying attention to the individual probabilities of the scattering mechanisms acting on the particle state after the free flight, so that

$$\sum_{j=1}^{m-1} \Gamma_j(s, \mathbf{k}) < r\tilde{\Gamma} < \sum_{j=1}^{m} \Gamma_j(s, \mathbf{k}). \tag{2.24}$$

Afterwards, the mth scattering is evaluated in order to choose a final state (s' and $\mathbf{k}'$) for the particle, according to the probability distribution depending on the wavevector orientation and final sub-band. This means that the final state must be conveniently selected taking into account the probability distribution of the integrand in equation (2.14). Also, some mechanisms can also imply the need of using rejection techniques, as it will be seen in the following sections.

Once that the state after the collision –$\mathbf{k}'$ in the sub-band s'–, has been conveniently chosen, the term $[1 - f_{s'}(\mathbf{k}')]$ from equation (2.10) must be now taken into account in order to consider the Pauli exclusion principle and consequently, degeneracy effects. A simple way to deal with this at the material level within EMC, is the Lugli-Ferry technique [93]. This method involves a rejection procedure based on setting a limit to the particle occupation in the cells of a discretized $\mathbf{k}$-space, N_{c} [3]. In a two-dimensional system, this quantity is given by:

$$N_{\mathrm{c}} = g_s g_v \frac{\Delta k_x \Delta k_y}{(2\pi)^2} \xi^{-1}, \tag{2.25}$$

being ξ the relative weight of each particle in terms of carrier density, and Δk_x and Δk_y the cell dimensions in each direction for a Cartesian discretization of the reciprocal space. The factors g_s an g_v are the spin[4] and valley[5] degeneracies, and ξ is the weight of each particle[6]. Once the final state after a scattering mechanism is chosen, the inequality $NP(s', \mathbf{k}') < rN_{\mathrm{c}}(s', \mathbf{k}')$ is evaluated, being r a newly calculated random number, and $NP(s', \mathbf{k}')$ the amount of particles populating the differential cell that contains the wavevector $\mathbf{k}$ in the sub-band s. If such condition is fulfilled, the transition is accepted. Otherwise, due to Pauli rejection, it is assumed that the scattering event did not take

---

[3] The local distribution function in the momentum space can be calculated as the quotient of the number of particles in the cell and the maximum allowed: $f_s(\mathbf{k}) = NP(s, \mathbf{k})/N_{\mathrm{c}}(s, \mathbf{k})$.

[4] Spin degeneracy is taken as $g_s = 2$ along this thesis, as no study concerning spin polarization has been carried out.

[5] g_v equals the number of valleys that share the same energy-momentum dispersion and are treated as one in the distribution function.

[6] In the material simulator this quantity is determined as $\xi = \frac{n}{NP}$, being n the carrier density and NP the number of simulated particles.

place and the particle does not change its state at the end of its free flight, and a new subsequent free flight takes place.

2.3.5 Out-of-equilibrium phonons

Electron transport in a periodic crystal is subjected to scattering due to collective excitations of atoms in the crystalline structure. In quantum mechanics these modes of vibration are quantified by quasi-particles called phonons [94]. As a result of the scattering activity of charge carriers with phonons, the later can be excited through emission processes, usually with high-energy electrons that transfer part of their energy to the lattice in the form of new phonons. In a complementary process, phonons can be absorbed, in which case the phonon energy is transferred to an electron. When carriers are taken out of equilibrium (for example, increasing their energy by applying a strong electric field or a laser pulse), phonon absorption processes will be outnumbered by emissions. When the characteristic relaxation times of phonons are longer than the rate at which they are created, the phonon population grows. Such circumstance also alters the scattering rates, that are enhanced due to the elevated phonon population. This phenomenon is known as the *hot phonon* (HP) effect [95–98], and it is a critical issue in nonlinear electronic transport at high fields. Therefore, dealing with this enhanced phonon population is an issue to be tackled in a careful manner.

Similarly as in the case of electrons, phonon dynamics and transport can be modeled by the BTE [99, 100, 97]. In a simplified version, the phonon scattering collision integral is substituted by a simple relaxation term. Then, the BTE for phonons reads:

$$\left(\frac{\partial}{\partial t}+\frac{\partial \mathbf{r}}{\partial t}\nabla_{\mathbf{r}}\right) n_\nu(\mathbf{q}) = \left[\frac{\partial n_\nu(\mathbf{q})}{\partial t}\right]_{\text{coll}}. \tag{2.26}$$

Now, we simplify this equation by substituting the collision integral by a relaxation term ruled by a phenomenological decay time. This simplified treatment is known as the relaxation time approximation [101], and applied to the phonon BTE, it yields:

$$\left(\frac{\partial}{\partial t}+\frac{\partial \mathbf{r}}{\partial t}\nabla_{\mathbf{r}}\right) n_\nu(\mathbf{q}) = -\frac{n_\nu(\mathbf{q})-n_\nu^{\text{eq}}(\mathbf{q},T_L)}{\tau_\nu}, \tag{2.27}$$

where $n_\nu(\mathbf{q})$ holds the same meaning as in equation (2.17), τ_ν is the characteristic relaxation time, and $n_\nu^{\text{eq}}(\mathbf{q},T_L)$ is the phonon occupation at $\mathbf{q}$ in thermal equilibrium given by the Bose-Einstein statistics [102]:

$$n_\nu^{\text{eq}}(\mathbf{q},T_L) = \left\{\exp\left[\frac{\hbar\omega_\nu(\mathbf{q})}{k_B T_L}\right]-1\right\}^{-1}, \tag{2.28}$$

with k_B being the Boltzmann constant, and T_L the lattice temperature. In a bulk material context, under homogeneous conditions, the previous equation yields:

$$\frac{\partial n_\nu(\mathbf{q})}{\partial t} = -\frac{n_\nu(\mathbf{q}) - n_\nu^{\text{eq}}(\mathbf{q}, T_L)}{\tau_\nu}. \tag{2.29}$$

This equation reflects the trend to recover a phonon population in equilibrium through an exponential decay of the excited modes characterized by the relaxation time τ_ν. Characteristic life times for the different phonon modes can be obtained experimentally [103–105], or theoretically by means of molecular dynamics simulations [106, 107].

Implementation of the electron/hole-phonon coupled system is performed the following way [108]: first, the areas of the reciprocal space with wavevectors expected to intervene in electron-phonon scattering events are discretized in a mesh. This mesh is duplicated to create a histogram, $h_\nu(\mathbf{q})$ in which the emission and absorption events are recorded. Every time an inelastic phonon scattering takes place, an emission (+1) or absorption (−1) is added up in the corresponding cell of the histogram for the transition vector $\mathbf{q}$. Once that all carriers are simulated along a time step, the phonon population is updated, by integrating equation (2.29) as follows:

$$n_\nu(\mathbf{q}, t_0 + \delta t) = n_\nu(\mathbf{q}, t_0) - \frac{n'_\nu(\mathbf{q}, t + \delta t) - n_\nu^{\text{eq}}(\mathbf{q}, T_L)}{\tau_\nu}\delta t, \tag{2.30}$$

where $n'_\nu(\mathbf{q}, t)$ represents the phonon population after the last iteration as:

$$n'_\nu(\mathbf{q}, t_0 + \delta t) = n_\nu(\mathbf{q}, t_0) + \Delta_\nu h_\nu(\mathbf{q}), \tag{2.31}$$

with the factor Δ_ν equal to:

$$\Delta_\nu = \frac{(2\pi)^2}{\Delta q_x \Delta q_y}\xi, \tag{2.32}$$

where Δq_x and Δq_y are the mesh sizes in Cartesian discretization of the reciprocal space.

After the phonon population has been updated, the histogram h_ν is set to zero. Then, the electron-phonon scattering probabilities are updated. Since a probability mapping according to the phonon population grid would require large computational resources, a rejection technique is employed instead. Phonon scattering probabilities are calculated by substituting $n_\nu(\mathbf{q})$ in equation (2.17) by the maximum occupation according to equation (2.30), $n_\nu^{(\max)}$. That gives an enhanced scattering probability that is compensated as follows: a final state, and therefore a transition vector $\mathbf{q}$, is selected considering a uniform distribution of $n_\nu(\mathbf{q})$. Then, if the inequality that involves the random number r

$$r\left[n_\nu^{(\max)} + \tfrac{1}{2} \pm \tfrac{1}{2}\right] < \left[n_\nu(\mathbf{q}) + \tfrac{1}{2} \pm \tfrac{1}{2}\right] \tag{2.33}$$

is true, the scattering is accepted, and rejected otherwise.

2.3.6 Self-consistent Joule heating

Another concern in high-field transport, that also relates with the electron-lattice interaction, is self-heating or Joule heating [109]. The dissipation of the heat generated by electron-phonon processes becomes a critical issue to determine the electron transport properties of 2D materials, particularly taking into account the influence that the underlying substrate may exert.

To include Joule heating effects in the EMC code, we considered the one dimensional thermal series resistance heat dissipation model proposed by Dorgan, Bae, and Pop [110, 111], as illustrated in figure 2.2. The temperature increment is computed as follows:

$$T_{2\mathrm{D}} - T_0 \approx P(R_B + R_{\mathrm{sub}} + R_{\mathrm{wafer}}), \tag{2.34}$$

where T_0 is the ambient temperature, $T_{2\mathrm{D}}$ is the 2D material temperature, $R_B = (h_{\mathrm{K}}A)^{-1}$ is the thermal boundary or Kapitza resistance associated with the 2D material and the substrate [112] (h_{K} being the thermal conductivity of this interface, and A the area of the sample), $R_{\mathrm{sub}} = t_{\mathrm{sub}}(\kappa_{\mathrm{sub}}A)^{-1}$ is the thermal resistivity of the substrate, t_{sub} its thickness, κ_{sub} its thermal conductivity, and $R_{\mathrm{wafer}} = (2\kappa_{\mathrm{wafer}}\sqrt{A})^{-1}$ the wafer thermal resistance, with κ_{wafer} the conductivity of the wafer material (usually doped Si). P is the dissipated power, which could be determined from macroscopic experimental quantities

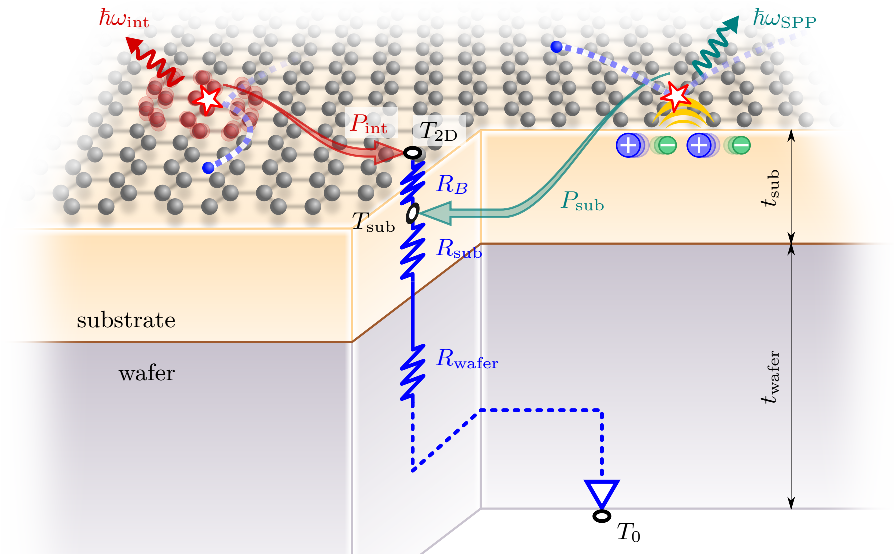

Figure 2.2: Illustration of the distributed resistance model for the Joule heating approach in EMC for graphene supported on a dielectric substrate. Heat flows from the 2D material towards the wafer. P_{int} and P_{sub} are the net power emitted by intrinsic and substrate phonons respectively due to scattering with charge carriers.

as $P = \Delta VI$. Such model can be easily adapted to the material EMC simulator, as it is valid for relatively large samples where the influence of the contacts and the edges is not very important. In the EMC model, instead of using the dissipated energy obtained from the current density, the net power transferred to each phonon mode can be recorded every time step like:

$$P = \sum_{\nu,\mathbf{q}_0} P_{\nu,\mathbf{q}_0}, \tag{2.35}$$

where $P_{\nu,\mathbf{q}_0}$ is the power transferred via the accepted scattering mechanisms with the phonon mode ν with wavevector $\mathbf{q}_0$, which reads [113]:

$$P_{\nu,\mathbf{q}_0} = \sum \left[\varepsilon - \varepsilon'\right] \delta t^{-1} \xi, \tag{2.36}$$

where the summation refers to all the accepted scattering events with the phonon mode ν during the time step δt, and $\varepsilon - \varepsilon' = \pm\hbar\omega_\nu(\mathbf{q}_0)$ are the energy shifts corresponding to the difference associated to the states before and after the scattering. This way, the power transferred to intrinsic (i.e., towards the 2D material) and to the substrate phonon modes[7] can be easily isolated as P_{int} and P_{sub} respectively by summing over the corresponding phonon modes. Finally, every time step the temperatures are updated as [109]:

$$T_{\text{sub}} - T_0 = (P_{\text{int}} + P_{\text{sub}})(R_{\text{sub}} + R_{\text{wafer}}) \tag{2.37a}$$

$$T_{\text{2D}} - T_{\text{sub}} = P_{\text{int}} R_B, \tag{2.37b}$$

where T_0 is the ambient temperature external to the sample. In the case of a free-standing sample, when a substrate is not present, this simplifies to:

$$T_{\text{2D}} - T_0 = P_{\text{int}} R_B. \tag{2.38}$$

2.3.7 Generation and recombination mechanisms

The EMC simulator allows interband processes between valence and conduction bands, that is, the production or annihilation of electron-hole pairs. Among these processes one could list phonon assisted generation/recombination, impact ionization and Auger processes, or band-to-band tunneling, among other possible sources.

Scattering processes that imply a final state in a different band (i.e. from conduction to valence, or vice-versa) can be treated straightforwardly as just another scattering mechanism. However, this approach can only be applied to recombination mechanisms, since a free particle must select the particular kind of collision.

---

[7] Surface Polar Phonon modes will be presented for the case of graphene in the forthcoming section 2.4.6.

A second option is to compute a total number of particles to generate and recombine, that is implemented as follows. First, a scattering probability ($\Gamma^{i}_{\mathrm{G/R}}$) is computed, and assigned to an initial state of a carrier. Such initial state can be characterized by the sub-band, s and its energy, $\Gamma^{(\mathrm{i})}_{\mathrm{G/R}}(s,\varepsilon)$, wavevector, $\Gamma^{(\mathrm{i})}_{\mathrm{G/R}}(s,\mathbf{k})$, or wavevector magnitude, $\Gamma^{(\mathrm{i})}_{\mathrm{G/R}}(s,k)$. We suppose that these states are full[8], and consequently under this assumption we can compute the number of electron-hole pairs that would undergo a particular i mechanism of generation or recombination during a time step as:

$$N^{(\mathrm{i})}_{\mathrm{G/R}} = \sum_{s,\varepsilon} \Gamma^{(\mathrm{i})}_{\mathrm{G/R}}(s,\varepsilon)\mathrm{DoS}(s,\varepsilon)\Delta\varepsilon\Delta t \tag{2.39}$$

for probabilities associated with the energy, being DoS is the density of states associated to the dispersion of the sub-band s at energy ε, and $\Delta\varepsilon$ is the step of the energy discretization in the simulator. After the calculation of these two quantities, N_{G} attempts of generation and N_{R} of recombination will be made along the simulation of the time step. In each try, the mechanism is selected according to the contribution of each type of transition to the total. Afterwards, the initial wavevector $\mathbf{k}$ and sub-band s are selected taking into consideration the probability distribution and the density of states considered in equation (2.39), which are also stored in memory. Then, since we have considered that the initial states are full, a rejection step is performed by testing the condition $f_s(\mathbf{k}) > r$. If it is not met, then we give up on this try to generate or recombine a carrier in this state. On the contrary it means that there are enough carriers to perform the transition. In the case that we are attempting a recombination process, we look for a carrier with the state closest to the chosen one. In the case of a generation mechanism, we just move to the next step, which consist in looking for a final sub-band s' and wavevector $\mathbf{k}'$ the same way it is done in intraband mechanisms. If any self-rejection (like for example, in the treatment of hot phonons) must be done for the particular i mechanism, it is done in this step as well. Once the final state is decided, the Pauli exclusion principle is treated as explained in section 2.3.4. The final step is performing the transition. In the case of a recombination mechanism, a new particle must be found close to the final state. Then both particles would be taken out of simulation. In the case of a generation event, a hole is created in the valence band and an electron in the conduction band.

As it regards the two possible approaches for treating carrier recombination, several tests have been made in the context of out of equilibrium dynamics (photoexcitation) and carrier transport, yielding almost the same results, with negligible differences.

---

[8] This means, that the valence band would be full of electrons, and the conduction band –if the probability is applied here– full of holes (depleted of electrons).

2.4 Physical model of Monolayer Graphene

Once that the basis of the simulation approach has been settled in the previous sections, here, the particularities of monolayer graphene (MLG) will be detailed.

Graphene is a one atom thick allotrope of carbon, with its atoms arranged in an hexagonal (usually referred to as *"honeycomb"*) lattice [114]. This structure can be seen as two overlapping triangular lattices that feature two atoms per unit cell, as pictured in figure 2.3.

2.4.1 Band structure

From the tight-binding Hamiltonian, considering that electrons in graphene can hop up to next-nearest-neighbor atoms, and assuming electron-hole symmetry the eigenenergies have the form [114, 33, 115]:

$$\varepsilon_s^{\mathrm{TB}}(\mathbf{k}) \approx s\gamma\sqrt{1+4\cos\left(\frac{\sqrt{3}a}{2}k_x\right)\cos\left(\frac{a}{2}k_y\right)+4\cos^2\left(\frac{a}{2}k_y\right)}, \tag{2.40}$$

where, s is the sub-band index ($s = 1$ for the conduction band π^*, and $s = -1$ for the valence band π), and γ is the hopping energy, which is usually taken as a fitting factor to *ab-initio* calculations [114, 116], ranging between 2.7 eV to 3.1 eV.

Since the main interest throughout this thesis is the investigation of carrier transport properties for electronic applications –i.e., at relatively small energies and carrier concentrations–, the focus must be set close to the conduction band minima and valence band maximum. Graphene features zero-band gap conical dispersion around the six cor-

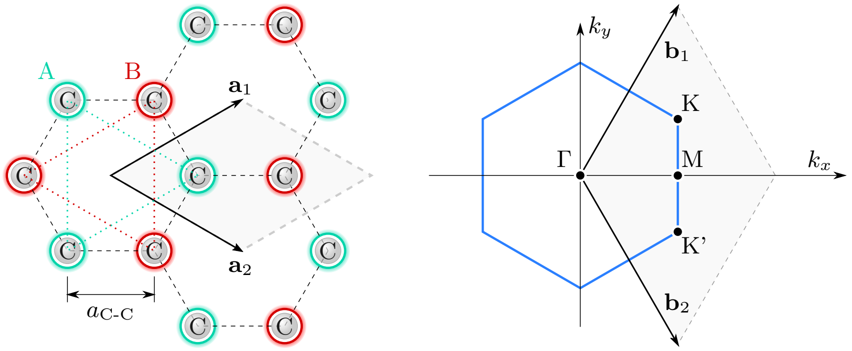

Figure 2.3: (Left) Representation of the Bravais lattice of graphene. The bravais lattice is composed of two interpenetrated triangular lattices A and B with unit cell vectors $\mathbf{a}_1$ and $\mathbf{a}_2$, with $a = \sqrt{3}a_{\mathrm{C-C}}$, being $a_{\mathrm{C-C}} \approx 1.42$ Å the carbon-carbon interatomic distance. (Right) First Brillouin zone, with reciprocal lattice vectors $\mathbf{b}_1$ and $\mathbf{b}_2$.

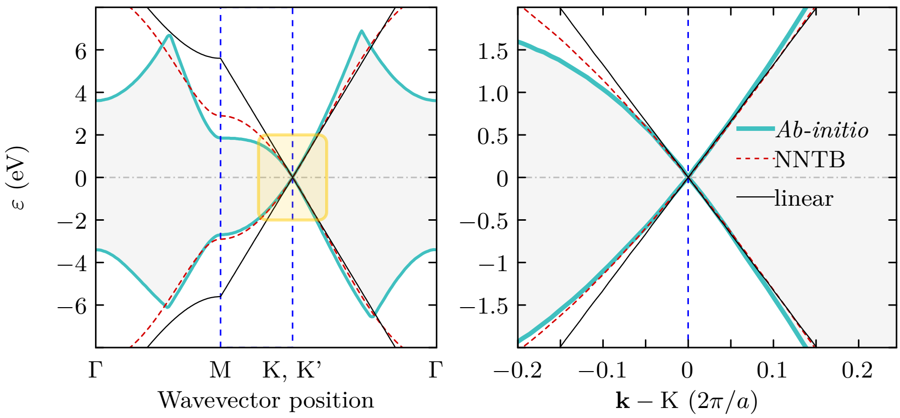

Figure 2.4: *Ab-initio* band structure of graphene calculated by means of the DFT (LDA-GW_0), adapted from [116] (light green thick solid line) and its comparison with the nearest-neighbour tight-binding model (red dashed line) with $\gamma = 2.9\,\mathrm{eV}$, and he isotropic linear approximation (black thin solid line), being $v_F = 1 \times 10^6\,\mathrm{m/s}$. The right panel allows comparing the good agreement between the linear approximation and the rest of the models in the low-energy range.

ners of the hexagonal first Brillouin zone, giving rise to two valleys at the points K and K′ in the reciprocal space as seen in figure 2.4. These are known the Dirac points [114, 117], and are precisely the conduction band minimum and valence band maxima where conducting electrons and holes will mostly lie. Expanding the tight-binding expression of the energy eigenstates around these symmetry points, one has [118, 33]:

$$\varepsilon_s(\mathbf{k} \sim \mathrm{K}) \approx s\hbar v_F \left|\mathbf{k} - \mathrm{K}\right|, \tag{2.41}$$

with K being the position of the corresponding Dirac point in the reciprocal space. This expression[9] resembles the linear energy-momentum relation of the Dirac equation describing massless particles, where the speed of light is replaced by the Fermi velocity, $v_F = 4\gamma a/2 \approx 1 \times 10^6\,\mathrm{m/s}$, according to the aforementioned hopping energy range, being in good agreement with estimations from experimental results [119]. In the right pane of figure 2.4 the energy dispersion of MLG for the π and π^* bands obtained from *ab-initio* calculations, the nearest-neighbour tight-binding method, and the linear approximation are shown, where a good match can be obtained even at energies as high as 1 eV.

Degenerate valleys will be used along this thesis, which means both K and K′ valleys will be treated as one ($g_v = 2$). So, for convenience in the ε-$\mathbf{k}$ relationship, from now on, we take $\mathbf{k}$ as the electron or hole wavevector with origin at the Dirac point,

$$\varepsilon_s(\mathbf{k}) = s\hbar v_F |\mathbf{k}|. \tag{2.42}$$

---

[9] For simplicity, in this equation the symmetry point K was considered, but it also applies to the K' point.

From this expression, one obtains the group velocity as $\hbar^{-1}\nabla_{\mathbf{k}}\varepsilon_s(\mathbf{k})$:

$$\mathbf{v}_s(\mathbf{k}) = s v_F \frac{\mathbf{k}}{|\mathbf{k}|}, \tag{2.43}$$

that is, carriers travel as if they were massless particles, with a constant group velocity (v_F) [118, 117] independently on their energy, with an orientation that is parallel to their wavevector.

Finally, the density of states (DoS) in our energy range of interest is [114]:

$$\mathrm{DoS}(\varepsilon) = g_s g_v \frac{|\varepsilon|}{2\pi(\hbar v_F)^2}. \tag{2.44}$$

2.4.2 Scattering with intrinsic phonons

The crystalline structure of graphene features six phonon branches [120, 116], as shown in figure 2.5. Borysenko et al. studied in [121], by means of a first-principles density-functional perturbation theory analysis, the electron-phonon coupling with the different modes. Given the reflection symmetry, σ_h, the two out-of-plane (ZA and ZO) modes barely couple to the charge carriers. As for the remaining phonon branches (in-plane modes), comparable electron-phonon couplings are found at room temperature. The most relevant cases are the optical TO-K, K′ (intervalley) and LO-Γ (intravalley), due to Kohn anomalies at such symmetry points [122, 123]. Acoustic LA and TA modes couple

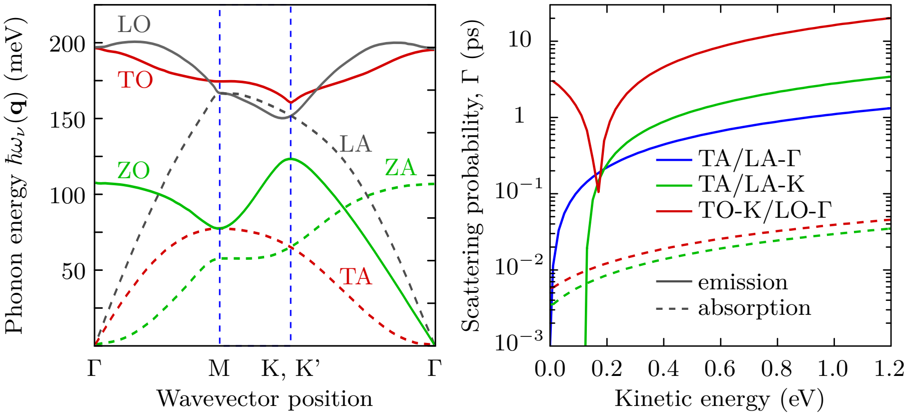

Figure 2.5: (Left panel) *Ab-initio* phonon dispersion in MLG, adapted from [116]. (Right panel) electron-phonon scattering rates at $T_0 = 300\,\mathrm{K}$ with deformation potentials as proposed by [121]. Scattering probability due to optical phonon emission at energies below $\hbar\omega_{\text{TO-K/LO-}\Gamma}$ corresponds to transitions from the conduction band towards valence band (phonon assisted recombination). Although not shown, the same feature takes place for phonon absorption of electrons in the valence band at energies over $-\hbar\omega_{\text{TO-K/LO-}\Gamma}$ due to phonon assisted generation.

at long wavelengths (Γ), and are also responsible for intervalley transitions (K, K'), as it is clearly visible from the onset of phonon emission at $\sim 120\,\mathrm{meV}$. The scattering coupling matrices obtained in this study, are not believed to be significantly sensitive to the environment (e.g. substrates) [124].

A simple scheme has been adopted in the spirit of [121] to include scattering mechanisms with intrinsic phonons. For the TA-Γ and LA-Γ modes, the first-order deformation potential approximation [125] is used. The scattering matrix reads:

$$\left|\mathcal{H}^{D_{1,\nu}}_{s,\mathbf{k},s',\mathbf{k}'}\right|^2 = \frac{{D_{1,\nu}}^2 \hbar |\mathbf{q}|}{2\varOmega \rho_m v_\nu} F(s,\mathbf{k},s',\mathbf{k}'), \tag{2.45}$$

where $D_{1,\nu}$ is the first-order deformation potential, ρ_m the sheet mass density, and v_ν the sound velocity (related to the slope of the acoustic phonon mode dispersion), and $F(s,\mathbf{k},s',\mathbf{k}')$ is the wavefunction overlap, which in MLG is given by [126]:

$$F(s,\mathbf{k},s',\mathbf{k}') = \frac{1 + ss'\cos(\theta_{\mathbf{k},\mathbf{k}'})}{2} = \frac{1}{2}\left(1 + ss'\frac{\mathbf{k}\cdot\mathbf{k}'}{|\mathbf{k}||\mathbf{k}'|}\right), \tag{2.46}$$

with $\theta_{\mathbf{k},\mathbf{k}'}$ being the angle between the vectors $\mathbf{k}$ and $\mathbf{k}'$.

Putting equations (2.14) and (2.17) together, one has:

$$\Gamma_{D_{1,\nu}}(s,\mathbf{k}') = \sum_{s'} \frac{\varOmega}{(2\pi)^2} \int_{\mathbf{k}'} \frac{2\pi}{\hbar} \frac{{D_1}^2 \hbar |\mathbf{q}|}{2\varOmega \rho_m v_\nu} F(s,\mathbf{k},s',\mathbf{k}') \\ \left[n_\nu(\mathbf{q}) + \tfrac{1}{2} \pm \tfrac{1}{2}\right] \delta[\varepsilon' - \varepsilon \mp \hbar\omega_\nu(\mathbf{q})]\, d\mathbf{k}\,. \tag{2.47}$$

For the combined TA/LA mode at Γ, providing it is a non-degenerated phonon system, we can apply equipartition conditions [127], which allows to approximate $n_\nu(\mathbf{q}) \approx k_B T_L / \hbar\omega_\nu(\mathbf{q})$ for temperatures above the Bloch-Grüneisen temperature [128]. Considering that the phonon energy grows linearly around Γ as $\hbar\omega_{\mathrm{TA/LA}}(\mathbf{q} \sim \Gamma) \approx v_{\mathrm{TA/LA}}|\mathbf{q}|$, being $v_{\mathrm{TA/LA}}$ the sound velocity in graphene. As a consequence, the phonon occupation approximates as $n_{\mathrm{TA/LA}}(\mathbf{q} \sim \Gamma) \approx k_B T_L / \hbar v_{\mathrm{TA/LA\text{-}\Gamma}}|\mathbf{q}|$. Moreover, given the difference between electron and phonon dispersion slopes, this scattering can be considered as *quasi-elastic*. Therefore, the exchange energy in the collision is negligible and we can consider $\omega_{\mathrm{TA/LA}}(\mathbf{q} \sim \Gamma) \approx 0$. As a consequence, the magnitude of the final and initial wavevectors (energies) are very similar, so

$$\Delta_{\mathrm{TA/LA\text{-}\Gamma}}(s,\mathbf{k},s',\mathbf{k}') = \frac{2 k_B T_L}{\hbar v_{\mathrm{TA/LA\text{-}\Gamma}}|\mathbf{q}|}\delta(\varepsilon' - \varepsilon). \tag{2.48}$$

Due to the negligible electron energy shift, also interband transitions are ruled out. With all this, equation (2.47) turns into:

$$\Gamma^{(\mathrm{MLG})}_{D_{1,\nu}}(s,\mathbf{k}') = \frac{{D_{1,\nu}}^2 k_B T_L}{2\pi \rho_m {v_\nu}^2} \int_{\mathbf{k}} F(s,\mathbf{k},s',\mathbf{k}')\delta(\varepsilon' - \varepsilon)\, d\mathbf{k}\,. \tag{2.49}$$

From here on, we will take advantage of the isotropic nature of the electron band dispersion, which allows us to obtain the carrier energy-dependent scattering probabilities performing the integral over $\mathbf{k}'$:

$$\Gamma_{D_{1,\nu}}^{(\mathrm{MLG})}(\varepsilon) = \frac{{D_{1,\nu}}^2 k_B T_L |\varepsilon|}{2\hbar^3 {v_F}^2 \rho_m {v_\nu}^2}. \tag{2.50}$$

The most relevant parameter for this scattering mechanism is the deformation potential. A value of $D_{1,\text{TA/LA-}\Gamma} = 6.8\,\text{eV}$ allows to capture the contribution of both modes, while the sound velocity $v_{\text{TA/LA-}\Gamma} = 2 \times 10^4\,\text{m/s}$, that has been taken as the average for the TA and LA branches [128].

The wavefunction overlap term brings up anisotropy to this mechanism, which suppresses backscattering [128]. Since equation (2.50) contains summation of probabilities for all final $\mathbf{k}'$ directions, at every scattering event with TA/LA-Γ phonons, the relative angle between the final and initial wavevectors is determined in a Monte Carlo routine according to the distribution $\cos^2(\theta_{\mathbf{k},\mathbf{k}'}/2)$.

As it regards the inelastic acoustic (TA/LA-K) and optical (TO-K and LO-Γ), the zeroth-order deformation potential [125] formalism is used. Its scattering matrix is:

$$\left|\mathcal{H}_{s,\mathbf{k},s',\mathbf{k}'}^{D_{0,\nu}}\right|^2 = \frac{{D_{0,\nu}}^2 \hbar}{2\Omega \rho_m \omega_\nu(\mathbf{q})}. \tag{2.51}$$

Again, the scattering matrix is applied, as previously done, in equation

$$\Gamma_{D_{0,\nu}}(s,\mathbf{k}) = \sum_{s'} \frac{\Omega}{(2\pi)^2} \int_{\mathbf{k}'} \frac{2\pi}{\hbar} \frac{{D_{0,\nu}}^2 \hbar}{2\Omega \rho_m \omega_\nu(\mathbf{q})} \left[n_\nu(\mathbf{q}) + \tfrac{1}{2} \pm \tfrac{1}{2}\right] \delta[\varepsilon' - \varepsilon \mp \hbar\omega_\nu(\mathbf{q})]\, d\mathbf{k}\,. \tag{2.52}$$

From here, in order to obtain the corresponding rates for electron-phonon scattering with these modes, negligible dispersion is assumed: $\omega_\nu(\mathbf{q} \sim \mathbf{q}_0) \approx \omega_{\nu,\mathbf{q}_0}$, being $\mathbf{q}_0$ the symmetry point. Integrating over $\mathbf{k}'$, we get the final expression for intrinsic inelastic (emission and absorption) phonon scattering as a function of the carrier energy:

$$\Gamma_{D_{0,\nu}}^{(\mathrm{MLG})}(\varepsilon) = \sum_{s'} \frac{{D_{0,\nu}}^2 (\varepsilon \mp \hbar\omega_{\nu,\mathbf{q}_0})}{2(\hbar v_F)^2 \rho_m \omega_{\nu,\mathbf{q}_0}} \left[n_\nu(\mathbf{q}) + \tfrac{1}{2} \pm \tfrac{1}{2}\right]. \tag{2.53}$$

The summation over the possible final bands has been kept since it is expected that optical phonons provide an interband pathway for carrier generation (via phonon absorption) and recombination [129] (via phonon emission) for energies such that $|\varepsilon| < \hbar\omega_{\nu,\mathbf{q}_0}$. The contributions for the optical phonons have been included though a combined TO-K/LO-Γ mode, being its energy $\hbar\omega_{\text{TO-K/LO-}\Gamma} = 164.5\,\text{meV}$, with a deformation potential $D_{0,\text{TO-K/LO-}\Gamma} = 100\,\text{eV/nm}$ [121]. The independent contributions of intervalley and intravalley modes is of little relevance, since the K and K' valleys of the band structure are considered as degenerate. As for the inelastic intervalley acoustic phonons, the total contribution of the TA/LA-K has been accounted for with a deformation potential $D_{0,\text{TA/LA-K}} = 35\,\text{eV/nm}$ and energy $\hbar\omega_{\text{TA/LA-K}} = 124\,\text{meV}$ [121].

The right panel of figure 2.5 shows the scattering rates in MLG calculated with the above expressions for a temperature of 300 K.

MLG inelastic phonon lifetimes

The interaction of electrons with out-of-equilibrium optical phonons has already been a research topic in the context of high-field transport [67], and optical excitation [130, 131]. Also, molecular dynamics studies have explored the thermal transport properties and lifetimes of the acoustic modes [132]. In this work, the values chosen for the phonon lifetimes are 2.5 ps for the optical (TO-K/LO-Γ) phonons, as measured experimentally [131] from time-resolved differential transmission spectroscopy, and 5 ps for the TA/LA-K mode, as obtained from molecular dynamics simulations [132].

2.4.3 Carrier-carrier scattering

Collisions between carriers have also been included in the MLG physical model. The carrier-carrier scattering matrix depends on the initial and final states of two carriers, and is given by [133–135]:

$$\left|\mathcal{H}^{\text{c-c}}_{s,\mathbf{k},s',\mathbf{k}',s_2,\mathbf{k}_2,s_2',\mathbf{k}_2',}\right|^2 = \frac{1}{2}\left[|V_d|^2 + |V_e|^2 - V_d V_e\right], \tag{2.54}$$

where the prefactor 1/2 aims to exclude interactions between carriers with parallel spin[10], and includes the contribution of the direct, $V_d = V(s,\mathbf{k} \rightarrow s',\mathbf{k}'; s_2,\mathbf{k}_2 \rightarrow s_2',\mathbf{k}_2')$, and exchange, $V_e = V(s,\mathbf{k} \rightarrow s_2',\mathbf{k}_2'; s_2,\mathbf{k}_2 \rightarrow s',\mathbf{k}')$ processes, being $V(...)$ the Fourier transform of the screened Coulomb potential:

$$V(s_A,\mathbf{k}_A \rightarrow s_A',\mathbf{k}_A'; s_B,\mathbf{k}_B \rightarrow s_B',\mathbf{k}_B') = \frac{2\pi e^2}{\Omega q\bar{\epsilon}\epsilon(q,\omega)} F(s_A,\mathbf{k}_A,{s_A}',{\mathbf{k}_A}') F(s_B,\mathbf{k}_B,{s_B}',{\mathbf{k}_B}'), \tag{2.55}$$

where $q = |\mathbf{k_A} - \mathbf{k_A'}|$, $\bar{\epsilon} = 4\pi\epsilon_0(\kappa_0^{\downarrow} + \kappa_0^{\uparrow})/2$ is the background dielectric constant [136], with ϵ_0 being the vacuum electrical permittivity, $\kappa_0^{\uparrow}$ and $\kappa_0^{\downarrow}$ the static relative permittivities of the top and bottom dielectrics (air in the case of suspended graphene), and $\epsilon(q,\omega)$ is the dielectric function, which will be discussed in section 2.4.7.

---

[10] This approximation is valid given the fact that spin polarization is not being considered along this work. An appropriate treatment within a context with explicit spin consideration would imply removing the 1/2 term, and perform a selection of only carriers with parallel spin.

From equations (2.13) and (2.16), the probability that a carrier with initial wavevector $\mathbf{k}$ in sub-band s scatters with another one in sub-band s_2 with wavevector $\mathbf{k}_2$, and ending with final states $s', \mathbf{k}'$ and $s_2', \mathbf{k}_2'$, is finally:

$$P_{\text{c-c}}(s, \mathbf{k} \to s', \mathbf{k}'; s_2, \mathbf{k}_2 \to s_2', \mathbf{k}_2') = \frac{2\pi}{\hbar} \left| H^{\text{c-c}}_{s,\mathbf{k},s',\mathbf{k}' s_2,\mathbf{k}_2,s_2',\mathbf{k}_2'} \right|^2$$
$$\delta(\varepsilon + \varepsilon_2 - \varepsilon' - \varepsilon_2')\delta(\mathbf{k} + \mathbf{k_2} - \mathbf{k}' - \mathbf{k_2}'). \tag{2.56}$$

For a given state, we are interested in obtaining the scattering rate with all the carriers in the system. To achieve this, we have to apply the previous transition probability in equation (2.12), make a summation over the occupied states $s_2, \mathbf{k}_2$, and then follow the summation over the final states $s', \mathbf{k}'$ as in equation (2.14), thus obtaining:

$$\Gamma_{\text{c-c}}(s, \mathbf{k}) = \frac{1}{2} \sum_{s_2,\mathbf{k_2},s',\mathbf{k_1}'} f_{s_2}(\mathbf{k}_2) \frac{2\pi}{\hbar} \left| H^{\text{c-c}}_{s,\mathbf{k},s',\mathbf{k}' s_2,\mathbf{k}_2,s_2',\mathbf{k}_2'} \right|^2$$
$$\delta(\varepsilon + \varepsilon_2 - \varepsilon' - \varepsilon_2')\delta(\mathbf{k} + \mathbf{k_2} - \mathbf{k}' - \mathbf{k_2}').,\tag{2.57}$$

or in integral form:

$$\Gamma_{\text{c-c}}(s, \mathbf{k}) = \frac{1}{2} \frac{\Omega^2}{(2\pi)^4} \frac{1}{2} \sum_{s_2,s'} \int_{\mathbf{k_2}} \int_{\mathbf{k}'} f_{s_2}(\mathbf{k}_2) \frac{2\pi}{\hbar} \left| H^{\text{c-c}}_{s,\mathbf{k},s',\mathbf{k}' s_2,\mathbf{k}_2,s_2',\mathbf{k}_2'} \right|^2 \delta(\varepsilon + \varepsilon_2 - \varepsilon' - \varepsilon_2')$$
$$\delta(\mathbf{k} + \mathbf{k_2} - \mathbf{k}' - \mathbf{k_2}')\, d\mathbf{k_2}\, d\mathbf{k}'\,. \tag{2.58}$$

The first 1/2 factor in the two latest equations aims to avoid a duplicity of scattering [137] since a single event involves two particles. However, a correct selection of the scattering partner-particle must follow after the introduction of this factor, according to the distribution of probabilities regarding the initial states of both carriers [138].

The last expression is the most general approach for carrier-carrier scattering. Now, two cases can be distinguished: intraband ($s = s_2$), and interband ($s = -s_2$) scattering.

In a collision involving two particles of the same kind (two electrons or two holes), the continuum of final states for the selecting particle, $s', \mathbf{k}'$, must belong to the space region defined by the two Dirac deltas in equation (2.58), that for MLG, in agreement with equation (2.42), translates to the system:

$$\mathbf{k} + \mathbf{k_2} = \mathbf{k}' + \mathbf{k_2}' \tag{2.59a}$$
$$s\hbar v_F|\mathbf{k}| + s_2\hbar v_F|\mathbf{k_2}| = s'\hbar v_F|\mathbf{k}'| + s_2'\hbar v_F|\mathbf{k}_\mathbf{2}'|. \tag{2.59b}$$

Now, let us focus on the intraband case ($s = s_2$) where both particles remain in the same band ($s' = s_2' = s$), as in figure 2.6 (a). Then, energy conservation in equation (2.59) implies:

$$|\mathbf{k}| + |\mathbf{k_2}| = |\mathbf{k}'| + |\mathbf{k}_\mathbf{2}'|. \tag{2.60}$$

If one thinks in the space $(k_x, k_y, \varepsilon/\hbar v_F)$, it can see that the possible final states constrained by this system of equations is the intersection of a plane with normal vector $\mathbf{n} = (k_x+k_{2x}, k_y+k_{2y}, |\mathbf{k}|+|\mathbf{k_2}|)$ containing the points $(k_x, k_y, s_1|\mathbf{k}|)$ and $(k_{2x}, k_{2y}, s_2|\mathbf{k_2}|)$. The intersection of this plane with the Dirac cone is an ellipse that contains all the possible final states for both particles, as it can be seen in figure 2.6 (a).

Lets consider now, the interband interaction case $(s = -s_2)$ without net exchange of carriers between bands $(s' = -s'_2)$ of two electrons, as illustrated in figure 2.6 (b). Now, the energy conservation condition reads:

$$|\mathbf{k}| - |\mathbf{k_2}| = |\mathbf{k}'| - |\mathbf{k}'_\mathbf{2}|. \tag{2.61}$$

In this case, the plane's normal vector is $\mathbf{n} = (k_x + k_{2x}, k_y + k_{2y}, s|\mathbf{k}| + s_2|\mathbf{k_2}|)$, and cuts the two halves of the cone, giving rise to a hyperbola. However, in a simulation scheme involving electrons and holes, it requires a correction of the conservation laws. Since a hole represents an *"empty electron state"*, the initial and final states of one of the particles must be switched: ${k_2}^{(\mathrm{e})} \Leftrightarrow {k'_2}^{(\mathrm{h})}$ and ${k'_2}^{(\mathrm{e})} \Leftrightarrow {k_2}^{(\mathrm{h})}$, so, making the change $k_2 \Leftrightarrow k'_2$, we have:

$$\mathbf{k} - \mathbf{k_2} = \mathbf{k}' - \mathbf{k_2}' \tag{2.62a}$$

$$|\mathbf{k}| + |\mathbf{k_2}| = |\mathbf{k}'| + |\mathbf{k}'_\mathbf{2}|, \tag{2.62b}$$

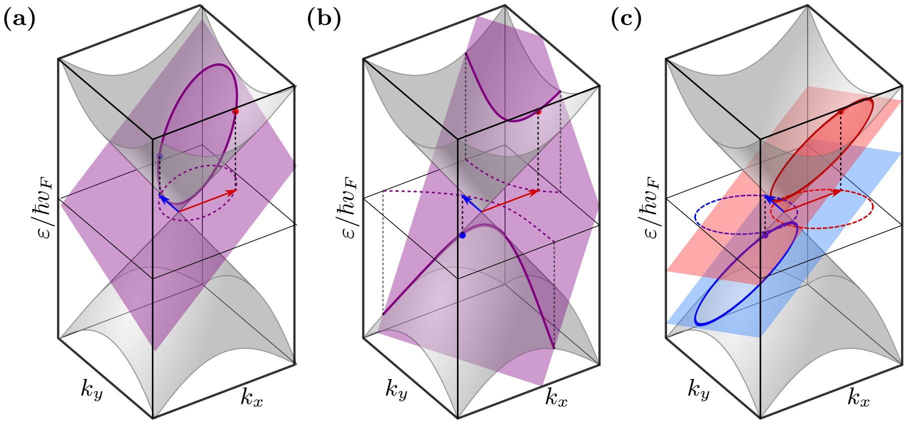

Figure 2.6: Representation of the allowed final states for the short-range Coulomb interaction of an electron in the conduction band with $k_1 = (k_0, 0)$ and (a) another electron in the conduction band, (b) another electron in the valence band, and (c) a hole in the valence band with $k_2 = (0, \frac{1}{2}k_0)$ in the $\mathbf{k} - \varepsilon/\hbar v_F$ space. Thick solid lines represent the final states in momentum and energy, while the dashed ones, are the projection over the $\varepsilon = 0$ $(k_x k_y)$ plane.

.

which translates to an equal (instead of opposite) energy [11] and momentum shift for the two particles. In this case, we obtain two different geometric spaces for the final states of each particle, being both of them two ellipses that result from the cut of two parallel planes with normal vector $\mathbf{n} = (k_x - k_{2x}, k_y, k_{2y}, |\mathbf{k_2}| - |\mathbf{k}|_1)$ each of them containing the points $(k_x, k_y, s|\mathbf{k}|)$ and $(k_{2x}, k_{2y}, s_2|\mathbf{k_2}|)$, as illustrated in figure 2.6.

After this analysis, it is convenient to introduce the MLG-specific scattering probabilites:

$$\Gamma^{(\mathrm{MLG})}_{\text{c-c}}(s, \mathbf{k}) = \frac{1}{2} \frac{\mathit{\Omega}^2}{(2\pi)^4} \sum_{s_2} \int_{\mathbf{k_2}} f(s_2, \mathbf{k}_2) \int_0^{2\pi} \Xi(s, \mathbf{k}, s_2, \mathbf{k}_2, \theta')\, d\mathbf{k_2}\, d\theta', \tag{2.63}$$

where intraband and interband interactions can be considered independently by splitting the summation over s_2'. Here, we have transformed the integral over $\mathbf{k}'$ into a polar integral over its orientation by means of the function $\Xi(...)$, that binds the initial and final states through the Dirac deltas, and can be understood as the probability that a particle with initial state $s, \mathbf{k}$ that scatters with another particle with state $s_2, \mathbf{k}_2$ changes its wavevector's angle to θ':

$$\Xi(s, \mathbf{k}, s_2, \mathbf{k}_2, \theta') = \frac{2\pi}{\hbar^3 {v_F}^2} \left| H^{\text{c-c}}_{s,\mathbf{k},s',\mathbf{k}' s_2,\mathbf{k}_2,s_2',\mathbf{k}_2'} \right|^2 |\mathbf{k}'|, \tag{2.64}$$

where the final wavevector for the main particle is determined by a polar description of an ellipse from one of its foci:

$$\mathbf{k}' = \frac{s|\mathbf{k}| + s_2|\mathbf{k_2}|}{2} \frac{1-\chi^2}{1-\chi\cos(\theta'-\theta_c)} \left(\cos\theta',\, \sin\theta'\right), \tag{2.65}$$

being $\chi = |s\mathbf{k}{+}s_2\mathbf{k_2}/(|\mathbf{k}|{+}|\mathbf{k_2}|)$ the eccentricity of the ellipse, θ_c the angle of $\mathbf{k}{+}\mathbf{k_2}$. The wavevector $\mathbf{k_2}'$ is obtained from $\mathbf{k}'$ through the momentum conservation law as stated in equations (2.59) and (2.61).

In general, it is not possible to fulfill energy and momentum conservation laws involving interband (Auger) transitions [139]. However, there is a limit case that overlaps between the two previous cases, when the relative angle between the two carriers wavevectors is $(1{+}ss_2)\pi/2$. In these circumstances the wavevectors are aligned along a generatrix of the conical energy dispersion, and this same line corresponds to the phase space where the final states of both particles are restricted to. When this condition is met, net exchange of carriers between bands can be achieved in the so-called Auger recombination and impact ionization processes, as seen in figure 2.7. In this collinear situation the solution for Ξ is cumbersome due to operations with the Dirac deltas. However this has already been dealt with by a number of authors [140, 139, 141]. As the process is

---

[11] Here, this refers to absolute energy, since an opposite shift in kinetic energy happens due to the fact that the interacting particles are in bands where kinetic energy grows towards opposite directions.

k

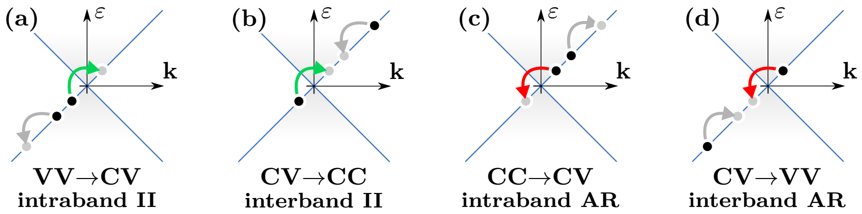

Figure 2.7: Representation of different collinear interactions in the section of the $\mathbf{k}-\varepsilon$ space. Net exchange carriers through (a, b) impact ionization (II) and (c, d) Auger recombination (AR) due to intraband (a, c) and interband (b, d) collisions.

collinear, the scattering can be treated in terms of energy, and reads:

$$\Gamma^{(\mathrm{MLG})}_{\mathrm{coll}}(s,\mathbf{k}) = \frac{\Omega^2}{(2\pi)^4}\sum_{s_2}\int_{-\infty}^{\infty} f(s_2,\mathbf{k}_2)\int_{-\infty}^{\infty}\Xi_{\mathrm{coll}}(\varepsilon,\varepsilon_2,\varepsilon')\,d\varepsilon_2\,d\varepsilon'_1, \tag{2.66}$$

where

$$\Xi_{\mathrm{coll}}(\varepsilon,\varepsilon_2,\varepsilon') = \frac{2\pi^2}{\hbar^4 {v_F}^3}\sqrt{\left|\frac{\varepsilon_2\varepsilon'\varepsilon'_2}{\varepsilon}\right|}\left|H^{\text{c-c}}_{s,\mathbf{k},s',\mathbf{k}'s_2,\mathbf{k}_2,s'_2,\mathbf{k}'_2}\right|^2, \tag{2.67}$$

$s_i = \mathrm{sign}(\varepsilon_i)$, $\mathbf{k_i} = (\varepsilon_i/\hbar v_F)s_i\mathbf{k}/|\mathbf{k}'|$ and where it has to be noted that in collinear processes $F(s,\mathbf{k},s',\mathbf{k}')$ equals unity. To get the expression in terms of energy, the occupation function is considered isotropic, so $f_{s_2}(\mathbf{k}_2) \to f(\varepsilon_2)$.

Since the use of electrons and holes involves a cautious treatment of such phenomena, the reader is kindly referred to appendix A in order ot obtain further details on the implementation of the subroutines regarding carrier selection, and final state calculation for carrier-carrier scattering in the EMC simulator.

2.4.4 Impurities

Impurities represent a potential source of scattering consequence of the Coulomb coupling with charged centers that may be present due to residues left in an imperfect fabrication process. Impurity scattering is modeled by means of a screened Coulomb potential, $V_{\mathrm{scr}}(q,\omega,d) = V(q,d)/\epsilon(q,\omega)$, being

$$V(q,d) = -\frac{2\pi Z e^2\exp(-qd)}{\Omega\bar{\epsilon}q} \tag{2.68}$$

the Fourier transform of the bare Coulomb potential, where Ze is the impurity charge and d the electron distance to the impurities. Hence, the scattering matrix is:

$$\left|\mathcal{H}^{\mathrm{imp}}_{s,\mathbf{k},s',\mathbf{k}'}\right|^2 = N_{\mathrm{imp}}\left|V_{\mathrm{scr}}(q,\omega,d)\right|^2 F(s,\mathbf{k},s',\mathbf{k}'), \tag{2.69}$$

with N_{imp} the total impurity number.

Upon this scattering matrix, the functional $\Delta_{\mathrm{elastic}}$, and by introducing the local impurity density as $n_{\mathrm{imp}} = N_{\mathrm{imp}}/\Omega$, we arrive to the scattering probability with impurities in its most general form:

$$\Gamma_{\mathrm{imp}}(s, \mathbf{k}) = \frac{n_{\mathrm{imp}} 2\pi e^4}{\hbar \bar{\epsilon}} \int_{\mathbf{k}'} \left| \frac{\exp(-2|\mathbf{q}|d)}{|\mathbf{q}|\epsilon(|\mathbf{q}|, \omega \to 0)} \right|^2 F(s, \mathbf{k}, s', \mathbf{k}')\delta(\varepsilon' - \varepsilon)\, d\mathbf{k}' \,. \tag{2.70}$$

And, for the particular case of graphene, one can follow the same steps as for the acoustic intravalley phonon scattering, which yields:

$$\Gamma_{\mathrm{imp}}^{(\mathrm{MLG})}(\varepsilon) = \frac{n_{\mathrm{imp}} 2\pi e^4}{\hbar^3 {v_F}^2 \bar{\epsilon} |\varepsilon|} \int_0^{2\pi} \left| \frac{\exp(-2|\mathbf{q}|d)}{|\mathbf{q}|\epsilon(|\mathbf{q}|, \omega \to 0)} \right|^2 \frac{1 + \cos\theta_{\mathbf{k},\mathbf{k}'}}{2}\, d\theta_{\mathbf{k},\mathbf{k}'} \,. \tag{2.71}$$

Strong angular dependence of the relative angle between initial and final wavevectors comes from the overlap and dielectric functions, which requires a Monte Carlo selection routine based on the distribution of such integral.

2.4.5 Defects

Atomic scale defects can be critical to describe electronic transport in fabricated samples, particularly to provide an accurate description of the mobility dependence with the carrier density. Both point defects and dislocations can be treated as a single scattering according to the approximation given by Ferry [70]. The treatment is similar to the case of impurity scattering, but substituting the Fourier transform of the electrostatic potential by a constant term. Thus, the matrix elements becomes:

$$\left| \mathcal{H}^{\mathrm{def}}_{s,\mathbf{k},s',\mathbf{k}'} \right|^2 = \left| -\frac{1}{\Omega} V_0 {L_{\mathrm{def}}}^2 \right|^2 F(s, \mathbf{k}, s', \mathbf{k}'), \tag{2.72}$$

where V_0 is the energy associated to the average defect potential, and L_{def} is the effective potential range, that can be related to the size of the puddles formed in graphene due to rippling and corrugations. As in the case of impurity scattering, considering Fermi's Golden rule and the local number and density of defects (N_{def} and n_{def} respectively), we get:

$$\Gamma_{\mathrm{def}}(s, \mathbf{k}) = \frac{n_{\mathrm{def}}}{2\pi\hbar} \left| V_0 {L_{\mathrm{def}}}^2 \right|^2 F(s, \mathbf{k}, s', \mathbf{k}')\delta(\varepsilon' - \varepsilon)\, d\mathbf{k}' \,. \tag{2.73}$$

Again, operating like in the case of first order deformation potential, one has, for monolayer graphene:

$$\Gamma_{\mathrm{def}}^{(\mathrm{MLG})}(\varepsilon) = \frac{n_{\mathrm{def}} \left| V_0 {L_{\mathrm{def}}}^2 \right|^2}{2\hbar^3 {v_F}^2} |\varepsilon| = \frac{\alpha_{\mathrm{def}}}{2\hbar^3 {v_F}^2} |\varepsilon|, \tag{2.74}$$

where a new parameter α_{def} has been defined as $\sqrt{n_{\mathrm{def}}} V_0 L_{\mathrm{def}}$, and whose values tipically range between 0.1 and 0.5 eV nm [70]. Since the anisotropy of this scattering is analogous to the quasielastic acoustic phonon, the treatment for the final states calculation is done accordingly.

2.4.6 Remote phonon scattering

Scattering with remote oxide surface polar optical phonons (SPP) has been found for quite long to be crucial to explain transport phenomena in inversion layers of Silicon FETs [142–144]. Due to the fact that for 2D materials the whole thickness of the channel is at very short distance from the substrates, this kind of scattering may decisively affect to electronic transport in these materials [68, 36, 145–147].

For SPPs the scattering matrix is [143, 148]:

$$\left|\mathcal{H}^{\mathrm{SPP},\nu}_{s,\mathbf{k},s',\mathbf{k}'}\right|^2 = \frac{e^2{\mathcal{F}_\nu}^2 \exp\left(-2|\mathbf{q}|d_{\mathrm{VdW}}\right)}{2\bar{\epsilon}|\mathbf{q}|\epsilon(|\mathbf{q}|,\omega)^2} F(s,\mathbf{k},s',\mathbf{k}'), \tag{2.75}$$

where d_{VdW} is the distance between the electron and the surface of the substrate (which in monolayers correspond to the Van der Waals distance between the 2D material and the substrate[12]), and $\mathcal{F}_\nu$ is the Frölich coupling constant given by:

$${\mathcal{F}_\nu}^2 = \frac{\hbar\omega_\nu}{2\Omega\epsilon_0}\left[\frac{1}{\kappa^{\downarrow}_{\infty}+\kappa^{\uparrow}_{\infty}} - \frac{1}{\kappa^{\downarrow}_{0}+\kappa^{\uparrow}_{0}}\right] = \frac{\hbar\omega_\nu}{2\Omega\epsilon_0}\beta, \tag{2.76}$$

being ω_ν the SPP phonon frequency, $\kappa^{\downarrow}_{0}$ and $\kappa^{\uparrow}_{0}$ the low frequency, and $\kappa^{\downarrow}_{\infty}$ and $\kappa^{\uparrow}_{\infty}$ the high frequency dielectric constants of the bottom and top substrates.

According to equations (2.14) and (2.17), the general expression for SPP scattering becomes:

$$\begin{aligned}\Gamma_{\mathrm{SPP},\nu}(s,\mathbf{k}) = \sum_{s'} \frac{\Omega}{(2\pi)^2}\int_{\mathbf{k}'} \frac{2\pi}{\hbar}\frac{e^2{\mathcal{F}_\nu}^2 \exp\left(-2|\mathbf{q}|d_{\mathrm{VdW}}\right)}{2\bar{\epsilon}|\mathbf{q}|\epsilon(|\mathbf{q}|,\omega)^2} F(s,\mathbf{k},s',\mathbf{k}') \\ \left[n_\nu + \tfrac{1}{2} \pm \tfrac{1}{2}\right]\delta[\varepsilon' - \varepsilon \mp \hbar\omega_\nu]\, d\mathbf{k}' \,.\end{aligned} \tag{2.77}$$

Following the same strategy as for inelastic phonons, one has, for MLG:

$$\begin{aligned}\Gamma^{(\mathrm{MLG})}_{\mathrm{SPP},\nu}(\varepsilon) = \frac{e^2\omega_\nu\beta}{8\pi\epsilon_0(\hbar v_F)^2}|\varepsilon \mp \hbar\omega_\nu|\left[n_\nu + \tfrac{1}{2} \pm \tfrac{1}{2}\right] \\ \sum_{s'}\int_0^{2\pi} \frac{\exp(-2|\mathbf{q}|d_{\mathrm{VdW}})}{q\epsilon(|\mathbf{q}|,\omega)} F(s,\mathbf{k},s',\mathbf{k}')\, d\theta_{\mathbf{k}'} \,.\end{aligned} \tag{2.78}$$

The phonon frequencies for the surface polar modes, which depend on the low and high-frequency dielectric permittivities and on the TO an LO optical phonons, can be found in references [149, 150] and are also compiled in the appendix A.

2.4.7 Dielectric screening

In the previous description of the scattering mechanisms, for those that are related to Coulomb interactions (carrier-carrier, impurities and SPPs) their associated potentials

---

[12] In MLG this distance is around 4 Å

appears in an screened way through the dielectric function $\epsilon(q,\omega)$. In general, the dielectric function is given by the Lindhard formula [151]

$$\epsilon(q,\omega) = 1 + V(q, d\to 0)\Pi(q,\omega), \tag{2.79}$$

where $V(...)$ is the Fourier transform of the bare Coulomb potential, as seen in equation (2.68), and $\Pi(q,\omega)$ is the polarizability, which in the random phase approximation it is given by [152, 153]:

$$\Pi(q,\omega) = g_s \lim_{\eta\to 0} \sum_{s,s',\mathbf{k}} \frac{f_s(\mathbf{k}') - f_{s'}(\mathbf{k})}{\hbar(\omega + \imath\eta) + \varepsilon - \varepsilon'} F(s,\mathbf{k},s',\mathbf{k}'), \tag{2.80}$$

where $\mathbf{k}' = \mathbf{k} + \mathbf{q}$, and, in thermal equilibrium $f_s(\mathbf{k}) = f(\varepsilon)$ can be parametrized by the Fermi-Dirac occupation function:

$$\mathscr{F}(\varepsilon,\mu,T_c) = \left[1 + \exp\left(\frac{\varepsilon-\mu}{k_B T_c}\right)\right]^{-1}, \tag{2.81}$$

being μ the chemical potential and T_c the carrier temperature.

In this thesis, polarization in the static limit ($\omega \to 0$) will be considered, along with further effects that arise from the consideration of dynamical screening such as plasmons [152, 154] or their hybridization with remote polar phonon modes [155].

Introducing the band dispersion of MLG, and operating on equation (2.80), we obtain the static polarizability as a function of the chemical potential and carrier temperature [156]:

$$\begin{aligned}\Pi^{(\mathrm{MLG})}(q,\omega\to 0,\mu,T_c) = &-\frac{g_s g_v}{2\pi(\hbar v_F)^2} \\ &\left\{\mu + \frac{\pi\hbar v_F q}{8} + 2k_B T_c \log\left[1+\exp\left(-\frac{\mu}{k_B T_c}\right)\right]\right. \\ &\left.-\hbar v_F \int_0^{q/2}\sqrt{1-\frac{2k}{q}}\left[\mathscr{F}(\hbar v_F k,\mu,T_c) + \mathscr{F}(\hbar v_F k,-\mu,T_c)\right]dk\right\}.\end{aligned} \tag{2.82}$$

To compute this polarizability, chemical potential and carrier temperatures must be also calculated. With such purpose, the following equations that link both variables are periodically solved:

$$n^{(\mathrm{EMC})} - p^{(\mathrm{EMC})} = n(\mu,T_c) - p(\mu,T_c) \tag{2.83a}$$

$$\varepsilon_{k,n}{}^{(\mathrm{EMC})} + \varepsilon_{k,p}{}^{(\mathrm{EMC})} = \varepsilon_{k,n}(\mu,T_c) + \varepsilon_{k,p}(\mu,T_c), \tag{2.83b}$$

where n and p are the electron and hole densities, and $\varepsilon_{k,n}$ and $\varepsilon_{k,p}$ the total kinetic energies of all electrons and holes. The members of the LHS, marked with superscript (EMC), are the quantities obtained from the EMC simulation, and the RHS terms, those obtained from carriers statistics according to the parameters μ and Tc. The quantities n and p are obtained by a simple summation of the free particles of each type multiplied by the factor ξ, while for the total kinetic energies, we have:

$$\varepsilon_k{}^{(\mathrm{EMC})} = \xi \sum_{i}^{NP} |\varepsilon_i - \varepsilon^0_{s_i}| \Theta(\pm s_i), \tag{2.84}$$

where the summation is done over all the active particles, ε_i is the energy of the ith particle, $\Theta(x)$ is the Heaviside function so that $\Theta(\pm s_i)$ selects the particle kinetic energy of only electrons $(+s_i)$ or holes $(-s_i)$, and $\varepsilon^0_{s_i}$ is the bottom energy of the sub-band s_i.

As for the members of the RHS, we have:

$$n = \sum_{s>0} \int_{-\infty}^{\infty} \mathrm{DoS}(s,\varepsilon) \mathscr{F}(\varepsilon,\mu,T_c)\, d\varepsilon \tag{2.85a}$$

$$p = \sum_{s<0} \int_{-\infty}^{\infty} \mathrm{DoS}(s,\varepsilon) \left[1 - \mathscr{F}(\varepsilon,\mu,T_c)\right] d\varepsilon \tag{2.85b}$$

$$\varepsilon_{k,n} = \sum_{s>0} \int_{-\infty}^{\infty} \mathrm{DoS}(s,\varepsilon) |\varepsilon - \varepsilon_0(s)| \mathscr{F}(\varepsilon,\mu,T_c)\, d\varepsilon \tag{2.85c}$$

$$\varepsilon_{k,p} = \sum_{s<0} \int_{-\infty}^{\infty} \mathrm{DoS}(s,\varepsilon) |\varepsilon - \varepsilon_0(s)| \left[1 - \mathscr{F}(\varepsilon,\mu,T_c)\right] d\varepsilon, \tag{2.85d}$$

Taking advantage of the simple band dispersion in graphene and the density of states from equation (2.44), one gets for the RHS of equation (2.83):

$$n = \frac{g_s g_v}{2\pi} \left(\frac{k_B T_c}{\hbar v_F}\right)^2 \mathscr{F}_1\left(\frac{\mu}{k_B T_c}\right) \tag{2.86a}$$

$$p = \frac{g_s g_v}{2\pi} \left(\frac{k_B T_c}{\hbar v_F}\right)^2 \mathscr{F}_1\left(\frac{-\mu}{k_B T_c}\right) \tag{2.86b}$$

$$\varepsilon_{k,n} = \frac{g_s g_v (k_B T_c)^3}{2\pi(\hbar v_F)^2} 2\mathscr{F}_2\left(\frac{\mu}{k_B T_c}\right) \tag{2.86c}$$

$$\varepsilon_{k,p} = \frac{g_s g_v (k_B T_c)^3}{2\pi(\hbar v_F)^2} 2\mathscr{F}_2\left(\frac{-\mu}{k_B T_c}\right), \tag{2.86d}$$

where $\mathscr{F}_j$ is the Fermi-Dirac integral of order j. In this way, μ and T_c are dynamically solved with a Newton-Raphson algorithm. Since we will analyze some situations with strong out-of-equilibrium carrier distributions, to correctly compute the polarizability, equation (2.80) will be evaluated numerically.

Chapter 3

Carrier transport phenomena in Graphene

Graphene is in the spotlight of future developments for electronic devices and applications, in many of which electronic transport is bound to occur under high electric field conditions. Consequently, a thorough understanding of the transport properties and the effects associated to the high-field regime becomes of special importance for fundamental physics and from a device design point of view in order to make these applications feasible.

There are two main objectives in this chapter: The first one is to introduce the reader into the first results of the material EMC simulator described in section 2.4, and explore the validity of the physical model . With this purpose we will contrast simulation results and experimental measurements. This introduction to the ensemble Monte Carlo model capabilities is presented in section 3.1.

The second objective is devoted to the study of the transport properties and the effects related to the high-field regime. When compared to the case of low fields, where the system remains close to equilibrium, under high fields the dynamics is very different: carriers are quickly taken to high energies [157] due to the electric field action, bringing up new phenomena. Among these, the heat generation in graphene at high current densities [158] is of particular relevance in the field of electronics. The exceptional thermal properties of graphene, related to the unique nature of two-dimensional phonon transport [159, 160], have been a subject of intensive research [161]. Thermal in-plane conductivities as high as $\sim 2500\,\mathrm{WmK^{-1}}$ have been measured using Raman optothermal techniques [162, 163] for suspended CVD graphene at room temperature. However, thermal coupling with a supporting substrate can reduce graphene's conductivity significantly. As an example, when supported on SiO_2, it has been found to lie around $\sim 600\,\mathrm{Wm^{-1}K^{-1}}$ [164], which, although far from the conductivity of suspended samples, is still much higher than for bulk Si ($\sim 140\,\mathrm{Wm^{-1}K^{-1}}$ [165]). Graphene field effect transistors present large thermally activated breakdown current densities, which can even reach those of carbon nanotubes by using diamond substrates [166]. The influence of the fabrication methods has also been proven to be of relevance in the breakdown of graphene devices, as CVD ones dissipate three times more power than the epitaxial counterparts due to morphological irregularities implicit to the synthesis method [167]. Additionally, graphene can be used as a heat-escaping channel in GaN devices [168], improving the thermal management of the transistors. In section 3.2 we provide a study on the combined effect of Joule heating and hot phonons in the transport properties of graphene

Generation and recombination mechanisms is another of the essential topics in hot-electron transport, since altering the number of conducting carriers presents potentially strong implications on the transport properties in semiconductor materials and device channels. Among these, impact ionization is one of the most relevant mechanisms [169–171]. Essentially, it consist in a generation process triggered by highly energetic electrons that transfer part of its energy to another bound electron that undergoes a promotion to a state in the conduction band, originating an electron-hole pair. The opposite phenomenon is called Auger recombination [172, 173]. Rigorous treatment of impact ionization and Auger recombination involves the consideration of the band structure, along with the conservation laws. This supposes a tough to overcome challenge in semi classical, and hence, Monte Carlo models [174, 172] in the field of traditional semiconductors. Instead, some approximations like the parametric Keldysh formula [175, 176] or the Thoma formalism [177] are used. In these models, an energy threshold is necessary for impact ionization to occur [178–181], therefore requiring strong electric fields to drive carriers into energetic states above this limit and produce electron-hole pairs. In section 3.3 we present an analysis on the sheet current-field behavior of monolayer graphene stressing the importance of interband mechanisms as a source of current enhancement. In graphene, the linear gap-less band structure implies a totally different premise. The existence of a continuum of energy states around the degenerate Dirac points also implies a continuum of energies at which a carrier can trigger an impact ionization event. Also, the highly energetic ($\sim 165\,\mathrm{meV}$) optical phonon opens up a wide generation and recombination channel path via emission and absorption scattering events. Such interband pathways reach generation and recombination rates in the $10^{24}\,\mathrm{cm}^{-2}\mathrm{s}^{-1}$ range depending upon the carrier density and temperature [129].

The chapter is organized as follows: In section 3.1 we explore the validity of the model by contrasting EMC results with experimental measurements, finding that impurities and defects play a significant role in fabricated samples. The combined impact of hot phonons and self-heating on the transport characteristics, and also the interaction of both phenomena is investigated in section 3.2. Finally, the contribution of excess carriers created due to interband interactions stimulated by high electric fields is dealt with in section 3.3.

3.1 Influence of defects and impurities in mobility

The physical model of monolayer graphene described in section 2.4 mostly relies in first-principles calculations, and it is free from exogenous parameters. In order to test the reliability of the simulator, its results must be contrasted with real experimental measurements. Low-field mobility is the most suitable physical quantity for this purpose. Since it is related to states close to the equilibrium, hot electron phenomena do not suppose an further issue to take into account.

Fabricated samples are usually bound to be contaminated with impurities originated in the synthesis and fabrication process [182, 183] These can work as scattering centers, and have been proven to be a source for the degradation of graphene conductivity [184], and a cause of device variability [185, 186]. Also, crystalline defects have been suggested to be a factor than can affect negatively the electronic transport [187, 188]. To account for these issues, we included in the model the scattering with homogeneously distributed impurities in section 2.4.4, and defects in section 2.4.5. In figure 3.1 we show the low-field mobility for graphene on a SiO$_2$ substrate for varying values of the impurity density and defect parameter. Both the existence of impurities and defects reduce the carrier mobility. Each of the scattering sources have a different impact depending on the carrier density. While the influence of impurities is a reduction of the mobility, specially for small carrier densities, the decrease induced by defects is more homogeneous. Such influence for small n is a result of the Coulomb nature of the screened potential, which tends to reduce with the carrier concentration.

Let us explore now if the EMC model can reproduce experimental mobilities. In [110] low-field mobility results for graphene on SiO$_2$ were presented. The structure consists of a graphene monolayer supported on a SiO$_2$ substrate of thickness 300 nm over a Si wafer. The values of the mobility, which are reproduced in figure 3.2 (a), are quite below those obtained in the ideal case of $n_{\mathrm{imp}} = 0$ and $\alpha_{\mathrm{def}} = 0$, as presented in figure 3.1. On the other hand, the authors report a residual carrier density arising from impurity-induced puddles of around $\sim 8.9 \times 10^{11}\,\mathrm{cm}^{-2}$. So, according to theoretical predictions, the observed mobility has to be influenced by the existence of impurities, and their effect should be included in the simulations. We iteratively performed low-field simulations varying n_{imp} and α_{def} until a good match to the experimental mobility was found. In the same figure we show the results for an impurity concentration of

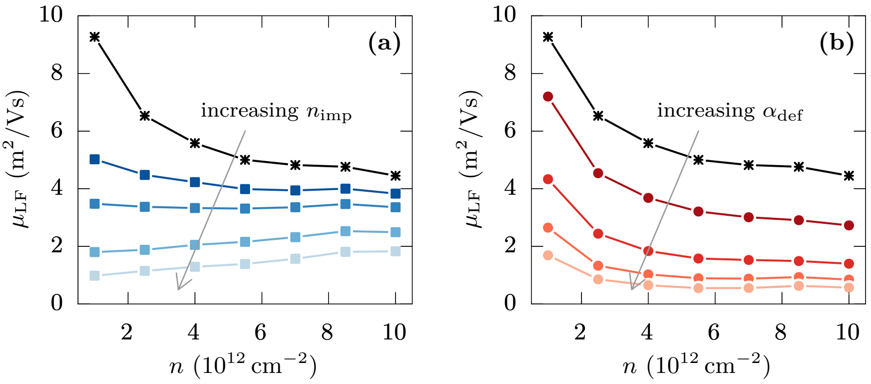

Figure 3.1: Low field carrier mobility in graphene on SiO$_2$ at $T = 300\,\mathrm{K}$ as a function of the electrostatically doped carrier (electron or hole) density for varying values of (a) the impurity density, with $n_{\mathrm{imp}} =$ 0, 0.5×10^{11}, 1×10^{11}, 1.5×10^{11} and $2 \times 10^{11}\,\mathrm{cm}^{-2}$, and (b) the defect parameter, with $\alpha_{\mathrm{def}} = 0$, 0.05, 0.1, 0.15 and 0.2 eV nm.

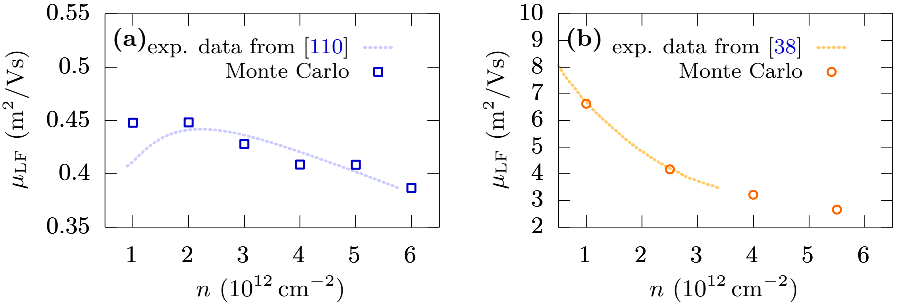

Figure 3.2: Experimental (dotted lines) and EMC-computed mobility (symbols) at $T_0 = 300\,\mathrm{K}$ for (a) graphene on SiO$_2$ as obtained from [110] , and (b) graphene encapsulated on h-BN as obtained from [38].

$n_{\mathrm{imp}} = 9.5 \times 10^{11}\,\mathrm{cm}^{-2}$ and $\alpha_{\mathrm{def}} = 0.07\,\mathrm{eV\,nm}$. A reasonable agreement is met, specially at high carrier concentrations.

On the other hand, electronic mobilities one order of magnitude higher than previously measured of CVD graphene have been reported for graphene on hexagonal boron nitride (h-BN) [189, 37], showing that the choice of the substrate is critical. In the particular case of h-BN, the increase in mobility is attributed to the low presence of dangling bonds in the h-BN/graphene interface, a similar hexagonal crystalline structure with matching lattice constant and a reduced rate of carrier-SPP scattering [190, 191]. In figure 3.2 (b) we compare the mobility calculated from experimental conductivity data at room temperature against the carrier density. In this case, a very good agreement is obtained with the EMC results, with extremely low values of impurity density and defects ($n_{\mathrm{imp}} = 7.5 \times 10^{10}\,\mathrm{cm}^{-2}$ and $\alpha_{\mathrm{def}} = 35\,\mathrm{meV\,nm}$), supporting the claim about the favorable characteristics of the h-BN/graphene interface for the electronic transport.

We can go beyond the low-field close-to-equilibrium conditions and explore the whole velocity-field curves. Strong electric fields take carriers to high energies, giving rise to hot-electron phenomena. While some of these effects will be explored in-depth later, in section 3.2 and section 3.3 we present here the first velocity-field results in graphene in order to assess the validity of the model. In [111] experimental velocity-field curves for the same graphene on SiO$_2$ structure already introduced in [110] are presented. Here, the authors argue a dependence on the impurity density (or traps) in the SiO$_2$/graphene interface with the applied gate voltage, and hence with the carrier density. We considered in our velocity-field simulations the gate voltage (carrier concentration) relation with the density of ionized centers in the interface. Self-heating with temperature-dependent thermal conductivity of SiO$_2$ and Kapitza resistance has been also included (see section 2.3.6). The velocity-field results at 300 K taken from [111] (dotted lines and filled

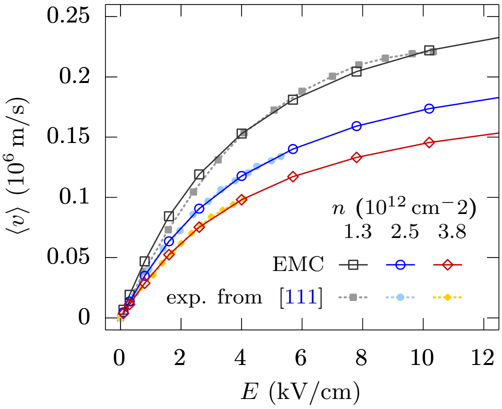

Figure 3.3: Experimental (dotted lines) and EMC-computed drift velocity-electric field curves of graphene on SiO_2 at room temperature $T_0 = 300\,\mathrm{K}$. Experimental data was obtained from [111].

symbols) and the EMC simulation data (continuous lines and open symbols) are presented in figure 3.3. We note that the area of the sample ($7 \times 4\,\mu\mathrm{m}$) guarantees that the 1D model for the heat dissipation flow is adequate [109]. As already explained in sections 2.3.5 and 2.4.2, we introduce the hot phonon effect, with relaxation the times of 2.5 fs for the TO-K/LO-Γ mode as measured in [131] and, 5.0 ps for the TA/LA-K mode as theoretically predicted in [132]. SPP phonon modes from the SiO_2 substrate will be treated out of equilibrium (hot) within the same formalism used for the intrinsic modes. However, given that they are a surface manifestation of TO and LO modes of SiO_2 and have much space to diffuse towards the insides of the oxide, SPPs are expected to behave with a fast decay rate. So, characteristic decay times for SPPs were chosen in order to find the best agreement between EMC and experimental velocity field curves at $T_0 = 300\,\mathrm{K}$, resulting in $\tau_{\mathrm{SPP}} = 0.33\,\mathrm{ps}$. Note that this value is an order of magnitude smaller than those of intrinsic modes. The defect parameter for best matching result was $\alpha_{\mathrm{def}} = 95\,\mathrm{meV\,nm}$. Upon these considerations, we observe a very good agreement for all the sampled electric fields between the experimental data and the EMC results, and for the three carrier densities studied.

The use of impurities and defects allows to mimic both mobility and velocity field curves from experimental data. In collaboration with the Autonomous University of Barcelona (group of professor D. Jiménez), we have managed to study the scalability and performance of graphene-based field-effect transistors [192, 193]. To achieve this, a drift diffusion simulator coupled to a Poisson solver was fed with the EMC data of the carrier-dependent velocity-field curves considering several impurities density and defect parameters. Velocity dependence with the electric field was described by means of parametrized analytical expressions, being these parameters set by finding the best fit with the EMC results. The expression for the velocity given a particular carrier density, n is [110, 194]:

$$v(n, E) = \mu_{\mathrm{LF}}(n)\left[1 + \left|\frac{\mu_{\mathrm{LF}}(n)}{v_{\mathrm{sat}}(n)}E\right|^{\beta}\right]^{-1/\beta}, \tag{3.1}$$

where v_{sat} is the saturation (high-field) drift velocity, and β is factor that mostly determines how soft is the transition from the linear region (governed by the slope of μ_{LF}) towards the saturation regime. We take the saturation velocity as that obtained from the EMC simulator at $E = 20\,\mathrm{kV/cm}$. The low-field mobility $\mu_{\mathrm{LF}}(n)$ and saturation velocity, $v_{\mathrm{sat}}(n)$, are described by analytical expressions as well:

$$\mu_{\mathrm{LF}}(n) = \mu_0\left[1 + \left(\frac{n}{a_1}\right)^{b_1}\right], \tag{3.2a}$$

$$v_{\mathrm{sat}}(n) = v_{\mathrm{sat}}^0\left[1 + a_2\left(\frac{n}{n_0}\right)^{b_2}\right], \tag{3.2b}$$

where $n_0 = 10^{12}\,\mathrm{cm}^{-2}$ is the reference carrier density, and the parameters μ_0, a_1, b_1, v_{sat}^0, a_2, b_2, are set so that the expressions best fit to the EMC data for various carrier concentrations that usually lie in the range $5 \times 10^{11}\,\mathrm{cm}^{-2}$ to $1 \times 10^{13}\,\mathrm{cm}^{-2}$.

The results of the hybrid EMC-Drift-Diffusion model successfully compared with experimental results of fabricated devices [192, 193]. Regarding the RF performance, it was demonstrated that increasing graphene quality (reducing impurities and defects) improved the figures of merit (f_T and f_{max}). However, K-Δ analysis revealed that these devices could become unstable: there is trade-off involving the graphene quality, bias point and device escalation, so a balance needs to be found for practical applications. We refer the reader to references [192] and [193] for a detailed discussion.

Electrical characterization of monolayer graphene over insulator samples

With the purpose to perform the characterization of the electronic mobility in monolayer graphene on insulator samples, we were provided with access to the characterization laboratory belonging to the NANOELEC group, and a basic training for the use of the Cascade M150 probe station. The graphene samples, stocked by GRAPHENEA, consisted in $1\,\mathrm{cm} \times 1\,\mathrm{cm}$ single graphene layers grown on copper by chemical vapor deposition technique, and then transferred to $300\,\mathrm{nm}$ $\mathrm{SiO_2}$ and $500\,\mathrm{\mu m}$ quartz substrates. Their respective Raman spectra are presented in figure 3.4. The graphene samples transferred to $\mathrm{SiO_2}$ were also placed on top of a Silicon wafer. Samples on quartz substrates were also employed for transient optical experiments reported in section 5.2.

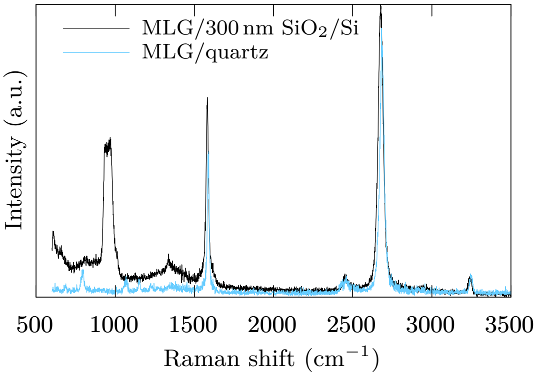

Figure 3.4: Raman spectra of the provided different monolayer graphene samples for electrical and optical characterization.

Electronic characterization is usually performed on ad-hoc designed structures (being Hall bars the most typical example), comprising the realization of metalizations to create the electrodes [195], therefore requiring fine post-processing of the samples. Since such processing tasks are out of the scope of the present work, we opted for more immediate and accessible alternatives. Particularly, we based on by point-contact techniques [196, 197], more precisely in the two-point configuration. The basic idea is to avoid the need of processing the electrodes by using point-contacts probes instead, as seen in figure 3.5 (a), forming a so-called pseudo-MOSFET [197]. Upon the application of a voltage bias between the two needles in contact with the material we want to characterize, the current is measured simultaneously. In comparison with the four-contact technique [196], the two-point method is easier to carry out, as no care needs to be taken regarding the needle alignment. On the other hand, the contact resistances ($R_{\rm con}$) has a great impact, and can mask the intrinsic conductivity of the sample under study [196]. Considering the circuit depicted in figure 3.5 (a) the total resistance is:

$$R_{\rm T} = \frac{\Delta V_{12}}{I_{12}} = R_{\rm g} + 2R_{\rm con} + 2R_{\rm W} = R_{\rm g} + R_{\rm par}, \tag{3.3}$$

where $R_{\rm g}$ is the resistance of the graphene sample under investigation, $R_{\rm con}$ are the point-contact resistance, and $R_{\rm w}$ are the wire resistances, and $R_{\rm par}$ groups all the parasitic resistances. Note that $R_{\rm par}$ is constant in the setup regardless of the distance between needles. Taking into account a four-point configuration where the material resistance relates to the sheet resistivity, $\rho_{\rm Sg}$, and a form factor W [198, 199], we have that the total resistance in the two-point configuration is

$$R_{\rm T} = \frac{\Delta V_{12}}{I_{12}} = \frac{\rho_{\rm Sg}}{W} d + R_{\rm par}. \tag{3.4}$$

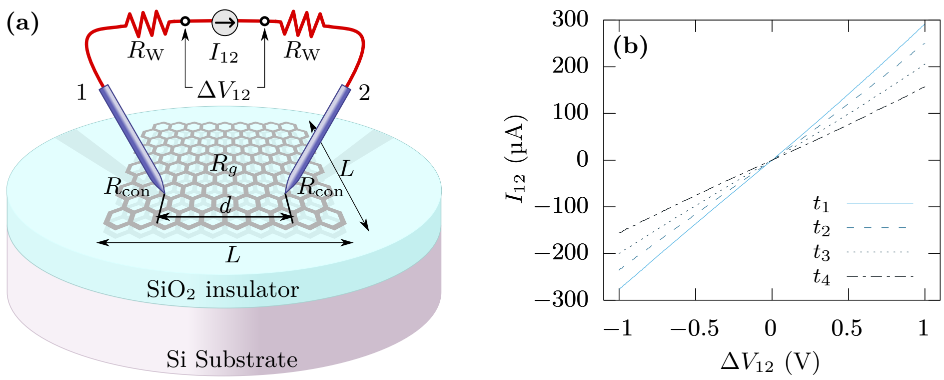

Figure 3.5: (a) Illustration of the circuit and the setup of a two-point configuration for the measurement of the conductivity of bulk graphene on insulator samples. (b) Current versus applied voltage between the two probes, in a two-point configuration at different times after making the contacts with the graphene sample, being $t_1 < t_2 < t_3 < t_4$.

This is the equation of a line with slope ρ_{Sg}/W and a constant shift of R_{par}. So, by varying the distance between the two probes, we should be able to infer both the values of the contact resistances (given the wire resistances are known) and the graphene sheet resistivity. Finally, since $\sigma_{\mathrm{g}} = en\mu_{\mathrm{LF}}$, one can obtain the mobility as $\mu_{\mathrm{LF}} = (\rho_{sg}qn)^{-1}$.

Despite the apparent simplicity of the experimental setup and the method, we came across some hindrances that made the measurements troublesome. While measuring I_{12} we observed a progressive degradation after consecutive measurements. In figure 3.5 (b) we show some results of current-voltage sweeps at $d = 0.75\,\mathrm{mm}$ obtained after probing at the same point positions at different times after placing the probes. A degradation with time of the total resistance is evident, which suggest a progressive deterioration of the point contact. We attribute this mainly to the likely mechanical damage that could be produced to the graphene layer at the moment of the physical realization of the contact with the tip of the probe needle. Besides, in [198] it was shown that the pressure applied with the probe on the sample has a great impact on the resistivity, which adds a further complexity to the procedure. Due to the lack of control of the pressure applied with probe(s) and the progressive time degradation of the point contacts, the linear trend with the probe distance described in equation (3.4) could not be achieved in a consistent and repeatable routine.

3.2 Hot phonons and Joule heating in high-field transport

Charge transport in the diffusive regime at high-field conditions is a non-equilibrium process: the elevated energies reached by carriers lead to an enhancement of inelastic electron-phonon scattering. In these collisions, part of the electron energy is transferred to the lattice, which translates into an effective increase of the temperature, a phenomenon known as Joule heating or self-heating (SH) [200, 201]. Along with the raise of the lattice temperature, this scattering activity also leads to the onset of an out-of-equilibrium phonon population. When the decay rate of phonons is much slower than their generation rate (as it can happen, for example, due to phonon emissions by inelastic scattering at strong fields and large carrier densities) the so called hot phonon (HP) effect takes place, as explained in section section 2.3.5. Consequently, heat generation and non-equilibrium transport are microscopically related, with emission and absorption of inelastic phonons as a common nexus. Some works have investigated the issue of self-heating and energy dissipation in graphene both at the bulk material level and in graphene-based devices [109, 111], finding that the interaction with surface polar phonons and a good thermal coupling with the graphene layer increase the energy transfer towards the substrate in high-bias conduction [202]. Also, it has been found that thermal failure in these devices shows a strong dependence with morphological irregularities bound to their fabrication [167]. On the other hand, the relevance of the HP effect at high fields has been demonstrated in graphene [67, 203]. Since both Joule heating and hot phonons are the result of inelastic phonon scattering processes, it is particularly important to evaluate their interaction when they act simultaneously. We will explore their combined and individual effect on the transport characteristics in order to reveal which is dominant or more relevant in fabricated samples. Also, the influence of HPs in the lattice temperature is going to be evaluated. With this purpose, in this section we will study transport characteristics in stationary conditions (drift velocity, dissipated power, temperature, etc.), with focus on the combined role played by HP and SH, but also including them separately for comparison purposes.

We base our simulations on the structure presented in [111], for which good agreement between simulation and experimental data has already been presented in figure 3.3 of section 3.1. In order to evaluate the impact of self-heating and hot phonons, simulations with each of the effects separately activated were also performed. In figure 3.6 we present the velocity-field curves obtained with the EMC model up to $E \leq 50\,\mathrm{kV/cm}$ for the four possible cases regarding the consideration of hot phonons and Joule heating. The largest electron drift velocity is obtained when in the model both Joule heating and hot phonons are not considered, and the smallest electron drift velocities are obtained with the full

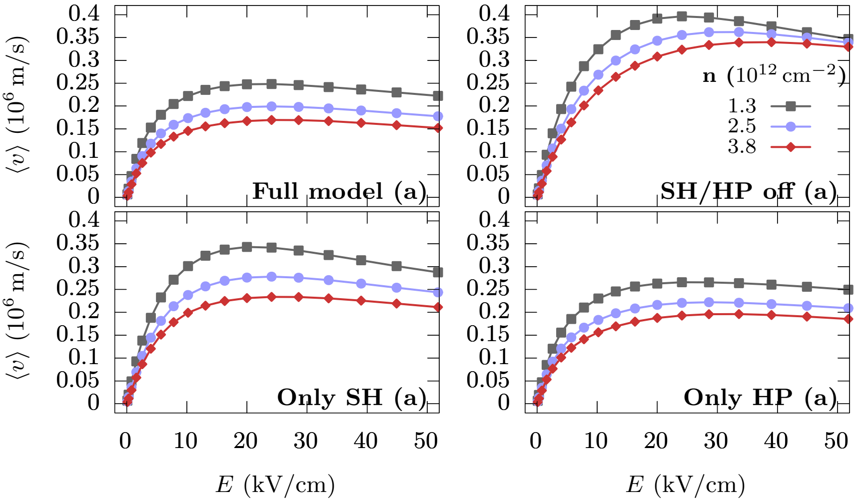

Figure 3.6: Drift velocity as a function of the applied electric field in the graphene on SiO_2 structure presented in [111] when (a) Joule heating and hot phonons are considered, (b) both efects are ruled out in simulation, (c) only self heating is included, and (d) only hot phonons are considered. The electron densities considered were n: $1.3 \times 10^{12}\,\mathrm{cm}^{-2}$, $2.5 \times 10^{12}\,\mathrm{cm}^{-2}$ and $3.8 \times 10^{12}\,\mathrm{cm}^{-2}$.

model featuring both effects, HP and SH. Therefore, neglecting either SH or HP effect results in a overestimation of the drift velocity, which is represented in figure 3.7 for the cases considering only either hot phonons or self-heating. This overrating is larger if the HP effect is neglected, tending to saturate to a 40% of the actual drift velocity for electric fields close to the beginning of the negative differential conductance ($\sim 20\,\mathrm{kV/cm}$). If only self-heating is neglected, the overestimation of the drift velocity increases monotonically with the electric field, growing with the carrier concentration within the range considered.

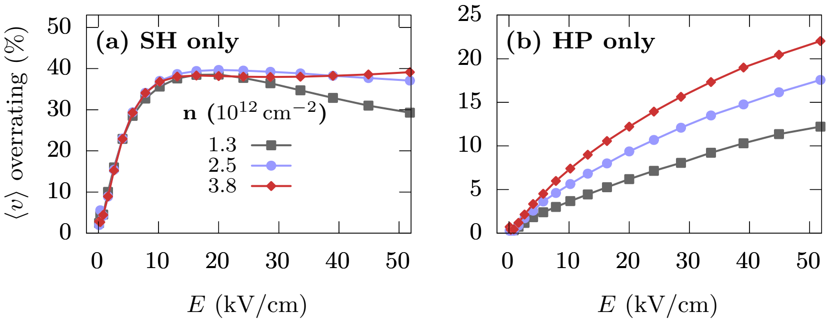

Figure 3.7: Drift velocity overrating with respect to the full moden when only (a) self-heating, and (b) hot phonons are considered.

The maximum overrating is 22% for the sampled carrier densities and electric fields. Consequently, the HP effect appears to be dominant over Joule heating regarding the limitation of the high-field velocity in graphene. From a modeling perspective, in the structure under study, none of the effects should be neglected in order to obtain a correct description of the drift velocity under high-field conditions.

We will set our attention now to the steady-state lattice temperature. The hot phonon effect is not only critical for the carrier velocity: it also acts in conjunction with self-heating, affecting decisively to the system temperature. Figure 3.8 shows the steady state graphene layer temperature (T_{g}) versus the applied electric field and carrier concentration with (solid blue lines) and without (dashed black lines) considering the HP effect. Temperature increases monotonically with the electric field for all the carrier concentrations considered, with a slight trend to saturate at small carrier concentrations as the electric field grows. By neglecting the out-of-equilibrium phonon effect, a hotter temperature is obtained in comparison with results from the complete model. Peaking over 1600 K without HP and at 1300 K in the full model (for the largest carrier density and electric field under consideration), this means more than a 20% overestimation of T_{g} with respect to the most complete model. It is therefore particularly relevant to incorporate the hot phonon effect in the modeling graphene self-heating, since otherwise the resulting temperature would not be accurate.

The differences observed in the temperatures reached when the out-of-equilibrium phonon population is taken into account can be explained by paying attention to behavior of the main heating source: scattering with inelastic phonons. Their influence is

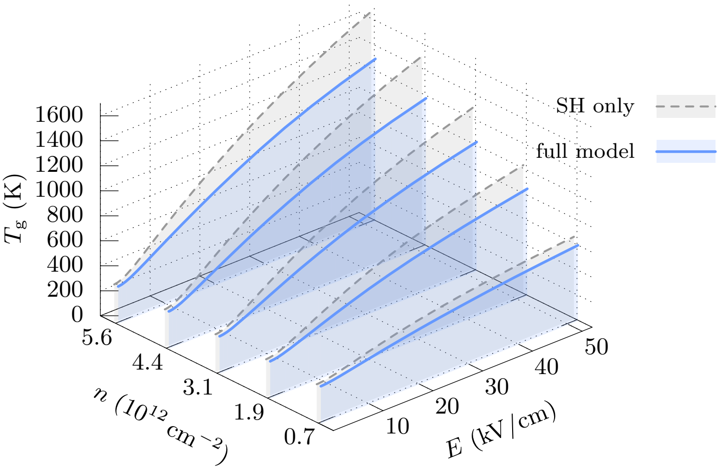

Figure 3.8: Temperature of a graphene monolayer on SiO_2 in the steady state for the model neglecting the HP effect (dashed lines), and bottom: the complete model (solid lines).

characterized by the net emitted power per unit area, which reveals the energy that is transferred from electrons towards the graphene lattice and the substrate via electron-phonon scattering. This quantity, computed according to equation (2.35) in section 2.3.5 of plotted in figure 3.9 versus the applied electric field. The net emitted power in the absence of self-heating is also computed in the same way, although it must be reminded that in this case it does not contribute to the lattice heating. This would mean assuming that the heat generated is dissipated instantaneously, which is not a realistic situation, but it is shown also in the figure for comparison purposes. Within the range of electric fields under consideration, $P_{\text{int}} = P_{\text{TA/LA-K}} + P_{\text{TO-K/LO-}\Gamma}$ –figure 3.9 (a)–, corresponding to the power transferred through intrinsic acoustic and optical phonons, shows an almost linear dependence. When either the hot phonon effect or self-heating are neglected, the net emitted power is comparatively larger than in the complete model, for which the smallest emitted power is obtained. Neglecting HPs yields a greater overestimation of P_{int} in comparison to ruling out Joule heating. With regard to the emitted power due to SPPs, a similar contribution to that of the intrinsic inelastic mechanisms is found at fields below 25 kV/cm, from where a trend for saturation is observed. At high fields, therefore, the net exchanged power with the substrate is significantly less that the power transferred to the graphene lattice through intrinsic phonons. Similarly as it occurred with P_{int}, P_{sub} is smaller when the full model is considered. At medium and small fields, no relevant differences are found between disregarding HP or SH. However, at large fields (≥ 25 kV/cm) the overestimation of the net exchanged power is larger when neglecting self heating than when hot phonons are deactivated. To explain these power transfer

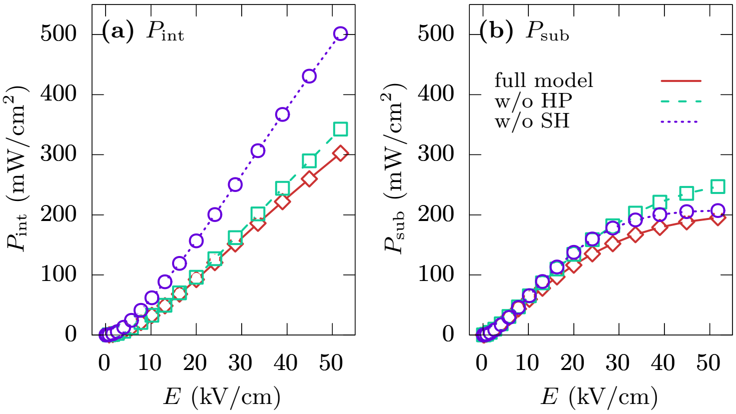

Figure 3.9: Net emitted power due to scattering with (a) intrinsic phonons, and (b) the SiO_2 substrate polar phonons when SH (circles) or HP (squares) are not considered, and when both are included in the simulations (diamonds).

overestimations, it must be noted that any growth in the phonon population (either due to self heating or to emission through collision with carriers) implies an increase of the scattering rate, but even more importantly, larger $n_\nu(\mathbf{q})$ also means a reduction of the emission/absorption ratio. As a result, neglecting any of these phenomena (SH or HP) turns out in an unrealistically reduced phonon population, which in turn yields an excess of power exchange due to an excessive emission/absorption ratio. Hence, the lattice temperature is overestimated in a scenario where only self-heating is taken into account. In the most complete model, the phonon population rise due to the fact that both effects are superimposed, which explains why the emitted power is the smallest. In the case of intrinsic phonons, this ratio seems to be more reduced due to the HP effect, while for SiO_2 SPPs self heating is more relevant.

Now, we will explore the origins of the differences found between the overestimation of transferred power of intrinsic and SPP phonon modes examining more deeply the interplay between self-heating and the out-of-equilibrium phonon populations. To achieve this, it is convenient to examine the phonon temperatures (that are directly provided by the phonon occupation numbers [204] consistently obtained in the simulations) and their

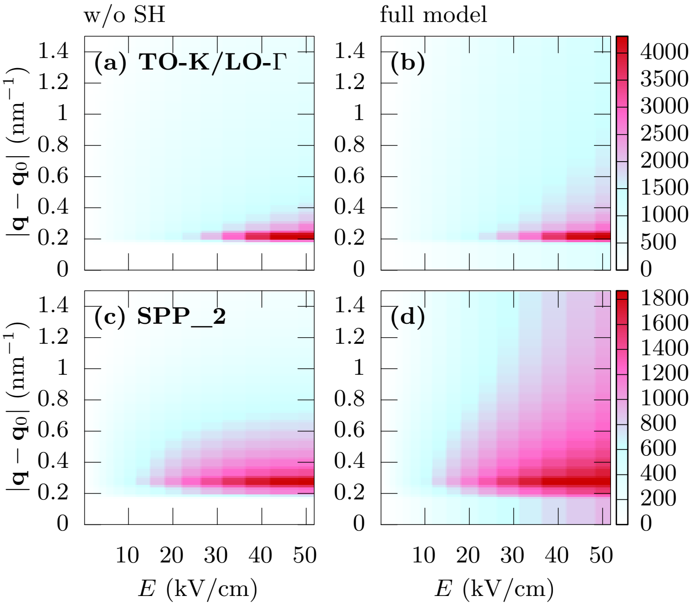

Figure 3.10: Angle-averaged phonon temperature as a function of the wavevector, $T_\nu(|\mathbf{q}-\mathbf{q}_0|)$, and the applied electric field for the intrinsic optical (top) and the smallest energy SiO_2 SPP mode ($\hbar\omega_{\mathrm{SPP}_1} = 59.98\,\mathrm{eV}$, bottom), with a carrier concentration of $n = 3.8\times10^{12}\,\mathrm{cm}^{-2}$. (a)/(b) and (c)/(d) correspond to the cases when SH effects are turned OFF/ON, respectively.

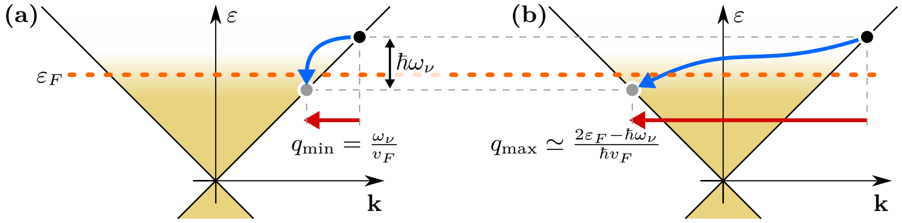

Figure 3.11: Minimum (a) and maximum (b) wavevectors for phonon emission due to scattering close to the Fermi level (orange dotted line) with no electron momentum reorientation and backscattering respectively.

dependence with the phonon wavevector and the applied electric field[1]. Figure 3.10 shows the results for two different scenarios, when self-heating is taken into account and when it is neglected. The results are shown for the intrinsic intervalley optical phonons and for the SPP$_1$ ($\hbar\omega_{\mathrm{SPP}_1} = 59.98\,\mathrm{eV}$) for being the most meaningful for the observed differences. In the case of intrinsic optical phonons –figure 3.10 (a) and (b)–, only small differences are observed between the full model and the case in which SH is neglected, which evidences a weak dependence of the intrinsic phonon population with the lattice temperature increase due to Joule heating. However, due to the weak scattering activity, at small electric fields ($< 5\,\mathrm{kV/cm}$), only phonons with short wavevectors become barely hotter than the lattice. More specifically, since at low fields carrier distributions are close to equilibrium, phonons can scatter only close to the Fermi energy, where there are both free carriers and available states. This limits the phonon wavevectors involved in emission events from a minimum of [2] $|\mathbf{q}| \geq \omega_\nu(\mathbf{q}_0)/v_F$, corresponding to a transition with no wavevector reorientation, up to a maximum of $|\mathbf{q}| \lesssim [2\varepsilon_F - \hbar\omega_\nu(\mathbf{q}_0)]/\hbar v_F$, related to backscattering transitions, as sketched in figure 3.11 (b). At electric fields stronger than $30\,\mathrm{kV/cm}$ the phonon temperatures noticeably increase, overpassing significantly T_{g} and reaching values around $4000\,\mathrm{K}$. In this case, the out-of-equilibrium phonon population extends to larger wavevector values, since the electron distribution spreads above the Fermi level in a non-equilibrium situation. However, hottest phonon temperatures are found very close to the minimum possible wavevector, $\omega_\nu(\mathbf{q}_0)/v_F$, as depicted in figure 3.11 (a). This is because the available phase space shrinks with the wavevector length, while transitions involving wavevectors close to this minimum are possible independently on the initial electron kinetic energy. The high phonon population related to such elevated temperatures provokes a strong directionality of the interaction characterized by the

---

[1] Here, we compute the phonon temperature by solving for the Bose-Einstein statistics at each $\mathbf{q}$, so $T_\nu(\mathbf{q}) = \hbar\omega_\nu(\mathbf{q})/k_B \log[1 + n_\nu(\mathbf{q})^{-1}]$. Then, $T_\nu(\mathbf{q})$ is angularly averaged around the relevant symmetry point $\mathbf{q}_0$ in order to obtain $T_\nu(|\mathbf{q} - \mathbf{q}_0|)$.

[2] Note that phonons are considered to be dispersionless in the model, so $\omega_\nu(\mathbf{q} \simeq \mathbf{q}_0) \simeq \omega_\nu(\mathbf{q}_0)$.

preference of interactions involving these small $|\mathbf{q}|$ (weak carrier reorientation) mediated by the hot phonon effect.

On the contrary, the phonon temperatures of the SPP$_1$ mode, shown in figures 3.10 (c) and (d), exhibit a stronger dependence on self-heating. At medium and high fields ($\gtrsim 20\,\mathrm{kV/cm}$), self-heating provokes an increase of the phonon temperature above that provoked by the HP effect. As discussed in section 2.4.6, given the nature of carrier and surface polar phonons coupling, this kind of scattering is highly anisotropic, with preference for small angle transitions and therefore shorter wavevectors. For this reason, the increase of phonon temperature over T_g in figure 3.10 (d) at long $|\mathbf{q}-\mathbf{q_0}|$ not as prominent as in the intrinsic optical mode, where phonon emission dominates. The reason why surface polar phonons are affected to a lesser extent by the HP effect in comparison with intrinsic modes is that their relaxation time is one order of magnitude shorter; therefore, SPP phonon relaxation and emission rates are comparable, so the out-of-equilibrium population is not so prone to remain for so long time as in the intrinsic phonon modes. Additionally, in the case of the $\mathrm{SiO_2}$ SPP$_1$ mode, its small energy provokes its phonon population is strongly responsive to changes in the substrate temperature, rather than by its own scattering-induced phonon population growth: it is the lattice temperature raise due to the Joule effect that mostly drives the increase of the SPP$_1$ phonon population.

Therefore, since the HP effect is weaker for surface polar phonons, the influence of self-heating becomes comparatively more critical than in the case of intrinsic phonons, explaining why the overestimation of the emitted power is larger when self-heating is disregarded. On the other hand, the isotropic nature of the TO-K/LO-Γ mode, slower relaxation rate and larger phonon energy, makes it more affected by the HP effect, reaching larger phonon temperatures up to short phonon wavelengths.

3.3 Ambipolar transport induced by interband scattering

The strong short-range Coulomb coupling between charge carriers in graphene has been proven to be of great relevance in electronic transport [135] and also in the thermalization of transient relaxation processes after photoexcitation [205–207]. Among this sort of interactions, we can differentiate between intraband –as depicted in figure 2.6– and interband processes –figure 2.7–. The latter ones (i.e., impact ionization and Auger recombination) occur in the collinear limit, that is, when the two interacting carriers have the same wavevector orientation, as described in section 2.4.3, and have been theorized to be of great importance under photoexcitation conditions [208, 209], with substan-

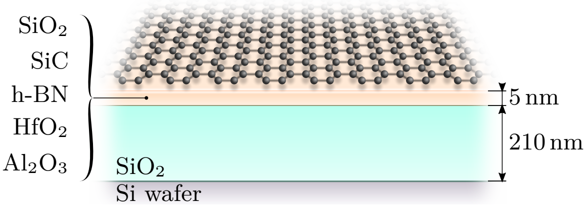

Figure 3.12: Simulated structure.

tial experimental evidence of the resulting carrier multiplication [139, 210]. Therefore, such processes –particularly impact ionization– are expected to be of importance also under strong stationary electric fields, in particular at low degenerate and highly energetic (hot) carrier distributions. Its effect has already been investigated in the context of graphene-based field-effect transistors [211], showing that electrons and holes created in the channel due to a net generation rate arising from collinear interactions are responsible for the "up-kick" of the current characteristics at small gate potentials and moderate drain biases. In the present study, also interband transitions assisted by intrinsic and substrate phonons are included, as detailed in section section 2.3.7. The objective of this subsection, is to investigate through a microscopic analysis how the contributions of interband processes modulate the electric current across the graphene layer in a bulk material framework and under steady electric field conditions.

The structure under study, presented in figure 3.12, consists of a graphene monolayer sheet deposited on a thin (5 nm) layer that rests on top of a 210 nm thick SiO$_2$ substrate beneath which there is a 300 nm silicon wafer. This multilayer configuration is commonly found in the literature [212, 213] and has been chosen so that the thin thickness of the top dielectric layer minimizes its effects on the overall heat dissipation, that is accounted for in the distributed thermal resistance model, as detailed in section 3.2. A comparative study among different substrates, comprising some of the most commonly used in fabricated samples (SiO$_2$, SiC, h-BN, HfO$_2$ and Al$_2$O$_3$) will be presented.

Many studies on graphene usually acknowledge constant carrier concentrations, setting the drift velocity as the main figure of merit in the electronic transport [68, 147, 111, 70]. This hypothesis is true only under quasi-equilibrium conditions, such as in the case low fields applied to extract mobilities. However, as we will see, due to the action of interband mechanisms, the free carrier concentration would not remain constant when an electric field of enough magnitude is applied. As a consequence, also a significant population of minority carriers will be generated, which in turn can interact with the majority ones and increase the heat production via phonon scattering, hence degrading the overall carrier velocity. Due to the existence of non-fixed electron and hole

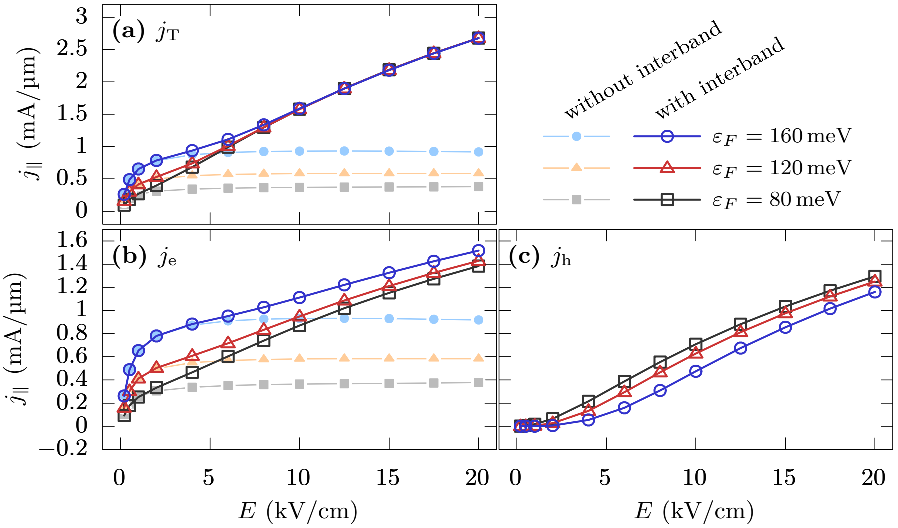

Figure 3.13: (a) Total, (b) electron, and (c) hole components to the total sheet current density in graphene on SiO$_2$ as a function of the electric field when interband transitions are enabled/disabled. Three Fermi energies are considered: 80, 120, 160 meV, corresponding to net carrier densities at equilibrium $n - p$: 5×10^{11}, 10^{12}, and $2 \times 10^{12}\,\mathrm{cm}^{-2}$, respectively.

concentrations bound to interband transitions, it is recommendable to observe the sheet current density, $j = e(p\langle v_h\rangle - n\langle v_e\rangle)$, as the main quantity of interest, where $\langle v_{e,h}\rangle$ are the drift velocities for electrons and holes, respectively. Additionally, in order to set a framework for the comparison between the models including and neglecting interband transitions, the net carrier density, $n - p$ is considered to be fixed, and identified by the Fermi energy, $\varepsilon_F = \mathrm{sign}(n-p)\hbar v_F\sqrt{\pi|n-p|}$, being n and p the electron and hole concentrations respectively. In the study, we set a doped carrier concentration such that majority carriers will always be the electrons. Given the conduction and valence bands structure symmetry at the relevant energies, the results apply also to a hole doping of the same magnitude.

The current sheet densities obtained considering constant free carrier population and including interband transitions are depicted in figure 3.13 (a) as a function of the electric field for the case of graphene on SiO$_2$ and different Fermi energies. When interband processes are neglected in the model, the current density reaches a saturation value (with even a slight negative differential conductance at very large fields) for fields $\gtrsim 5\,\mathrm{kV/cm}$. On the other hand, when phonon assisted and collinear interband transitions are included, similar current values are obtained at small fields. However, starting from certain electric fields that depend on the Fermi energy (for example, ∼2.5 and ∼4.5 kV/cm for $\varepsilon_F =$ 80 and 160 meV respectively), the trend to saturate breaks and the current shows a quasi-linear increase, with a convergence of the values for all the Fermi energies under consideration. This yields current densities more than 5 times larger than the ones observed at the saturation level for the smallest Fermi energy at 20 kV/cm.

Let us now examine the individual contribution of electrons and holes to the sheet current. It must be pointed out that if interband transitions are neglected, the minority carrier density at 300 K is negligible, and so is their contribution to the current. Figure 3.13 (b) shows the component of the current due to the motion of electrons (majority carriers) alone. The global trend is similar to the total current when interband transitions are considered, with the only exception that the curves for the three Fermi energies do not meet at strong fields within the studied range. Also, the slope of the mononotic region is lower, so top values of electron sheet current are around half of the total in the range under consideration. The minority (holes) component of the current is depicted in figure 3.13 (c). This contribution smoothly takes off from a close-to-zero value towards an almost linear trend. Likewise to the electron component, the contribution of the interband transitions becomes more appreciable at stronger fields the larger is the Fermi energy. Contrarily to the electron component, that is shifted due to the existence of free carriers at low fields, the hole contribution is larger when the Fermi energy is smaller, leading the total sheet current-field curves to overlap in the linear region. In any case, it must be highlighted that the existence of a non-negligible hole current is the clear signature of impact ionization. Although there seems to be a threshold field, it is difficult to identify it, since the effect is very progressive.

Let us take a look at the excess electron and hole densities depicted in figure 3.14 (a)[3]. Excess carrier concentration grows monotonically with the electric field, being larger as the Fermi energy is smaller. Hole densities surpass the electron concentrations in equilibrium at 5, 8, 15 kV/cm for each of the cases under consideration. For the strongest electric field (20 kV/cm) and the smallest Fermi energy (80 meV), the majority carrier concentration is more than 8 times larger than at equilibrium, thus leading to similar electron and hole densities. On the other hand, for ε_F =160 meV the majority concentration shows a two-fold increase, much limited in comparison with the previous case. This behavior is a consequence of degeneracy; as more carriers occupy electronic states due to extrinsic doping, it becomes harder for possible new electron-hole pairs to find free states that actually lie around small kinetic energies, and therefore impact ionization events are blocked by the Pauli exclusion principle, even if there are more carriers at elevated energies when ε_F is higher.

Now, we turn to analyze the velocity-field curves. Figure 3.14 (b) allows comparing

---

[3] In the present context, we define excess carriers as those free carriers that exist in a particular steady state due to interband transitions. In other words, it is the difference between the electron and hole densities in a particular steady state and in equilibrium, $n_{\mathrm{ex}} = n - n_0 = p - p_0$.

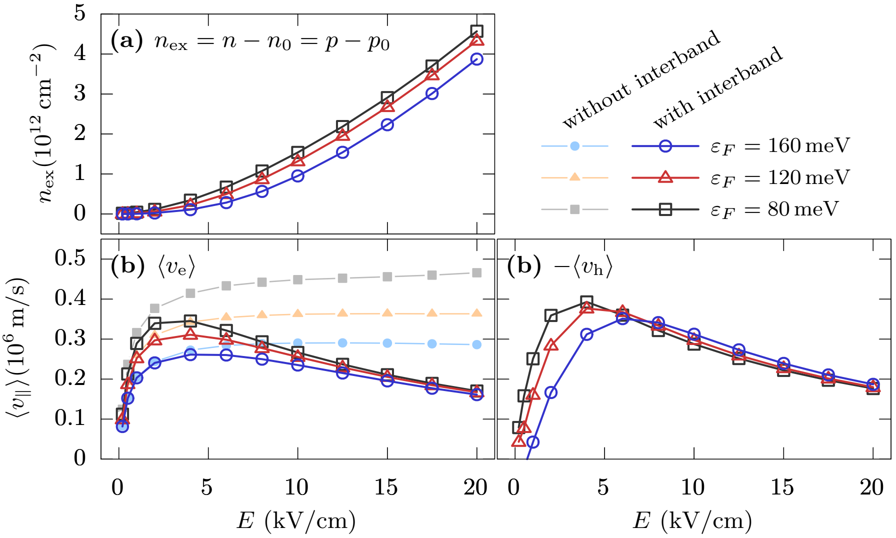

Figure 3.14: (a) Excess carrier density of electrons and holes (over the equilibrium concentrations), (b) electron and (c) hole drift velocities in graphene on SiO_2 as a function of the applied electric field. The Fermi energies are the same as in figure 3.13.

the drift velocity of majority carriers including and ruling out interband transitions. At very small fields, the drift velocity is similar in the two models, as expected. Without interband contributions the typical increase of velocity towards saturation from a threshold electric field behavior is found. This agrees with the behavior of the current density-field curves described previously, since minority carrier contribution is negligible. Under the presence of interband scattering drift velocities are reduced, except at very small fields. Also, a maximum velocity appears, that is smaller and occurs at stronger electric fields with increasing Fermi energies. Following this maximum, the electron ensemble presents a trend to reach a similar drift velocity for fields larger than $\gtrsim 15\,\mathrm{kV/cm}$, regardless of the Fermi energy within the discussed examples. It must be reminded that in this electric field range, a lot of excess carriers are created, and the majority carrier densities are very similar: degeneracy effects is critical to understand this reduction of the ensemble velocity.

A comparable behavior of the hole drift velocity can be observed in figure 3.14 (c), although in general this type of carriers travel faster due to a smaller degeneracy in comparison to electrons. In any of the cases under consideration the increase of carriers by far compensates the decrease of the drift velocity when the electric field rises. Therefore, the current enhancement is the result of a big number of excess carriers even though the increased degeneracy provokes a drop of the drift velocity.

Understanding the previous macroscopic and ensemble quantities requires an analysis

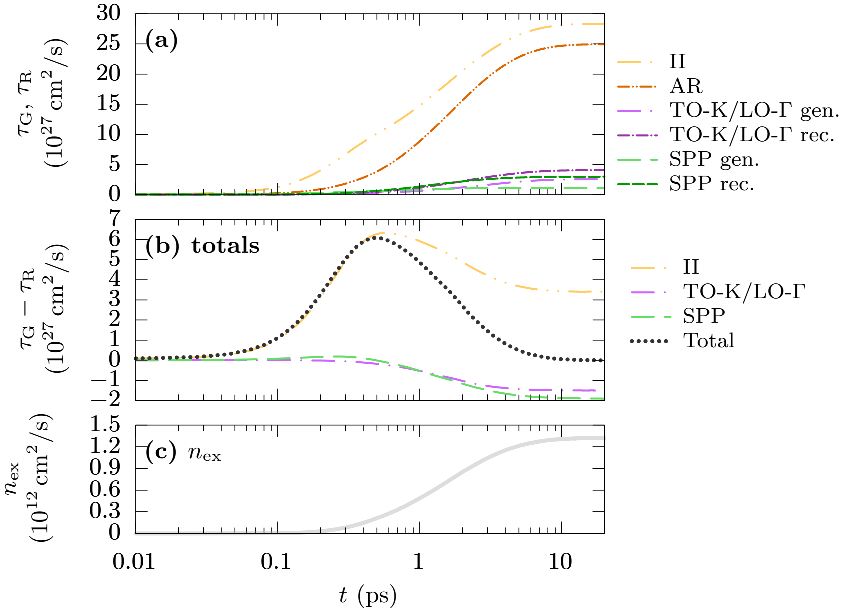

Figure 3.15: Instantaneous rates of (a) electron-hole generation via Impact Ionization, intrinsic and SPP phonon absorption, and recombination via Auger processes, intrinsic and SPP phonon emission, and (b) net total generation rates due to collinear collisions, intrinsic and substrate phonons, and (c) instantaneous excess carrier density for graphene on SiO_2, under the action of a field of 10 kV/cm and a $\varepsilon_F = 0.12$ eV.

at a microscopic level, disentangling which mechanisms are responsible for such excess populations, and to what extent. In the simulations, the electric field is applied to an ensemble of carriers in equilibrium, and therefore the electronic system goes through a transient until reaching a stationary state. In figure 3.15 (a) we show the instantaneous generation and recombination rates for the interband mechanisms considered from the instant when the electric field is switched on ($t = 0$) up to $t = 20$ ps, when the steady state is achieved. During the first ~ 80 fs there are barely any interband interactions provoking any change in the carrier populations. Starting from this instant, new electron-hole pairs start to be created due to impact ionization. This is associated to the time that it takes to the system (under this particular electric field) to excite hot electrons that trigger impact ionization events and to leave enough free small energy states to allow new free electron-hole pairs to be created. Shortly after (~ 200 fs) Auger recombination starts recombining some of the excess carriers. With regard to phonon assisted interband transitions, both emission and absorption rates are almost one order of magnitude smaller than collinear processes. Also, generation and recombination events assisted by phonons remain balanced practically until 0.5 ps, where emissions noticeable overtake absorptions.

All these rates grow steadily up to 10 ps, when they start to saturate. Looking at the net generation rates, depicted in figure 3.15 (b), collinear processes show a maximum between 0.4 ps to 0.5 ps, until the proportional increase of the weight of Auger recombination events makes the net rate decrease. As for phonon assisted transitions, the net trend is to recombine carriers, being slightly more relevant the remote phonon interactions from the SiO_2 substrate (SPPs). So, excess carriers appear due to impact ionization, being the electron-hole pairs created by phonon-assisted absorption negligible, and the final steady equilibrium is achieved by the Auger and phonon-assisted recombination.

Let us now gather more information about how are the electron-hole pairs are created and annihilated due to carrier-carrier collinear scattering. Figure 3.16 shows the net generation-recombination rate, $\tau_{\mathrm{G}}(\mathbf{k}) - \tau_{\mathrm{R}}(\mathbf{k})$ due to these interactions as a function of the wavevector around the K and K' symmetry points. Most electrons promoting from valence to conduction band are created close to the Dirac points with a slight displacement against the direction of transport. Away from this area, the generation rate drops progressively. In the positive part for $k_{\|}$ and close to $k_{\perp} \sim 0$, it turns to negative values, which indicates a prevalence of recombination processes in that region. Both types of carriers tend to diminish their population where their occupation is maximum. The generation-recombination rate for holes shows similar trend in comparison with that of the majority carriers. In essence, impact ionization and Auger recombination leave their signature according to the Pauli exclusion principle: carriers are generated where there are available free states, and then recombine from the states that are more densely occupied. According to this analysis, it has to be noted that collinear processes in the presence of an electric field show a directional preference to create carriers with group

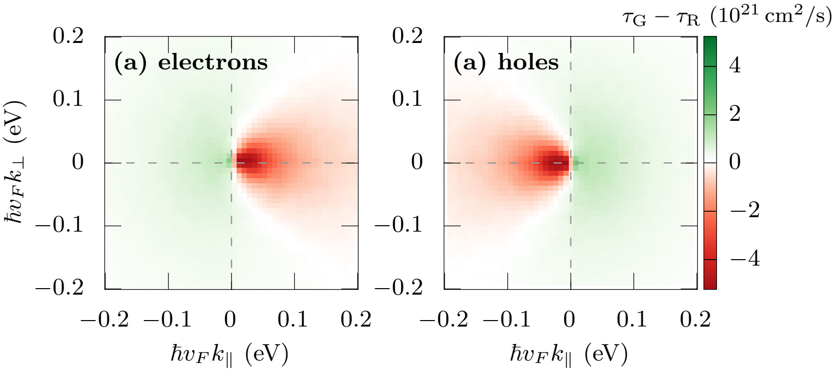

Figure 3.16: Net generation due to interband collinear Coulomb interactions of (a) electrons and (b) holes in the reciprocal space around the K and K' symmetry points up to energies of ~ 0.2 eV in graphene on SiO_2 with an applied field of 10 kV/cm and $\varepsilon_F = 0.12$ eV.

velocity against the direction of transport, and to recombine electron-hole pairs whose velocity contributes to the electronic transport according to the orientation of the applied field.

Now that it is clear that the leading role in the enhancement of the sheet current density is taken by the concentration of free carriers, we turn to analyze the impact that the underlying substrates may have in this quantity. Figure 3.17 (a) depicts the excess carrier density as a function of the Fermi energies for various substrates. It can be observed that the higher the Fermi energy is, the fewer carriers can be promoted to conduction states, due to the increased degeneracy at low energies. Graphene on silicon carbide would be the case where more carriers are allowed to be created, followed by graphene on boron nitride and on SiO_2. When graphene lies on HfO_2 and on Al_2O_3 the excess population scores in much smaller figures. Given the Coulomb nature of the impact ionization and Auger processes, they are affected by the background screening provided by the surrounding environment, –i.e., the substrate–. According to this, the small excess density observed in graphene on Al_2O_3 and HfO_2 could be explained by their large dielectric constant. However, the screening factor fails to quantitatively fully address the differences found in the excess carrier densities, , so we must look at the SPPs, which must play a role as well. Since the amount of generated carriers are conditioned by the available free states, the carrier cooling power due to SPP scattering is the key factor. This can be understood as the ability of these mechanisms to effectively reduce the carrier energy, by means of reiterative attempts to absorb their $\hbar\omega_{\mathrm{SPP}}$ from the electron or hole via carrier-phonon scattering, thus taking them towards lower energy states. A higher cooling power

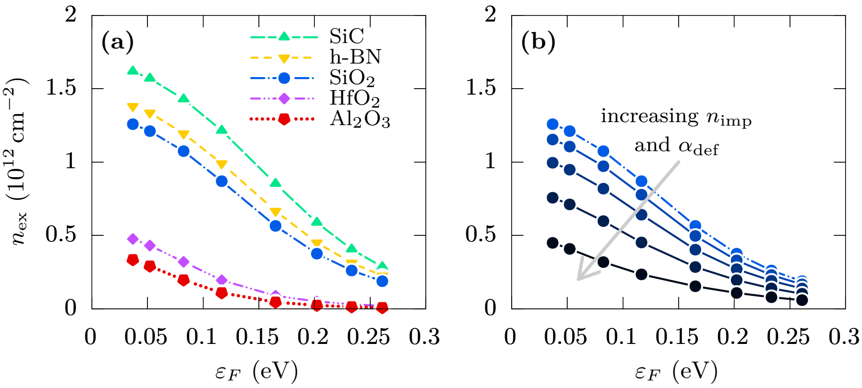

Figure 3.17: Excess carriers as a function of the Fermi level for (a) graphene on different substrates, and (b) for graphene on SiO_2 and different leves of impurities and defects (n_{imp} =0, 2×10^{11}, 5×10^{11}, 10^{12}, and $2\times10^{12}\,\mathrm{cm}^{-2}$; α_{def} = 0, 0.03, 0.05, 0.07, and 0.1 eV nm, respectively). The applied electric field is 8 kV/cm for all the cases.

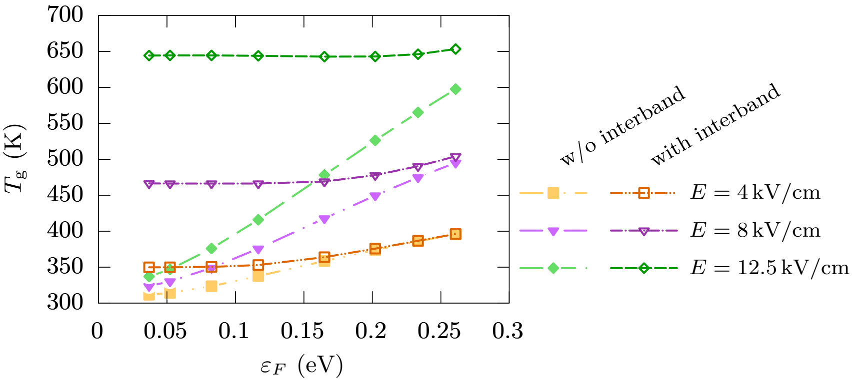

Figure 3.18: Graphene temperature predicted by the distributed thermal resistance model at three different electric fields as a function of the Fermi level, including and neglecting interband transitions.

provokes a carrier distribution more degenerated at smaller energies, allowing for fewer impact ionization transitions, which directly correlates with the observed excess carriers. By approximating this *"cooling power"* concept as $\hbar\omega_{\mathrm{SPP}}(\Gamma_{+\mathrm{SPP}} - \Gamma_{-\mathrm{SPP}})$, Al_2O_3 tops, followed in order by HfO_2, SiO_2, h-BN and SiC.

The same principle applies when other kinds of extrinsic scattering sources come into play. Figure 3.17 (b) shows the concentration of excess carriers with different levels of impurities and crystalline defects. These interactions are elastic, and therefore do not effectively reduce the carrier energy. In this case, the degeneracy attained near the Dirac point that blocks the interband transitions occurs by means of successive carrier wavevector reorientation due to elastic collisions and the continuous drag from the electric field. As a consequence, it can be seen that there is an inverse relation of excess carriers and impurity/defect concentrations.

Finally, we want to stress the influence on lattice temperature of the elevated carrier densities that are achieved due to impact ionization. Since more carriers are free to move and scatter with inelastic phonons, this implies more heat generation. In figure 3.18, the temperature in the graphene layer as a function of the Fermi energy is compared for three different electric fields. It can be appreciated how when interband transitions are considered an almost constant temperature is achieved. This happens as a consequence of a steady-state power dissipation rate, resulting from the balance between electric field induced carrier heating, the relaxation due to scattering, and the number of carriers. It is only at very elevated Fermi levels when there is a deviation from this flat trend, corresponding to the Fermi energy at which there is so much degeneracy close to the Dirac point that impact ionization is mostly forbidden, and therefore the amount of free carriers present in the graphene layer is entirely controlled by the extrinsic doping.

Chapter summary

Influence of defects and impurities in mobility

The dependence of graphene electronic mobility with the carrier density in graphene on h-BN and SiO_2 has been validated against experimental data in the literature. A very good agreement is obtained between the ensemble Monte Carlo and experimental measurements by considering impurities and defects that exist on the fabricated samples. Also, the influence of the onset of scattering sources has been extended to the high-field regime. The resulting data was employed in a drift-diffusion device model by means of compact parametric descriptions of the velocity-field curves, allowing to analyze the performance and stability of graphene based field-effect transistors and their dependence on the quality of graphene.

Hot phonons and Joule heating in high-field transport

We analyzed two of the effects that result from high-field transport: Joule heating and hot phonons. Drift velocity is penalized to a higher extent due to the appearance of an out-of-equilibrium phonon population as compared to the heating of the graphene channel. However, considering both effects simultaneously suppose further reduction of high-field velocity. Since both phenomena are a result of the same scattering processes with phonons, we observed and quantified their interplay. Disregarding hot phonons can lead to an overestimation of the calculated dissipated power, and hence steady state graphene temperature, of more than a 20% depending on the carrier density and electric field. Even though the consideration of hot phonons was found to be more significant to correctly model the transport characteristics, not including self-heating causes a wrong description of the phonon population density of the less energetic modes (especially the lowest energy SiO_2 surface optical phonon), leading to a scattering activity in which phonon absorption of long wavevectors is underrepresented.

Ambipolar transport induced by interband scattering

A parameter-free modeling approach of impact ionization and Auger recombination has been developed for the first time in a semi-classical Monte Carlo model of graphene. Also, the phonon-assisted recombination pathway result of the gapless graphene band structure were included. Sheet electric current density is enhanced by the rise of electron and hole densities resulting from impact ionization, showing a linear trend at high electric fields regardless of the externally imposed Fermi energy. The appearance of a minority carrier density reveals a soft and progressive activity of impact ionization, which is more noticeable as the extrinsic carrier density is reduced. Impact ionization is basically enabled by the reduction of carrier population close to the Dirac points as a result of carrier heating. This effect is reduced by extrinsic scattering sources like impurities and defects, that lead to less energetic carrier distributions . Differences between different supporting dielectrics have been observed, attributed mainly to their carrier cooling power of the SPP scattering, and also due to increased screening of Coulomb interactions, which damps impact ionization. The analysis of the temperature revealed that the dissipated power becomes a function of the electric field at low extrinsic carrier doping.

Chapter 4

Fluctuation phenomena in graphene

In this chapter we will study some of the phenomena related to fluctuations associated to the electronic transport in graphene at the material level. In the context of this work, we refer to fluctuations of a particular quantity as its continuous change with respect to a mean value. More specifically, fluctuations are related to the variations in time of quantities relevant to the carrier motion. The stochastic nature of the Monte Carlo method makes it an ideal tool to study this kind of phenomena, since fluctuations in the model are intrinsic to the treatment of transport as the motion of a large ensemble of traveling particles that obey probabilistic rules.

Graphene's most promising applications in the field of electronics are those in which the absence of a bandgap is not a drawback, so the devices can benefit from the excellent electronic transport properties of this material [214]. In particular, graphene-based field effect transistors (GFETs) have been proposed as very appealing candidates for developing new devices aimed for high frequency analog applications [215, 216]. Cut-off frequencies over 300 and 427 GHz have been reported for experimental devices, with values reaching the THz range projected by static measurements and simulations [217, 218, 46, 219]. However, in this context, the practical feasibility of future applications based on graphene analog technology will be determined not only by their operation frequencies, but also and specially, by the noise properties intrinsic to this material and their influence on the device performance. Low-frequency noise has been studied by several authors in monolayer graphene [220, 221] and GFETs [222–224]. Recently, it has been also shown the influence of the substrate on the $1/f$ noise in a GFET, evidencing low-frequency noise redution in the case of h-BN-graphene-h-BN GFETs as compared to that in non-encapsulated graphene devices on Si/SiO2, due to h-BN capping and barrier layers. h-BN also produces strong positive effect on mobility in graphene channel, finding values in the range $30\,000\,\mathrm{cm^2V^{-1}s^{-1}}$ to $36\,000\,\mathrm{cm^2V^{-1}s^{-1}}$ [225]. Concerning the high-frequency noise performance, some works have dealt with this subject in graphene devices (see, e.g. [226–228]). In the microwave frequency range (a usual range for amplifiers) thermal noise has been shown to be dominant in GFETs [228]. Within this context, a deep understanding of the frequency-dependent noise properties of graphene at the bulk material level seems timely.

Along this chapter, we will analyze fluctuations in several conditions, employing appropriate tools for each of them. In section 4.1 we will study the noise power introduced by intrinsic sources by extracting the carrier differential mobility and diffusivity, which allows obtaining the frequency-dependent noise temperature. Section 4.2 will cover the analysis of fluctuations during abrupt changes of the applied field. Finally, in section 4.3 the capability of harmonic generation will be explored, with special emphasis on their masking due to the noise intrinsic to the diffusive regime and its implications for the detection of such harmonics.

4.1 Noise temperature

The noise temperature [229] is an interesting parameter for characterizing experimentally and theoretically, the thermal noise behavior of materials and devices, including also GFETs [230, 228]. This way, a link can be established between the local noise sources and the macroscopic noise performance of the devices. The noise temperature has been successfully employed for the study of noise in traditional semiconductors at the material level, e.g. in Si, GaAs, GaN, InN [231–233], etc. Such studies have evidenced the importance of a deep understanding of the differential mobility, power spectral density of current fluctuations (diffusion coefficient) and noise temperature, and their spectra, to examine the high frequency noise behavior of these materials. The frequency dependent noise temperature is related to the maximum fluctuating power per unit bandwidth displayed to an output circuit [231]. It provides additional information about the high-frequency performance, combining noise and dynamic properties of the system [231]. Numerical simulation tools, in particular the Monte Carlo method, have proved its suitability to achieve this goal [234]. In the case of graphene, some considerations must be taken into account.

Let us consider a graphene sheet with dimensions $L \times W$ (with L in the x direction) and a carrier density n, with two contacts at the ends (i.e., $x = 0$ and $x = L$). The power spectral density of the current fluctuations generated by a single carrier is given by: [235]

$$S_{\Delta i}(f) = \frac{e^2}{L^2} S_{\Delta v_x}(f) = 4\frac{e^2}{L^2} D(f), \tag{4.1}$$

being $S_{\Delta v_x}(f)$ the power spectral density of velocity fluctuations, that is related to the diffusion coefficient $D(f)$ through the Wiener-Kintchine theorem [234]:

$$D(f) \simeq D_{\delta v_x}(f) = \frac{1}{4} S_{\delta v_x}(f) = \frac{1}{4} \int_0^a C_{\delta v_x}(t) \exp(-2\pi\imath f t)\, dt, \tag{4.2}$$

with $C_{\delta v}$ being the correlation function of the velocity fluctuations, which reads

$$C_{\delta v_x}(t) = \langle \delta v_{i,x}(t') \delta v_{i,x}(t' + t) \rangle \,, \tag{4.3}$$

being $\delta v_{i,x}(t)$, the velocity fluctuation (in the x direction) of a particle i at an instant t: $\delta v_{i,x} = v_{i,x}(t) - \langle v_{i,x}(t) \rangle$. The total number of carriers is $N = nWL$. In non-degenerate systems, the contributions each carrier therefore is [235]:

$$S_{\Delta I}(f) = N S_{\Delta i}(f) = nWL S_{\Delta i}(f) = 4\frac{e^2 nW}{L} D(f), \tag{4.4}$$

with $I(t)$ being the total current. In the case of graphene the system is degenerate, so the electrons are no longer independent, the ratio $\Delta \langle N \rangle^2 / \langle N \rangle$, where $\Delta \langle N \rangle^2$ is the variance of the number of carriers and $\langle N \rangle$ is the average total number, must be taken into account in equation (4.4), so one gets:

$$S_{\Delta I}(f) = \frac{4e^2 nW}{L} D(f) \frac{\Delta \langle N \rangle^2}{\langle N \rangle}. \tag{4.5}$$

From statistical mechanics [235, 236], this ratio $\Delta \langle N \rangle^2 / \langle N \rangle$ can be expressed as:

$$\frac{\Delta \langle N \rangle^2}{\langle N \rangle} = \frac{k_B T_c}{n} \frac{\partial n}{\partial \varepsilon_F}, \tag{4.6}$$

with ε_F being the Fermi level, k_B the Boltzmann constant and T_c the system temperature. Considering equation (2.86a), and defining $\eta = \varepsilon / k_B T_c$, we get:

$$\frac{\Delta \langle N \rangle^2}{\langle N \rangle} = \frac{\displaystyle\int_0^\infty \eta \frac{\exp(\eta - \eta_F)}{[1 + \exp(\eta - \eta_F)]^2} d\eta}{\displaystyle\int_0^\infty \frac{\eta}{1 + \exp(\eta - \eta_F)} d\eta}, \tag{4.7}$$

so one gets:

$$S_{\Delta I}(f) = 4 \frac{e^2 nW}{L} D(f) \frac{\displaystyle\int_0^\infty \eta \frac{\exp(\eta - \eta_F)}{[1 + \exp(\eta - \eta_F)]^2} d\eta}{\displaystyle\int_0^\infty \frac{\eta}{1 + \exp(\eta - \eta_F)} d\eta}. \tag{4.8}$$

The power spectral density of current fluctuations can be obtained as [237, 235]:

$$S_{\Delta I}(f) = 4 k_B T_{\mathrm{n}}(f) \Re[Y(f)] p(f), \tag{4.9}$$

where $\Re[Y(f)]$ is the real part of the complex admittance –$Y(f) = enW\mu_{\mathrm{dif}}(f)/L$–, $\mu_{\mathrm{dif}}(f)$ is the real part of the differential mobility, T_{n} the noise temperature [237] and $p(f)$ is the quantum correction factor for thermal noise [235]:

$$p(f) = \frac{hf / 2k_B T_c}{\tanh(hf / 2k_B T_c)}. \tag{4.10}$$

The frequency-dependent generalized Einstein relation in graphene is therefore:

$$T_{\mathrm{n}}(f) = \frac{eD(f)}{k_B \mu_{\mathrm{dif}}(f) p(f)} \frac{\displaystyle\int_0^\infty \eta \frac{\exp(\eta - \eta_F)}{[1 + \exp(\eta - \eta_F)]^2} d\eta}{\displaystyle\int_0^\infty \frac{\eta}{1 + \exp(\eta - \eta_F)} d\eta}. \tag{4.11}$$

We turn now to explain how to obtain from the EMC simulator the quantities needed to determine the noise temperature: the diffusion coefficient and differential mobility, each of which require a different procedure. The diffusion coefficient is calculated through the Fourier analysis of instantaneous velocity fluctuations, that provides the power spectral density and, according to equation (4.3), $D(f)$. Degeneracy implies considering two sets of particles as described in [238]: the background carriers, that represent the standard carrier concentration and obey the non-linear BTE, and the excess carrier population that

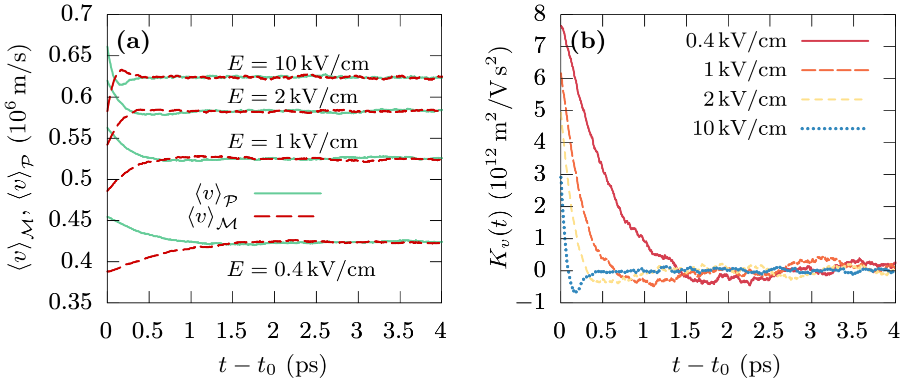

Figure 4.1: (a) Instantaneous drift velocity of carriers in the $\mathcal{P}$ (red lines) and $\mathcal{M}$ (green lines) ensembles for various values of the electric field, 0.4, 1, 2 and 10 kV/cm, and (b) instantaneous response function $K_v(t)$. The graphene layer is placed on top of a SiO_2 substrate. A small perturbation to carrier momentum (10% of the average value) has been applied.

evolves according to the linearized BTE [239] and must fulfill some requirements. First, it has to be small enough to represent a small perturbation of the system ($\sim$ 10% of the background particles), and secondly, it must not interfere in the background population dynamics. This is achieved by means of an exchange mechanism [239] that couples the two populations adequately. This methodology has already been successfully applied to the case of suspended graphene and graphene on a substrate [240, 150].

The frequency-dependent differential mobility is obtained by using the method described by Price [241]. It consists on studying the time evolution of two separate halves of the excess carrier population, $\mathcal{P}$ and $\mathcal{M}$. After having the system reached the stationary state, at a given time t_0, particles in the $\mathcal{P}$ set increase their individual momentum $\mathbf{p_i}$ by a small amount $\delta\mathbf{p}$, and carriers in the $\mathcal{M}$ set decrease it by the same amount. Afterwards all carriers are allowed to return to the stationary condition while the time evolution for the velocity of each half is recorded This way, one gets the response function K_v as [241]:

$$K_v(t) = \frac{e}{2|\delta\mathbf{q}|}\left(\langle v_i\rangle_{\mathcal{P}} - \langle v_i\rangle_{\mathcal{M}}\right). \tag{4.12}$$

Finally, the frequency-dependent differential mobility is given by

$$\mu_{\text{dif}}(f) = \int_0^\infty K_v(t)\exp(-\imath\pi f t)\,dt\,. \tag{4.13}$$

Figure 4.1 (a) shows the drift velocity evolution of the $\mathcal{P}$ and $\mathcal{M}$ sets for graphene on SiO_2 for different values of the stationary applied field (0.4, 1, 2 and 10 kV/cm) and a background carrier concentration fixed at 10^{12} cm^{-2}. The system returns to the stationary situation very quickly, with this transient becoming shorter as the applied

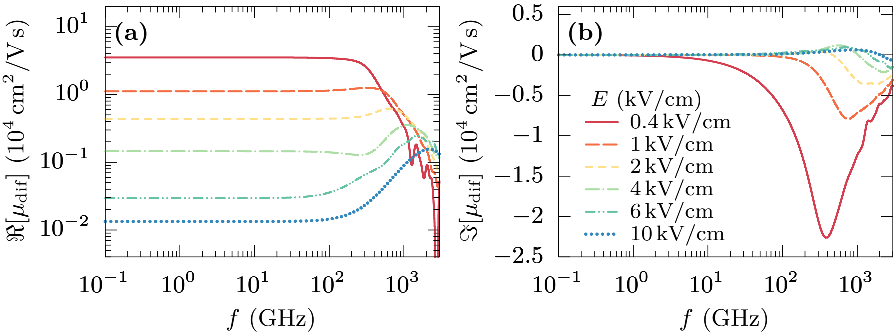

Figure 4.2: Real (a) and imaginary (b) parts of the differential mobility as a function of frequency, for several electric fields applied, in graphene on SiO$_2$.

electric field is stronger. A crossover of the mean velocities of the two sets appears at around ∼2 ps for 0.4 kV/cm, ∼1 ps for 1 kV/cm, ∼0.5 ps for 2 kV/cm and ∼200 fs for 10 kV/cm, after which the $\mathcal{M}$ set shows slightly larger velocities than the $\mathcal{P}$ set for a short time. The linear response coefficient, K_v shown in figure 4.1 (b), follows a progressive decay, result of the trend of two sets of particles to achieve the stationary, that is, reaching the same drift velocity. K_v reaches negative values at times determined by the $\mathcal{M}$ and $\mathcal{P}$ velocity crossovers.

Once that K_v is determined, the differential mobility $\mu_{\text{dif}}(f)$ is obtained with equation (4.13), as previously discussed. The results are shown in figure 4.2. The real part remains practically constant at the lowest sampled frequencies (10^8 Hz to 10^{10} Hz). This ranges to different spectra depending on the electric field. At low fields, $\mu_{\text{dif}}(f)$ has a Lorentzian shape, with the constant low-frequency mobility kept from hundreds of GHz to the THz range. A bump appears at strong fields, becoming more evident as the field is increased. This is a consequence of a larger negative part of the K_v at very short times. This negative response has its origin in the decoupling of velocity and energy relaxation [232, 231]. The imaginary part of the mobility is related to a reactive contribution to the material conductance [232]. It shows negligible values at low frequencies and a maximum at the corner frequency of the real part for low applied fields. Experimental measurements have shown a Drude-Smith frequency dependence for $\Im[\mu_{\text{dif}}(f)]$ in graphene [242], which is consistent with the present results.

The diffusion coefficient as a function of frequency for several electric fields is presented in figure 4.3 (a). It has a Lorentzian shape: the low-frequency value is reduced as the applied field is increased, and the corner frequency reaches higher frequencies for higher fields. This higher corner frequency is related to the loss of velocity correlation, that appears sooner as the applied electric field is stronger, as a consequence of more

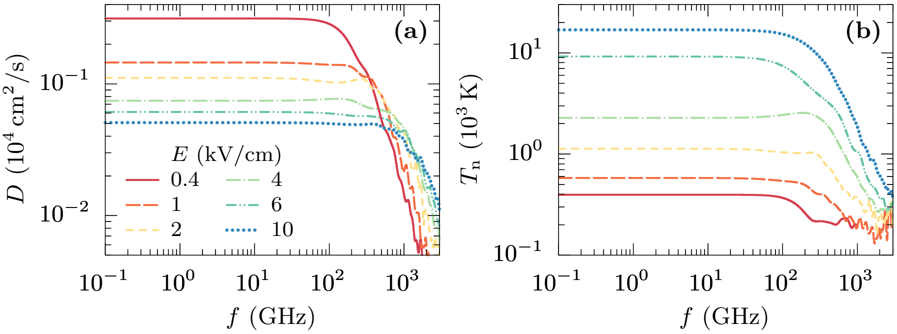

Figure 4.3: Diffusion coefficient (a) and noise temperature (b) as a function of frequency for several electric fields applied, in graphene on SiO_2.

intense scattering activity, particularly for optical phonons and remote polar phonons from the substrate [150]. The diffusion coefficient is reduced as the applied electric field is larger, due to the faster loss of velocity correlation induced by the growing scattering activity of increasingly energetic carrier profiles.

Once that the frequency-dependent mobility and diffusion coefficient are determined, the noise temperature can be directly obtained from equation (4.11). Their results are shown in figure 4.3 (b). The noise temperature shows a monotonic trend to increase with the electric field. This comes as consequence of the ratio between $D(f)$ and $\mu_{\text{dif}}(f)$; both quantities are reduced as the electric field is higher. However, the differential mobility drop with increasing E is more abrupt. In other words, the alterations in the dynamic behavior of perturbed carriers makes the noise originated by fluctuations (diffusion coefficient) be more amplified as the electric field grows. At low frequencies and electric fields, the noise temperature remains close to the equilibrium value (290 K) and rises significantly up to 10^4 K when the electric field is increased. At high frequencies close to the THz range the noise temperature experiences a progressive reduction that is driven by the drop in the diffusivity. This behavior is similar to that of Si, GaAs and semiconductor nitrides [231–233]. It cannot be understood in terms of a Lorentzian function based on physical parameters; in traditional semiconductors comparable curves have been interpreted in terms of complex analytical expressions derived from the linearization of the BTE [231, 232].

The substrate type has an important influence on T_n, as it can be observed in figure 4.4, particularly regarding the low-frequency value of this quantity, where three different structures were considered: graphene on SiO_2, graphene on h-BN and suspended graphene. At weak fields T_n is close to the ambient temperature in all cases. Then it grows with the electric field with a greater intensity in the case o suspended graphene,

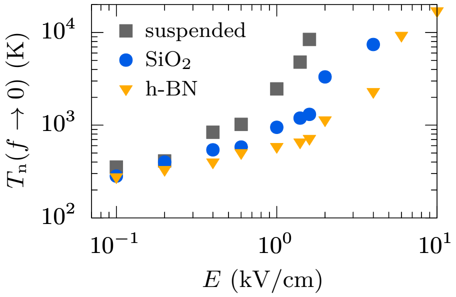

Figure 4.4: Low-frequency (0.1 GHz) noise temperature as a function of the applied electric field for graphene on SiO_2, graphene on h-BN and suspended graphene.

followed by graphene on h-BN. These results lie in the same order of magnitude as those observed in GaAs [231]. This difference is a result of the faster drop in the differential mobility, being more evident in suspended graphene and graphene on h-BN due to a more pronounced negative differential conductivity in the velocity-field curves [150]. In the case of suspended graphene this drop in the differential mobility is related to a more intense optical phonon activity, that strongly reorients the electron wavevector and translates into a reduction of the average velocity for a given applied field. In the case of graphene on SiO_2, SPPs dominate and provoke a reduction of the carrier energy without such a big velocity and wavevector reorientation in comparison with intrinsic optical phonons, leading to a not so severe reduction of the differential mobility. In the case of graphene on h-BN its intermediate situation is explained by its higher SPP energies, that appease the influence of this type of scattering. At strong fields, the onset of negative differential mobility makes T_n reach also negative values, and consequently it could not be defined according to equation (4.11), as in the case of III-V diodes [243]. In suspended graphene this condition is reached at lower fields than in graphene on substrates.

To analyze the frequency dependence of T_n we choose an intermediate field (1 kV/cm), for which the noise temperature is defined in all cases, as plotted in figure 4.5 (b). The corner frequency is smaller for suspended graphene, and has the largest value for graphene on SiO_2. This is due, firstly, to a smaller corner frequency in the power spectral density of velocity fluctuations [150] (and therefore also in the diffusivity), and secondly, to the larger comparative increase of the mobility in suspended graphene –figure 4.5 (a)–, consequence of a faster free carrier response to a linear perturbation, providing K_v ranges with negative values.

Reggiani et al. have related the noise temperature to the output power emitted by a sample as a consequence of the electromagnetic radiation produced by carriers in their microscopic movement composed of free flights under the accelerating field and scattering

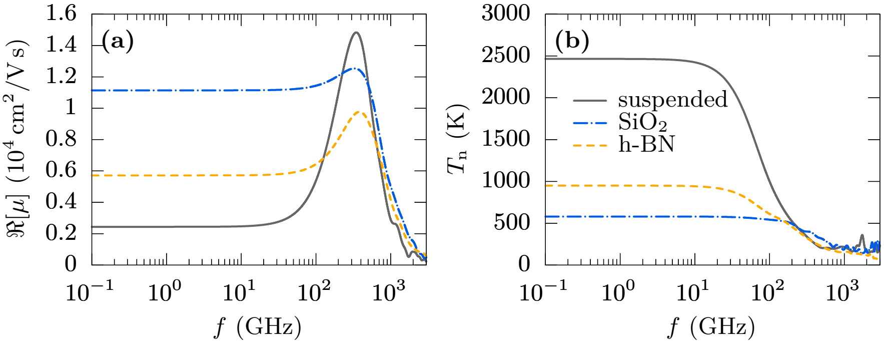

Figure 4.5: Real part of the differential mobility (a) and noise temperature (b) as a function of frequency for graphene on SiO_2, graphene on h-BN and suspended graphene. The applied electric field is 1 kV/cm.

interactions. Bearing this in mind, it can be concluded that the emitted noise power at low frequencies is much less for graphene on SiO_2 than in other cases. At high frequencies, the differences between graphene on h-BN and suspended graphene are reduced, providing a similar noise power.

4.2 Fluctuations under switching field conditions

In most analog and digital electronic applications, the motion of carriers inside the conducting channel are subjected to the variation in time of the electric fields originated by the switching potentials that are applied to their terminals. In this section, a study on velocity fluctuations of charge transport in MLG will be presented with particular focus on the transient regimes originated by switching conditions. This will be modeled by means of abrupt changes of the electric field magnitude: from low to high values and vice versa. Such analysis allows to quantify the noise and to know its microscopic origin, which is of interest for practical applications where switching field conditions are relevant.

As previously seen in section 4.1, the velocity correlation function [240] is one of the most basic tools to study velocity fluctuations. However, the correlation function defined in equation (4.3) describes fluctuation related to a fixed time. While this is enough for the study of stationary regimes, the study of transient situations under switching conditions requires the use a two-time (or transient) autocorrelation. This means that the correlation of velocity fluctuations at a particular instant depends on the history of instantaneous fluctuations during the transient time span. It is defined as [244]:

$$C_{\delta v}(t,\tau) = \langle \delta v_i(t)\delta v_i(t-\tau)\rangle, \tag{4.14}$$

where t and $t-\tau$ are the instants for which the correlation is calculated, $v_i(t)$ is the velocity on the direction of interest of a given particle, i, at the instant t. The different contributions to the velocity fluctuations are considered [245]:

$$\delta v(t) = \langle \delta v_{\varepsilon_i}(t) + \delta v_{i,\mathbf{k}}(t) \rangle \,, \tag{4.15}$$

where the first term of the right hand side of the equation is the so called convective contribution and it is associated with the fluctuations of the electron energy , being $\delta v_{\varepsilon}(t) = v_{\varepsilon}(t) - \langle v(t) \rangle$, and $v_{\varepsilon}(t)$ the average velocity of the particles with an energy between ε and $\varepsilon_i + \Delta\varepsilon$ at an instant t. The second term of equation (4.15) is the thermal contribution, $\delta v_{i,\mathbf{k}}(t) = v_i(t) - v_{\varepsilon_i}(t)$, and it is associated with the fluctuations of the electron momentum. Also, two more terms could be regarded: The first one is associated to the intervalley transitions; however, as discussed in section 2.4.1, K and K′ are considered to be degenerate, and since they are equivalent in terms of electronic transport, i.e., valley drift velocity, its contribution would be null. The last one is related to the change in the number of carriers. Nevertheless, no interband transitions were considered in this transient analysis. From these considerations, the autocorrelation function matrix reads:

$$\begin{aligned} \mathbf{C}_{\delta v}(t,\tau) &= \begin{bmatrix} C_{\delta v,\varepsilon\varepsilon}(t,\tau) & C_{\delta v,\varepsilon\mathbf{k}}(t,\tau) \\ C_{\delta v,\mathbf{k}\varepsilon}(t,\tau) & C_{\delta v,\mathbf{kk}}(t,\tau) \end{bmatrix} \\ &= \begin{bmatrix} \langle \delta v_{\varepsilon_i}(t) \delta v_{\varepsilon_i}(t-\tau) \rangle & \langle \delta v_{\varepsilon_i}(t) \delta v_{i,\mathbf{k}}(t-\tau) \rangle \\ \langle \delta v_{i,\mathbf{k}}(t) \delta v_{\varepsilon_i}(t-\tau) \rangle & \langle \delta v_{i,\mathbf{k}}(t) \delta v_{i,\mathbf{k}}(t-\tau) \rangle \end{bmatrix} , \end{aligned} \tag{4.16}$$

with $C_{\delta v,\varepsilon\varepsilon}$ and $C_{\delta v,\mathbf{kk}}$ being the convective and thermal terms respectively. The analysis is completed with the transient power spectral density (TPSD), described as [246]

$$S_{\delta v}(t,f) = \frac{1}{t-t_0} \left\langle \left| \int_{t_0}^{t} \delta v(\tau) \exp[2\pi\imath f(\tau - t_0)] \, d\tau \right|^2 \right\rangle , \tag{4.17}$$

where t_0 is the instant when the electric field is switched. For most practical applications, graphene is used lying on top of a substrate. Therefore, besides suspended graphene, the velocity fluctuations of graphene on two different substrates (SiO_2 and h-BN) are also analyzed.

First of all, it is important to stress that the impurity density and the defect parameters are adjusted so that the mobility for graphene on SiO_2 as a function of the carrier density reproduces the experimental results in [110] as it was previously done in section 3.1. According to this, figures 4.6 (a), (c), and (e) show the drift velocity, average energy and mean wavevector as a function of the electric field for suspended graphene, graphene on h-BN and on SiO_2 substrates, where the same impurity density and defect parameter is kept for the three structures. The electric fields for the study of switching

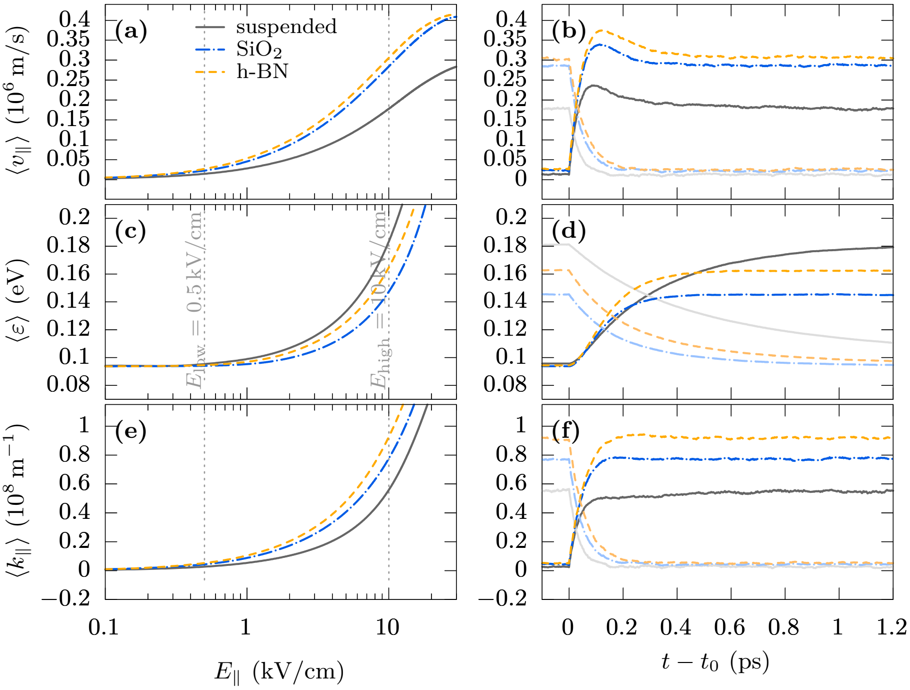

Figure 4.6: Ensemble averages as a function of the applied electric field of (a) drift velocity in the field direction, (c) energy, and (e) wavevector in the direction of the electric field. Crossing with the dashed vertical lines determine the average values at low field (0.1 kV/cm) and high field (10 kV/cm). Instantaneous ensemble averages as a function of the time switching from both high-to-low and from low-to-high field of (b) drift velocity in the direction of the electric field, (d) energy, and (f) wavevector in the field direction.

conditions have been chosen so that under the application of the low field, E_{low}, the average drift velocity low but still noticeable, and a high field, E_{high}, for which the ensemble velocity is around 10 times larger than that for the low field. They are indicated in the figure with dashed vertical lines. Transients for the electric field switching from the low-to-high values, as well as from high-to-low will be studied. It is remarkable that the ensemble velocities of graphene on SiO$_2$ and h-BN substrates are noticeably larger than for suspended graphene. This is mainly due to the effect of the scattering with SPPs, that reduce carrier energy with moderate wavevector (velocity) reorientation [150]. It has to be noted that as a result of the constant velocity (v_F) at which electrons travel in MLG at small energies, velocity fluctuations are restricted [240] to the range $[-2v_F, 2v_F]$. Velocity relaxation through scattering mechanisms depends only on the momentum reorientation (and not on the kinetic energy) which it is strongly affected by the scattering mechanisms anisotropy.

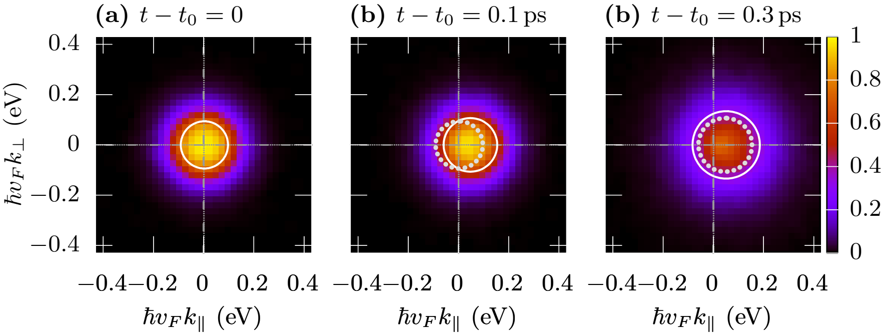

Figure 4.7: Density plots of the distribution functions in momentum space for the low-to-high field transient at different intervals $t-t_0$: (a) 0 (low-field stationary state), (b) 100, and (c) 300 fs of graphene on SiO$_2$. The white solid circles represent the average thermal energy centered at the average wavevector for the given situation, while the dotted ones show for comparison the circles of the previous situation.

Figures 4.6 (b), (d), and (f) depict the transient drift velocity in the direction of the applied field, momentum and the energy averaged over the ensemble. In the low-to-high field transient in the three cases under consideration we can observe a velocity overshoot peaking at around ∼100 fs before reaching the stationary value. However, regarding the parallel wavevector, it reaches its maximum at around ∼200 fs and stays steady thereafter. On the other hand, the average energy presents a slower evolution than $\langle v_\parallel \rangle$ and $\langle k_\parallel \rangle$ and marks out the time lapse of the transients, that is 0.6 ps for graphene on substrates and over 1.2 ps for suspended graphene. This transient is dominated by an initial strong drift by the high electric field, that pushes the electron distribution against its direction in momentum space, originating a monotonous increase of the mean energy as seen through the evolution from the steady state for the low-field –figure 4.7 (a)– towards 100 fs after the application of the high-field –figure 4.7 (b) to (c)–. Afterwards, the distribution increases its electronic temperature, i.e., it tends to spread, but remaining displaced from the Dirac point, resulting in a steady value of the averaged momentum but a reduction of the ensemble velocity, together with an energy increase –figure 4.7 (c)–.

In the second case –the high-to-low field transient–, the parallel velocity and wavevector evolve with a similar trend, arriving to a stationary value at 200 ps, while the energy decay is slower. Again, suspended graphene presents the longest transient time. Here, the dynamics of the ensemble happens in a similar way. First, the hot momentum displaced distribution gets closer to the Dirac point in the absence of a high electric field, and then it cools down. In this case, the slower evolution of $\langle \varepsilon \rangle$ in comparison with the averaged velocity and wavevector is directly related to inelastic mechanisms, being

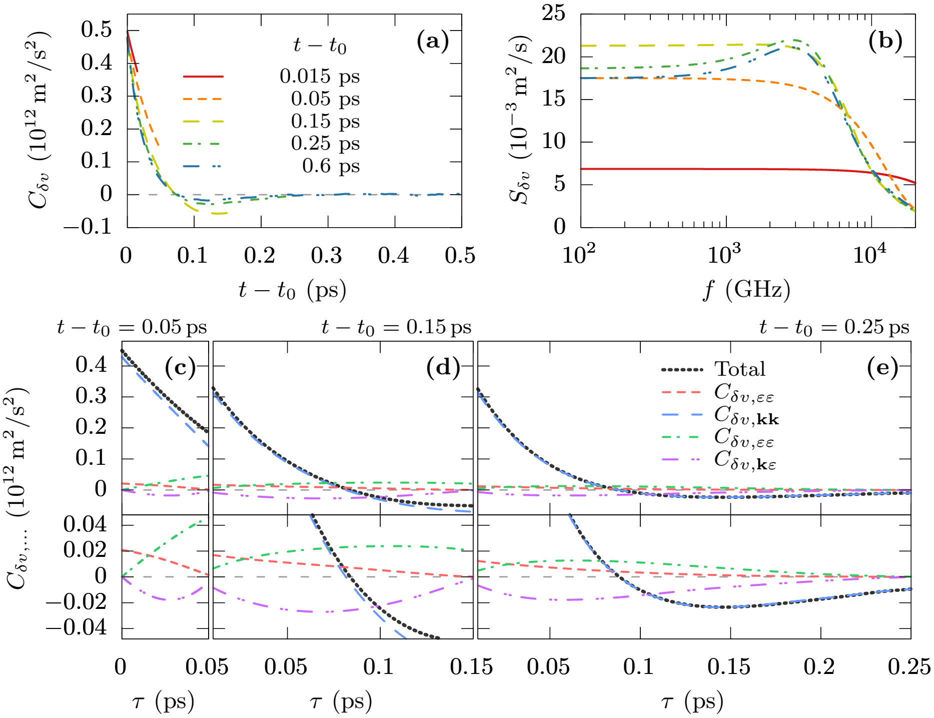

Figure 4.8: Low-to-high field transient (a) autocorrelation function, and (b) power spectral density of the velocity fluctuations for graphene on SiO$_2$ at different instants. The considered components of the autocorrelation function at $t-t_0$: (c) 50, (d) 150, and (e) 250 fs, as described in equations (4.15) and (4.16)

suspended graphene where carriers relax on a lower pace due to the absence of substrate SPPs. In contrast to the previous case, this transient is more heavily ruled by the effect of the scattering mechanisms that lead the system to a stationary state of equilibrium, since the low-field steady state is fairly close to it.

Let us now focus on the graphene on SiO$_2$ configuration. In figure 4.8 (a) we plot the transient autocorrelation function for various instants after the application of a low-to-high step in the electric field. At the earliest instants ($t-t_0 = 15$ and 50 fs), the initial value of the autocorrelation decreases as the ensemble velocity grows. Also, a progressive steepening of the initial slope and a minimum at around 140 fs, with a negative value for $C_{\delta v}$ can be seen. Both phenomena are a consequence of the increasing scattering activity that takes place as the electric field makes the carrier distribution more energetic and shifted in momentum space. In this situation, hot carriers would mostly move with a higher velocity than the ensemble average (positive velocity fluctuation) and are due to be backscattered with TO-K/LO-Γ or TA/LA-K phonons, with

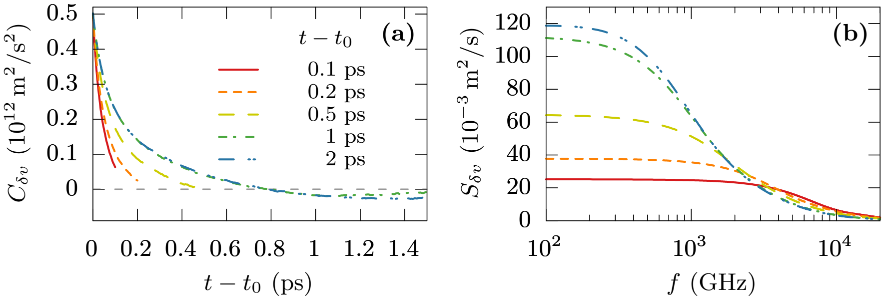

Figure 4.9: High-to-low field transient (a) autocorrelation function, and (b) transient power spectral density of the velocity fluctuations for graphene on SiO_2 at different instants.

a resulting velocity after the collision lower than the ensemble average, presenting now a negative velocity fluctuation. On the other hand, cold carriers would have a velocity lower than the ensemble average (negative velocity fluctuation) and because of the drift of the electric field, they gain velocity and may end having a positive velocity fluctuation before suffering the same process described above. Both processes for hot and cold carriers result in a change of the sign of the velocity fluctuations, originating the increasingly faster decay and the negative part of the autocorrelation function. For longer times ($t - t_0 = 250$ fs to 600 fs), the value of the minimum moderates, and the autocorrelation function mostly approaches that of the stationary situation for $E = E_{\text{high}} = 10$ kV/cm. The results of the different components of the total velocity autocorrelation function, shown in figures 4.8 (c), (d), and (e), indicate that the thermal contribution, related to momentum fluctuations, is the dominant one. However, for this transient, the convective contribution (related to the energy fluctuation), although relatively low, is not negligible. This convective term appears as a direct consequence of an initial temporary appearance of a positive fluctuation of newly occupied energy levels, happening concurrently with the velocity overshoot. In figure 4.8 (b), the transient power spectral density (TPSD) provides information about the velocity fluctuation phenomena in the frequency domain. The TPSD grows with a Lorentzian-like shape up to 150 fs. From that moment a maximum starts to appear at 2.5 THz and the low-frequency values start to drop. The values of the spectral density decrease until reaching the stationary behavior corresponding to the steady state of the final electric field. This is revealed by the constant TPSD at longer times, which in this particular case are $\gtrsim 300$ fs, as it will be seen later.

Figures 4.9 (a) and (b) allow examining the second scenario (high-to-low field transient). Here, the autocorrelation function evolves by reducing its slope as time passes, which indicates that the velocity fluctuations change their sign less frequently as the transient evolves. Microscopically, it can be explained by the quick transition from a carrier

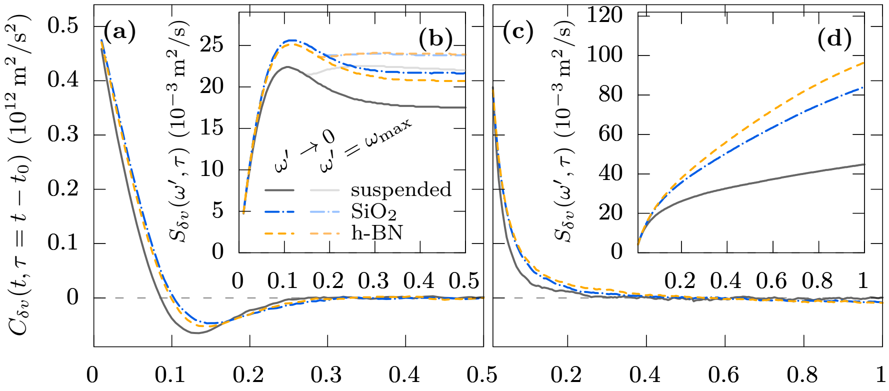

Figure 4.10: Temporal evolution of (a) and (c) the correlation of the velocity fluctuations between times t and t_0 ($\tau = t - t_0$), and (b) and (d) the low-frequency transient power spectral density at low frequenciy (100 GHz), and at the frequency where the maximum TPSD occurs ($\omega_{\max}$) for the (a)-(b) low-to-high, and (c)-(d) high-to-low field transients.

distribution where energetic carriers are highly oriented and backscattering (strong negative fluctuation) is strongly favored, towards an almost isotropic distribution. Zero crossing occurs at longer times after the field switching than in the low-to-high transient, and is displaced towards larger τ as the transient evolves. A minimum is achieved at long times (around ∼1.5 ps), standing out the reduced scattering activity relocating the particle velocity once the steady state for the low field conditions has been achieved. In this case, the convective term is negligible, meaning that there is not a noticeable change of the averaged carrier velocities in the different energy levels, and only the wavevector reorientation is playing a role in this transient. Finally, the TPSD reveals that the power dissipated due to velocity fluctuations is larger at low frequencies, and even the tail progressively diminishes and shifts towards smaller frequencies, which is attributed to the decrease of scattering activity in the low-field steady state.

Finally, a brief comparative analysis between the three configurations (suspended graphene, graphene on SiO$_2$ and graphene on h-BN) is provided. Suspended graphene showed the fastest response to the electric field shift with regard to the parallel velocity and momentum –figures 4.6 (b) and (f)–, but the slowest for the average carrier energy –figure 4.6 (d)–. In the graphene on h-BN and SiO$_2$ cases the trends are very due to their mutual resemblance of SPP interactions and background permittivity. On the other hand, in suspended graphene this interaction with remote polar phonons does not exist and the reduced screening enhances the interaction with impurities, which are dominant for the n_{imp} considered. Figure 4.10 (a) shows the evolution of the autocorrelation of velocity fluctuations at a time t and the initial conditions ($\tau = t - t_0$). In the low-to-high transient, the correlation is lost at shorter times in suspended graphene, followed by graphene on SiO_2 and on h-BN. The minimum is reached at 125 fs, while for graphene on SiO_2 and h-BN is at 140 fs and 150 fs respectively. Also, the shorter the time at which the minimum is reached, the more negative is its value. In figure 4.10 (b) the evolution of the TPSD at low frequencies (10 GHz, darker lines) and its maximum value (lighter line) is shown. Both curves coincide until the appearance of the maximum in the power spectral density, that locates at frequencies of ∼2.2 THz for graphene on h-BN, ∼2.4 THz for graphene on SiO_2 and ∼2.8 THz for suspended graphene. The low-frequency power spectral density evolution shows similar trends for the three cases: a fast initial rise until reaching a maximum, followed by a smooth drop and its stabilization towards the value of the high field steady state. With regard to the high-to-low field transient, although the initial correlation is higher for suspended graphene, it presents a faster decay of the velocity correlation. As it concerns the low-frequency power spectral density, for the three cases, it grows until saturation for times longer than 2 ps.

In comparison with III-V semiconductors [246] a similar qualitative behavior of the TPSD is observed in the low-to-high and high-to-low transients. In the low-to-high field switch, GaAs and InP feature a displacement of the peak of the TPSD towards lower frequencies as the transient evolves. This feature is not as noticeable in the graphene case presented here. Besides, such peak appears in graphene above 2 THz, while in GaAs and InP is below 1 THz. The spectral density in this case shows smaller values in graphene in comparison with GaAs and InP due to a quick drop of the correlation of velocity fluctuations. As it regards the high-to-low transient, the stationary power spectral density of the velocity fluctuations is achieved earlier (∼2 ps in graphene versus >10 ps in GaAs and in >30 ps in InP), which is in good agreement with the faster ensemble response in terms of velocity and energy.

4.3 Harmonic generation

The THz range has been the subject of intense investigation in the last decades due to the enormous potential of this region of the electromagnetic spectrum for applications such as imaging, sensing, communications and spectroscopy [247–250]. In this context, the need of THz sources and detectors becomes a major issue. In particular, high-order harmonic generation is an interesting option to reach the THz range, and consequently this path has been explored in the case of devices based on traditional semiconductors [251–253]. Regarding graphene, some works have tackled the topic of high-order harmonic generation, considering polarized light excitation [254], THz pulses [255] or plasma-assisted generation [256], just to cite some examples. However, when dealing with the feasibility of a given material for high-harmonic generation, attention should be paid also to the noise phenomena, that can mask the generated signal at these harmonic frequencies [257, 258]. The intrinsic noise of a material under an alternating electric field can be described in terms of the velocity fluctuations of the individual carrier instantaneous velocity with respect to the instantaneous ensemble-averaged velocity. It must be taken into account that this average velocity is a time-periodic function and it is able to contain the high-order harmonics of the fundamental signal [258] due to the non-linear response of the carriers to the electric field. Consequently, analyzing the physical mechanisms related to harmonic generation in conjunction with the intrinsic noise phenomena at the material level becomes a key question when exploring the possibilities of graphene in the THz range.

To evaluate the intrinsic noise under high-harmonic generation conditions, we carry out a thorough analysis of instantaneous drift velocity fluctuations when an oscillating electric field is applied to a graphene sample as follows. The time-dependent electric field is described by:

$$E(t) = E_{\mathrm{AC}} \cos(2\pi f_{\mathrm{AC}} t), \tag{4.18}$$

being E_{AC} the amplitude, and f_{AC} the frequency. The time-dependent drift (ensemble-averaged) velocity, $\langle v(t) \rangle$, will then be a periodic function, with the same frequency of $E(t)$, and featuring harmonics of the fundamental frequency. This quantity is calculated at each time step, that in the present work is considered to be $\lesssim 2\,\mathrm{fs}$[1], by averaging over the whole ensemble of particles. In the results presented here, the number of simulated particles equals to 10^4. The complex m^{th} order Fourier coefficients are obtained as:

$$v_m = \frac{1}{T_{\mathrm{AC}}} \int_0^{T_{\mathrm{AC}}} \langle v(\theta) \rangle \exp(-i 2\pi m f \theta)\, d\theta \tag{4.19}$$

where T_{AC} is the period of the signal (equal to $1/f_{\mathrm{AC}}$) and θ is a time within the interval $[0,\, T_{\mathrm{AC}}]$. In this way, the m^{th} harmonic intensity $|v_m|^2$ can be determined.

In order to calculate the intrinsic noise induced by velocity fluctuations, we considered two approaches: the correlation function of velocity fluctuations, and the finite Fourier transform [257]. In the correlation function approach, it has to be taken into account that in the presence of an oscillating excitation electric field the process is non stationary. Therefore, like in the case of transient phenomena under switching field conditions (section 4.2), the correlation function can not be described in terms of a single time function, and it depends on two times [258], θ and τ:

$$C_{\delta v \delta v}(\theta, \tau) = \langle v(\theta) v(\theta + \tau) \rangle - \langle v(\theta) \rangle \langle v(\theta + \tau) \rangle\,, \tag{4.20}$$

where, again θ is within $[0,\, T_{\mathrm{AC}}]$. At a given time within the cycle, the spectral density of velocity fluctuations can be determined as:

---

[1] The time step (Δt) is chosen so that the period of the applied alternating electric field is an integer multiply of this quantity.

$$S_{\delta v \delta v}(\theta, f) = \int_{-\infty}^{+\infty} C_{\delta v \delta v}(\theta, s) \exp(i2\pi f \tau)\, d\tau\,. \tag{4.21}$$

Finally, the mean spectral density of velocity fluctuations $\overline{S}_{\delta v \delta v}(f)$ is obtained by properly averaging $S_{\delta v \delta v}(\theta, f)$ in the whole cycle. In a finite time interval T, the spectral density of the instantaneous drift velocity can be finally calculated including the contribution of the harmonics and velocity fluctuations parts as [257, 258]:

$$S^{T}_{vv}(\nu_m) = \overline{S}_{\delta v \delta v}(\nu_m) + 2T|v_m|^2. \tag{4.22}$$

We can calculate also this spectral density through the second mentioned procedure: the finite Fourier transform approach [257, 258]. In our EMC case for a set of N particles along the time interval [0, T]:

$$g_i(f_n) = \frac{1}{T} \int_0^T v_i(t) \exp(-2\pi i f_n t)\, dt, \tag{4.23}$$

$$S^{T}_{vv}(f_n) = 2T \frac{1}{N} \sum_{i=1}^{N} |g_i(\nu_n)|^2\,, \tag{4.24}$$

where $f_n = n/T$, with $n = 0, \pm 1, \pm 2, ...$, and T is chosen as an integer multiple of the fundamental period T_{AC}.

Furthermore, the frequency bandwidth used by a receiver is a critical parameter for the extraction of the signal harmonics. It can be obtained from the harmonics intensity and the spectral density of velocity fluctuations as [258]:

$$\Delta f_{\mathrm{th}} = \frac{2|v_m|^2}{\overline{S}_{\delta v \delta v}(f_m)}. \tag{4.25}$$

In figure 4.11 the drift velocity time response is presented for different excitation frequencies and under various applied electric fields. For comparison purposes, a quasi-static case is also included: in that situation, an adiabatic approximation is considered, this is, an instantaneous response of the carrier velocity to changes of the electric field is assumed[2]. In this quasi-static case (equivalent to applying a low frequency alternating field), regardless of the applied electric field the velocity response presents a quite distorted shape, almost square-like. This is due to the non-linearity of the electric field-velocity curve of suspended graphene , which starts even below 1 kV/cm, combined with the instantaneous velocity response condition. At high frequencies (specially at 300 GHz), and low electric fields –figure 4.11 (a)–, the velocity response is more sinusoidal-like and

---

[2] The reader must keep in mind that we are simulating electrons, so the electric field exerts a drag force in the opposite direction.

presents an important delay related to the carrier inertia. When the absolute value of the alternating field increases, carriers respond very rapidly due to the overshoot effect in graphene as seen in section 4.2. On the other hand, when the absolute value of $E(t)$ diminishes, carriers can only adapt to the new field conditions by relaxing their momentum and energy through scattering processes, which need some time. When the relaxation times are comparable to the signal period, the electronic distribution can not adapt instantaneously to the electric field variations when the absolute value of $|E(t)|$ drops, so a delay takes place.

This ends up affecting the carrier distribution in the momentum space during the whole cycle, as it can be observed in figure 4.12. In a quasi-static case –figures 4.12 (a), (b) and (c)– there is an exact correspondence between the carrier distribution and the instantaneous electric field. At the instant when the maximum field ($\pm E_{\mathrm{AC}}$) is applied, the electronic distribution is displaced and expanded, and when the instantaneous field equals zero the electronic distribution is centered ($\langle \mathbf{k} \rangle \simeq 0$) and more compact (colder). However, at high frequency –figures 4.12 (c) and (d)–, the electronic distribution can no longer follow the electric field dynamics. It does not heat and cools so clearly as in the quasi-static case (this is related to a reduced variation of the average energy along the cycle, as it will be shown later), and there is a clear de-phasing (delay) with regard to the electric field.

In figure 4.13, the average energy versus time for the frequencies and electric field amplitudes under study are shown. For a given E_{AC}, the energy variations at low fre-

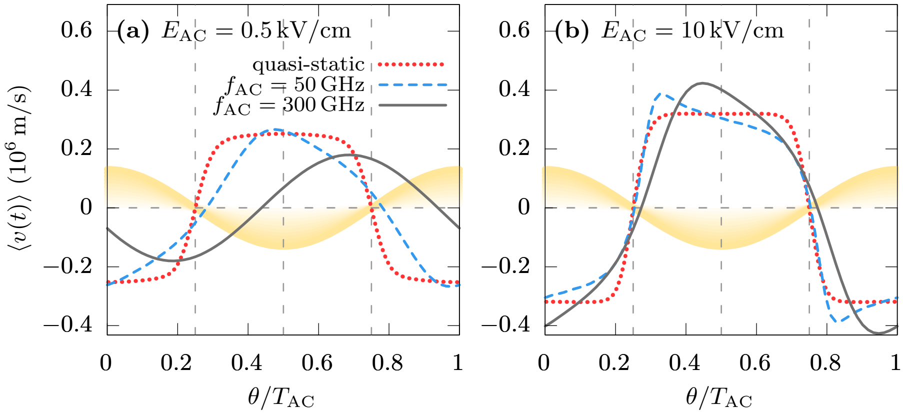

Figure 4.11: Average velocity response of the system, $\langle v(t) \rangle$, for the quasi-static case (dotted red lines) and for frequencies $f_{\mathrm{AC}} =$ 50 (dashed blue lines) and 300 GHz (black solid line), with an applied electric E_{AC} of: (a) 0.5 kV/cm, and (b) 10 kV/cm. The time scale is normalized by the period of the signal to allow an adequate comparison at different frequencies, and light yellow cosine function is a representation of the alternating electric field.

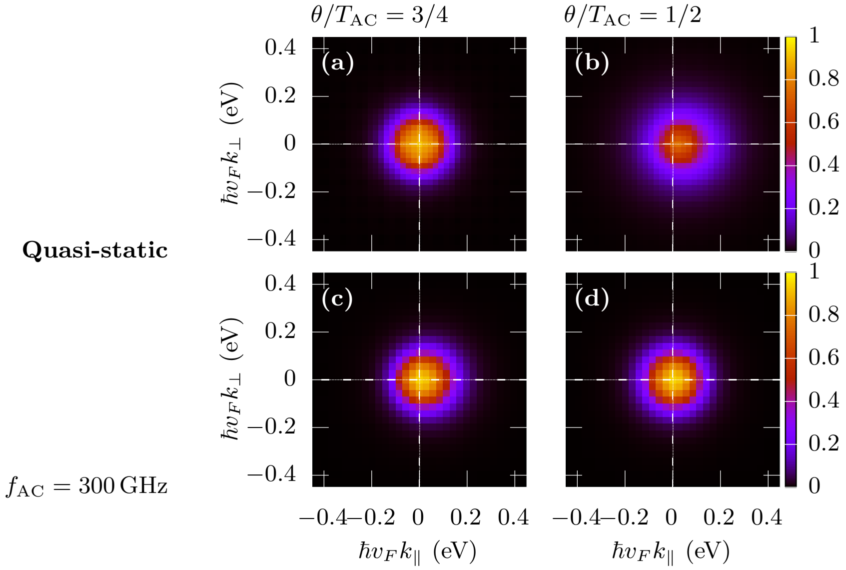

Figure 4.12: Carrier wavevector distribution at instants within the cicle of θ: (a, c) 1/2, where the electric field is $-E_{\mathrm{AC}}$, and (b, d) 3/4, where the electric field is 0 and evolves with a positive slope. The panes (a) and (b) correspond to the quasi-static case, while the panels (c) and (d) to the case where $f_{\mathrm{AC}} = 300\,\mathrm{GHz}$. The field amplitude, E_{AC} is $0.5\,\mathrm{kV/cm}$.

quencies (e. g. quasi-static case) are much larger than at high frequencies, which is in good agreement with the previously observed behavior of the instantaneous shots of

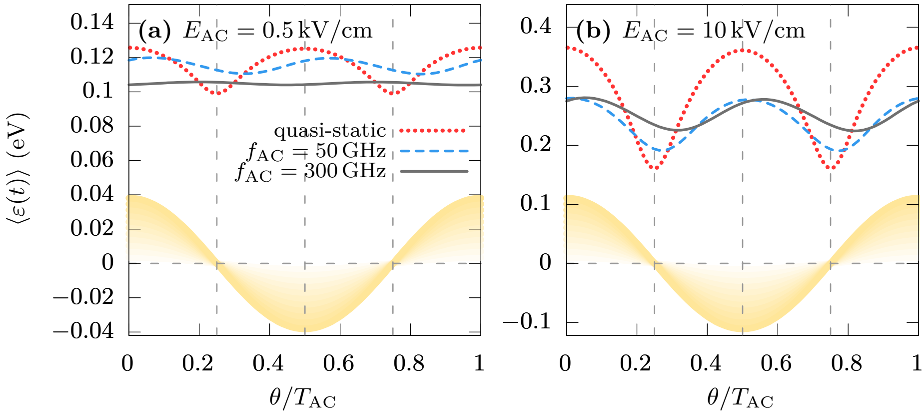

Figure 4.13: Time evolution along several cycles of the average carrier energy for the quasi-static case (dotted red line), frequencies of f_{AC}: $50\,\mathrm{GHz}$ (dashed blue line) and $300\,\mathrm{GHz}$ (solid black line) and applied electric fields of (a) $0.5\,\mathrm{kV/cm}$, and (b) $10\,\mathrm{kV/cm}$.

the electronic distribution in the momentum space. As the electric field increases, the average energy value along the whole cycle tends to increase comparatively for the larger frequencies, which is consistent with the fact that, in that case, the system is plunged into an excitation state characterized by a more complex excitation-relaxation dynamics.

Let us now focus on the harmonics generation consequence of the velocity response. In figure 4.14, the intensities of the first to ninth (odd) harmonic versus the electric field amplitude E_{AC} are reported for the quasi-static case and for an excitation frequency equal to 300 GHz. Even harmonics are canceled due to the symmetry of the velocity response and to the absence of a DC component of the excitation signal. As it can be seen, at low frequencies the intensity of the higher harmonics is significant, which is in good accordance with the more square-like shape of the instantaneous average velocity in that particular situation. At high frequencies and low fields, the intensity of the high-order harmonics is much attenuated, which is related to the more sinusoidal-like velocity response. As the electric field increases, at high frequency –figure 4.14 (b)– the high-order harmonic intensity also grows, since the larger scattering activity not only reduces the delay but also modifies the velocity shape –figure 4.11 (c)–.

In order to analyze the intrinsic noise under fluctuating field conditions, figure 4.15 presents the mean power spectral densities of velocity fluctuations for different values of the electric field amplitude and a signal with $f_{\mathrm{AC}} = 300$ GHz. The power spectral density presents a Lorentzian shape. This agrees with the behavior shown at low fields in III-V semiconductors [258]; however, contrarily to those materials, in suspended graphene no peak is observed at high fields. Such peaks were attributed to intervalley transfer towards upper valleys in III-V semiconductors, which does not exists in graphene. Besides, due

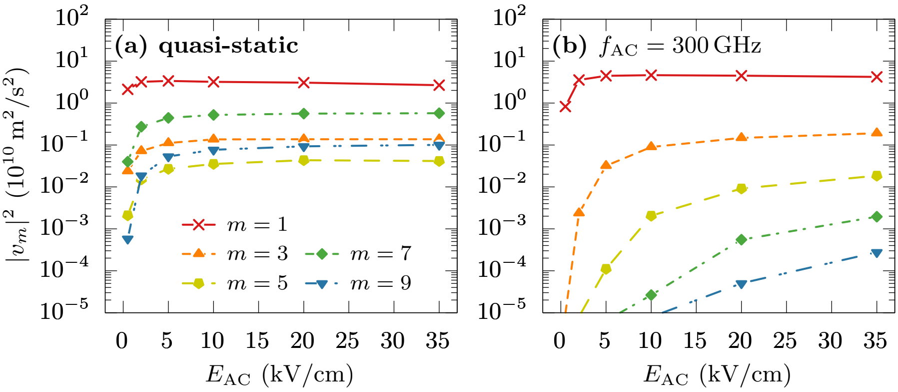

Figure 4.14: Fourier coefficient squares as a function the alternating electric field magnitude for the first to ninth harmonics for suspended graphene in (a) a quasi-static case, and (b) at $f_{\mathrm{AC}} = 300$ GHz.

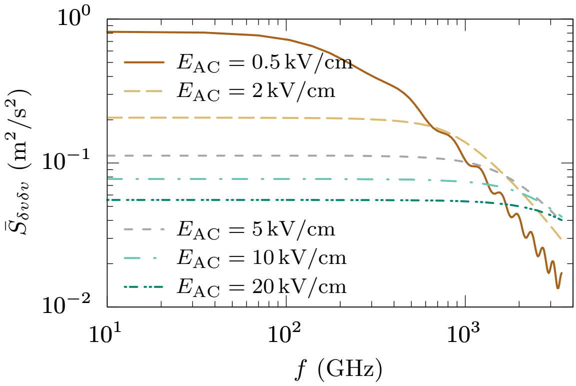

Figure 4.15: Mean spectral density of velocity fluctuations in suspended graphene under an alternating electric field with frequency $f_{AC} = 300\,\mathrm{GHz}$, for several values of its amplitude.

to the shorter momentum and energy relaxation times, as the electric field amplitude is increased, the low-frequency power spectral density of velocity fluctuations decreases with E_{AC}.

The comparative study of the generated harmonics and noise is made by means of the spectrum of the velocity response shown in figure 4.16, which has been determined for suspended graphene under different electric field amplitudes ($E_{AC} = 0.5\,\mathrm{kV/cm}$ and $10\,\mathrm{kV/cm}$ at $f_{AC} = 300\,\mathrm{GHz}$). The two methods (correlation function combined with Fourier coefficients, and the discrete Fourier transform) for determining this quantity show an excellent agreement. The time T was set equal to $300T_{AC}$, which would correspond to a minimum bandwidth of 1 GHz. The results show that, at low electric field

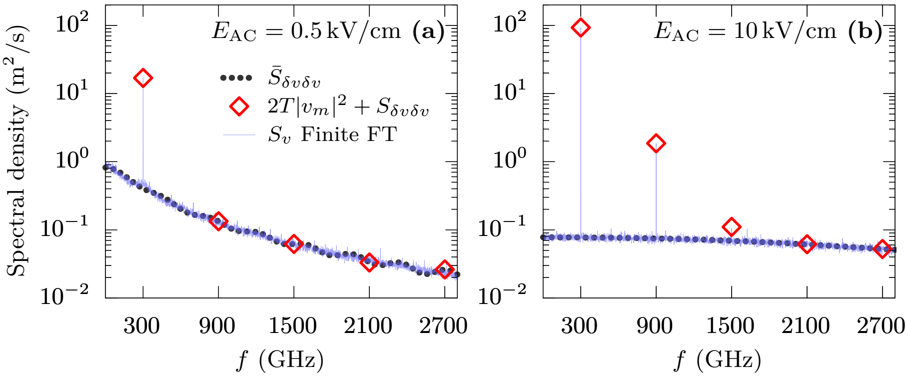

Figure 4.16: Spectral density of velocity response in suspended graphene with a finite time $T = 300T_{AC}$ with frequency $f_{AC} = 300\,\mathrm{GHz}$ and electric field amplitude E_{AC}: (a) $0.5\,\mathrm{kV/cm}$, and (b) $10\,\mathrm{kV/cm}$.

amplitude, noise masks practically all the harmonics: only the harmonic corresponding to the fundamental frequency is clearly evidenced, while the higher order harmonics are fully screened by noise. For large electric fields, such as 10 kV/cm, the first, third and even fifth harmonic are discernible. Similar trends were observed for larger electric field amplitudes. To put into context these results, in III-V materials such as InP, it is possible to discern up to the seventh harmonic for a frequency $f_{\mathrm{AC}} = 200\,\mathrm{GHz}$ and $E_{\mathrm{AC}} = 8\,\mathrm{kV/cm}$, with $T = 200T_{\mathrm{AC}}$ (minimum bandwith of 1 GHz) [258]. It is interesting also to notice that, disregarding the spikes, the noise contribution to the velocity response spectrum presents a relatively flat behavior as compared to the case of III-V devices [258]. At this point, it must be taken into account that the results presented in [258] did not include either hot phonon effects, which significantly increase acoustic and optical intervalley emissions, or carrier-carrier interactions: consequently, we can affirm that graphene has at least a comparable potential for high-order harmonic generation as III-V materials, at the expense of probably larger T times (i.e., narrower bandwidth).

Finally, it is possible to determine the bandwidth threshold for the detection of a given order harmonic. Figure 4.17 represents the regular (harmonics) and noise contributions to the velocity response spectrum, considering an external receiver with frequency bandwidth Δf equal to 10, 1 or 0.1 GHz. In this way, it is possible to determine the number of harmonics opened to such receiver. The results for $E_{\mathrm{AC}} = 10\,\mathrm{kV/cm}$ and two different frequencies, 300 GHz and 50 GHz are shown. With $\Delta f = 10\,\mathrm{GHz}$, only up to the fifth and third harmonics can be detected at 50 GHz and 300 GHz respectively. Using a narrower bandwidth (e. g., 0.1 GHz), the ninth harmonic at 50 GHz and the fifth at

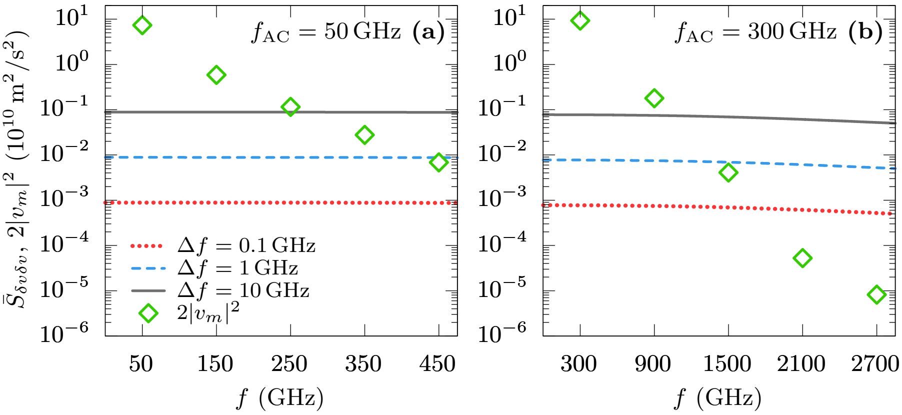

Figure 4.17: Comparison of the regular and noise contributions to the velocity response spectrum for suspended graphene at $E_{\mathrm{AC}} = 10\,\mathrm{kV/cm}$ and the frequencies, f_{AC}: (a) 50 GHz, and (b) 300 GHz.

300 GHz would be available, therefore opening the path to the THz regime by the use of high-order harmonics in a relatively wide fundamental frequency range below 300 GHz.

Chapter summary

Noise temperature

A method to extract the differential mobility from a small perturbation of the electronic system has been employed, combined with the analysis of velocity fluctuations in order to obtain the frequency dependent noise temperature in graphene. Fluctuation noise becomes progressively suppressed (to a lesser extent) by increasing the electric field, due to a growing scattering activity that provokes a faster loss of velocity correlation. However, the more pronounced relation of the differential mobility do drop with stronger applied fields explains the growth of the noise temperature with the electric field. Comparison between suspended graphene and graphene on SiO_2 and h-BN reveals that SPPs favors larger differential mobilities, thus reducing the noise temperature.

Fluctuations under switching field conditions

We also studied velocity fluctuations under transient conditions due to switching field conditions. In the low-to-high field transient a quick response of the electrons to the high field results in a velocity overshoot. The transient velocity fluctuation correlation function tends to decrease over time, and reaches a minimum between 120 and 140 fs, which corresponds to a maximum value of the power dissipated by the velocity fluctuations around 2.3 THz. Finally, for the high-to-low field transient, the velocity fluctuation correlation function increases over time because of the progressive lessening of the velocity reorientation by the scattering mechanisms. In comparison, velocity fluctuations in graphene on substrates show similar behaviour. However, when considered a suspended layer, a faster loss of the autocorrelation and lower values on the power spectral density are achieved as a consequence of the absence of substrate interactions. Clearly, the dominant term contributing to the velocity fluctuations is the thermal one; nevertheless, in the low-to-high transient the convective contribution is noticeable due to the fast shift of the electron distribution in the momentum space as a response to the change towards a higher electric field.

Harmonic generation

The generation of high-order harmonics in graphene under AC fields has been analyzed. The intensity of the harmonics is obtained for several frequencies and electric field amplitudes; high order harmonic generation falls as the frequency is increased, and as the applied maximum AC electric field is reduced. As the frequency of the excitation signal is raised, a delay or inertia of the carrier velocity is observed, along with a reduction of the maximum drift velocity values reached. This distortion is explained in terms of the carrier wavevector distribution, average energies and the scattering that competes with the oscillating electric field drag to take the system to equilibrium. Noise and regular contributions to the power spectral density of the velocity response are discerned, and the harmonic modes available for several bandwidths are discussed. Results show that it is possible to reach the THz range with conditions comparable to those found for III-V materials, at the expense of narrow bandwidths.

Chapter 5

Ultrafast dynamics of photoexcited carriers

This section will focus on the study of the dynamics of photoexcited carriers in monolayer graphene. Photoexcitation is a process in which electrons are taken from their ground state to another excited state of the quantum system by means of photon absorption. This a is key phenomenon in technological applications such as light sensing (like in photodiodes, or camera sensors), photovoltaic energy harvesting or generation of laser radiation by optical pumping. The natural trend of the photoexcited carriers is returning to its background state; this process is referred to as relaxation.

The particular linear and gap-less energy spectra for electrons and holes, provides monolayer graphene with a constant optical absorption with virtually no restriction to the photon wavelength. More precisely, a single layer of undoped graphene shows an opacity related to the fine-structure constant [259] of around $\sim 2.3\%$ for a very wide wavelength span. Another interesting feature is the possibility of tuning the Fermi energy by means of electrostatic gating as a way to modulate the optical absorption at desired frequencies [260, 261]. This features places it in a promising position for the development of a broad range of highly efficient photonic and optoelectronic applications, being of particular interest those that operate in the THz range [262, 250, 263]. The realization of such applications and devices must be supported by a thorough understanding of the dynamics that charge carriers undergo during and after the material is irradiated with light. Besides, experimental measurement of relaxation processes can provide insight into the physical phenomena that governs the carrier dynamics, and assess the validity of the physical models used to describe them. The research community has made in the recent years an intense effort in order to achieve a good understanding of the dynamics of carriers in graphene during and after light exposition [130, 131, 140, 206, 207, 210, 264–274] by means of diverse modeling techniques and also from an experimental point of view.

Let us suppose an undoped ($n = p$ and $\varepsilon_F \simeq 0$) graphene sample. When exposed to optical radiation, electrons in the ground state are able to absorb part of the radiation energy. Due to the direct band gap and linear band spectra, these electrons can be photoexcited, and promote from the valence band at $\varepsilon_{\text{ground}} = -\hbar\omega_{\text{pht}}/2$ to conduction band [265] at $\varepsilon_{\text{excited}} = \hbar\omega_{\text{pht}}/2$, being ω_{pht} the angular frequency of the incident photons, as seen in figure 5.1 (a). As a result, some excited electrons conform an out-of-equilibrium distribution in the conduction band, leaving an equivalent hole distribution in the valence band. Afterwards, these populations, undergo a very fast thermalization: photoexcited carriers tend to occupy energies above and below the excitation energy towards a hot Fermi-like distribution, as depicted in figure 5.1 (b). This process takes place within very short timescales –tens of femtoseconds [266, 275]–, and is driven by Coulomb interactions of the photocarriers with themselves. Simultaneously, cooling starred mainly by the transference of the carriers energy to the lattice by cascade emission of phonons occurs

ε

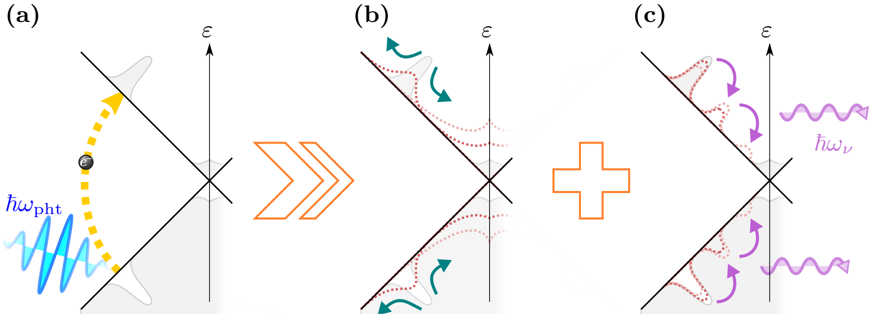

Figure 5.1: Schematic representation of graphene carrier population in the band structure and the following phenomena: (a) photogeneration of excited carriers due to photon absorption, (b) thermalization of carriers due to carrier-carrier interactions, and (c) photoexcited carrier cooling due to phonon cascade emission. Symbols indicate that after photoionization processes (a) and (b) operate together thermalizing and cooling the out-of-equilibrium carrier distribution.

as depicted in figure 5.1 (c). This process, although taking place at the same time as thermalization, is effective at longer timescales that lie in the picosecond scale [275].

A general exploration of this relaxation processes by means of Ensemble Monte Carlo simulation of photoexcited carriers will be carried out in section 5.1.1. Special emphasis will be given to the phenomenon of carrier multiplication in section 5.1.3.

The existence of hot electrons –in this case generated by means of optical photon absorption–, implies that their excess energy must be transferred somewhere else in order to reach a situation of thermal equilibrium. Such transference of energy is mostly attained by means of phonon emission. That is, the kinetic energy of hot carriers is invested into the excitation of lattice vibrations. As a result, phonons are created out-of-equilibrium, which affect the scattering activity by means of the hot phonon effect. A thorough study of this phenomena is carried out in section 5.1.4.

Monoatomic layers of electronic materials are usually employed lying on a substrate, that confers mechanical support. There is literature issuing photocarrier dynamics on various substrates. To cite some examples, in [131], by measuring degenerated relaxation dynamics by means of DTS, the intrinsic optical phonon lifetime is measured in graphene on SiC and on quartz. In [276] AFM imaging, Raman spectroscopy and DTS techniques were employed in the study of intrinsic samples of suspended graphene and graphene grown on SiC, finding different dynamics as a function of the position due to SiC-graphene coupling irregularities. In [130], vsisible pump and near infrared probe spectroscopy was employed with CVD samples of graphene deposited on SiO_2 and grown on SiC, finding different relaxation trends at picosecond scales depending on the substrate type and the number of layers. However, thorough investigation focused solely on the implications of the substrate choice has not been performed. Moreover, within an experimental framework there are some factors inherent to the fabrication methods and processes that may complicate the examination of different samples. One example is the existence of multiple graphene layers, since the interaction with the substrate decreases exponentially with the separation with the interface, thus making its repercussion troublesome to measure [277]. Other examples are imperfections, the presence of impurities, or rippling in transferred graphene samples, which create an irregular interface. In this context modeling and simulation stands as the best resource to investigate the impact of carrier-substrate interactions on the photocarrier dynamics. In section 5.1.5 we compare the dynamics of photoexcited carriers in graphene on various substrates under the ideal conditions only feasible by means of simulation.

All these phenomena will be presented in this chapter as follows. In section 5.1 the numerical EMC method will be used to explore these relaxation dynamics: First, a general overview of these processes will be given in section 5.1.2. In section 5.1.3 we will observe the influence of the collinear processes, which were already discussed in section 3.3 within the context of transport under stationary conditions. Then, in section 5.1.4 the interplay between hot photoexcited carriers and the phonon system will be explored. Finally, a comparative study of the influence of different substrates on these dynamics will be carried out in section 5.1.5. In section 5.2 an experimental approach to measure these photoexcitation and relaxation phenomena will be presented, along with some tests comparing the results obtained with our Monte Carlo model.

5.1 EMC modeling of relaxation dynamics

5.1.1 Photoexcited carriers

In this section the relaxation process of photoexcited carriers will be studied with the EMC method. For this purpose, we need to consider the interaction of an ultrafast light pulse that promotes carriers to an excited state. A detailed treatment of photoexcitation (like those proposed in [278, 265] or [279, 280] to cite some examples) lies beyond the scope of this thesis. Instead, we will add to the (thermal) equilibrium distribution the excess carriers generated via photoexcitation at the start of the simulation as if they were generated instantaneously at the instant $t = t_0$. Consequently, the effect of the interactions along the photoionization stage is not taken into account. The photoexcited carriers distribution obey the following Gaussian profile [140]:

$$f_{\mathrm{excit}}(\varepsilon) = \Psi_{\max} \exp\left[-\frac{\left(\varepsilon - \frac{1}{2}\hbar\omega_{\mathrm{pht}}\right)^2}{2(\hbar\Delta\omega_{\mathrm{pht}})^2}\right],[1] \tag{5.1}$$

where $\Delta\omega_{\mathrm{pht}}$ determines the spectral bandwidth of the pulse, $\Psi_{\max}$ is the maximum occupation probability limited up to 1. This distribution relates to the density of photocarriers, $p_{\mathrm{excit}} = n_{\mathrm{excit}}$, as:

$$n_{\mathrm{excit}}(\varepsilon) = \int_0^{\infty} f_{\mathrm{excit}}(\varepsilon)\mathrm{DoS}(\varepsilon)\, d\varepsilon\,. \tag{5.2}$$

A value for $\hbar\Delta\omega_{\mathrm{pht}} = 100\,\mathrm{meV}$ has been chosen, which is sufficiently large for a Gaussian Fourier-limited pulse of a 8 fs temporal full width at half maximum. The study focuses on intrinsic graphene ($\varepsilon_F = 0$) at ambient temperature $T_0 = 300\,\mathrm{K}$. Regarding $\Psi_{\max}$, it is chosen in order to establish a known initial photocarrier density. It must be noted that n_{excit} is therefore set as a parameter, instead of the pulse fluence although these two quantities are inherently related. The pulse wavelength will be taken also as a parameter. Afterwards, the simulation runs and the results from the relaxation transient are recorded. It is well known thats carrier distributions are non isotropic, with strong dependence on the polarization of the pulse [265, 272]. On the other hand we included photocarrier distributions obtained after photoexcitation under coherent regime as calculated in [279, 280]. When compared with a Gaussian profile with similar spectral characteristics, as seen in figure 5.2 (b) and the same excited carrier density the differences found in the dynamics were minimal as it concerns the results presented in this thesis.

5.1.2 General view of the carrier dynamics in suspended graphene

The simulation starts with a set of electrons and holes in an out-of-equilibrium distribution produced by a pulse characterized by photon wavelength $\hbar\omega_{\mathrm{pht}}$ with a particular power that enables the creation of a photocarrier density n_{excit} at t_0. The resulting distribution for a 790 nm pulse wavelength ($\hbar\omega_{\mathrm{pht}} = 1.6\,\mathrm{eV}$) that originates a $10^{13}\,\mathrm{cm}^{-2}$ photocarrier density is plotted with a gray line in figure 5.3. The natural trend of these carriers is to return to the thermal equilibrium. This means, that, two processes have to occur simultaneously: as photocarriers are concentrated around $\pm\hbar\omega_{\mathrm{excit}}$, they must lose the energy that has been absorbed from the light excitation. Also this excess population with respect to the equilibrium situation must be recombined. In figure 5.3 we

---

[1] This equation applies only to electrons. The corresponding distribution for holes would be $f_{\mathrm{excit}}(\varepsilon) = \Psi_{\max} \exp\left[-(\varepsilon + \frac{1}{2}\hbar\omega_{\mathrm{pht}})^2/2(\hbar\Delta\omega_{\mathrm{pht}})^2\right]$.

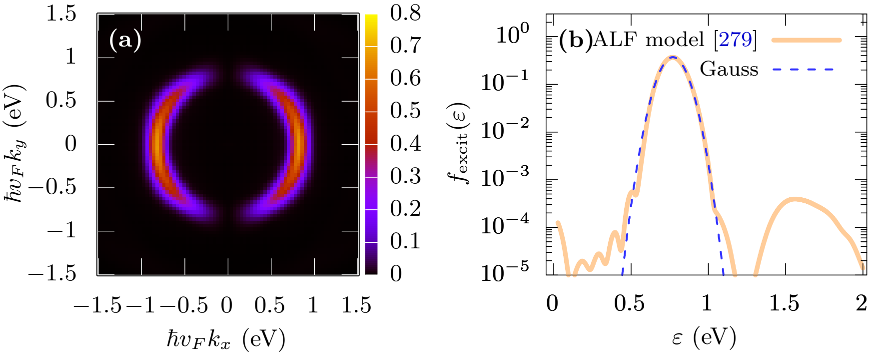

Figure 5.2: (a) Density plot of the probability for electrons to promote from the ground state (valence band) to an excited state (conduction band) in the **k**-space around the K and K' valleys of monolayer graphene obtained with the two-level ionization model presented O. Zurrón and L. Plaja from the Laser Aplications and Photonics (ALF) research group in [279] after the application of a 20 fs $y-$polarized laser pulse centered at $\lambda_{\text{pht}} = 800\,\text{nm}$ ($\hbar\omega_{\text{pht}} \simeq 1.54\,\text{eV}$) with $E \simeq 3 \times 10^3\,\text{kV/cm}$ under the consideration of coherent excitation. (b) Comparison of the energy distribution of photoexcited carriers according to results presented in (a) and the best fitting gaussian profile descibed in equation (5.1), which is obtained with the parameters $\Psi_{\max} = 0.37$ and $\Delta\hbar\omega_{\text{pht}} = 70\,\text{meV}$.

also present some snapshots of the distribution function. A gradual depletion of the excitation energy region is attained very fast; at $t - t_0 = 20\,\text{fs}$ the initial Gaussian profile is already not distinguishable. In the first femtoseconds carriers are very energetic, and there are a lot of free states at lower and higher energies, which favors scatterings of all kinds to occur. This process of carrier energy redistribution and depletion of the excitation region is the thermalization process, and is driven mainly by Coulomb interaction between carriers. The result of this process of thermalization is the attainment of two Fermi-like (thermal) distributions in the conduction and valence bands. It must be taken into account that Coulomb interactions between carriers can also lead to interband transitions. In section 5.1.3 we will focus on these processes, and the consequences of not taking them into account in the modeling framework. Depletion of the bands (carrier recombination) can be observed in the distribution function by comparing instants in the picosecond scale (2 ps and 5 ps), where occupation of high-kinetic energy levels close to $\pm\hbar\omega_{\text{pht}}/2$ almost approaches 0, most carriers are very close to the Dirac point, where the DoS shrinks.

Coulomb processes can not take the system to equilibrium on their own, as due to its elastic nature, there is no way to transfer the excess carriers energy. Cooling is the parallel process in which this energy is dissipated, which occurs mainly via phonon scattering. This process is characterized by longer timescales than thermalization, due to the fact

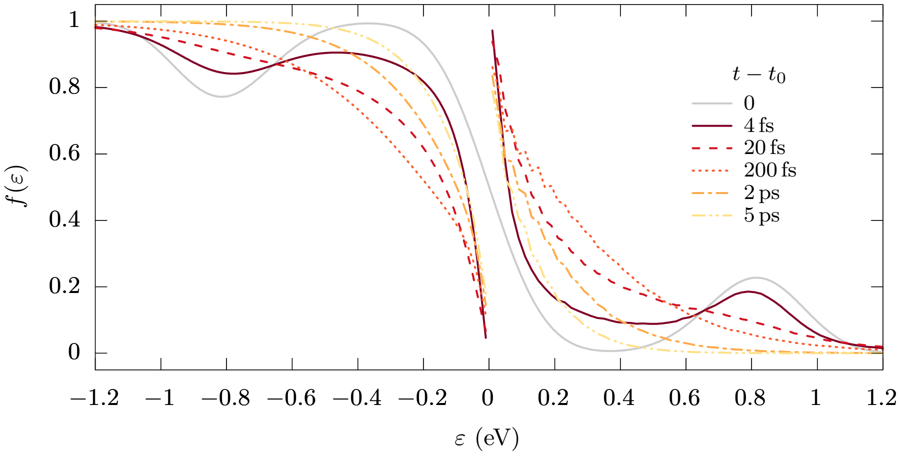

Figure 5.3: Snapshots of the carrier occupation in energy at different instants after photoionization with a pulse of $\hbar\omega_{\text{pht}} = 1.6\,\text{eV}$ that generates a photocarrier density $n_{\text{excit}} = 10^{13}\,\text{cm}^{-2}$.

that carrier-phonon coupling is not as strong as carrier-carrier interaction in Coulomb collisions. The progressive loss of energy, evident from the filling of the distribution close to $\varepsilon = 0$, is a result of this energy transfer towards the lattice via phonon scattering. These two complementary process can be distinguished by disabling in the model the most active mechanism (i.e., carrier-carrier scattering). In figure 5.4 we show snapshots of the energy occupation at different instants past photoionization. When the complete model is considered –left panel, (a)– the fast depletion of the excited states towards a wide span of energies is already noticeable in the first 10 fs, and the initial Gaussian profile has disappeared at 50 fs. In the right panel (b) carrier-carrier interactions are disregarded, and therefore all the dynamics is ruled by phonons. The cascade phonon emission is evident due to the replication of the initial distribution at 0.8 eV towards lower energies in steps corresponding to the TO-K/LO-Γ mode.

Fermi-like distributions can then be described by two parameters: a quasi-Fermi level, and a temperature for each of the type of carrier[2]. We compute these parameters by solving the system of equations (2.86a) and (2.86c) for the conduction band (or electron temperature, T_e, and quasi-Fermi level, μ_e), and equations (2.86b) and (2.86d) for the valence band (or hole temperature, T_h, and quasi-Fermi level, μ_h). The quantities of the left hand side (the electron and hole densities and their kinetic energies) are taken directly from the EMC results. Although these parameters link the carrier density in each band, and their total energy (under the assumption that these are distributed according to a

---

[2] Since here we are focusing on the case of intrinsic graphene, and the dynamics of electrons and holes is almost identical due to the symmetric band structure, we can refer to a single carrier temperature, T_c provided that $T_e \simeq T_h$, and a quasi-Fermi level $\mu_c = \mu_e \simeq -\mu_h$.

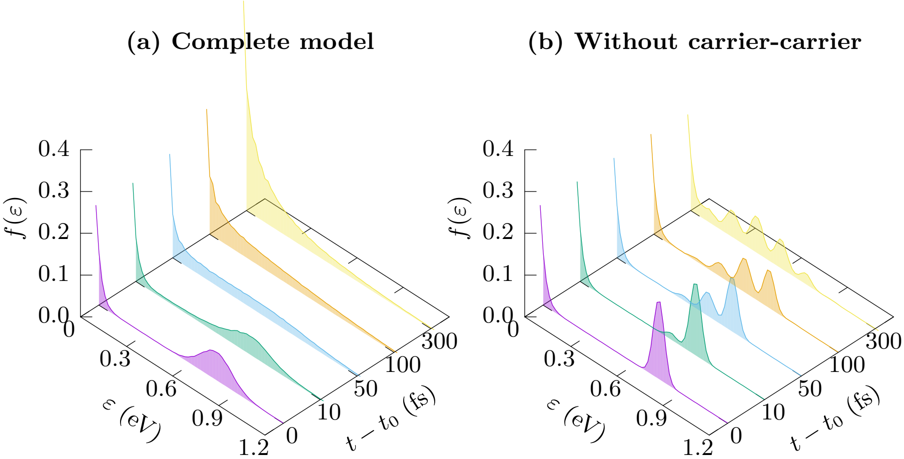

Figure 5.4: Energy occupation function obtained through EMC simulations at various instants after photoexcitation of an electron and hole density of $2 \times 10^{12}\,\mathrm{cm}^{-2}$ with a photon energy of 1.6 eV when (a) when intraband carrier-carrier is activated, and (b) when they are is not considered in the simulation.

Fermi-Dirac-like function), the reader should be aware that we compute and present this parameter even in the first instants, when such type of thermal distribution is still far to be achieved, since even in this conditions, carrier temperature allows for a comparison of the energetic profile of carriers.

In figure 5.5 we show the evolution of the number of free carriers, carrier temperature and quasi-Fermi levels for various initial photoexcitation conditions. During the first ∼100 fs after t_0, an increase in the number of carriers can be observed in all cases under consideration. This fast creation of electron-hole pairs is a consequence of the favorable conditions for impact ionization that occur after photoexcitation. Right afterwards, entering in the picosecond scale the carrier densities drop, with a trend to approach the thermal concentration at long times. An in-depth insight into the generation and recombination channels governing this evolution will be covered in section 5.1.3. As it regards the evolution of carrier temperature, it is characterized by a constant decay with differentiated slopes. First, a quick decay appears right after photoionization, showing a temporal coincidence with the creation of new carriers. Its slope turns more prominent with the photon energy, and diminishes when the photocarrier density grows. This stage is related to the transition from the initial strong out-of-equilibrium excited state towards a quasi-equilibrium thermal distribution. A stage with a less steep slope follows, which relates to progressive cooling of the carriers. In the case of suspended graphene, this cooling is featured mainly by optical phonons, as it has been already demonstrated by the successive cascade emission in figure 5.4, through which the excess electron and hole

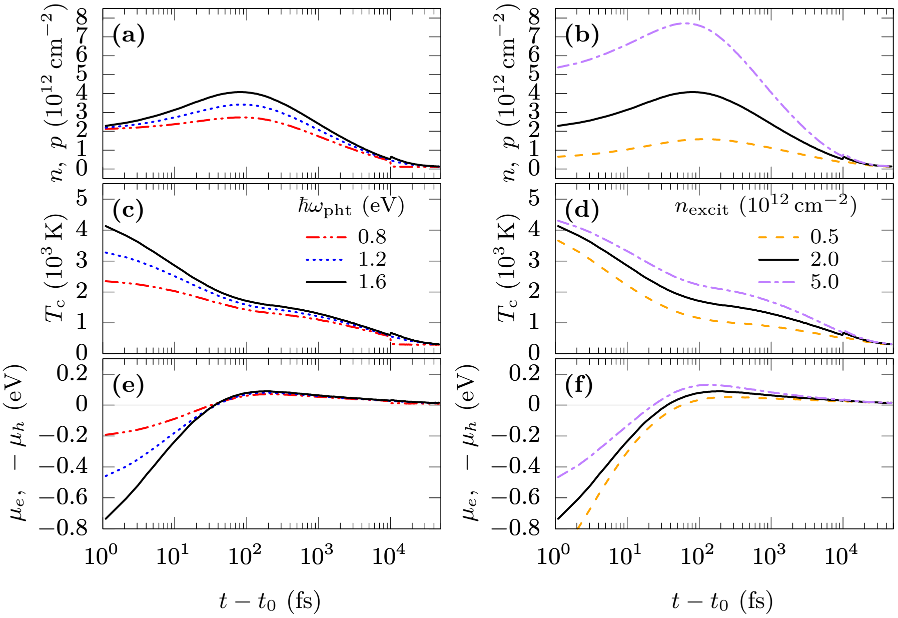

Figure 5.5: Carrier temperature as a function of time after photoexcitation for (a) various photon wavelengths at $n_\mathrm{excit} = 2 \times 10^{12}\,\mathrm{cm}^{-2}$, and (b) different photocarrier densities at $\hbar\omega_\mathrm{pht} = 1.6\,\mathrm{eV}$.

energy is transferred to the lattice. From the last quantity, –the quasi-Fermi levels– we can gather information about the relation of the number of carriers and their energy. Quasi-Fermi levels reveal how the carrier density and temperature relate to each other. When they are in the opposite bands of the carrier type they represent, it reveals that the carriers have an excess of energy. On the contrary, if its value is in the same band, this means that carriers are tending to pack in the low-energy levels, and there is an excess of carriers. Therefore zero-crossing (in the case of intrinsic graphene) of the quasi-Fermi levels sets the instant when the system has reached a hot thermal distribution, being around 20 fs to 60 fs depending mainly on the photocarrier density. These values are in good agreement with those mentioned in the literature [264].

5.1.3 Coulomb driven carrier multiplication

We have already seen that Coulomb interaction between carriers drives the fast thermalization after photoinversion. In [139, 210] the signatures of carrier multiplication as a part of the relaxation dynamics were presented. Such phenomenon is the result of the particular carrier-carrier interactions in the collinear limit which were introduced in section 2.4.3 and whose effects have been already explored in section 3.3 in the case of transport under a uniform electric field. In this section we explore the influence of these interactions after photoexcitation, which sets a quite different scenario.

In figures 5.6 (a) and (b) we show the net generation rate for collinear scattering as a function of time after photoionization, for various photon energies and excited carrier densities. In all the cases shown there is an initial fast creation of free carriers ($\tau_\mathrm{G} - \tau_\mathrm{R} > 5 \times 10^{30}\,\mathrm{cm}^{-2}$) due to the dominant effect of impact ionization events, being higher when the excited carrier density and photon energy are larger. The distribution function after photoionization conditions generates the ideal scenario for quick impact ionization to occur: a large number of electrons at high energies, together with empty states of low energy in the conduction band and fully occupied states at the top of the valence band. Highly energetic photoexcited electrons couple with those in the valence band lying close to the band maximum. When impact ionization events occurs, low states close to the Dirac point become more occupied, while the photoexcited electrons loses energy (see figure 2.7 in section 2.4.3). The dependence with n_excit is a result of a larger quantity of interacting particles that can trigger impact ionization (II) collisions,

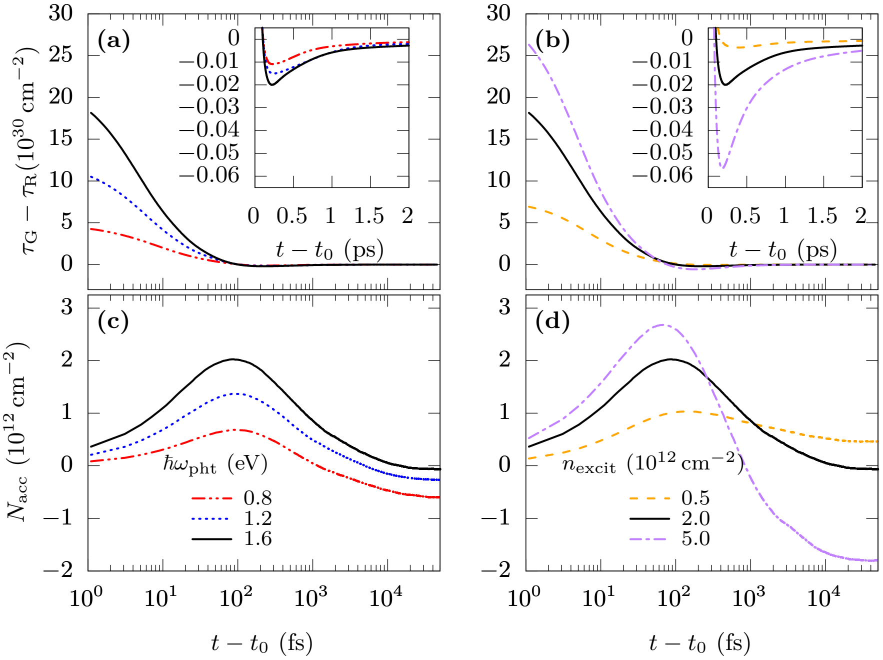

Figure 5.6: Instantaneous net generation rate due to collinear scattering (impact ioniozation and Auger recombination) as a function of time after photoexcitation, for varying values of (a) the pulse photon wavelenght at constant $n_\mathrm{excit} = 2 \times 10^{12}\,\mathrm{cm}^{-2}$, and (b) the photocarrier density at constant $\hbar\omega_\mathrm{pht} = 1.6\,\mathrm{eV}$. (c) and (d) represent the accumulated number of created carriers due to the interactions in (a) and (b) respectively.

while the increase with $\hbar\omega_{\mathrm{pht}}$ occurs due to a larger phase space where new electron-hole pairs can be created, along with a coupling between carriers that grows with their energy. This net generation drops fast during the first hundred of femtoseconds, until negative values are reached. The insets show the relevant time range where the net generation rate takes negative values (collinear events tend to recombine carriers instead of generating them). This effect is a consequence of the creation of non thermal electrons and hole distributions, with states more densely occupied (with $\mu_e > 0$ and $\mu_h < 0$) than in a thermal distribution with $\mu_e = \mu_h = 0$. The cooling process, mainly driven by optical phonons, and the implication of the hot phonon effect is discussed in the next section. So, after a strong activity of II, a slower but more lasting stage dominated by Auger recombination (AR) follows. Afterwards, an almost neutral generation rate (Auger recombinations and impact ionizations are almost compensated) is attained for collinear events.

In order to better observe the consequences of this succession of events in the free carrier density, we compute the accumulated number of created electrons and holes for a particular mechanism i as $N_{\mathrm{acc}}^{(\mathrm{i})}(t) = \int_{t_0}^{t} [\tau_{\mathrm{G}}^{(i)}(t) - \tau_{\mathrm{R}}^{(i)}(t)]\, dt$, and depict it figures 5.6 (c) and (d). The figures reflect the two stage of carrier generation (positive slope) and recombination (negative slope). The behavior is very similar for different wavelengths –figure 5.6 (c)–. By varying the photocarrier density –i.e., the power of the pulse as seen in figure 5.6 (d)–, different trends are observed. First, the maximum free carrier density is achieved faster. This is completely consistent with figure 5.5 (b), however, we are now only focusing on the carrier-carrier induced interband transitions. In the carrier recombination stage, many more electron-hole pairs are destroyed as n_{excit} is raised, allowing to differentiate cases where at long times ($\gtrapprox 5\,\mathrm{ps}$) collinear scattering is effectively contributing to effective carrier recombination. This is explained by the quicker filling of the low energy states, that happens at earlier times as there are more highly-energetic carriers triggering (II) events. The formation of these densely occupied low energy levels, along with the phonon-assisted cooling of the tail of the distribution enhances the subsequent Auger recombination dominance.

We turn now to analyze the electron-hole pairs creation dependence with the initial conditions. Carrier multiplication can be defined as the creation of new electron-hole pairs as a result of previously photogenerated hot carriers [281]. This figure is important for the performance of photovoltaic energy harvesting applications [281, 282] and can be evaluated at any instant by the quotient of the free carrier concentration and the initial excited photocarrier density. We show the dependence of the maximum of such figure in figure 5.7. The dependence with the photon energy is linear within the range considered. The excitation with shorter wavelengths allows for a wider energy range to be filled with carriers coming from impact ionization at the same time that more of these events can be

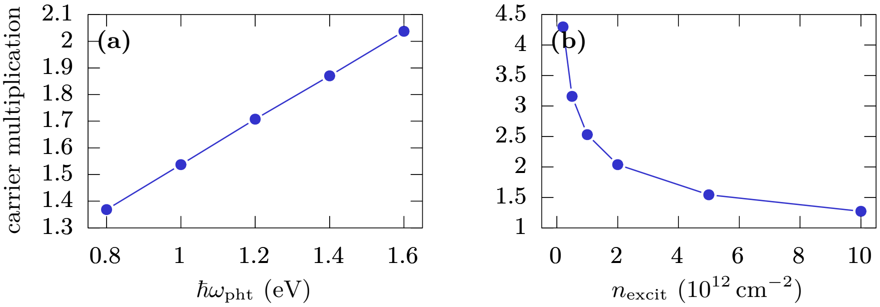

Figure 5.7: Maximum carrier multiplication as a function of (a) the photon wavelength for $n_{\mathrm{excit}} = 2 \times 10^{12}\,\mathrm{cm}^{-2}$, and as a fucntion of (b) the photocarier density for $\hbar\omega_{\mathrm{pht}} = 1.6\,\mathrm{eV}$.

triggered by photoexcited carriers. The inverse trend of carrier multiplication with n_{excit} is explained by the limited available density of states at energies below the excitation region, which sets a boundary to the maximum possible carriers to generate through impact ionization.

Let us now analyze how the suppression of interband mechanisms in the model would affect the description of carrier dynamics. In figure 5.8 (a) we compare the evolution of the instantaneous number of free carriers as a function of time. The most evident consequence of neglecting collinear processes (red dashed line) would be the absence of carrier multiplication, for being impact ionization –the only mechanism able to create a noticeable amount of free carriers– ruled out in simulation. As a result, phonon-assisted carrier recombination starts as soon as the energy levels below the phonon frequency

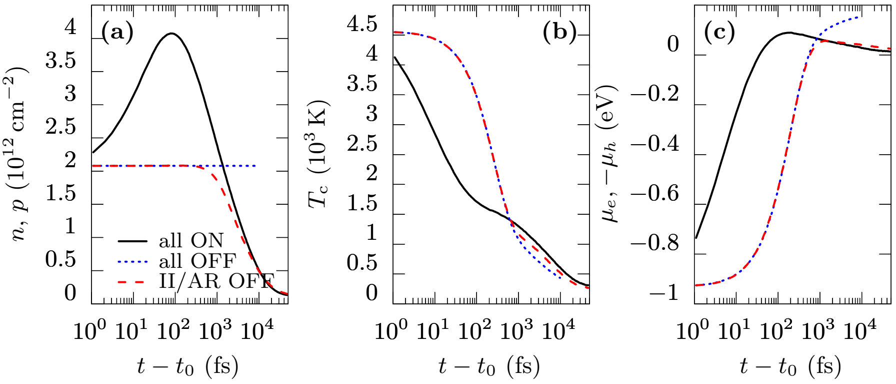

Figure 5.8: Time evolution of (a) the instantaneous free electron and hole densities, (b) the carrier temperature, and (c) the quasi-Fermi leves under various considerations of active/inactive types of interband transitions, after excitation of a photocarrier density $n_{\mathrm{excit}} = 2 \times 10^{12}\,\mathrm{cm}^{-2}$ with a 1.6 eV photon energy laser pulse.

start being fully occupied by electrons and holes.

Phonon assisted recombination starts on a picosecond scale. We can also set the start of *effective recombination*, understood as the time from which the free carrier density starts to become lower than the photoexcited carrier density, n_{excit}, in the same range as the start of phonon-assisted recombination, which is in good agreement with experimental observations [264]. The suppression of impact ionization also has an effect on the energetic profile, which can be reflected in the carrier temperatures shown for comparison in figure 5.8 (b). The fast initial drop of the temperature during the first ∼100 fs is lost, since it comes explained by the fact that when collinear events are activated new free carriers appear at energies below the excitation wavelength, while at the same time, carriers with such energy lose a fraction of it. Also, for the same reason, the evolution of the quasi-Fermi levels is slower where collinear events are deactivated. In other words, the creation of new electron-hole pairs through repetitive impact ionization events lowers carrier temperatures. As a result of neglecting carrier-carrier interband transitions, during the first instants there are fewer free carriers, and they have a higher average kinetic energy, with the outcome of a larger carrier temperature and the quasi-Fermi levels closer to zero.

As we have seen, after the maximum carrier multiplication has been achieved, Auger processes recombines most of the carriers created by impact ionization. As a result, at the picosecond scale there is a good agreement between the electronic temperature and quasi-Fermi levels, as recombination phenomena in the picosecond scale is determined mainly by phonons. From a modeling perspective, we can evaluate the impact of interband mechanisms on the relaxation. If all the channels for carrier exchange between bands are ruled out in the simulator (blue dotted line), there is good agreement of T_{c} and μ_e with the case where only collinear events are neglected up to around ∼300 fs. Afterwards, since excess electrons are not able to get back to the ground state (valence band), the quasi-Fermi level tends to $\mu_e \simeq \hbar v_F \sqrt{\pi n_{\text{excit}}}$ and the electronic temperature is below the other two cases. In this simulation scenario, the final allowed state is the coexistence of two Fermi-like distributions of electrons and holes in equilibrium with the ambient temperature. So, from a modeling perspective, collinear processes –i.e., impact ionization and Auger recombination– could be disregarded if only the recombination stage at the picosecond scale is going to be observed. However, neglecting carrier-carrier interband transitions leads to an overestimation of the carrier temperature, and the impossibility to observe carrier multiplication, which can be critical in some conditions

5.1.4 Electron-phonon coupled dynamics

Carrier cooling is a process that involves the transference of energy towards the crystal lattice. In the suspended graphene case, this is mostly achieved through optical phonon emission. Therefore, a direct consequence of photoexcited carrier cooling is the generation of out-of-equilibrium phonons. While some studies regard the out of equilibrium phonons [267, 269], some others consider the phonon number to remain in equilibrium [140, 270, 273]. The EMC method can provide the microscopic information to quantitatively evaluate the differences between the two approaches, and describe how the HP affect these relaxation processes.

To illustrate the HP effect after a laser photoexcitation, in figure 5.9 the resulting instantaneous scattering rate, computed as the number of occurred collision events per unit time and particle as a function of the time after ionization is depicted for the intrinsic phonon modes. In general, it can be said that scattering (specially phonon emission) with the TO-K/LO-Γ mode dominates over the TA/LA-K mode. This occurs because of its stronger coupling with carriers, that results from a larger deformation potential (see section 2.4.2). Also, due to the fact that its energy is greater, we can say that cooling is mediated mainly by optical phonons. Despite of this, both modes show a similar qualitative behavior. When hot phonons are considered (black lines), the emission rate (solid lines) shows a steady decay over time until a faster drop occurs passed ∼1 ps. On its behalf, the absorption rates (dashed lines) grow steadily until reaching a maximum that lies close to the phonon emission rate at around 1 ps for the TO-K/LO-Γ mode and 3 ps for the TA/LA-K mode. Then it drops concurrently with the emission rate, which always stays above during the relaxation process. As it concerns the

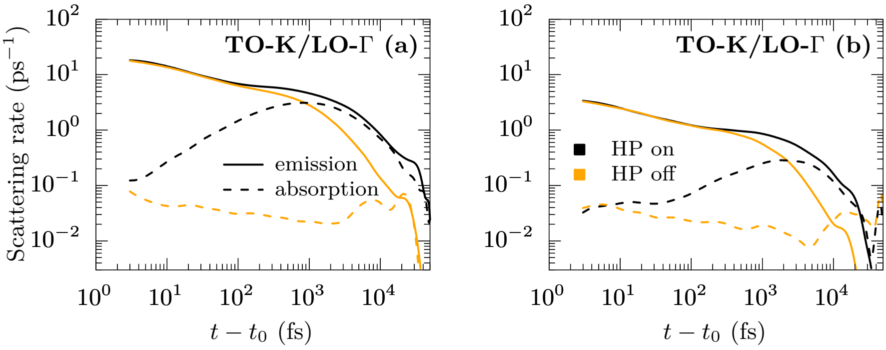

Figure 5.9: Phonon emission and absorption rates per unit time and particle after photoexcing an electron and hole density of 2×10^{12} cm^{-2} with a photon energy of 1.6 eV for (a) the TA/LA-K mode, and (b) the TO-K/LO-Γ mode. Black lines represent scattering rates when hop phonons are activated, and orange lines when they are turned off.

model neglecting hot phonons (orange lines), a similar trend is observed in the emission rate. However, for both modes the decay is faster than in the model that includes hot phonons, and therefore phonon emission rates are comparatively smaller in most of the simulation time window. On the other hand, the absorption rate shows a steady decrease over time. As a consequence, the overall implication of neglecting HPs is an increase of the emission/absorption ratio, provoking an overestimated transmission of energy from electrons to the lattice.

We can observe the consequences of the out-of-equilibrium phonons in the carrier temperature, which is plotted as a function of time in figure 5.10 (a), regarding and ruling out the HP effect. In all the cases there is an evolution of the carrier temperature characterized by a constant decay. Discrepancies between the two situations appear due to scattering with hot carriers start in a sub-picosecond scale, around the first 100 fs. In the case where phonons are considered in equilibrium (according to the Bose-Einstein occupation at room temperature, T_0), carrier cooling is faster. As a result, after 10 ps for any of the examined photon wavelenghts, $T_c^{(\mathrm{BE})}$ tend to the room temperature. This means that, around such time span after photoionization electrons and holes have established two Fermi distributions with such minimum possible temperature. Yet, there is an excess of free carriers that must recombine in order to achieve the total equilibrium. On the contrary, in the case where hot phonons are included, different temperatures depending on the photon wavelength are obtained, being all of them above $T_\mathrm{c}^{(\mathrm{BE})}$. In figure 5.10 (b)

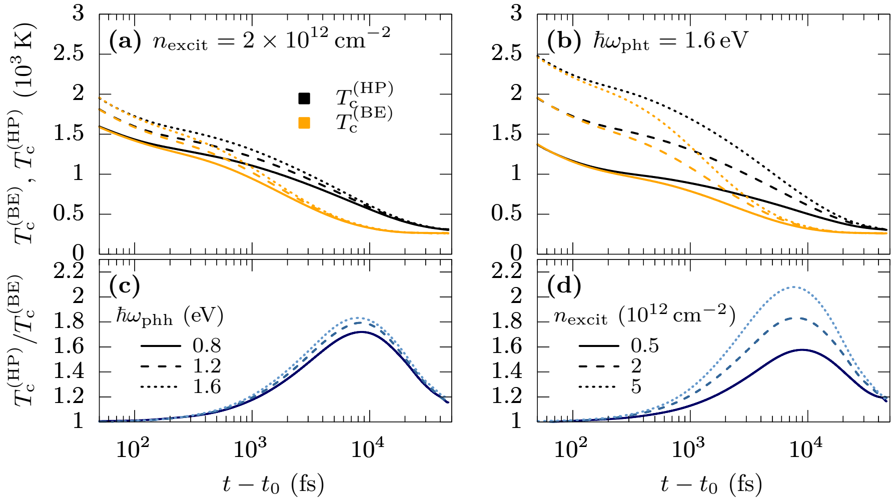

Figure 5.10: (a) Electron temperature considering a phonon population in equilibrium ($T_\mathrm{c}^{(\mathrm{BE})}$, orange lines), and including hot phonons ($T_\mathrm{c}^{(\mathrm{HP})}$, black lines) as a function of time after photoexcitation for different photon energies, and (b) ratio of the electronic temperatures considering HPs and phonons remaining in equilibrium.

we plot the ratio of the two carrier temperatures for matching photon wavelength and excitation density in order to determine the dependence of the hot phonon effect with these parameters. This ratio grows steadily until reaching a maximum after ∼5 ps have passed after excitation. In the most extreme case this comparison between $T_\text{c}^{(\text{BE})}$ and $T_\text{c}^{(\text{HP})}$ yields a maximum of more than twice $T_\text{c}^{(\text{BE})}$ in a picosecond scale, and it is a 60% larger in the less severe case under consideration. This means, that the HP effect on the carrier temperature is enhanced the shorter is the pulse wavelength (larger excitation energy), and when the initial number of photoexcited carriers is larger. The dependence with the photon wavelength is explained by the fact that phonon-carrier coupling grows stronger with energy, thus producing more phonon emissions (phonon heating) in the first instants. Moreover, the number of successive phonon emissions required to occupy the low energy states increases with the excitation energy. As for the dependence with the initial photocarrier density, it is explained by the number of free carriers that are able to undergo phonon emission scattering events. However, there is not a linear relation between the free carrier density and phonon heating, since due to the Pauli exclusion principle, scattering transitions towards lower energy levels (with smaller DoS) become more limited as the degeneracy increases.

In the same way that out-of-equilibrium phonons slow down the cooling phase, their presence also affects the recombination rates, making them slower and therefore increasing the time that electrons (holes) remain in the conduction (valence) band after photoionization. As it concerns the carrier recombination processes, we observe that, when out-of-equilibrium phonons come into play the overall recombination rates become lower than in the case where they are not considered. In general, it would be expected that the existence of out-of-equilibrium phonons that involve interband transitions ($|\mathbf{q}-\mathbf{q_0}| < \omega_{\text{TO-K/LO-}\Gamma}\,/v_F$) would slow down the recombination rate due to a reduction of the emission (carrier recombination)/absorption (carrier generation) ratio, in the same way it takes place for intraband transitions. However, as we will immediately see, the presence of a competing interband contribution of carrier-carrier interactions in the collinear limit changes this picture. Figure 5.11 (a) shows the temporal recombination and recombination rates due to optical phonons in intrinsic graphene. The enhancement of the emission rates due to out-of-equilibrium phonons can be observed, as expected. However, the absorption rate is increased in the same degree, which leaves almost equal net recombination rates associated to the TO-K/LO-Γ pathway, regardless of the consideration of HPs, as seen in figure 5.11 (c). The main difference is observed when looking at the rates of II and AR, depicted in figure 5.11 (b). Here, the inclusion of HPs implies an indirect rise of impact ionization over Auger recombination, provoking important differences in the net contribution of collinear scattering –figure 5.11 (c)– in the 100 fs to 200 fs range. Such effect is a direct consequence of carrier distributions with

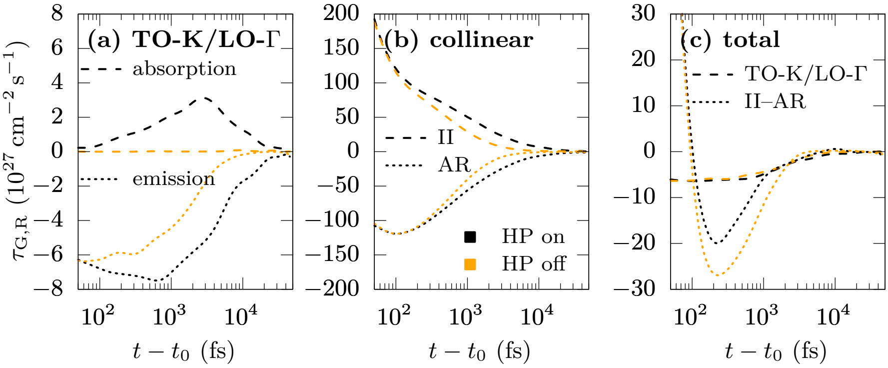

Figure 5.11: Carrier generation (positive) and recombination (negative) rates as a function of time for (a) optical phonon assisted interband due to absorption (generation) and emission (recombination), (b) impact ionization and Auger recombination, and (c) net collinear and TO-K/LO-Γ assited generation rates for the particular case of $n_{\text{excit}} = 2 \times 10^{12}\,\text{cm}^{-2}$ and $\hbar\omega_{\text{pht}} = 1.6\,\text{eV}$.

different temperatures: hotter carriers leave more free states at low kinetic energies, and accommodate in distributions with longer tails (larger energies). This enhances the impact ionization occurrences to a larger extent than Auger recombination ones. Therefore, neglecting HPs results in an overestimation of the interband recombination rates of free carriers due to an interplay with Auger processes.

Let us now focus on the evolution of the phonon population. In figure 5.12 (a), time-tracking of the phonon temperature is plotted for both the TO-K/LO-Γ and TA/LA-K modes considered in the model. Phonons heat quickly until reaching a maximum at ∼ 1 ps and ∼ 2 ps for the TO-K/LO-Γ and TA/LA-K modes respectively. Acoustic intervalley mode manifests similar trend to the optical branch, but heating to a lesser degree. In all the photoexcitation scenarios under consideration the qualitative trend is similar, with different maximum temperatures. Figures 5.12 (b) and (c) present the value of the maximum phonon temperature as a function of photon wavelength and photocarrier density, showing a linear dependence with both quantities. Such maximum is determined by the instant in which the conditions for fast phonon emission are not given anymore. This is characterized by the carriers reaching a Fermi-like distribution of temperature close to T_0, which by means of Pauli-blockage of transitions towards low energy states helps to balance emission and absorption rates. Afterwards a slower cooling follows, starred by natural phonon population decay and enhanced absorption mediated by carrier scattering, as seen in figure 5.9. Differences found in the phonon temperature evolution regarding the pumping pulse wavelength and the photocarrier density supports the previous statements about the energetic evolution discussed in figure 5.10. These

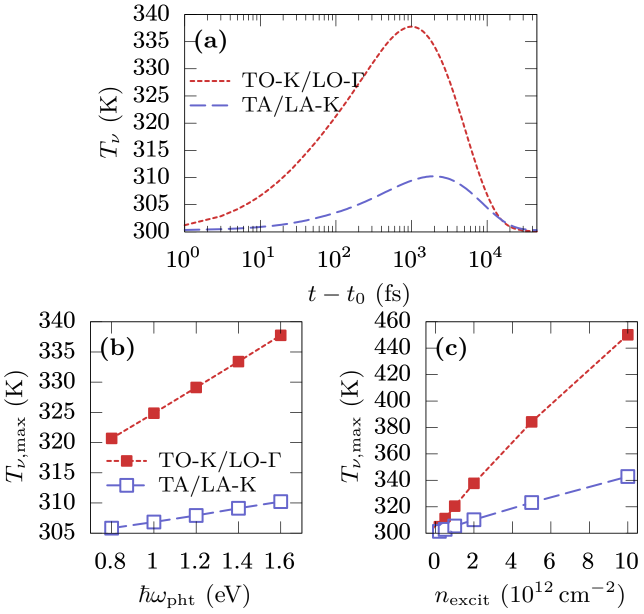

Figure 5.12: Time evolution of the phonon temperature for (a) the TO-K/LO-Γ , and TA/LA-K modes after a photoionization with a pulse of $\hbar\omega_{\mathrm{pht}} = 1.6\,\mathrm{eV}$ that generates $n_{\mathrm{excit}} = 2 \times 10^{12}\,\mathrm{cm}^{-2}$. Maximum temperature for the two modes (c) as a function of the photon energy, considering an excited photocarrier concentration of $n_{\mathrm{excit}} = 2 \times 10^{12}\,\mathrm{cm}^{-2}$, and (d) as a function of the photocarrier concentration with $\hbar\omega_{\mathrm{phtn}} = 1.6\,\mathrm{eV}$.

differences are explained, first, by the well differentiated electron-phonon coupling as can be seen in figure 2.5 and already discussed with regard to the emission and absorption rates already presented in figure 5.9. Scattering probabilities are higher with TO-K/LO-Γ , thus leading to more collisions that increase this phonon population. On the other hand, the $\omega_{\text{TO-K/LO-}\Gamma} > \omega_{\text{TA/LA-K}}$, which holds two implications: one is that for an equal increase of the phonon number, its temperature is raised to a higher extent, explaining the differences in the heating degree (over $\sim 150\,\mathrm{K}$ heating over ambient temperature for the optical modes versus $\sim 43\,\mathrm{K}$ for acoustic ones at the most extreme conditions). Another is that the emission/absorption ratio tends to be closer to unity the smaller is the phonon energy, and as a consequence, emissions and absorptions are more equilibrated in the TA/LA-K mode. Phonon cooling can take place either by absorption by electrons, or through a phenomenological relaxation characterized by a decay time. So, the effective cooling is determined by the balance between emissions, and absorptions together with its characteristic decay rate. The decay rate of TA/LA-K , which is two times slower in the TO-K/LO-Γ mode as seen in section 2.4.2, therefore explains its slower cooling rates.

In order to explore the phonon dynamics in more detail, in figure 5.13 we present the time and momentum-resolved dynamics of phonons by computing the time derivative of $T_\nu(\mathbf{q}-\mathbf{q}_0)$. We focus on the TO-K/LO-Γ mode for being dominant, and because the forthcoming analysis would qualitatively apply also for the acoustic modes. At low photocarrier concentrations –figure 5.13 (a)–, phonons are emitted at the fastest rate during the first instants due to the presence of highly energetic photocarriers with plenty of free states to scatter into. This turns into heating of phonons with wavevectors close to the minimum required by the phonon energy for intraband transitions, that is $|\mathbf{q}-\mathbf{q}_0| \geq \omega_{\text{TO-K/LO-}\Gamma}/v_F$. Heating in the first instants extends to longer wavevectors, but with decreasing intensity. Also, some phonons are created below this limit, implying phonon-assisted recombination, which is possible thanks to the depletion of the valence band and filling of the conduction band at low energies featured by impact ionization and carrier-carrier thermalization. Between t_0 and $\sim 500\,\text{fs}$ heating shrinks both in intensity and in the extension of the wavevectors. At this point, net phonon cooling materializes,

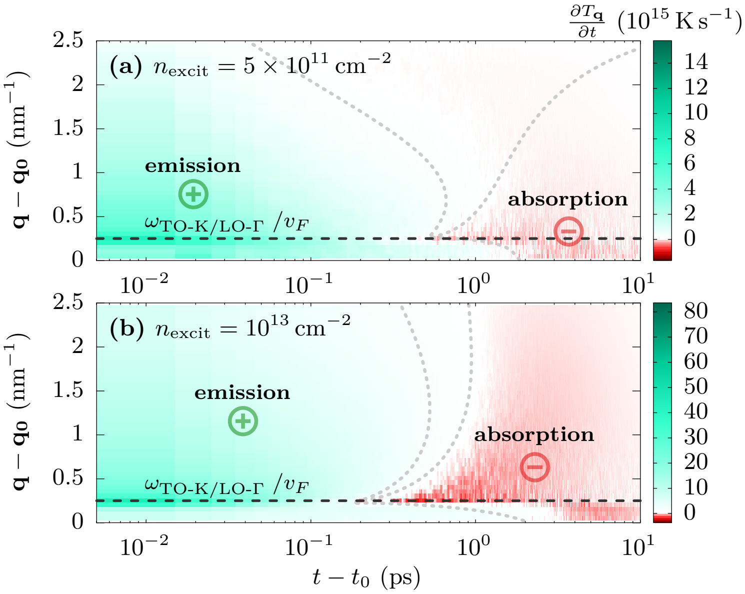

Figure 5.13: Instantaneous heating computed as the time derivative of the phonon temperature as a function of the transition wavevector $\mathbf{q}$ around the symmetry point $\mathbf{q}_0$ for the dominant TO-K/LO-Γ mode, after an excitation with a pulse of $\hbar\omega_\text{phtn} = 1.6\,\text{eV}$ which originates a photocarrier density, n_excit of (a) $5\times10^{11}\,\text{cm}^{-2}$, and (b) $10^{13}\,\text{cm}^{-2}$. The horizontal dashed line represents the wavevector below which phonon emissions and absorptions imply generation/recombination of electron-hole pairs (phonon assisted interband transitions). Dotted lines are a guide to the eye in determining the regions where phonon heating or cooling occurs.

starting at the wavevectors that have reached hotter temperatures and afterwards extending towards shorter wavelengths. As for wavevectors involving interband transitions, cooling starts after 1 ps. Slightly distinct behavior is observed with larger excited carrier densities –figure 5.13 (b)–. Here, phonon heating does not reduce so drastically with time and shrinking $|\mathbf{q}-\mathbf{q_0}|$. This comes as a result of the existence of a large number of carriers than remain at high energy states. Such energetic carriers would be the result of carrier-carrier thermalization, which is enhanced with large photocarrier densities. In these conditions low energy states would be rapidly filled, at the expense of creating a long-tailed distribution, with carriers that would only relax through phonon emission scattering. Cooling of short wavevectors over the intraband-interband transition limit starts at ~200 fs due to a faster attainment of Fermi-like distributions, while at the same time some heating of longer wavevectors still occurs. As a result, the transition from heating to cooling is more abrupt than in the low-density case for all the $\mathbf{q}$ sampled range. Finally, it can be seen that the phonon heating is less pronounced below the limit that separates intraband and interband phonon-assisted transitions than above it. The fact that the DoS is quite reduced below $\hbar\omega_{\text{TO-K/LO-}\Gamma}$ explains the upper limitation of recombination phonon emission rate. Therefore, in this region, phonon heating becomes independent on the carrier density as long as these energy states remain full of electrons and holes. Moreover, at high excess carrier concentrations, Auger recombination poses as a competing mechanism able to recombine electron-hole pairs faster than optical phonons.

5.1.5 Substrate influence

The previous study has focused on suspended graphene. For most practical purposes, and in order to provide a mechanical support to the atomic carbon layer, graphene is employed usually on a polar dielectric substrate. As it has been seen in section 2.4.6 the interface between graphene and these polar substrates brings about new inelastic interactions with charge carriers due to their proximity. Besides, the presence of a polar substrate also modifies the dielectric properties, resulting in an enhanced screening of Coulomb interactions of the electrons in the graphene layer. For such reasons, the crucial role of substrate effects can be seen as a way of tuning graphene properties in optoelectronic applications [276]. In this section we will focus on a single photoionization case study, with $n_{\text{excit}} = 2\times10^{12}\,\text{cm}^{-2}$ and $\hbar\omega_{\text{pht}} = 1.6\,\text{eV}$. Results with five substrates (the most common employed for graphene) will be shown: SiO_2, h-BN, SiC, HfO_2 and Al_2O_3. The results already presented of suspended graphene will be included for comparison.

Let us start by reviewing the instantaneous number of free carriers, as shown in figure 5.14 (a). It can be seen that, even though the evolution of free carriers is similar in

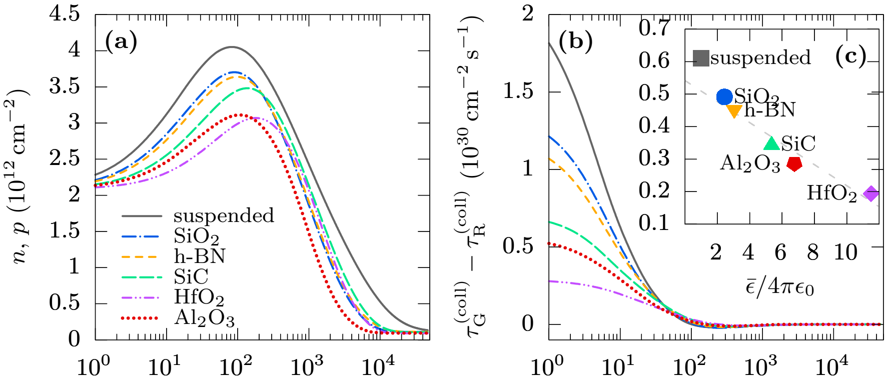

Figure 5.14: (a) Free electron and hole densities, and (b) net generation rate for collinear carrier-carrier scattering as a function of time after photoionization. The inset (c) shows the same quantity as (b) at $t - t_0 = 20$ fs as a function of the relative background dielectric constant for each of the substrates.

all the cases, the presence of a substrate provokes a reduction of carrier multiplication. Maximum carrier multiplications range from ∼1.5 (graphene on HfO_2 and Al_2O_3) to ∼2 (suspended graphene). Such maxima are also attained with each substrate at different times: a displacement towards longer times occurs as the generation rates –shown in figure 5.14 (b)– are smaller during the first 100 fs. As previously seen in this section, the creation of free carriers via impact ionization takes place during a short time window right after photoionization. As already discussed in section 3.3, different carrier generation rates can be attributed to the effect of substrate screening, and the higher occupation of low energy levels due to the onset of carrier relaxation via SPPs. In the particular case of a photocarrier profile, the differences between the carrier generation rates for each substrate can be attributed mainly to the effect of screening, due to the existence of abundant free states close to the Dirac cone. To verify this statement, we show in the inset –figure 5.14 (c)– the net generation rate at 20 fs versus the background dielectric constant associated to each of the substrates. A good correlation is observed, which supports the previous assertion.

We now examine the energetic evolution of the ensembles by looking at electron and hole temperatures as plotted in figure 5.15 (a). Two different timescales can be appreciated when comparing this quantity among the substrates. The first lasts around 100 fs and is characterized by a quick drop from ∼4500 K to ∼1600 K. In the first part of the relaxation process, carrier temperature is higher in graphene on the substrates, where the carrier multiplication was smaller, that is, for those which offer larger screening. This is because the generation of electron-hole pairs by means of II is importantly affected

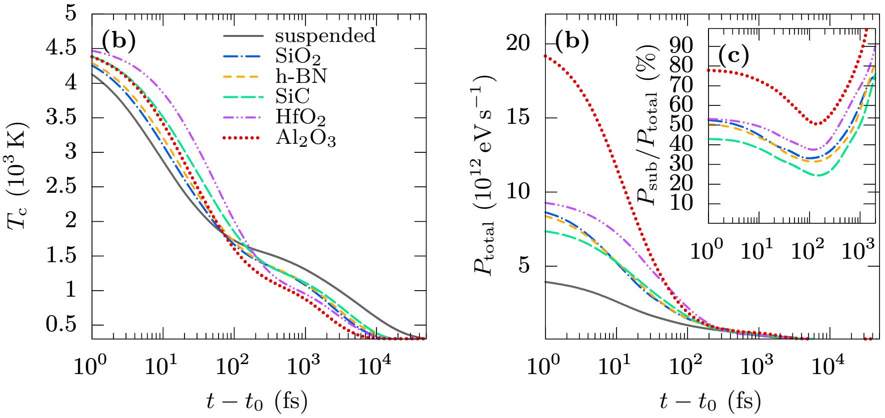

Figure 5.15: Instantaneous (a) carrier temperature, (b) dissipated power per unit particle, and (c) proportion of dissipated power starred by SPPs with respect to the total in each of the substrates under consideration.

by screening, since it is a Coulomb type of interaction. The transition from the first to the second stage is shifted towards longer times (and lower carrier temperatures) for the substrates in which T_c was larger in the initial instants of the previous stage. So, a crossing occurs, and in the second stage the trend is inverted: now, electrons in suspended graphene are the hottest, while those which have HfO$_2$ and Al$_2$O$_3$ as a substrate are the coldest. To explain this, let us now look at the power dissipated per particle and unit time, as illustrated in figure 5.15 (b), which is calculated in the same way as in section 3.2. In most of the substrates the initial power dissipated lies in a similar range, except in the suspended case and in graphene on Al$_2$O$_3$, which exhibits dissipated powers around twice and half respectively as large as the rest of the supported graphene cases, circumstance that makes carrier temperature drop faster than the other cases in the first stage. It must be reminded that although in the first instants carrier cooling is due mainly impact ionization, the energy transference via phonon scattering is playing a role too. It is most clear in the case of Al$_2$O$_3$, for which, despite being one of the substrates with highest enhanced screening, the slope in the first cooling stage is steeper than in the rest of the substrates due to a more effective SPP relaxation channel. In the inset, figure 5.15 (c), the proportion of the dissipated power due to the SPP relaxation pathway over the total is shown. In each of the examined cases, an initial drop (reaching a minimum around 200 fs) is observed. Afterwards, a monotonic increase of the SPP contribution follows. In Al$_2$O$_3$ the SPP contribution is always dominant ($\geq 50\%$), reaching 80% in the very early instants. HfO$_2$ follows, being SiO$_2$ and h-BN very close. SiC SPP is the less active contributor to the carrier cooling becoming dominant only $\sim$1 ps after photoionization. The trend for the relative weight of SPP cooling in the picosecond scale is to surpass

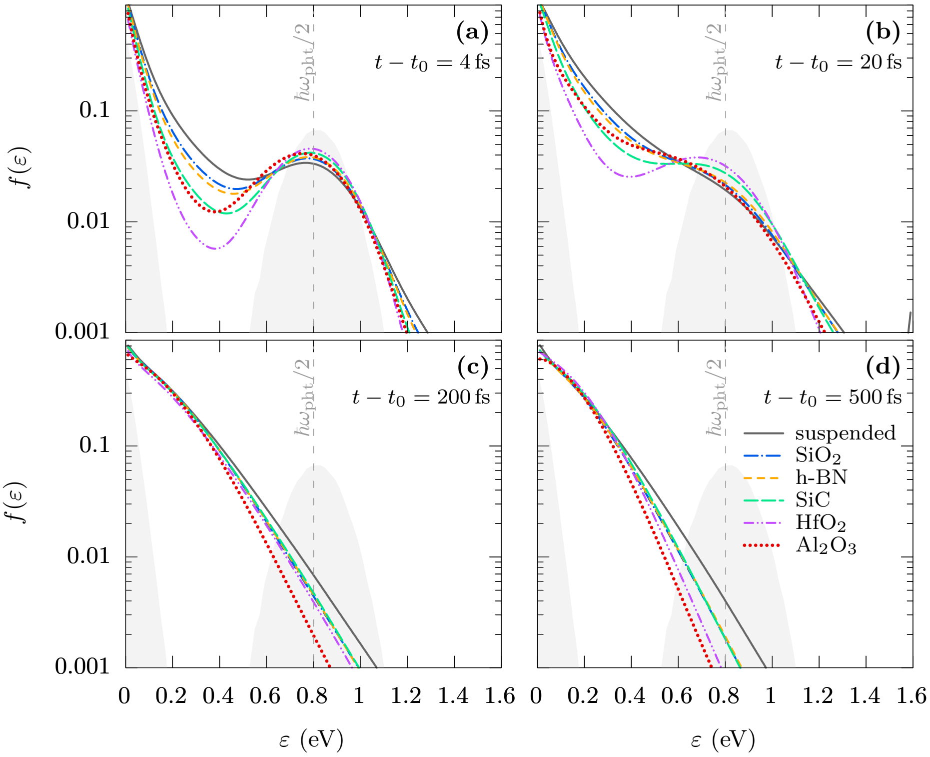

Figure 5.16: Instantanous energy distribution functions in the conduction band for all the considered substrates at instants $t - t_0$: (a) 4, (b) 20, (c) 200, and (d) 500 fs. Gray shaded region represents the initial carrier profile that exists at the instant of photoexcitation, t_0.

100%. This means, that in this time range, in the presence of a substrate, graphene intrinsic phonon modes would relax through absorption interactions with electrons. The energy gained by them, would in turn be transferred to SPPs.

A more deep and complete view of the implications of the substrate choice can be achieved by looking at the evolution of the energy distribution function. In figure 5.16 we plot, for each of the substrates under consideration, the energy distribution function of electrons at four different instants. The shaded region depicts the initial distribution for thermal and photoexcited carriers (Gaussian profile centered at $\varepsilon = 0.8$ eV). At 4 fs a clear difference from the initial conditions can be observed. Some depletion of the energetic region of photoionization is seen, along with higher occupations above 1.1 eV. However, the most important increase in population is observed below the energy of the pump wavelength. Depletion from the center of the Gaussian profile towards upper and lower energies is starred by elastic carrier-carrier interactions, which takes them towards a thermal distribution. Along with photocarriers depleting the excitation region, electron-hole pairs created through impact ionization add up to the occupation at energy levels below 0.8 eV. In fact, the population at ∼0.3 eV is in perfect agreement with the number of carriers depicted in figure 5.14 (a). The panel (b) –$t - t_0 = 20$ fs– illustrates the transition from the previous instant towards a thermal distribution. In the case of suspended graphene, the profile is almost monotonic, while for graphene on HfO_2 and SiC, it still reminds of the initial photoexcited distribution, as these substrates provide the most enhanced screening environment, which damps carrier-carrier interactions. Let us recall here, the strong relaxation power attributed to Al_2O_3 SPPs, that is taking carriers towards lower energies, as it can be deduced from the similar occupation levels with regard to the suspended graphene case around the excitation profile. After 200 fs Fermi-like distributions are achieved in all the cases. Here, at small energies ($\lesssim 0.4$ eV) all profiles almost meet, while the occupation level at the tail (high energies) determines the carrier temperature and gives an idea of the number of carriers. This way, suspended graphene and graphene on Al_2O_3 present the opposite trends among the observed cases: in suspended graphene the largest excess carriers are created at the first stage, but that population takes longer to be recombined and transfer its energy in order to relax, while in Al_2O_3, few excess carriers are generated through collinear scattering, but the system cools down faster due to a more efficient power dissipation. Letting the system evolve for more time would tell us how electrons return to equilibrium (the shaded region observable at ε<0.3 eV) in the process of cooling, being determined by the recombination and relaxation rates obtained for each substrate. For example, at $t - t_0 = 500$ fs, it can be seen that electrons in graphene on HfO_2 and on Al_2O_3 have attained a distribution closer to equilibrium than those in graphene on SiO_2, h-BN and SiC. The suspended graphene sample is where the cooling dynamics is the slowest at long times.

We turn now to analyze the interband cooling properties. In figure 5.17 we plot the accumulated number of electron-hole pairs created or recombined (the same way as we did in section 5.1.3) for collinear scattering, the intrinsic TO-K/LO-Γ and the substrate SPPs phonon pathways. Collinear scattering stands primarily as an electron-hole pair creator. During the first 100 fs to 200 fs (depending on the substrate analyzed) II is dominant over AR –i.e., the slope is positive–, and afterwards AR gains prevalence until the end of the simulations. Phonon interband transitions always produce net recombination (the result is negative) since the emission/absorption probability ratio is > 1. Looking simultaneously at panels (b) and (c) of figure 5.17, it is straightforward to realize that recombination through TO-K/LO-Γ and SPPs are competing mechanisms, since the larger is the accumulated number of recombined carriers by the substrate phonons, the lesser is associated with the intrinsic optical phonon. Despite recombining a reduced amount of electrons and holes in comparison with the suspended graphene case, a bump (short period of net carrier generation) is observed in the cases of graphene on SiO_2, HfO_2

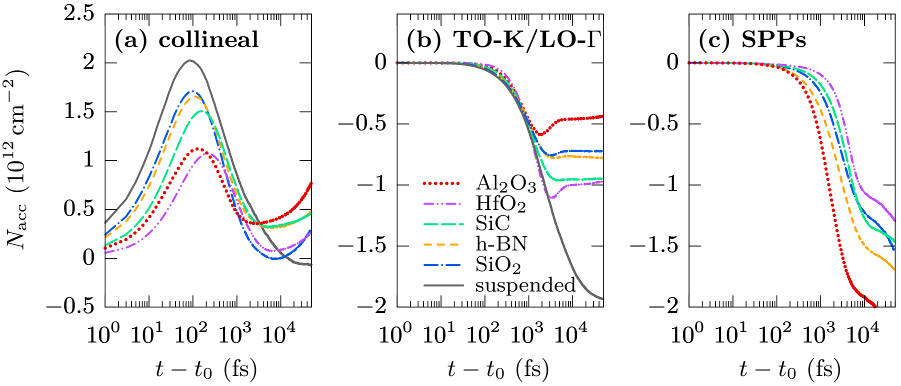

Figure 5.17: Accumulated number of created electron-hole pairs as a function of time passed after photoionization for (a) collinear scattering, (b) TO-K/LO-Γ , and (c) SPP assisted interband transitions.

and Al_2O_3. This is related to absorptions resulting from the preceding heating of the TO-K/LO-Γ mode made possible by the leading role of the surface polar phonon. On behalf of SPP assisted recombination, its magnitude is dependent on the Frolich coupling constant, but also on the SPP phonon frequency, as this would heighten the maximum carrier kinetic energy necessary for recombination to occur, and thus the phase where these transitions can take place. As an examples, Al_2O_3 presents a relatively energetic SPP_2 (the highest energy substrate remote phonon) and a big β factor (see section 2.4.6) while for HfO_2, the small energies of its phonons penalizes the DoS available for recombination.

To finish this section we will review the phonon dynamics by means of the averaged temperatures of the four modes considered in the model, which are plotted in figure 5.18. The reduction of temperatures observed in the intrinsic modes shows the relevance of the competing nature of the surface polar modes when a substrate is present. Using graphene on Al_2O_3 supposes a reduction of intrinsic acoustic and optical phonon heating of 45% and 30% respectively, while for the rest of the substrates it oscillates around $\sim 25\%$. Also, the maximum temperatures are achieved sooner due to a prompter filling of low energy states in the range of hundreds of femtoseconds, from when SPPs start to dominate as seen in figure 5.15 (b). Surface polar phonon modes heat to a lessen extend in comparison with intrinsic ones. This is because wavevector transitions in these interactions are restricted due to the angular distribution of the probability, as previously commented in section 3.2. As a result, phonons are heated only around a narrow area close to $\mathbf{q} \simeq \omega_{\mathrm{SPP}}/v_F$, which leads to averaged temperatures colder than in intrinsic modes. Maxima are reached sooner as the phonon energy is larger, as it happens also between the acoustic and optical intrinsic branches. The fast decay rates associated to surface phonons allows them to completely achieve thermal equilibrium within the 10 ps

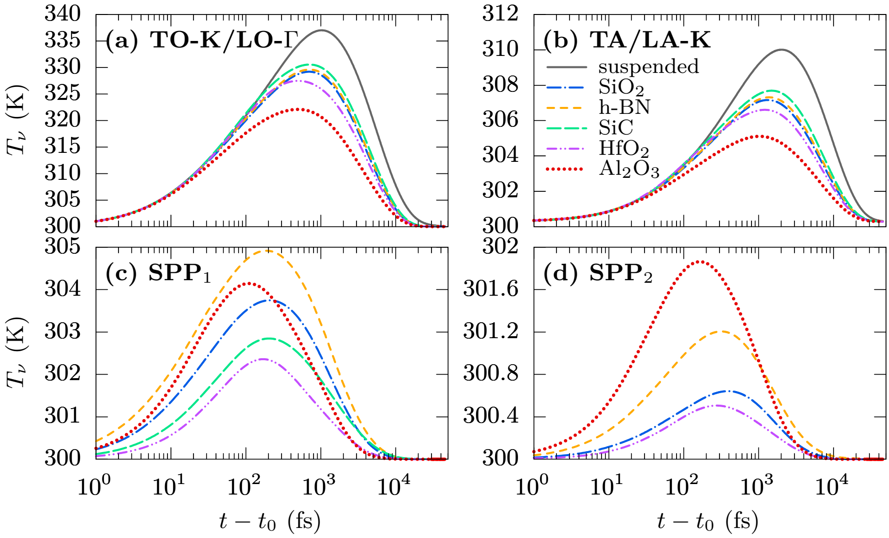

Figure 5.18: Average phonon temperatures for (a) TO-K/LO-Γ , (b) TA/LA-K , (c) SPP$_1$ (highest energy), and (d) SPP$_2$ (smallest energy) modes.

that the simulation lasts.

5.2 Experimental characterization of relaxation processes

One approach to experimentally observe the relaxation processes after photoexcitation is the time-resolved differential transmission spectroscopy (DTS). This kind of methods rely on the so-called pump and probe experiments [283], which consists in exciting a sample with a strong stimulus (pump), and obtaining a measure with another one (probe). In the case of DTS, and in order to measure such fast processes, ultrashort laser pulses are employed [284]. Figure 5.19 (a) illustrates the concept of a pump-probe experiment in transmission configuration. The pumping is depicted with the large pulse that is reaching the sample. Due to the interaction of this intense optical beam, part of the power from the pulse would be absorbed and the sample would turn to an excited state. Another pulse with a certain delay is shot into the same area, and after passing through the sample is measured with a proper device. The time resolution is obtained by means of controlling the delay between the two pulses: if the probe arrives before the pump ($t - t_0 < 0$), the measured signal would be related to the transmittance corresponding to the sample in equilibrium, usually identified as $\mathcal{T}_0$. On the other hand, if it arrives after the pump has reached the sample ($t - t_0 \geq 0$), since the system has been in an

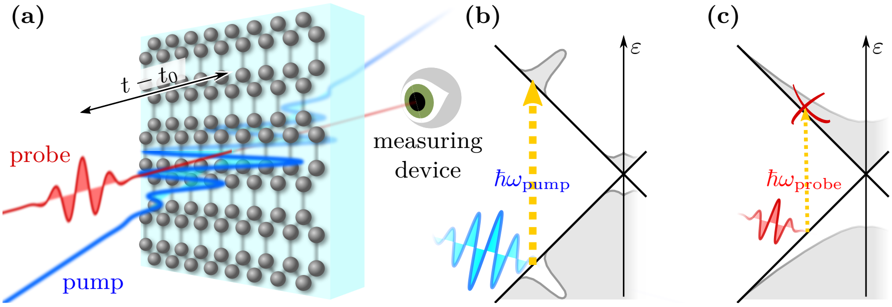

Figure 5.19: (a) Depiction of a pump-probe experiment: the blue optical pulse represents the pump excitation at the instant t_0 of incidence on the graphene sample. The red pulse, which is delayed a time $t - t_0$ with respect to the pump beam and examined after passing through the sample, represents the probe beam. (b) Generation of a photocarrier population of electrons and holes at $\pm\hbar\omega_{\mathrm{pump}}$. (c) Probing after a time $t - t_0$ when the carrier distribution has evolved from the excited state. Pauli blocking due to occupied states at $\hbar\omega_{\mathrm{probe}}$ increases the sample transmittance.

excited state, different values of the transmittance could be measured as a function of the delay. Such time-dependent signal reveals information about the dynamics towards the equilibrium inside the sample. The difference between the signal obtained in equilibrium with that obtained at a time $t > t_0$ is denoted as $\Delta\mathcal{T}(t)$. The results of differential transmission are represented as $\Delta\mathcal{T}(t)/\mathcal{T}_0$.

The (intense) pump beam produces a large population inversion, as depicted in figure 5.19 (b), due to the absorption of some photons with energy $\hbar\omega_{\mathrm{pump}}$. In the particular case of graphene, carrier optical response could be divided in intraband and interband transition processes [285, 54, 286]. These interactions become more or less dominant depending on the wavelength of the probe pulse: in the infrared and shorter wavelengths, interband transitions dominate. In this case, when the probe signal arrives there are fewer electrons in the valence band that can promote to the conduction bandin comparison with the system in equilibrium, as depicted in figure 5.19 (c). Also, the existence of occupied states in the conduction band, supposes another drawback for these transitions, usually referred to as Pauli blocking [57]. As a result, in these wavelengths an increase in transmission is observed with respect to that obtained in equilibrium. On the contrary, in the far-infrared region and below, intraband free-carrier absorption would dominate [274, 264], in good accordance with a Drude model [287]. Therefore, in this wavelength range, a larger proportion of the probe beam power would be absorbed after photo inversion due to a larger number of existing free carriers in comparison with the equilibrium situation.

In collaboration with the group of Ultrafast Lasers and Magnetodynamics Spec-

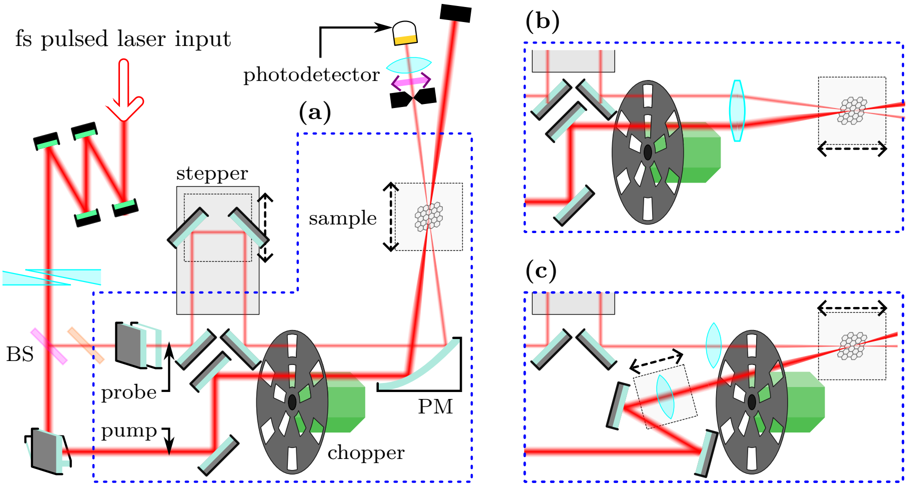

Figure 5.20: Pump-and-probe setups employed for differential transmission spectroscopy in graphene. (a) Degenerate non-collinear setup used in the group of Ultrafast Lasers and Magnetodynamics Spectroscopy from the University of Porto. Modifications done in the optics laboratory of the University of Salamanca, using (b) a single 2 inch lens, and (c) two independent lenses with different focal lengths.

troscopy from the University of Porto (Portugal) we carried out differential transmission spectroscopy experiments in graphene. The employed set-up is illustrated in figure 5.20 (a). It has the following features: a Titanium:Sapphire ultrafast oscillator provides sub-8 fs laser pulses with central infrared wavelength of 800 nm, with repetition rate of 80 MHz and energy of 2.5 nJ. After a dispersion compensation block, the pulses are separated between pump and probe by a thin low dispersion beam splitter. 2% of the power is left for the probe line. Since both beams come from the same source, both share the same spectrum. This is call a degenerate setup [3]. Pump then is reoriented in a periscope which twists the polarization by 90 degrees. Probe line is made to go through a delay stage, controlled by a electromechanical stepper with steps of 0.4 µm (temporal delay of ∼2.6 fs). Afterwards the two beams are aligned in parallel, and then focused into the sample with a parabolic mirror. Then, the two signals reach the sample in a non collinear way. This means that pump and probe beams propagate in different directions at the point they hit the sample. This design offers a good signal-to-noise ratio, since the pump power does not reach the detector. However, it requires special care on the alignment of the two beams in order to hit the same spot in the sample.

The measuring stage is composed of the following components. First, due to the low

---

[3] Experimental arrangements involving different colors for exciting and measuring beams are called two-color pump-probe setups.

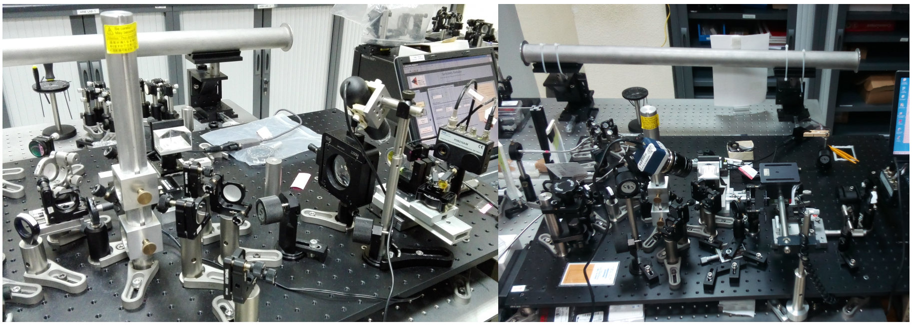

Figure 5.21: Photographs of the experimental setup in the optics laboratory of the University of Salamanca. Left and right pictures correspond to figure 5.20 (b) and figure 5.20 (c) arrangements, respectively.

relative differential signal that graphene offers (in the order of 10^{-4}), it is necessary some filtering in order to isolate it from any noise sources that might mask it behind. Lock-in amplification [288] is usually employed with this purpose. By chopping of one of the signals at a frequency ω_1 and another ω_2 the amplifier allows to filter the signal at $\omega = \omega_1 + \omega_2$, coinciding with a peak in the Fourier transform for the product of the two periodic functions. A polarizer and a spacial filter (pin-hole) are used to minimize the possible scattered light originated by the pump hitting the sample that arrives to the measurement device. Afterwards, the signal is focused on a photodiode for the measurement of the transmitted signal. A further step would be the measurement of the differential signal with spectral resolution by taking advantage of the wide spectrum of an 8 fs pulse. A spectrometer would then be used instead of a photodiode. Also, more sophisticated signal filtering methodologies would be needed. The employed samples were supplied by GRAPHENEA, and were composed of a single multi granular graphene layer grown by chemical vapor deposition on copper, and transferred to a 500 µm quartz substrate, as already presented in section 3.1, with its Raman spectrum plotted in figure 3.4.

The experimental characterization of the photoresponse of graphene revealed to be extremely challenging. Initially, we started by measuring differential signal in materials like ZnSe[4], whose response does not require fine filtering. This allowed us to perform the initial tuning and optimization of the setup. An example of the differential is shown in figure 5.22. However, in the case of graphene the results were not satisfactory. A simple set-up without spectral resolution did not allow detecting the photoresponse. At this stage, the main hindrances for obtaining the differential signal were attributed to the uncertainty of spatial overlap between pump and probe beams in the 1-atom thin layer

---

[4] In this material, a non-linear two-phonon absorption process creates the population inversion. Then the differential transmission is negative due to Drude absorption of free carriers [289].

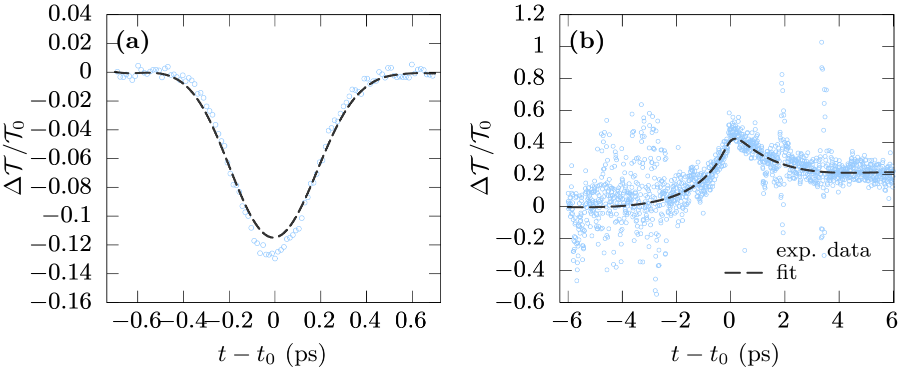

Figure 5.22: Differential transmission signal obtained for (a) a ZnSe sample used to test an calibrate the system, and (b) a graphene sample deposited on a quartz substrate.

of graphene. So, the use of parabolic mirrors was a major issue. However, the alternative approach, that is, the use of glass lenses is not feasible with ultrashort pulses due to the chromatic and spatial dispersion that its use would imply.

In order to try to avoid the problems related to the setup without spectral resolution, the major part of the setup was brought to the optics laboratory of the University of Salamanca, in collaboration with the research group in Photonics and Laser Applications. There, the facilities include a two-stage Titanium-Sapphire laser, with an output from the oscillator of pulses with a temporal length of 120 fs centered at 795 nm wavelength a 1 mJ energy. With this parameters, the compensation block was not necessary, and glass lenses could be used to focalize the two beams in the sample, as illustrated in figure 5.20 (b) and (c). The two variations were tested. Using two individual lenses for each of the beams allowed for a better control on the relative spot sizes in the sample, and correcting aberrations obtained with a larger non-centered lens. After all these modifications to the experimental setup, we obtained the differential signal shown in figure 5.22 (b). However, we did not manage to obtain a cleaner signal and in a repeatable way. A possible issue was the instability of the alignment, as the experimental setup was quite far from the oscillator, which prevented day-to-day repeatability. Also, there was still some uncertainty about the spatial overlap of the two beams on the graphene sample.

Finally, we decided to analyze the results of our simulations with some of the experimental data found in the literature. To achieve this, EMC simulations (where the most critical parameters were set according to the the experimental conditions) have been performed. In figure 5.23 the differential transmission traces were calculated from the time-dependent distribution function taking into account that for wavelengths in the infrared and visible range, the transmittance depends on the distribution function as

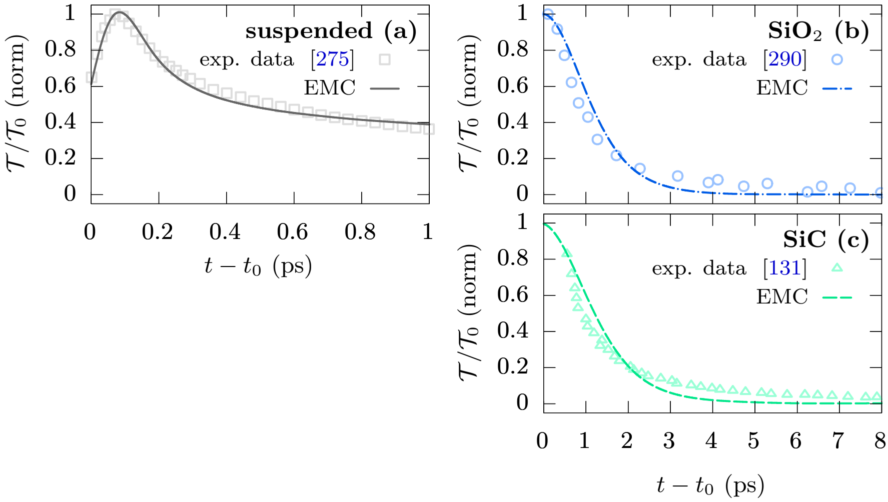

Figure 5.23: Experimental (symbols) and simulated (solid lines) normalized DTS as a function of the delay between pump and probe pulses for (a) suspended graphene, (b) graphene on quartz (SiO_2), and (c) graphene on SiC. Simulations weere made setting the initial conditions so that they would resemble the photoexcited situations given the pump pulse wavelength and power for each of the experimental results that were obtained (a) from fig. 1 in [275], (b) from fig. 1 (d) in [290], and (c) from fig. 1 (b) in [131].

$\Delta\mathcal{T}/\mathcal{T}_0 \propto [\Delta f_{\mathrm{h}}(-\frac{1}{2}\hbar\omega_{\mathrm{pht}}) + \Delta f_{\mathrm{e}}(\frac{1}{2}\hbar\omega_{\mathrm{pht}})]$ [268], where $\Delta f_{\mathrm{e,h}}(\varepsilon)$ represents the difference in the occupation probability of electrons and holes, respectively, at energy ε with regards to the system in equilibrium. We find experimental and simulated data to be in a good agreement, which confirms the excellent performance of the developed simulator.

Chapter summary

EMC modeling of relaxation dynamics

In this chapter we have explored the relaxation dynamics in graphene through the EMC technique. We have observed and analyzed the carrier multiplication phenomena attributed to Auger processes. Its dependence is directly proportional to the photon wavelength, and inversely proportional to the photocarrier density. Collinear processes can contribute to a substantial deal of interband carrier cooling (recombination of excess carriers) when the photocarrier concentration is long enough, due to early filling of low-energy states. From a modeling perspective, not taking into account collinear processes provokes an overestimation of the carrier temperature at the very early stages. The fact that hot phonons suppose a bottleneck for carrier cooling has been demonstrated. This effect slows down the intraband energy relaxation due to the growth of excited phonon absorptions. On its behalf, out-of-equilibrium phonons suppose a deceleration of the interband balancing due to an interplay of the resulting hotter electron temperature and collinear scattering. Finally, the tunability of these relaxation properties via the choice of the polar substrate has been explored in depth, being impact ionization and carrier-carrier thermalization damping via dielectric screening, enhanced cooling and recombination via carrier-SPP coupling the key factors to consider.

Experimental characterization of relaxation processes

Finally, we performed differential transmission spectroscopy measurements based on ultrafast (femtosecond laser) pump-probe experiments. Although we measured clear time-resolved differential signals for other materials, obtaining measurements for monolayer graphene turned out to be extremely challenging. The comparison of data found in the literature and our EMC results show very good agreement on different substrates for energies in the infrared spectrum.

Chapter 6

Graphene-based devices

The study of carrier transport phenomena at the material level is of great importance to understand and evaluate the potential of new materials, as in the case of graphene. However, the use of novel 2D materials for the development of new generations of devices is also extremely relevant, particularly in the framework of today's electronics, where the end of the roadmap and Moore's law pushes forward the search for alternatives to Silicon. In this context, it is of primary importance to investigate the behavior of 2D materials when they are part of a device, like a transistor, or a diode.

A Monte Carlo device simulator can be regarded as an extension of the bulk material simulator in which some conditions (like the electric field, carrier density, temperature, etc.) are local, that is, they change in space depending on certain external conditions, such as the potential applied to the contacts.

The objective of this chapter is to present a preliminary version of a Monte Carlo device simulator for electronic devices based on graphene, and potentially other 2D materials. It is organized as follows: The improvements needed to transform the material simulation tool into a device simulator are presented in section 6.1. Section 6.2 provides an introductory review of the operating physical principles of graphene-based field-effect transistors. Finally, some results of a GFET simulated with the Monte Carlo device simulator are presented in section 6.3.

6.1 Monte Carlo device simulator for 2D materials

In the material simulator we could just assume an extrinsic carrier density as a condition for the simulation. On the other hand in a device, the carrier density can change across the position of the channel and depending on the conditions imposed to its terminals. We defined the quantity ξ as the density of states that a Monte Carlo particle represents in the EMC material simulator. So, now that the real space comes into play, it is necessary to take into account the Monte Carlo particle to electron or hole equivalence. So, let us introduce the parameter PE (standing for *particle equivalent*), which is the number of electrons or holes that a Monte Carlo particle represents.

The most important issues for the device simulator are the spacial constraints and definition of the materials, the motion of the particles on a locally varying environment, and the self-consistent calculation of the electric fields. All these topics are detailed in the following subsections.

6.1.1 Geometric definition and transport boundaries

The first requirement to build a a device simulation tool is the geometric description. The device definition is made on a Cartesian basis, $\mathbf{r} = (x, y, z)$. This space is discretized in a mesh whose spacings are defined fo every of the three axis: δx_i, δy_j and δz_k. In this space, we consider the graphene (or 2D channel) to be in the plane $z = 0$, so the carrier motion is restricted to the x and y directions. Assuming the limit case in which the channel is an ideal flat 2D entity, the graphene layer is considered to be placed between the cells with $z > 0$ and $z < 0$. The two set of cells right above and below the graphene plane correspond to the separation between the channel itself and the top and bottom substrates. So, the dimensions of these two layers are forced to be $\delta z_0 = \delta z_{-1} = d_{\mathrm{VdW}}$ (which, for graphene is $\sim$4 Å). This is a quite small distance; dividing the space with an homogeneously sized mesh for devices with typical height dimensions of hundreds of nanometers, would produce a very large number of cells. Due to the computational requirements to solve the electric field –that will be seen in the forthcoming subsection–, we are interested in reducing the number of cells in the z direction. To achieve this, we set a gradual increase of the cells size as the these are further from the graphene sheet. The relative increase is a configurable factor, usually small enough ($< 10\%$) in order to ensure that the distance mismatch does not suppose a problem for the solution of the electric field.

After setting the mesh spacings and device dimensions, in each of the cells the type of material for every given coordinate (i, j, k) within the device limits is defined. In general, two kinds of materials (apart from the graphene layer itself) are considered: dielectrics (which include air and vacuum), and metallic contacts. By default, cells right below and above $z = 0$, where the graphene sheet is placed, are considered vacuum –i.e. these represent the separation between the graphene or 2D material sheet, and the top and bottom substrates–. However, if any other material is associated to these cells, it is assumed that there is an edge in the 2D conductive medium. Consequently, a boundary condition for the carrier motion must be set. If at the other side of the edge there is a dielectric cell, then the carrier is specularly reflected. Further considerations like charge trapping by edge states or edge roughness (non-specular reflection) are not included in the initial version of the simulator. On the other hand, if the edge is an interface with a metal, the carrier is considered to be absorbed by the metallic contact[1], and taken out of the simulation. In these cases of carrier absorption by a contact, the event is accounted for in order to determine the instantaneous (at a given time step Δt) electric current associated to that contact.

Some device geometries, like typical planar FETs, under the assumption of large device width, allow the consideration of a simple projection of the structure. Although

---

[1] There is a special case of metallic contact considered in the simulator used to measure potentials, instead of injecting charge and setting a voltage. In these, no electric current is allowed (either by injection or absorption), and therefore carriers are reflected as in the case of a 2D material/dielectric edge.

the simulation tool has been designed to consider also any arbitrary 3D structure, in this thesis we focused in graphene FETs, where the previous assumption can be considered true for being one of the dimensions homogeneous. In this case, a single plane (xz) is considered, and therefore the transport in the y is not relevant.

6.1.2 Self-consistent electrostatics

While in the bulk material simulator we considered quantities such as the electric field and carrier density to be homogeneous in space, in a device their local variations must be taken into account. The electric field inside a device is the result of the voltages applied to the terminals, and the local charges that exist in each cell of the simulation domain.

The calculation of such fields is done from the local electrostatic potential $\phi(x, y, z)$ calculated by solving the Poisson equation:

$$\nabla_{\mathbf{r}}^2 \phi(\mathbf{r}) = -\frac{\rho(\mathbf{r})}{\epsilon(\mathbf{r})}, \tag{6.1}$$

where $\rho(\mathbf{r})$ is the local density of charge, and $\epsilon(\mathbf{r})$ is the electric permittivity of the medium. In practice, equation (6.1) is translated into finite differences and solved numerically in the nodes of the mesh grid, so $\rho(\mathbf{r})$ becomes $\rho_{i,j,k}$.

As it regards the graphene or 2D material sheet, the free charge within the cell is accounted for adequately weighing the in-cell flight time. So every time a particle flies an amount of time τ_{fc} inside a cell, its charge associated to the carriers is increased by $\mp e\,\mathrm{PE}\,\tau_{\mathrm{fc}}/\Delta t$, where $\mp e$ accounts for the electron or hole charge. Then, after the time step has finished, the surface charge associated to each node is computed as:

$$\sigma_{i,j,0} = \frac{\sum Q_{i,j}^{c}}{\sum A_{i,j}}, \tag{6.2}$$

where the summation is performed over the four cells surrounding the node at $z = 0$, $Q_{i,j}^{\mathrm{c}}$ is the net charge corresponding the cell at (i, j) resulting from the carriers accounted for during the flight of the particles along this cell, and $A_{i,j} = \delta x_i \delta y_j$, its area. The conversion to a volumetric charge is done as

$$\rho_{i,j,0} = \frac{2\sigma_{i,j,0}}{\delta z_0 + \delta z_{-1}}. \tag{6.3}$$

A complete description of the electrostatics in the device requires some additional considerations regarding the Poisson equation, by setting the appropriate boundary conditions in particular regions. In the device limits (the external limits of the mesh grid), we set Neumann conditions:

$$\frac{\partial \phi(\mathbf{r})}{\partial \mathbf{n}_{\perp}} = 0, \tag{6.4}$$

where $\mathbf{n}_\perp$ is the normal vector to the surface. In the dielectric/dielectric interface, where a non-zero net surface charge σ[2] can exist, the displacement vector must verify its continuity across the surface:

$$[\epsilon(\mathbf{r}_A)\mathbf{E}(\mathbf{r}_A) - \epsilon(\mathbf{r}_B)\mathbf{E}(\mathbf{r}_B)] \cdot \mathbf{n}_\perp = \sigma(\mathbf{r}). \tag{6.5}$$

Finally, in areas (nodes) where there are metallic contacts we impose Dirichlet conditions:

$$\phi(\mathbf{r}) = V_{\text{contact}}, \tag{6.6}$$

where V_{contact} is the potential applied to the contact connected to that metallic region.

Finally, the 2D electric field in the plane of the conducting material is computed at the cells as:

$$\mathbf{E}_{ij} = -\frac{1}{2}\left[\frac{\phi_{i+1,j,0} - \phi_{i,j,0} + \phi_{i+1,j+1,0} - \phi_{i,j+1,0}}{2\delta x_i}, \right. \\ \left. \frac{\phi_{i,j+1,0} - \phi_{i,j,0} + \phi_{i+1,j+1,0} - \phi_{i+1,j,0}}{2\delta y_j}\right]. \tag{6.7}$$

Afterwards, the value of the charges stored in each cell is reset to 0 in order to account for them in the following time step.

6.1.3 Motion of classical particles in graphene

As we have seen, the motion of the particles involve the application of some conditions concerning the boundaries of the cells in the plane of the graphene sheet. Besides, particle motion should obey the locally varying electric field. To achieve this, the crossing points of the classical particle flights with the mesh edges must be detected. So when a particle undergoes a free flight, it must be checked if during this displacement, the particle crosses any of the boundaries of the current cell. In general, this involves calculating how much time it would take to a particle with a given initial state and under the action of a local electric field to reach each of the four borders of the cell, as illustrated in figure 6.1 In this graphical example, the particle exits the cell from its bottom edges, corresponding with a displacement in the y direction equal to $-\delta_{y-}$, after a flight time in the cell of $\tau_{\text{fc}} = \tau_{y-}$. The time τ_{x+} would not be considered for being larger, and the exit times related to the distances δ_{x-} and δ_{y+} take negative values, and therefore represent a time in the past.

Computing these times requires solving the equation(s)

$$\delta_\lambda = \left[\mathbf{v}_s(\mathbf{k}_0) + \int_0^{\tau_\lambda} \mathbf{v}_s\left(\mathbf{k}_0 + \tfrac{q}{\hbar}\mathbf{E}\right)\right] \cdot \mathbf{u}, \tag{6.8}$$

---

[2] This surface charges could be attributed to a interface between two dielectrics, but also to the graphene or 2D material free charge. Tests considering volumetric charge (general Poisson equation) and surface charge, showed no relevant differences for the solution of the electrostatics.

where λ represents the direction of displacement, so δ_λ equals δ_{x+}, $-\delta_{x-}$, δ_{y+}, or δ_{y-}, q is the charge of the particle, and $\mathbf{u}$ is the director vector of the axis parallel to δ_λ.

While for parabolic bands these equations have an analytic solution, in graphene finding this exit times is a more complicated task. On the other hand, the right-hand side of equation (6.8) evaluated for a time τ, and yields an analytical expression easily computable, and depends on s, $\mathbf{k}_0$, τ and $\mathbf{E}$. We will call this classical displacement $\delta\mathbf{r}_{\mathrm{MLG}}(s,\mathbf{k}_0,\tau,\mathbf{E})$. Taking it as a starting point, an efficient iterative approach that has been developed as follows: first, the instantaneous particle velocity is evaluated according to its current state, $\mathbf{v}_0 = \mathbf{v}(s,\mathbf{k}_0)$. The four exit times are computed assuming a constant velocity ($\mathbf{v}_0$), and the smallest positive one is considered to be the only appropriate time τ_{fc}, as seen in figure 6.1) i.e.,the flight time to exit the cell. The location after this flight is $\mathbf{r}' = \mathbf{r}_0 + \delta\mathbf{r}_{\mathrm{MLG}}(s,\mathbf{k}_0,\tau_{\mathrm{fc}},\mathbf{E}_{i,j})$. Now, we consider two possibilities: the first one is that $\mathbf{r}'$ is far from the edge. In this case, if the particle is inside the same cell, $\mathbf{r}'$ is taken as a new $\mathbf{r}_0$, and the wavevector is updated. Conversely, if $\mathbf{r}'$ is outside the cell, the final position after the flight is computed again but considering progressively reduced flight times (each time reduced by a factor $1/2$) until the final position of the particle is again inside the cell. With the new $\mathbf{r}_0$, the process is repeated until the position after the flight, r', is met (this is the next possibility). The other possibility one is that $\mathbf{r}'$ is *"close"* to the edge. In such case, the particle would be put right in the edge by considering a new short flight with constant velocity. The wavevector is updated according to the total flight time, and, if the resulting velocity points out of the cell, the boundary condition existing in the edge is applied. We consider the particle to be *"close"* to the edge when its distance to the border is below a configurable factor (taken usually as 2%) of the cell dimensions. With this method, we obtain a fast solution for the exit position and flight time in the cell, at the expense of a reasonable small error in the accuracy of the particle displacement.

During this thesis we focused in the usual planar field effect transistor structures. In these devices, if the geometry is homogeneous in the transversal (y) direction and

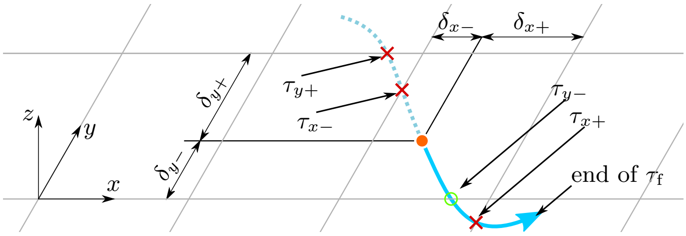

Figure 6.1: Cell exit times of a classical particle subjected to electric fields. Grey lines represent the mesh edges, and the thick orange arrow, the particle displacement path.

the width is large enough, border effects can be neglected, and we can stick to a 2D projection (in the xz plane) of the device. As a results, the in-cell flight times only depend on two boundaries, speeding up the calculations. In the following section, we present the operation principles of these devices.

6.2 Physical principles of GFET operation

Since the presentation of the first functional graphene-based field effect transistor, some works [291–296] have theoretically tackled the physical principles that rule their operation. In figure 6.2 we show the section of a dual gate graphene FET structure, where the conductive channel sits on a thick (usually 300 nm) dielectric with a doped Silicon wafer that serves as a bottom gate. A thin, usually high-κ dielectric isolates the channel from the top gate. Source and drain are separated by a distance L. Now let us assume the energy diagram at a particular position x, as presented in figure 6.3 (a) [296, 294]. The diagram represents, at each position across the length of the device, the electrostatic conditions in the channel. Here, $\phi_{a/b}$ are the oxide/graphene or oxide/metal energy offsets that arise from differences in the electronic affinities of the materials, V_{BG} and V_{TG} are the potentials applied to the bottom and top gates, and $E_{\mathrm{ox}i}$ are the voltage drops across the oxides. As it regards the channel, the energy of the Dirac point is determined by the electrostatic potential $-eV_{\mathrm{ch}}$, determined by the bias point and the charge inside the channel, which is related to the Fermi energy, ε_F.

In figure 6.3 (b) we present the longitudinal view of the energy of the Dirac point, and the Fermi energy for some bias conditions. We assume $V_{\mathrm{S}} = 0$ and $V_{\mathrm{GS}} = V_{\mathrm{G}} - V_{\mathrm{S}}$, being the potential in both gates the same for simplicity ($V_{\mathrm{G}} = V_{\mathrm{TG}} = V_{\mathrm{BG}}$). As the Fermi energy in the close vicinities of the source and drain electrodes is set as $\varepsilon_F(x = 0) = -eV_{\mathrm{S}}$ and $\varepsilon_F(x = L) = -eV_{\mathrm{D}}$, one or two differentiated regions with electron or hole majority

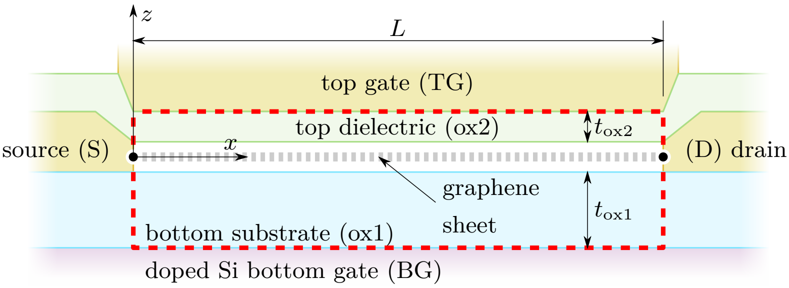

Figure 6.2: Section of the double gated GFET structure of length L. The red dashed line represents the simulation domain.

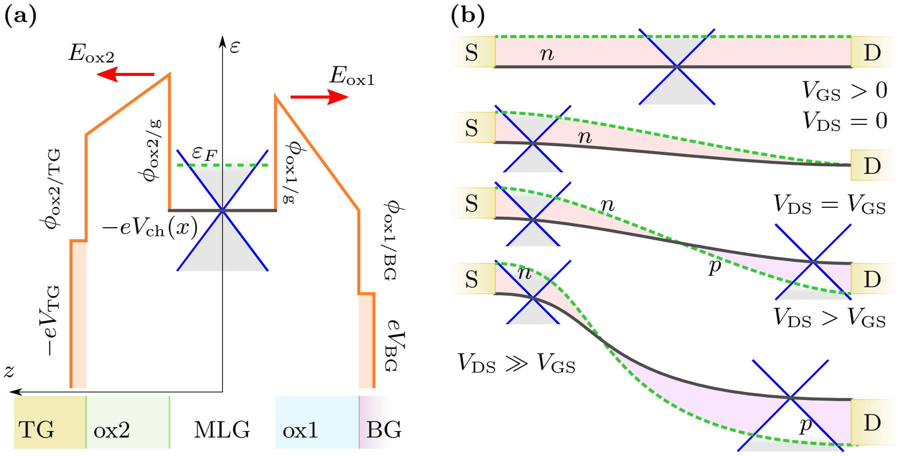

Figure 6.3: (a) Energy diagram at a position x of the channel considering the top gate configuration. The structure represented at the bottom corresponds to figure 6.3. (b) Schematic representation of the distributed carrier density, Fermi level and energy of the neutrality point along the channel for different bias configurations [297]. Values of $V_{\text{VG}} = V_{\text{BG}} = V_{\text{TG}}$, and $V_{\text{GS}} = V_{\text{G}} - V_{\text{S}} > 0$ were chosen in the example.

carriers may appear along the channel [296, 297] with the extension of the n-type and p-type regions depending on the polarization conditions.

This electrostatic analysis, along with the gapless band structure of graphene sets the basis for the appearance of ambipolar transport, and therefore the physical impossibility to effectively switch off a GFET device in this configuration.

6.3 Monte Carlo results

In this section we show some preliminary results of a graphene FET like the one presented in figure 6.2. The dimensions of the simulated device are $L = 200\,\text{nm}$, $t_{\text{ox1}} = 300\,\text{nm}$, $t_{\text{ox2}} = 30\,\text{nm}$, and the dielectrics are SiO_2 for the bottom substrate, and h-BN for the top substrate. No offsets between the oxides and the metals or the graphene sheet were considered, and the potential at the source contact is taken as the reference voltage ($V_{\text{S}} = 0$). In figure 6.4 (a) the transfer characteristics for various source-to-drain voltages are shown. It can be seen that the minimum conductivity is achieved at zero gate bias. However, when the gate voltage is varied the current is never cut, in agreement with the expected behavior of a FET with a graphene channel, due to its inexistent band gap. As a result of this feature, we observe the two different branches associated to the well differentiated majority hole and electron contributions to the device conductivity at strong gate bias. Between both branches we have the Dirac voltage, where the minimum

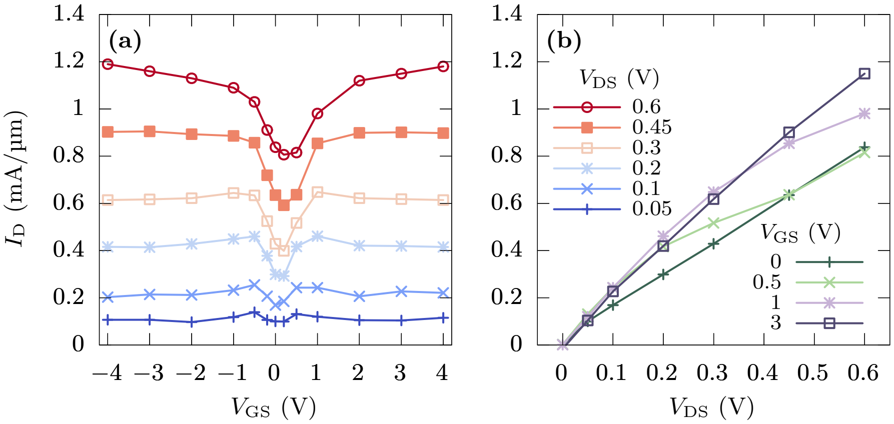

Figure 6.4: Device Monte Carlo simulator results for (a) the transfer, and (b) the output characteristics of the simulated graphene FET.

conductivity is achieved for a given value of V_{DS}. It must be highlighted that even at small gate polarizations, very high minimum currents are obtained as the source-to-drain voltage is raised, obtaining ∼400 µA/µm and ∼800 µA/µm for $V_{DS} = 0.3\,\mathrm{V}$ and 0.6 V, respectively. There is a displacement of the Dirac voltage towards larger gate voltages as higher drain biases are applied, in agreement with experimental observations [298] and other theoretical predictions [296, 299]. The output characteristics for various gate voltages are presented in figure 6.4 (b). No clear saturation trend is observed. The behavior of these $I_D - V_{DS}$ curves is compatible with predictions from drift-diffusion models for GFET devices with high-mobility channels [299].

In order to provide further insight into the feature of ambipolarity discussed with regards of the transfer characteristics, we plot in figure 6.5 (a) the concentration of electrons and holes in the channel as a function of the applied voltage, and in figure 6.5 (b) the contribution to the total drain current density of each carrier type at $V_{DS} = 0.3\,\mathrm{V}$. The gate shows a strong control over the populations of electrons and holes, as it can be deduced from the relative larger densities of electrons at high positive V_{GS}, and holes at negative V_{GS}. As a consequence, most of the current is contributed by these distinct majority type of carriers, at it can be seen in figure 6.5 (b), which gives origin to the two branches previously discussed. The zero Fermi energy ($n = p$), corresponding to the Dirac voltage, is shifted towards positive values of V_{GS} (around 0.2 V), being both populations much larger than the equilibrium population at T_0 [300]: $n \simeq p = 2 \times 10^{11}\,\mathrm{cm}^{-2} \gg \pi/6(k_B T_0/\hbar v_F)^2 \simeq 9 \times 10^9\,\mathrm{cm}^{-2}$. As the result of a non-zero drain bias, a negative Fermi level may appear in the vicinities of the drain contact (for a drain bias large enough, $V_D > V_G$), leading to the induction of a hole population, and a positive Fermi

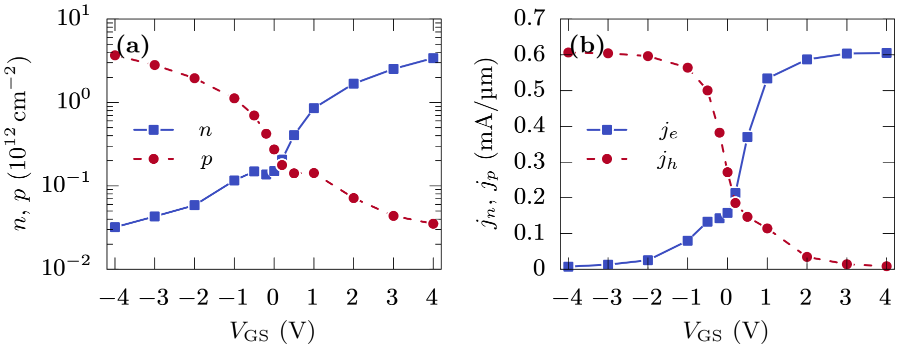

Figure 6.5: (a) Carrier concentration of electrons and holes, and (b) current attributed to each type of carriers as a function of the gate voltage for $V_{\mathrm{DS}} = 0.3\,\mathrm{V}$.

level in the vicinities of the source contact (as $V_{\mathrm{S}} < V_{\mathrm{G}}$). So, the existence of a non-negligible carrier concentration along the channel, either composed mainly of electrons or holes, provokes the device to never completely switch off.

To illustrate this control dependence of the carrier density in the vicinities of the contacts due to the voltage drop between source/drain and the gate, we plot in figure 6.6 the electron carrier density along the GFET channel for various source-to-drain biases. Note that electrons are the majority carriers, since in all cases $V_{\mathrm{GS}} > V_{\mathrm{DS}}$. Close to

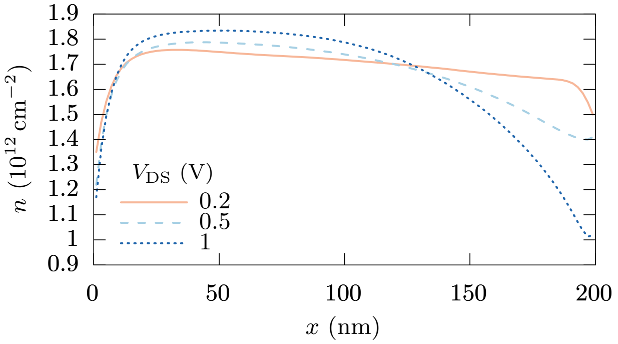

Figure 6.6: Electron concentration, n along the channel of the simulated GFET for various drain-to-source biases and $V_{\mathrm{G}} = 2\,\mathrm{V}$.

the drain contact, it can be clearly seen how the population of electrons is reduced as we set larger drain voltages. This is accompanied by a progressive increase of the hole population, specially close to the drain contact.

In summary, the simulator correctly reproduces the basic features of transport in graphene-based field-effect transistors.

Chapter summary

From the base of the graphene material simulator employed along the previous sections, a device simulation tool has been developed.

A brief introduction to the basic physical operation principles of graphene FETs is presented, with especial emphasis of the well differentiated electrostatic doping induction situation that occur due to distinct bias conditions.

In an early stage, we are able to simulate some features of the graphene based FET behavior as seen in the literature. The ambipolar transport appear evident in the transfer characteristics, and the control of the gate in the carrier population of electrons and holes was demonstrated.

Chapter 7

Conclusions and prospects

7.1 Conclusions

Monte Carlo transport model

A simulation tool of stochastic electron and hole transport in graphene based on a Monte Carlo approach of the semi-classical Boltzmann Transport equation has been presented. The fundamental intrinsic scattering mechanisms are included based upon first-principles calculations, interaction between electrons were included as well by considering the screened Coulomb potential. The model also includes critical out-of-equilibrium effects for the correct description of the carrier dynamics at high fields, like Joule heating and out-of-equilibrium phonons. Interband carrier-carrier scattering was included for the first time in a graphene Monte Carlo model, considering a parameter-free formalism that takes into account the phonon-induced transitions and many particle collinear interactions. The extrinsic scattering mechanisms considered were charged impurities, crystalline defects and the effect of the substrate via surface optical phonons.

Carrier transport phenomena in Graphene

By including extrinsic interactions due to the underlying substrate, and setting impurity densities and defects with levels compatible with those reported in the literature, good agreement of mobility and velocity versus field curves between the simulation results and experimental measurements were achieved. So, the model can describe the basic transport characteristics for a reasonable range of applied electric fields. Also, a full description in terms of the field and carrier density dependence of the drift velocity was introduced into a drift-diffusion simulator for graphene-based field effect transistors devices. The performance and stability was analyzed in terms of scaling, channel quality, an bias point.

We analyzed hot electron phenomena in graphene at high fields. A case study from a modeling perspective was made upon the consideration of the hot phonon and self-heating effects of graphene on SiO_2. Our work indicate that hot phonons are the effect that has a greatest impact on drift velocity, while self heating is of secondary importance. The onset of the two effects is additive as it concerns the reduction of drift velocity. Self-heating is critical for a correct definition of the graphene layer temperature, as the increased proportion of phonon absorption reduces the emitted power per unit area, and therefore the temperature. High-energy phonons heat to a higher extent due to electron-phonon scattering, while the population of the low-energy ones (especially the 59.9 meV SiO_2 SPP) is more sensitive to the temperature increase.

Soft and gradual impact ionization shows a dependence on the Fermi energy. At high fields, the total current, as seen from the contribution of electrons and holes, follows a linear trend with the electric field. As a result, the graphene temperature becomes a function of only the electric field unless the extrinsic doped concentration blocks the generation of electron-hole pairs. The effect of the substrate (a reduction of the excess carrier density) is attributed to an enhanced screening of carrier-carrier interactions and additional carrier cooling due to SPP scattering. Impurities also reduce impact ionization.

Fluctuation phenomena in graphene

The stochastic nature of the Monte Carlo method applied to the diffusive Boltzmann equation was employed to analyze the fluctuations of several quantities relevant to the transport phenomena in monolayer graphene.

A method to study differential mobility via analysis of the velocity response function after a small perturbation of excess carriers was employed. Along with the calculation of the diffusion coefficient from the spectral density of velocity fluctuations we were able to calculate the frequency-dependent noise temperature. At small fields, T_n calculated by this method correctly approaches room temperate, and the obtained values at high fields are comparable to those observed in GaAs and semiconductor nitrides. Comparison between substrates reveals a strong dependence on the SPP interactions, which reduce low-frequency noise due to a higher differential mobility. In the case of graphene on SiO_2 the emitted noise power at low frequencies is noticeably reduced as compared to the case of suspended graphene, and to a lesser extent to the case of graphene on h-BN.

Under transient conditions arising from switching electric fields from high-to-low and low-to-high, we studied the velocity fluctuations of carriers in suspended graphene, and graphene on SiO_2 and h-BN. The evolution of carriers during the transition between the two stationary states was analyzed from a microscopically perspective (wavevector, energy and drift velocity). Velocity fluctuations were analyzed by means of a two-time correlation function, decomposed into thermal and convective contributions. In low-to-high transients of the velocity autocorrelation function steepens with time after the switching. This, in conjunction with the occurrence of negative values, provokes that the spectral density of velocity fluctuations reaches a temporal maximum at low frequencies, and a spectral maximum at frequencies in the THz range. It was found that in the changes on the wavevector orientation (convective term) dominate over the energy fluctuations (thermal term). In the high-to-low field transient, the correlation drop becomes softer the longer is the time after the switch, leading to a Lorentzian-like spectral density of velocity fluctuations that grows with time at small frequencies.

The non-linear response of the drift velocity was examined as a possible approach to generate high-order harmonics under the application of an oscillating electric field.

Distinct instant ensemble velocity was observed depending on the frequency of the applied field and on its magnitude. By means of the Fourier coefficients, it was revealed that the highest harmonic power is obtained for lower frequencies and high fields. Besides, the resulting noise from velocity fluctuations was analyzed in order to evaluate the background noise that can hinder the detection of the generated harmonics. With such purpose, the spectral density of the periodic velocity autocorrelation function was evaluated. Discrete Fourier transform of individual particle velocity history yields the same spectral results for the noise and harmonic contribution. Finally, the possibility to generate and detect high-level harmonics is evaluated as a function of the threshold bandwidth obtained from the quantities previously obtained. Third harmonic could be detected with bandwidth of 10 GHz at 50 GHz and 300 GHz, but a 0.1 GHz bandwidth would be needed to detect the fifth harmonic for $f_{\mathrm{AC}} = 300\,\mathrm{GHz}$ and the ninth for $f_{\mathrm{AC}} = 50\,\mathrm{GHz}$ with $E_{\mathrm{AC}} = 10\,\mathrm{kV/cm}$. These are more restrictive values than those found in III-V compounds, although it should be taken into account that the hot phonon effect and carrier-carrier scattering is a great source of velocity fluctuations, and hence of background noise.

Ultrafast dynamics of photoexcited carriers

We studied the carrier dynamics of photoexcited intrinsic monolayer graphene, observing its dependence with the photon wavelength and the photocarrier density. The general energy evolution of the carrier ensemble was identified in terms of the carrier temperature. At short timescales (tens of femtoseconds) the dynamics are ruled by intraband and interband carrier-carrier scattering, provoking a quick drop of the carrier temperature.

Due to the initial free states at low energies, and the highly energetic photocarrier distribution, impact ionization generates a great amount of electron-hole pairs around the first 100 fs. Maximum carrier multiplication up to a four-fold increase of the free carriers was observed, being linearly dependent on the relation between the photon energy and the photocarrier density.

The previous process leads to the appearance of a thermal distribution. Afterwards the relaxation is starred by cooling due to the power transference from the carriers excess energy to phonons. At the picosecond scale, phonon assisted recombination pathway rules the interband cooling stage. Hot phonons are revealed to be a relevant factor in the carrier dynamics. Due to phonon emission of hot electrons, these become out-of-equilibrium, increasing the absorption/emission ratio, thus preventing a faster cooling of the electron/hole system.

A comparison between different substrates is offered. Background screening is relevant during the first instants of thermalization, as it damps collinear interband carrier-carrier interactions, thus reducing the carrier temperature decay rate. Furthermore, at longer times, the additional relaxation pathways that the substrate offers via SPP scattering accelerate carrier intraband cooling and the recombination rates. Besides, it was shown that adding competing cooling pathways (SPPs) damps intrinsic phonon heating.

Experimental characterization of these processes have been attempted by means of pump-probe differential transmission spectroscopy techniques. Some hindrances were found concerning the experimental alignment and amplification, and it was extremely difficult to get clear and repeatable results. On the other hand, we simulated differential transmission signals from the Monte Carlo results, finding good agreement with data found in the literature.

Graphene-based devices

The fundamental basis to extend the Ensemble Monte Carlo simulator to the device level was developed and presented: geometric definition, carrier motion in the real space, and self-consistent electrostatic solving is detailed.

The inherent bipolar transport in graphene, results of its zero band gap, poses challenges that are not usual in traditional semiconductors. In the first version of the graphene Monte Carlo simulator, for graphene-based FETs under small bias conditions the simulations yields output and transfer characteristics with trends that are compatible with literature reports and compact models. However, some improvements are needed in order to deal with extreme bias conditions. This can be attributed to several factors, the first one being related to problems in the carrier injection at large bias. The other factor, is the influence of Klein tunneling, that can be of great importance in graphene due to the lack of a band gap.

7.2 Current work and future prospects

During the elaboration of this thesis, I got involved in different topics that were not contained in the initial research plan. Besides graphene, the simulator was made modular and able to simulate other different 2D materials. At the point of writing this thesis, some studies on silicene have been made. The related publications are listed in appendix B.

We are actively working on the modeling of MoS_2 and other transition metal dichalcogenides, with plans to study carrier diffusion, fluctuations and the effects of degeneracy in these materials.

There is still work to do with respect to the material simulator, in order to make it function under bias where now it fails. Once these issues are solved, effects of the substrate, impurities and defects in the performance of GFETs could be theoretically evaluated. Also noise small-signal characterization will be attempted. The tool has been prepared to deal with devices defined in the three dimensions, as well as planar structures like self-switching diodes or ballistic deflection transistors, so these structures are also planned to be studied once the device simulator is mature.

Finally, at the time of finishing this thesis, we are working on a electrodynamic description of the carrier flow and electromagnetic fields via the *finite differences in the time domain* method. The main purpose is to analyze the dynamic graphene response to external perturbations and obtain the complex frequency-dependent AC conductivity.

7.3 Conclusiones

Monte Carlo transport model

Se ha desarrollado y presentado una herramienta para la descripción del transporte estocástico en grafeno, basado en el método Monte Carlo para el tratamiento de la ecuación de transporte semiclásico de Boltzmann. El modelo incluye los principales mecanismos de scattering obtenidos mediante cálculos basados en primeros principios; las interacciones entre electrones también se incluyen mediante el potencial Coulombiano apantallado. El modelo incluye además los fenómenos de no equilibrio críticos para una correcta descripción de la dinámica de los portadores a campos altos, como son el autocalentamiento y los fonones fuera de equilibrio. Las colisiones interbanda se han incluido por primera vez en un modelo monte carlo, considerando un formalismo libre de parámetros exógenos para el tratamiento de los mecanismos portador-portador, y las transiciones asistidas por fonones ópticos.

Carrier transport phenomena in Graphene

Mediante la consideración de interacciones extrínsecas al propio grafeno, como el substrato adyacente, impurezas y defectos cristalinos a niveles compatibles con la literatura, obtenemos un buen ajuste entre los datos obtenidos con el simulador y las medidas experimentales de movilidad y velocidad en función del campo aplicado. Por lo tanto, concluimos que el modelo puede describir las características básicas del transporte en un rango muy razonable de campos eléctricos. Además, se utilizaron los datos de las curvas velocidad-campo obtenidos mediante este modelo en un simulador de deriva-difusión de transistores de efecto campo basados en grafeno. De esta forma, se analizó el rendimiento y estabilidad de dichos dispositivos en términos de su escalado, calidad del canal, y punto de polarización.

Analizamos los fenómenos de portadores calientes en grafeno bajo la aplicación de campos altos. Desde una perspectiva del modelado, se hizo un estudio caso a caso respecto a la consideración de los efectos de fonones calientes y autocalentamiento en grafeno sobre SiO_2. Nuestro trabajo indica que los fonones calientes tienen el mayor impacto en la velocidad de deriva, mientras que el autocalentamiento presenta menor influencia, aunque el impacto de ambos se superpone cuando son considerados conjuntamente. La consideración de los fonones calientes es crítica a la hora de determinar la temperatura de la lámina de grafeno, pues estos hacen incrementar la proporción entre las colisiones de absorción y emisión, de modo que en último término se reduce la potencia total disipada, y en consecuencia, la temperatura. Los fonones más energéticos aumentan su población principalmente por la interacción electrón-fonón, mientras que los menos energéticos (especialmente el fonón polar superficial del SiO_2 de 59.9 eV) son más sensibles al incremento de la temperatura de la red.

Observamos una dependencia gradual de la ionización por impacto con el nivel de Fermi. La corriente total obtenida mediante la contribución conjunta de electrones y huecos, sigue un comportamiento lineal en función del campo cuando este es suficientemente alto. Como consecuencia, la temperatura que alcanza el grafeno en condiciones estacionarias es función sólo del campo eléctrico a no ser que el dopaje electrostático sea lo suficientemente elevado como para bloquear la generación de pares electrón-hueco. El efecto del sustrato (moderar la densidad de portadores en exceso) es atribuida al apantallamiento de las interacciones portador-portador y al impacto de las colisiones con fonones polares superficiales. También confirmamos la reducción de la ionización por impacto mediante la adición de impurezas.

Fluctuation phenomena in graphene

La naturaleza estocástica del método Monte Carlo al transporte difusivo fue empleada para el análisis de fluctuaciones de las magnitudes relevantes a los fenómenos de transporte en grafeno monocapa.

Empleando de un método numérico basado en la introducción de una pequeña perturbación de los portadores en exceso, obtuvimos la movilidad diferencial. En conjunto con el cálculo del coeficiente de difusión a partir de la densidad espectral de las fluctuaciones de velocidad, fuimos capaces de obtener la temperatura del ruido dependiente de la frecuencia. A campos bajos, la temperatura del ruido se aproxima correctamente a la temperatura ambiente, mientras que a campo alto los valores obtenidos son comparables a los observados en GaAs y nitruros semiconductores. Se encontró una fuerte dependencia de la temperatura del ruido con los fonones polares superficiales, que tieneden a reducirlo a baja frecuencia debido a una mayor movilidad diferencial. En el caso de grafeno sobre SiO_2, la potencia del ruido emitida a bajas frecuencias se reduce notablemente respecto al caso de grafeno suspendido, y de forma más moderada en comparación al caso de grafeno sobre h-BN.

En condiciones transitorias originadas por satos bruscos en el campo, estudiamos las fluctuaciones de velocidad en grafeno suspendido, sobre SiO_2 y sobre h-BN. La evolución de las propiedades (vector de onda, energía y velocidad de deriva medias) de los portadores entre los dos estados estacionarios se estudiaron microscópicamente. Las fluctuaciones se analizaron mediante una correlación a dos tiempos y descompuesta en dos contribuciones: convectiva y térmica. En los transitorios de campo bajo a alto, la función de correlación aumenta su pendiente con el tiempo transcurrido desde el salto. Junto a la aparición de valores negativos, esto provoca que la densidad espectral de las fluctuaciones de velocidad alcance un máximo en el dominio temporal a bajas frecuencias, y un máximo en el dominio espectral en el rango de THz. Las fluctuaciones de la orientación del vector de onda (contribución convectiva) dominan sobre las fluctuaciones de energía (término térmico). En el transitorio referente al salto de alto a bajo campo, la pérdida de correlación se atenúa a lo largo del tiempo pasado tras el salto, lo que produce una densidad espectral de las fluctuaciones de velocidad que se asemeja a una Lorentziana que crece para bajas frecuencias a medida que el tiempo transcurre.

La respuesta no lineal de la velocidad de deriva se examinó como un enfoque posible para la generación de armónicos de orden alto bajo la aplicación de un campo eléctrico oscilante. Observamos velocidades medias instantáneas bien diferenciadas dependiendo de la frecuencia y magnitud del campo oscilante. Mediante el estudio de los coeficientes de Fourier de esta respuesta, descubrimos que la mayor potencia de armónicos altos se consigue para frecuencias bajas y campos altos. Además se analizaron las fluctuaciones de velocidad para determinar el ruido de fondo que pudiera enmascarar la detección de los armónicos generados. Para este propósito se evaluó la densidad espectral de las fluctuaciones de velocidad. Mediante la transformada de Fourier discreta sobre la velocidad de partículas individuales obtuvimos los mismos resultados espectrales para las contribuciones superpuestas armónica y del ruido. Finalmente, la posibilidad de generar y detectar estos armónicos de orden alto se evaluó en función del ancho de banda límite mediante las magnitudes previamente calculadas. El tercer armónico se podría detectar con un ancho de banda de 10 GHz para f_{AC} de 50 y 300 GHz, mientras un ancho de banda de 0.1 GHz sería necesario para detectar el quinto armónico a una frecuencia de 300 GHz y el noveno para 50 GHz. Estos valores son más restrictivos que los que se encuentran en compuestos semiconductores III-V; sin embargo debería tenerse en cuenta que la consideración de fonones calientes e interacciones portador-portador supone una importante fuente de fluctuaciones de velocidad, y por tanto de ruido.

Ultrafast dynamics of photoexcited carriers

Estudiamos la dinámica de portadores fotoexcitados en grafeno monocapa intrínseco en relación a la longitud de onda del pulso de luz y la densidad de portadores excitados. La evolución del conjunto de portadores se identificó en términos de la temperatura de los mismos. A escalas de tiempo rápidas (decenas de femtosegundo), la dinámica está gobernada por procesos portador-portador (tanto intra- como interbanda), provocando una rápida caída de la temperatura de los portadores.

Debido a la cantidad de estados libres a energías bajas y la distribución altamente energética de los portadores excitados, se genera una gran cantidad de pares electrón hueco mediante ionización por impacto en los primeros 100 fs. Llegó a observarse una multiplicación de portadores de hasta cuatro veces la densidad de portadores fotoexcitados, siendo este factor dependiente de la relación entra la energía del fotón y la densidad de portadores fotoexcitados.

El proceso descrito conduce a la aparición de una distribución térmica. Seguidamente, la relajación está protagonizada por un proceso de enfriamiento caracterizado por la transferencia de energía desde los portadores hacia la red mediante colisiones portador-fonón. En una escala de tiempo de picosegundos, la recombinación asistida por fonones lidera la etapa de enfriamiento interbanda.

Los fonones calientes son un factor muy relevante en la dinámica de portadores fotoexcitados. Debido a la rápida emisión de fonones, estos son llevados lejos del equilibrio, lo que provoca un incremento en la proporción de colisiones de absorción respecto a las de emisión, lo que ralentiza la relajación del sistema de electrones y huecos en comparación con el caso en el que los fonones fuera de equilibrio no se considerasen.

Se ofreció una comparación considerando distintos sustratos. El apantallamiento producido por el entorno dieléctrico es relevante en los primeros instantes de la termalización, dado que las interacciones portador-portador se ven atenuadas, reduciéndose por tanto la tasa de enfriamiento. A tiempos más tardíos, la aportación de nuevos canales de relajación mediante colisiones con fonones polares superficiales acelera el enfriamiento intrabanda y las tasas de reombinación. Además, estas vias alternativas de enfriamiento reduce el calentamiento de los fonones intrínsecos del grafeno.

Mediante técnicas de espectroscopía diferencial resuelta en el tiempo basado en montajes experimentales de bombeo-sonda (pump-probe), se intentó llevar a cabo la caracterización de estos procesos. Se encontraron dificultades relativas a la alineación de los haces sobre la muestra y la amplificación de la señal, lo que dificultó la obtención de resultados en una forma clara y consistentemente repetible. Por otra parte, los resultados simulados de transmisión diferencial obtenida con el simulador Monte Carlo muestran un buen ajuste con los datos experimentales encontrados en la literatura.

Graphene-based devices

La base fundamental para extender el simulador de material hacia un simulador de dispositivos ha sido presentada, desarrollada, e implementada: la definición geométrica, el movimiento de los portadores en el espacio real, y la solución autoconsistente del campo eléctrico han sido debidamente detallados.

El transporte ambipolar, inherente a la carente de gap de la estructura de bandas del grafeno, presenta ciertas dificultades que no son usuales en semiconductores tradicionales. En una primera versión del simulador Monte Carlo de dispositivos basados en grafeno, en la configuración de transistores de efecto campo en condiciones de baja polarización, las características de transferencia y de salida son compatibles con las de prototipos experimentales encontrados en la literatura y los obtenidos con modelos compactos.

Sin embargo, son necesarias algunas mejoras para poder tratar condiciones de polarización más extremas. Esto puede ser debido a factores como ciertos problemas encontrados con la inyección en los contactos, o la influencia del fenómeno de túnel Klein, que es de gran importancia debido a la ausencia de gap en grafeno.

7.4 Trabajo actual y perspectivas futuras

Durante la elaboración de esta tesis, me he visto involucrado en diversas temáticas que no estaban contempladas en el plan de investigación inicial. El simulador ha sido desarrollado de forma modular, con el fin de poder simular otros materiales 2D. En el momento de la escritura de esta tesis, hemos realizado algunos estudios sobre siliceno; las publicaciones relacionadas están recogidas en el apéndice appendix B.

Actualmente estamos trabajando de activamente en el modelado de molibdenita (MoS_2) y otros dicalcogénos de metales de transición. Los planos a corto plazo consisten en estudiar la difusividad de los portadores, fluctuaciones y los efectos de la degeneración en estos materiales.

Aún queda trabajo por terminar en lo referente al simulador de dispositivos hasta conseguir su pleno funcionamiento en ciertas condiciones donde ahora falla. Una vez estas contingencias queden solucionadas, se podrán abordar el estudio teórico de los efectos de sustrato, impurezas y defectos en el rendimiento de FETs basados en grafeno, así como la caracterización de pequeña señal de estos dispositivos. Además, el simulador se ha preparado para lidiar con dispositivos definidos en las tres dimensiones, así como para geometrías planares como diodos autoconmutantes o transistores de deflección balística, de modo que llegado el momento es plausible que se estudie este tipo de estructuras una vez el simulador alcance el nivel necesario de madurez.

Para terminar, mientras se está escribiendo esta tesis, estamos trabajando en una descripción de la electrodinámica que acopla consistentemente el flujo de carga y campo electromagnético por medio de la técnica de las diferencias finitas en el dominio del tiempo. El propósito es analizar el comportamiento dinámico ante una perturbación externa, lo que permitiría obtener la conductividad AC dependiente de la frecuencia.

Bibliography

[1] E. J. Lilienfeld. “Method and apparatus for controlling electric currents”. US1745175 (A). Jan. 1930.

[2] E. J. Lilienfeld. “Device for controlling electric current”. US1900018 (A). Mar. 1933.

[3] J. Bardeen and W. H. Brattain. “The Transistor, A Semi-Conductor Triode”. In: *Physical Review* **74.2** (July 1948), pp. 230–231.

[4] W. Shockley. “Device for controlling electric current”. US2569347 (A). Sept. 1951.

[5] M. M. Atalla, E. Tannenbaum, and E. J. Scheibner. “Stabilization of Silicon Surfaces by Thermally Grown Oxides”. In: *Bell System Technical Journal* **38.3** (May 1959), pp. 749–783.

[6] F. Wanlass and C. Sah. “Nanowatt logic using field-effect metal-oxide semiconductor triodes”. In: “1963 IEEE International Solid-State Circuits Conference. Digest of Technical Papers”. Institute of Electrical and Electronics Engineers.

[7] H. Iwai. “Outlook of MOS devices into next century”. In: *Microelectronic Engineering* **48.1-4** (Sept. 1999), pp. 7–14.

[8] Y.-B. Kim. “Challenges for Nanoscale MOSFETs and Emerging Nanoelectronics”. In: *Transactions on Electrical and Electronic Materials* **11.3** (June 2010), pp. 93–105.

[9] F. Balestra et al. “Double-gate silicon-on-insulator transistor with volume inversion: A new device with greatly enhanced performance”. In: *IEEE Electron Device Letters* **8.9** (Sept. 1987), pp. 410–412.

[10] J.-P. Colinge. “Hot-electron effects in Silicon-on-insulator n-channel MOSFET’s”. In: *IEEE Transactions on Electron Devices* **34.10** (Oct. 1987), pp. 2173–2177.

[11] B. M. Haugerud, L. A. Bosworth, and R. E. Belford. “Mechanically induced strain enhancement of metal-oxide-semiconductor field effect transistors”. In: *Journal of Applied Physics* **94.6** (Sept. 2003), pp. 4102–4107.

[12] S. Campbell et al. “MOSFET transistors fabricated with high permitivity TiO_2 dielectrics”. In: *IEEE Transactions on Electron Devices* **44.1** (1997), pp. 104–109.

[13] I. Ferain, C. A. Colinge, and J.-P. Colinge. "Multigate transistors as the future of classical metal-oxide-semiconductor field-effect transistors". In: *Nature* **479.7373** (Nov. 2011), pp. 310–316.

[14] S. Bangsaruntip et al. "High performance and highly uniform gate-all-around silicon nanowire MOSFETs with wire size dependent scaling". In: "2009 IEEE International Electron Devices Meeting (IEDM)". IEEE, Dec. 2009.

[15] A. W. Topol et al. "Three-dimensional integrated circuits". In: *IBM Journal of Research and Development* **50.4.5** (July 2006), pp. 491–506.

[16] J. A. del Alamo. "Nanometre-scale electronics with III-V compound semiconductors". In: *Nature* **479.7373** (Nov. 2011), pp. 317–323.

[17] N. Waldron. "III-V Devices and Technology for CMOS". In: "High Mobility Materials for CMOS Applications". Elsevier, 2018, pp. 231–280.

[18] P. D. Kirsch et al. "Challenges of III-V materials in advanced CMOS logic". In: "Proceedings of Technical Program of 2012 VLSI Technology, System and Application". IEEE, Apr. 2012.

[19] K. Y. Cheng, M. Feng, D. Cheng, and C. Liao. "Sub-100 nm Gate III-V MOSFET for Digital Applications". In: "Fundamentals of III-V Semiconductor MOSFETs". Springer US, 2010, pp. 285–306.

[20] M. L. Green, E. P. Gusev, R. Degraeve, and E. L. Garfunkel. "Ultrathin (<4 nm) SiO_2 and Si-O-N gate dielectric layers for silicon microelectronics: Understanding the processing, structure, and physical and electrical limits". In: *Journal of Applied Physics* **90.5** (Sept. 2001), pp. 2057–2121.

[21] A. Nainani et al. "Enhancing hole mobility in III-V semiconductors". In: *Journal of Applied Physics* **111.10** (May 2012), p. 103706.

[22] P. Goley and M. Hudait. "Germanium Based Field-Effect Transistors: Challenges and Opportunities". In: *Materials* **7.3** (Mar. 2014), pp. 2301–2339.

[23] A. Toriumi and T. Nishimura. "Germanium CMOS potential from material and process perspectives: Be more positive about germanium". In: *Japanese Journal of Applied Physics* **57.1** (Oct. 2017), p. 010101.

[24] H. Shang et al. "Germanium channel MOSFETs: Opportunities and challenges". In: *IBM Journal of Research and Development* **50.4.5** (July 2006), pp. 377–386.

[25] P. P. Manik et al. "Fermi-level unpinning and low resistivity in contacts to n-type Ge with a thin ZnO interfacial layer". In: *Applied Physics Letters* **101.18** (Oct. 2012), p. 182105.

[26] D. Kuzum et al. "High-Mobility Ge N-MOSFETs and Mobility Degradation Mechanisms". In: *IEEE Transactions on Electron Devices* **58.1** (Jan. 2011), pp. 59–66.

[27] D.-H. Kim, B. Brar, and J. A. del Alamo. "$f_{\mathrm{T}} = 688\,\mathrm{GHz}$ and $f_{\max} = 800\,\mathrm{GHz}$ in $L_{\mathrm{g}} = 40\,\mathrm{nm}$ $\mathrm{In_{0.7}Ga_{0.3}As}$ MHEMTs with $g_{m,\max} > 2.7\,\mathrm{mS}/\mu\mathrm{m}$". In: "2011 International Electron Devices Meeting". IEEE, Dec. 2011.

[28] S. Mokkapati and C. Jagadish. "III-V compound SC for optoelectronic devices". In: *Materials Today* **12**.**4** (Apr. 2009), pp. 22–32.

[29] P. Sangaré et al. "Experimental demonstration of direct terahertz detection at room-temperature in AlGaN/GaN asymmetric nanochannels". In: *Journal of Applied Physics* **113**.**3** (Jan. 2013), p. 034305.

[30] G. Fiori et al. "Electronics based on two-dimensional materials". In: *Nature Nanotechnology* **9**.**10** (Oct. 2014), pp. 768–779.

[31] K. S. Novoselov et al. "Circuit element utilizing semiconductive material". In: *Science* **306**.**5696** (2004), pp. 666–669.

[32] H. P. Boehm, R. Setton, and E. Stumpp. "Nomenclature and terminology of graphite intercalation compounds (IUPAC Recommendations 1994)". In: *Pure and Applied Chemistry* **66**.**9** (Jan. 1994), pp. 1893–1901.

[33] P. R. Wallace. "The Band Theory of Graphite". In: *Physical Review* **71**.**9** (May 1947), pp. 622–634.

[34] C. Lee, X. Wei, J. W. Kysar, and J. Hone. "Measurement of the Elastic Properties and Intrinsic Strength of Monolayer Graphene". In: *Science* **321**.**5887** (July 2008), pp. 385–388.

[35] K. Bolotin et al. "Ultrahigh electron mobility in suspended graphene". In: *Solid State Communications* **146**.**9-10** (June 2008), pp. 351–355.

[36] J.-H. Chen et al. "Intrinsic and extrinsic performance limits of graphene devices on SiO2". In: *Nature Nanotechnology* **3**.**4** (Mar. 2008), pp. 206–209.

[37] C. R. Dean et al. "Boron nitride substrates for high-quality graphene electronics". In: *Nature Nanotechnology* **5**.**10** (Aug. 2010), pp. 722–726.

[38] L. Banszerus et al. "Ultrahigh-mobility graphene devices from chemical vapor deposition on reusable copper". In: *Science Advances* **1**.**6** (July 2015), e1500222.

[39] N. Arora, J. Hauser, and D. Roulston. "Electron and hole mobilities in silicon as a function of concentration and temperature". In: *IEEE Transactions on Electron Devices* **29**.**2** (Feb. 1982), pp. 292–295.

[40] I. Thayne et al. "Review of Current Status of III-V MOSFETs". In: "ECS Transactions". ECS, 2009.

[41] I. Meric et al. "Graphene field-effect transistors based on boron nitride gate dielectrics". In: "2010 International Electron Devices Meeting". IEEE, Dec. 2010.

[42] D. K. Ferry. "Transport in graphene on BN and SiC". In: "2012 12th IEEE International Conference on Nanotechnology (IEEE-NANO)". IEEE, Aug. 2012.

[43] L. Banszerus et al. "Ballistic Transport Exceeding 28 μm in CVD Grown Graphene". In: *Nano Letters* **16**.**2** (Jan. 2016), pp. 1387–1391.

[44] A. S. Mayorov et al. “Micrometer-Scale Ballistic Transport in Encapsulated Graphene at Room Temperature”. In: *Nano Letters* **11.6** (June 2011), pp. 2396–2399.

[45] M. C. Lemme, T. J. Echtermeyer, M. Baus, and H. Kurz. “A Graphene Field-Effect Device”. In: *IEEE Electron Device Letters* **28.4** (Apr. 2007), pp. 282–284.

[46] R. Cheng et al. “High-frequency self-aligned graphene transistors with transferred gate stacks”. In: *Proceedings of the National Academy of Sciences* **109.29** (July 2012), pp. 11588–11592.

[47] Y. Wu et al. “200 GHz Maximum Oscillation Frequency in CVD Graphene Radio Frequency Transistors”. In: *ACS Applied Materials & Interfaces* **8.39** (Sept. 2016), pp. 25645–25649.

[48] X. Mei et al. “First Demonstration of Amplification at 1 THz Using 25-nm InP High Electron Mobility Transistor Process”. In: *IEEE Electron Device Letters* **36.4** (Apr. 2015), pp. 327–329.

[49] A. Tessmann, A. Leuther, H. Massler, and M. Seelmann-Eggebert. “A High Gain 600 GHz Amplifier TMIC Using 35 nm Metamorphic HEMT Technology”. In: “2012 IEEE Compound Semiconductor Integrated Circuit Symposium (CSICS)”. IEEE, Oct. 2012.

[50] S. Lee et al. “Record RF performance of 45-nm SOI CMOS Technology”. In: “2007 IEEE International Electron Devices Meeting”. IEEE, Dec. 2007.

[51] F. Schwierz. “Graphene Transistors: Status, Prospects, and Problems”. In: *Proceedings of the IEEE* **101.7** (July 2013), pp. 1567–1584.

[52] T. Das, B. K. Sharma, A. K. Katiyar, and J.-H. Ahn. “Graphene-based flexible and wearable electronics”. In: *Journal of Semiconductors* **39.1** (Jan. 2018), p. 011007.

[53] C. Sire et al. “Flexible Gigahertz Transistors Derived from Solution-Based Single-Layer Graphene”. In: *Nano Letters* **12.3** (Feb. 2012), pp. 1184–1188.

[54] K. F. Mak et al. “Measurement of the Optical Conductivity of Graphene”. In: *Physical Review Letters* **101.19** (Nov. 2008), p. 196405.

[55] M. Liu et al. “A graphene-based broadband optical modulator”. In: *Nature* **474.7349** (May 2011), pp. 64–67.

[56] M. Liu and X. Zhang. “Graphene benefits”. In: *Nature Photonics* **7.11** (Sept. 2013), pp. 851–852.

[57] Q. Bao et al. “Atomic-Layer Graphene as a Saturable Absorber for Ultrafast Pulsed Lasers”. In: *Advanced Functional Materials* **19.19** (Oct. 2009), pp. 3077–3083.

[58] N. Liu et al. “Large-Area, Transparent, and Flexible Infrared Photodetector Fabricated Using P-N Junctions Formed by N-Doping Chemical Vapor Deposition Grown Graphene”. In: *Nano Letters* **14.7** (June 2014), pp. 3702–3708.

[59] T. Mueller, F. Xia, and P. Avouris. “Graphene photodetectors for high-speed optical communications”. In: *Nature Photonics* **4.5** (Mar. 2010), pp. 297–301.

[60] P. Ma et al. “Plasmonically Enhanced Graphene Photodetector Featuring 100 Gbit/s Data Reception, High Responsivity, and Compact Size”. In: *ACS Photonics* **6.1** (Nov. 2018), pp. 154–161.

[61] K. Bourzac. “A Conversation with Tomás Palacios”. In: *ACS Central Science* **3.7** (July 2017), pp. 677–678.

[62] Q. H. Wang et al. “Electronics and optoelectronics of two-dimensional transition metal dichalcogenides”. In: *Nature Nanotechnology* **7.11** (Nov. 2012), pp. 699–712.

[63] S. Z. Butler et al. “Progress, Challenges, and Opportunities in Two-Dimensional Materials Beyond Graphene”. In: *ACS Nano* **7.4** (Mar. 2013), pp. 2898–2926.

[64] P. Miró, M. Audiffred, and T. Heine. “An atlas of two-dimensional materials”. In: *Chem. Soc. Rev.* **43.18** (2014), pp. 6537–6554.

[65] D. K. Ferry. “Carrier statistics in graphene at high electric field”. In: *Semiconductor Science and Technology* **32.2** (Jan. 2017), p. 025018.

[66] R. S. Shishir and D. K. Ferry. “Velocity saturation in intrinsic graphene”. In: *Journal of Physics: Condensed Matter* **21.34** (July 2009), p. 344201.

[67] T. Fang, A. Konar, H. Xing, and D. Jena. “High-field transport in two-dimensional graphene”. In: *Physical Review B* **84.12** (Sept. 2011), p. 125450.

[68] X. Li et al. “Surface polar phonon dominated electron transport in graphene”. In: *Applied Physics Letters* **97.23** (Dec. 2010), p. 232105.

[69] N. Sule and I. Knezevic. “Phonon-limited electron mobility in graphene calculated using tight-binding Bloch waves”. In: *Journal of Applied Physics* **112.5** (Sept. 2012), p. 053702.

[70] D. K. Ferry. “Short-range potential scattering and its effect on graphene mobility”. In: *Journal of Computational Electronics* **12.2** (Jan. 2013), pp. 76–84.

[71] P. Borowik, J.-L. Thobel, and L. Adamowicz. “Monte Carlo study of electron relaxation in graphene with spin polarized, degenerate electron gas in presence of electron-electron scattering”. In: *Semiconductor Science and Technology* **32.12** (Oct. 2017), p. 125006.

[72] N. Sule, K. J. Willis, S. C. Hagness, and I. Knezevic. “EMC/FDTD/MD simulation of carrier transport and electrodynamics in two-dimensional electron systems”. In: *Journal of Computational Electronics* **12.4** (Sept. 2013), pp. 563–571.

[73] A. Paussa et al. “Simulation of graphene nanoscale RF transistors including scattering and generation/recombination mechanisms”. In: “2011 International Electron Devices Meeting”. IEEE, Dec. 2011.

[74] J. K. David, L. F. Register, and S. K. Banerjee. “Semiclassical Monte Carlo Analysis of Graphene FETs”. In: *IEEE Transactions on Electron Devices* **59.4** (Apr. 2012), pp. 976–982.

[75] M. H. Kalos and P. A. Whitlock. “Monte Carlo Methods”. Wiley-VCH, 2008. ISBN: 9783527407606.

[76] K. M. Decker. "The Monte Carlo method in science and engineering: Theory and application". In: *Computer Methods in Applied Mechanics and Engineering* **89**.**1-3** (Aug. 1991), pp. 463–483.

[77] M. P. Allen and D. J. Tildesley. "Computer Simulation of Liquids (Oxford Science Publications)". Clarendon Press, 1989. ISBN: 9780198556459.

[78] D. Frenkel and B. Smit. "Understanding Molecular Simulation: From Algorithms to Applications (Computational Science Series, Vol 1)". Academic Press, 2001. ISBN: 0122673514.

[79] H. Müller-Krumbhaar. "Monte Carlo Simulation of Crystal Growth". In: "Monte Carlo Methods in Statistical Physics". Springer Berlin Heidelberg, 1986, pp. 261–299.

[80] D. M. Ceperley and M. H. Kalos. "Quantum Many-Body Problems". In: "Monte Carlo Methods in Statistical Physics". Springer Berlin Heidelberg, 1986, pp. 145–194.

[81] H. Rickman et al. "Monte Carlo methods to calculate impact probabilities". In: *Astronomy & Astrophysics* **569** (Sept. 2014), A47.

[82] D. Kasen, R. C. Thomas, and P. Nugent. "Time-dependent Monte Carlo Radiative Transfer Calculations for Three-dimensional Supernova Spectra, Light Curves, and Polarization". In: *The Astrophysical Journal* **651**.**1** (Nov. 2006), pp. 366–380.

[83] S. Selberherr. "Analysis and Simulation of Semiconductor Devices". Springer, 2011. ISBN: 3709187540.

[84] L. Boltzmann. In: "Kinetische Theorie II". Vieweg+Teubner Verlag, 1970, pp. 115–225.

[85] N. Bellomo and M. L. Schiavo. "From the Boltzmann equation to generalized kinetic models in applied sciences". In: *Mathematical and Computer Modelling* **26**.**7** (Oct. 1997), pp. 43–76.

[86] M. D. Ventra. "Electrical Transport in Nanoscale Systems". Cambridge University Press, 2010. ISBN: 0511755600.

[87] N. W. Ashcroft and N. D. Mermin. "Solid State Physics". Cengage Learning, 1976. ISBN: 0030839939.

[88] C. Jacoboni and L. Reggiani. "The Monte Carlo method for the solution of charge transport in semiconductors with applications to covalent materials". In: *Reviews of Modern Physics* **55**.**3** (July 1983), pp. 645–705.

[89] M. Akarsu and Ö. Özbaş. "Monte Carlo Simulation for Electron Dynamics in Semiconductor Devices". In: *Mathematical and Computational Applications* **10**.**1** (Apr. 2005), pp. 19–26.

[90] F. Moučka and I. Nezbeda. "The multi-particle sampling method in Monte Carlo simulations on fluids and its efficient implementations". In: *Molecular Simulation* **36**.**7-8** (June 2010), pp. 526–534.

[91] D. K. Ferry. "Quantum Mechanics: An Introduction for Device Physicists and Electrical Engineers, Second Edition". CRC Press, 2001. ISBN: 0750307250.

[92] C. Moglestue. "Monte Carlo Simulation of Semiconductor Devices". Springer Netherlands, 1993.

[93] P. Lugli and D. Ferry. "Degeneracy in the ensemble Monte Carlo method for high-field transport in semiconductors". In: *IEEE Transactions on Electron Devices* **32.11** (Nov. 1985), pp. 2431–2437.

[94] J. M. Ziman. "Electrons and Phonons: The Theory of Transport Phenomena in Solids (Oxford Classic Texts in the Physical Sciences)". Oxford University Press, 2001. ISBN: 0198507798.

[95] A. C. S. Algarte and R. Luzzi. "Time evolution of nonequilibrium photoexcited plasma in polar semiconductors". In: *Physical Review B* **27.12** (June 1983), pp. 7563–7574.

[96] W. Cai, M. C. Marchetti, and M. Lax. "Nonequilibrium electron-phonon scattering in semiconductor heterojunctions". In: *Physical Review B* **34.12** (Dec. 1986), pp. 8573–8580.

[97] P. Kocevar. "Hot phonon dynamics". In: *Physica B+C* **134.1-3** (Nov. 1985), pp. 155–163.

[98] B. K. Ridley. "Hot phonons in high-field transport". In: *Semiconductor Science and Technology* **4.12** (Dec. 1989), pp. 1142–1150.

[99] R. Peierls. "Quantum theory of solids". Oxford New York: Clarendon Press Oxford University Press, 2001. ISBN: 9780198507819.

[100] Y. Guo and M. Wang. "Lattice Boltzmann modeling of phonon transport". In: *Journal of Computational Physics* **315** (June 2016), pp. 1–15.

[101] P. L. Bhatnagar, E. P. Gross, and M. Krook. "A Model for Collision Processes in Gases. I. Small Amplitude Processes in Charged and Neutral One-Component Systems". In: *Physical Review* **94.3** (May 1954), pp. 511–525.

[102] Bose. "Plancks Gesetz und Lichtquantenhypothese". In: *Zeitschrift für Physik* **26.1** (Dec. 1924), pp. 178–181.

[103] A. Matulionis et al. "Hot-phonon temperature and lifetime in a biased $Al_xGa_{1-x}N$/GaN channel estimated from noise analysis". In: *Physical Review B* **68.3** (July 2003), p. 035338.

[104] I. Chatzakis et al. "Temperature dependence of the anharmonic decay of optical phonons in carbon nanotubes and graphite". In: *Physical Review B* **83.20** (May 2011), p. 205411.

[105] J. H. Leach et al. "Ultrafast decay of hot phonons in an AlGaN/AlN/AlGaN/GaN camelback channel". In: *Journal of Applied Physics* **110.10** (Nov. 2011), p. 104504.

[106] T. Zushi et al. "Molecular dynamics simulation on LO phonon mode decay in Si nanostructure covered with oxide films". In: "2010 International Conference on Simulation of Semiconductor Processes and Devices". IEEE, Sept. 2010.

[107] T. Ackbarow and M. J. Buehler. "Hierarchical Coexistence of Universality and Diversity Controls Robustness and Multi-Functionality in Protein Materials". In: *Journal of Computational and Theoretical Nanoscience* **5.7** (July 2008), pp. 1193–1204.

[108] M. Ramonas et al. “Hot-phonon effect on power dissipation in a biased $Al_xGa_{1-x}N$/AlN/GaN channel”. In: *Physical Review B* **71.7** (Feb. 2005), p. 075324.

[109] X. Li, B. D. Kong, J. M. Zavada, and K. W. Kim. “Strong substrate effects of Joule heating in graphene electronics”. In: *Applied Physics Letters* **99.23** (Dec. 2011), p. 233114.

[110] V. E. Dorgan, M.-H. Bae, and E. Pop. “Mobility and saturation velocity in graphene on SiO2”. In: *Applied Physics Letters* **97.8** (Aug. 2010), p. 082112.

[111] A. Y. Serov, Z.-Y. Ong, M. V. Fischetti, and E. Pop. “Theoretical analysis of high-field transport in graphene on a substrate”. In: *Journal of Applied Physics* **116.3** (July 2014), p. 034507.

[112] Z. Chen et al. “Thermal contact resistance between graphene and silicon dioxide”. In: *Applied Physics Letters* **95.16** (Oct. 2009), p. 161910.

[113] E. Pop. “Energy dissipation and transport in nanoscale devices”. In: *Nano Research* **3.3** (Mar. 2010), pp. 147–169.

[114] H.-S. P. Wong and D. Akinwande. “Carbon Nanotube and Graphene Device Physics”. Cambridge University Press, 2011. ISBN: 0521519055.

[115] J. W. McClure. “Band Structure of Graphite and de Haas-van Alphen Effect”. In: *Physical Review* **108.3** (Nov. 1957), pp. 612–618.

[116] H. Şahin et al. “Monolayer honeycomb structures of group-IV elements and III-V binary compounds: First-principles calculations”. In: *Physical Review B* **80.15** (Oct. 2009), p. 155453.

[117] H. Aoki and M. S. Dresselhaus. “Physics of Graphene (NanoScience and Technology)”. Springer, 2013. ISBN: 3319026321.

[118] A. H. C. Neto et al. “The electronic properties of graphene”. In: *Reviews of Modern Physics* **81.1** (Jan. 2009), pp. 109–162.

[119] K. S. Novoselov et al. “Two-dimensional gas of massless Dirac fermions in graphene”. In: *Nature* **438.7065** (Nov. 2005), pp. 197–200.

[120] M. Lazzeri, C. Attaccalite, L. Wirtz, and F. Mauri. “Impact of the electron-electron correlation on phonon dispersion: Failure of LDA and GGA DFT functionals in graphene and graphite”. In: *Physical Review B* **78.8** (Aug. 2008), p. 081406.

[121] K. M. Borysenko et al. “First-principles analysis of electron-phonon interactions in graphene”. In: *Physical Review B* **81.12** (Mar. 2010), p. 121412.

[122] W. Kohn. “Image of the Fermi Surface in the Vibration Spectrum of a Metal”. In: *Physical Review Letters* **2.9** (May 1959), pp. 393–394.

[123] S. Piscanec et al. “Kohn Anomalies and Electron-Phonon Interactions in Graphite”. In: *Physical Review Letters* **93.18** (Oct. 2004), p. 185503.

[124] J.-H. Chen et al. “Diffusive charge transport in graphene on SiO2”. In: *Solid State Communications* **149.27-28** (July 2009), pp. 1080–1086.

[125] D. K. Ferry. "Semiconductor Transport". CRC Press, 2000. ISBN: 0748408665.

[126] V. N. Kotov et al. "Electron-Electron Interactions in Graphene: Current Status and Perspectives". In: *Reviews of Modern Physics* **84.3** (July 2012), pp. 1067–1125.

[127] E. H. Hwang and S. D. Sarma. "Acoustic phonon scattering limited carrier mobility in two-dimensional extrinsic graphene". In: *Physical Review B* **77.11** (Mar. 2008), p. 115449.

[128] K. Kaasbjerg, K. S. Thygesen, and K. W. Jacobsen. "Unraveling the acoustic electron-phonon interaction in graphene". In: *Physical Review B* **85.16** (Apr. 2012), p. 165440.

[129] F. Rana et al. "Carrier recombination and generation rates for intravalley and intervalley phonon scattering in graphene". In: *Physical Review B* **79.11** (Mar. 2009), p. 115447.

[130] L. Huang et al. "Ultrafast relaxation of hot optical phonons in monolayer and multilayer graphene on different substrates". In: *Surface Science* **605.17-18** (Sept. 2011), pp. 1657–1661.

[131] H. Wang et al. "Ultrafast relaxation dynamics of hot optical phonons in graphene". In: *Applied Physics Letters* **96.8** (Feb. 2010), p. 081917.

[132] N. Bonini, J. Garg, and N. Marzari. "Acoustic Phonon Lifetimes and Thermal Transport in Free-Standing and Strained Graphene". In: *Nano Letters* **12.6** (May 2012), pp. 2673–2678.

[133] M. Moško, V. Cambel, and A. Mošková. "Electron-electron drag between parallel two-dimensional gases". In: *Physical Review B* **46.8** (Aug. 1992), pp. 5012–5015.

[134] O. Bonno and J.-L. Thobel. "Monte Carlo modeling of carrier-carrier scattering in semiconductors with nonparabolic bands". In: *Journal of Applied Physics* **104.5** (Sept. 2008), p. 053719.

[135] X. Li et al. "Influence of electron-electron scattering on transport characteristics in monolayer graphene". In: *Applied Physics Letters* **97.8** (Aug. 2010), p. 082101.

[136] C. Jang et al. "Tuning the Effective Fine Structure Constant in Graphene: Opposing Effects of Dielectric Screening on Short- and Long-Range Potential Scattering". In: *Physical Review Letters* **101.14** (Oct. 2008), p. 146805.

[137] A. Mošková and M. Moško. "Exchange carrier-carrier scattering of photoexcited spin-polarized carriers in GaAs quantum wells: Monte Carlo study". In: *Physical Review B* **49.11** (Mar. 1994), pp. 7443–7452.

[138] M. Moko and A. Moková. "Ensemble Monte Carlo simulation of electron-electron scattering: Improvements of conventional methods". In: *Physical Review B* **44.19** (Nov. 1991), pp. 10794–10803.

[139] D. Brida et al. "Ultrafast collinear scattering and carrier multiplication in graphene". In: *Nature Communications* **4.1** (June 2013).

[140] A. Tomadin et al. "Nonequilibrium dynamics of photoexcited electrons in graphene: Collinear scattering, Auger processes, and the impact of screening". In: *Physical Review B* **88.3** (July 2013), p. 035430.

[141] M. Trushin. "Collinear scattering of photoexcited carriers in graphene". In: *Physical Review B* **94.20** (Nov. 2016), p. 205306.

[142] C. Sah, T. Ning, and L. Tschopp. "The scattering of electrons by surface oxide charges and by lattice vibrations at the silicon-silicon dioxide interface". In: *Surface Science* **32.3** (Sept. 1972), pp. 561–575.

[143] K. Hess and P. Vogl. "Remote polar phonon scattering in silicon inversion layers". In: *Solid State Communications* **30.12** (June 1979), pp. 797–799.

[144] J. Leburton and G. Dorda. "Remote polar phonon scattering for hot electrons in Si-inversion layers". In: *Solid State Communications* **40.11** (Dec. 1981), pp. 1025–1026.

[145] S. Fratini and F. Guinea. "Substrate-limited electron dynamics in graphene". In: *Physical Review B* **77.19** (May 2008), p. 195415.

[146] V. Perebeinos and P. Avouris. "Inelastic scattering and current saturation in graphene". In: *Physical Review B* **81.19** (May 2010), p. 195442.

[147] A. Konar, T. Fang, and D. Jena. "Effect of high-κgate dielectrics on charge transport in graphene-based field effect transistors". In: *Physical Review B* **82.11** (Sept. 2010), p. 115452.

[148] B. Hu. "Screening-induced surface polar optical phonon scattering in dual-gated graphene field effect transistors". In: *Physica B: Condensed Matter* **461** (Mar. 2015), pp. 118–121.

[149] B. Scharf, V. Perebeinos, J. Fabian, and P. Avouris. "Effects of optical and surface polar phonons on the optical conductivity of doped graphene". In: *Physical Review B* **87.3** (Jan. 2013), p. 035414.

[150] R. Rengel, E. Pascual, and M. J. Martín. "Influence of the substrate on the diffusion coefficient and the momentum relaxation in graphene: The role of surface polar phonons". In: *Applied Physics Letters* **104.23** (June 2014), p. 233107.

[151] F. Stern. "Polarizability of a Two-Dimensional Electron Gas". In: *Physical Review Letters* **18.14** (Apr. 1967), pp. 546–548.

[152] E. H. Hwang and S. D. Sarma. "Dielectric function, screening, and plasmons in two-dimensional graphene". In: *Physical Review B* **75.20** (May 2007), p. 205418.

[153] T. Ando. "Screening Effect and Impurity Scattering in Monolayer Graphene". In: *Journal of the Physical Society of Japan* **75.7** (July 2006), p. 074716.

[154] F. Rana, J. H. Strait, H. Wang, and C. Manolatou. "Ultrafast carrier recombination and generation rates for plasmon emission and absorption in graphene". In: *Physical Review B* **84.4** (July 2011), p. 045437.

[155] Z.-Y. Ong and M. V. Fischetti. "Theory of interfacial plasmon-phonon scattering in supported graphene". In: *Physical Review B* **86.16** (Oct. 2012), p. 165422.

[156] E. H. Hwang and S. D. Sarma. "Screening-induced temperature-dependent transport in two-dimensional graphene". In: *Physical Review B* **79.16** (Apr. 2009), p. 165404.

[157] D.-H. Chae, B. Krauss, K. von Klitzing, and J. H. Smet. "Hot Phonons in an Electrically Biased Graphene Constriction". In: *Nano Letters* **10.2** (Feb. 2010), pp. 466–471.

[158] A. C. Ferrari et al. "Science and technology roadmap for graphene, related two-dimensional crystals, and hybrid systems". In: *Nanoscale* **7.11** (2015), pp. 4598–4810.

[159] D. L. Nika and A. A. Balandin. "Two-dimensional phonon transport in graphene". In: *Journal of Physics: Condensed Matter* **24.23** (May 2012), p. 233203.

[160] D. L. Nika and A. A. Balandin. "Phonons and thermal transport in graphene and graphene-based materials". In: *Reports on Progress in Physics* **80.3** (Jan. 2017), p. 036502.

[161] A. A. Balandin. "Thermal properties of graphene and nanostructured carbon materials". In: *Nature Materials* **10.8** (Aug. 2011), pp. 569–581.

[162] S. Chen et al. "Raman Measurements of Thermal Transport in Suspended Monolayer Graphene of Variable Sizes in Vacuum and Gaseous Environments". In: *ACS Nano* **5.1** (Dec. 2010), pp. 321–328.

[163] W. Cai et al. "Thermal Transport in Suspended and Supported Monolayer Graphene Grown by Chemical Vapor Deposition". In: *Nano Letters* **10.5** (May 2010), pp. 1645–1651.

[164] J. H. Seol et al. "Two-Dimensional Phonon Transport in Supported Graphene". In: *Science* **328.5975** (Apr. 2010), pp. 213–216.

[165] C. J. Glassbrenner and G. A. Slack. "Thermal Conductivity of Silicon and Germanium from 3ºK to the Melting Point". In: *Physical Review* **134.4A** (May 1964), A1058–A1069.

[166] J. Yu et al. "Graphene-on-Diamond Devices with Increased Current-Carrying Capacity: Carbon sp2-on-sp3 Technology". In: *Nano Letters* **12.3** (Feb. 2012), pp. 1603–1608.

[167] T. E. Beechem et al. "Self-Heating and Failure in Scalable Graphene Devices". In: *Scientific Reports* **6.1** (June 2016).

[168] Z. Yan, G. Liu, J. M. Khan, and A. A. Balandin. "Graphene quilts for thermal management of high-power GaN transistors". In: *Nature Communications* **3.1** (Jan. 2012).

[169] N. Sano, M. Tomizawa, and A. Yoshii. "Monte Carlo Analysis of Hot Electron Transport and Impact Ionization in Silicon". In: *Japanese Journal of Applied Physics* **30.Part 1, No. 12B** (Dec. 1991), pp. 3662–36665.

[170] X. F. Wang, I. C. da Cunha Lima, X. L. Lei, and A. Troper. "Hot-electron transport and impact ionization process inHg0.8Cd0.2Te". In: *Physical Review B* **58.7** (Aug. 1998), pp. 3529–3532.

[171] I. N. Volovichev, G. N. Logvinov, O. Y. Titov, and Y. G. Gurevich. "Recombination and lifetimes of charge carriers in semiconductors". In: *Journal of Applied Physics* **95.8** (Apr. 2004), pp. 4494–4496.

[172] K. Yeom, J. M. Hinckley, and J. Singh. "Calculation of electron and hole impact ionization coefficients in SiGe alloys". In: *Journal of Applied Physics* **80.12** (Dec. 1996), pp. 6773–6782.

[173] W. Shockley. “Problems related to p-n junctions in silicon”. In: *Solid-State Electronics* **2.1** (Jan. 1961), pp. 35–67.

[174] J. Y. Tang and K. Hess. “Impact ionization of electrons in silicon (steady state)”. In: *Journal of Applied Physics* **54.9** (Sept. 1983), pp. 5139–5144.

[175] L. V. Keldysh. “Kinetic Theory of Impact Ionization in Semiconductors”. In: *Soviet Physics: Journal of Theoretical and Experimental Physics* **10.3** (Mar. 1960), p. 509.

[176] L. V. Keldysh. “Concerning the Theory of Impact Ionization in Semiconductors”. In: *Soviet Physics: Journal of Theoretical and Experimental Physics* **21.6** (Mar. 1965), p. 1135.

[177] R. Thoma et al. “An improved impact-ionization model for high-energy electron transport in Si with Monte Carlo simulation”. In: *Journal of Applied Physics* **69.4** (Feb. 1991), pp. 2300–2311.

[178] M. Ershov and V. Ryzhii. “Temperature dependence of the electron impact ionization coefficient in silicon”. In: *Semiconductor Science and Technology* **10.2** (Feb. 1995), pp. 138–142.

[179] J. Bude and K. Hess. “Thresholds of impact ionization in semiconductors”. In: *Journal of Applied Physics* **72.8** (Oct. 1992), pp. 3554–3561.

[180] M. J. Martin, T. Gonzalez, J. E. Velazquez, and D. Pardo. “Simulation of electron transport in silicon: impact-ionization processes”. In: *Semiconductor Science and Technology* **8.7** (July 1993), pp. 1291–1297.

[181] J. Marsland. “A lucky drift model, including a soft threshold energy, fitted to experimental measurements of ionization coefficients”. In: *Solid-State Electronics* **30.1** (Jan. 1987), pp. 125–132.

[182] S. Al-Kamiyani and T. Mohiuddin. “Improved control in elimination of white impurities on graphene by chemical vapor deposition (CVD)”. In: *AIP Advances* **8.12** (Dec. 2018), p. 125325.

[183] K. M. Burson et al. “Direct Imaging of Charged Impurity Density in Common Graphene Substrates”. In: *Nano Letters* **13.8** (Aug. 2013), pp. 3576–3580.

[184] S. Adam, E. H. Hwang, V. M. Galitski, and S. D. Sarma. “A self-consistent theory for graphene transport”. In: *Proceedings of the National Academy of Sciences* **104.47** (Nov. 2007), pp. 18392–18397.

[185] G. Xu et al. “Variability Effects in Graphene: Challenges and Opportunities for Device Engineering and Applications”. In: *Proceedings of the IEEE* **101.7** (July 2013), pp. 1670–1688.

[186] Y. Zhang et al. “Origin of spatial charge inhomogeneity in graphene”. In: *Nature Physics* **5.10** (Aug. 2009), pp. 722–726.

[187] G. M. Rutter et al. “Scattering and Interference in Epitaxial Graphene”. In: *Science* **317.5835** (July 2007), pp. 219–222.

[188] Z. H. Ni et al. "On Resonant Scatterers As a Factor Limiting Carrier Mobility in Graphene". In: *Nano Letters* **10.10** (Oct. 2010), pp. 3868–3872.

[189] W. Gannett et al. "Boron nitride substrates for high mobility chemical vapor deposited graphene". In: *Applied Physics Letters* **98.24** (June 2011), p. 242105.

[190] M. A. Yamoah, W. Yang, E. Pop, and D. Goldhaber-Gordon. "High-Velocity Saturation in Graphene Encapsulated by Hexagonal Boron Nitride". In: *ACS Nano* **11.10** (Sept. 2017), pp. 9914–9919.

[191] I. Meric et al. "Graphene Field-Effect Transistors Based on Boron-Nitride Dielectrics". In: *Proceedings of the IEEE* **101.7** (July 2013), pp. 1609–1619.

[192] P. C. Feijoo et al. "Radio Frequency Performance Projection and Stability Tradeoff of h-BN Encapsulated Graphene Field-Effect Transistors". In: *IEEE Transactions on Electron Devices* **66.3** (Mar. 2019), pp. 1567–1573.

[193] P. C. Feijoo et al. "Scaling of graphene field-effect transistors supported on hexagonal boron nitride: radio-frequency stability as a limiting factor". In: *Nanotechnology* **28.48** (Nov. 2017), p. 485203.

[194] D. Caughey and R. Thomas. "Carrier mobilities in silicon empirically related to doping and field". In: *Proceedings of the IEEE* **55.12** (1967), pp. 2192–2193.

[195] F. Joucken, J.-F. Colomer, R. Sporken, and N. Reckinger. "Structural and electronic characterization of graphene grown by chemical vapor deposition and transferred onto sapphire". In: *Applied Surface Science* **378** (Aug. 2016), pp. 397–401.

[196] C. Fernandez et al. "On the effective mobility extraction by point-contact techniques on silicon-on-insulator substrates". In: *Journal of Applied Physics* **117.3** (Jan. 2015), p. 035707.

[197] S. Cristoloveanu and S. Williams. "Point-contact pseudo-MOSFET for in-situ characterization of as-grown silicon-on-insulator wafers". In: *IEEE Electron Device Letters* **13.2** (Feb. 1992), pp. 102–104.

[198] C. Fernández. "Application of the Pseudo-MOSFET Technique on Silicon-On-Insulator Wafers". Doctoral thesis. Universidad de Granada, 2016. ISBN: 9788491630104.

[199] D. K. Schroder. "Semiconductor Material and Device Characterization". Wiley-IEEE Press, 2015. ISBN: 0471739065.

[200] E. Pop, R. W. Dutton, and K. E. Goodson. "Monte Carlo simulation of Joule heating in bulk and strained silicon". In: *Applied Physics Letters* **86.8** (Feb. 2005), p. 082101.

[201] E. Pop and K. E. Goodson. "Thermal Phenomena in Nanoscale Transistors". In: *Journal of Electronic Packaging* **128.2** (2006), p. 102.

[202] M. Freitag et al. "Energy Dissipation in Graphene Field-Effect Transistors". In: *Nano Letters* **9.5** (May 2009), pp. 1883–1888.

[203] Y. Yin et al. "Graphene, a material for high temperature devices - intrinsic carrier density, carrier drift velocity and lattice energy". In: *Scientific Reports* **4.1** (July 2014).

[204] J. Liberis et al. "Hot-phonon temperature and lifetime in biased boron-implanted $SiO_2/Si/SiO_2$ channels". In: *Semiconductor Science and Technology* **21.6** (May 2006), pp. 803–807.

[205] K. J. Tielrooij et al. "Photoexcitation cascade and multiple hot-carrier generation in graphene". In: *Nature Physics* **9.4** (Feb. 2013), pp. 248–252.

[206] A. Satou, V. Ryzhii, and T. Otsuji. "Effects of carrier-carrier scattering on population inversion in graphene under pulse photoexcitation". In: *Journal of Physics: Conference Series* **584** (Jan. 2015), p. 012018.

[207] R. Kim, V. Perebeinos, and P. Avouris. "Relaxation of optically excited carriers in graphene". In: *Physical Review B* **84.7** (Aug. 2011), p. 075449.

[208] T. Winzer, A. Knorr, and E. Malic. "Carrier Multiplication in Graphene". In: *Nano Letters* **10.12** (Dec. 2010), pp. 4839–4843.

[209] E. Malic, T. Winzer, F. Wendler, and A. Knorr. "Review on carrier multiplication in graphene". In: *physica status solidi (b)* **253.12** (Oct. 2016), pp. 2303–2310.

[210] I. Gierz et al. "Tracking Primary Thermalization Events in Graphene with Photoemission at Extreme Time Scales". In: *Physical Review Letters* **115.8** (Aug. 2015), p. 086803.

[211] L. Pirro, A. Girdhar, Y. Leblebici, and J.-P. Leburton. "Impact ionization and carrier multiplication in graphene". In: *Journal of Applied Physics* **112.9** (Nov. 2012), p. 093707.

[212] E. Kim et al. "Exploring carrier transport phenomena in a CVD-assembled graphene FET on hexagonal boron nitride". In: *Nanotechnology* **23.12** (Mar. 2012), p. 125706.

[213] L. Zheng et al. "Property transformation of graphene with Al_2O_3 films deposited directly by atomic layer deposition". In: *Applied Physics Letters* **104.2** (Jan. 2014), p. 023112.

[214] K. S. Novoselov et al. "A roadmap for graphene". In: *Nature* **490.7419** (Oct. 2012), pp. 192–200.

[215] F. Schwierz. "Graphene transistors". In: *Nature Nanotechnology* **5.7** (May 2010), pp. 487–496.

[216] X. Yang et al. "Graphene Ambipolar Multiplier Phase Detector". In: *IEEE Electron Device Letters* **32.10** (Oct. 2011), pp. 1328–1330.

[217] L. Liao et al. "High-speed graphene transistors with a self-aligned nanowire gate". In: *Nature* **467.7313** (Sept. 2010), pp. 305–308.

[218] L. Liao et al. "Sub-100 nm Channel Length Graphene Transistors". In: *Nano Letters* **10.10** (Oct. 2010), pp. 3952–3956.

[219] J. Zheng et al. "Sub-10 nm Gate Length Graphene Transistors: Operating at Terahertz Frequencies with Current Saturation". In: *Scientific Reports* **3.1** (Feb. 2013).

[220] G. Iannaccone, A. Betti, and G. Fiori. "Noise in graphene and carbon nanotube devices". In: "Noise and Fluctuations (ICNF), 2011 21st International Conference on". June 2011, pp. 360–363.

[221] B. Pellegrini. “1/f noise in graphene”. In: *The European Physical Journal B* **86.9** (Sept. 2013).

[222] I. Heller et al. “Charge Noise in Graphene Transistors”. In: *Nano Letters* **10.5** (May 2010), pp. 1563–1567.

[223] Y. Zhang, E. E. Mendez, and X. Du. “Mobility-Dependent Low-Frequency Noise in Graphene Field-Effect Transistors”. In: *ACS Nano* **5.10** (Sept. 2011), pp. 8124–8130.

[224] J. S. Moon et al. “Low-Phase-Noise Graphene FETs in Ambipolar RF Applications”. In: *IEEE Electron Device Letters* **32.3** (Mar. 2011), pp. 270–272.

[225] M. A. Stolyarov et al. “Suppression of 1/f noise in near-ballistic h-BN-graphene-h-BN heterostructure field-effect transistors”. In: *Applied Physics Letters* **107.2** (July 2015), p. 023106.

[226] L. Ardaravicˇius et al. “High frequency noise of epitaxial graphene grown on sapphire”. In: *physica status solidi (RRL) - Rapid Research Letters* **7.5** (Apr. 2013), pp. 348–351.

[227] D. Mele et al. “High frequency noise characterisation of graphene FET device”. In: “Microwave Symposium Digest (IMS), 2013 IEEE MTT-S International”. June 2013, pp. 1–4.

[228] M. Tanzid, M. A. Andersson, J. Sun, and J. Stake. “Microwave noise characterization of graphene field effect transistors”. In: *Applied Physics Letters* **104.1** (Jan. 2014), p. 013502.

[229] M. Pospieszalski. “Modeling of noise parameters of MESFETs and MODFETs and their frequency and temperature dependence”. In: *IEEE Transactions on Microwave Theory and Techniques* **37.9** (1989), pp. 1340–1350.

[230] M. Andersson, O. Habibpour, J. Vukusic, and J. Stake. “Noise figure characterization of a subharmonic graphene FET mixer”. In: “Microwave Symposium Digest (MTT), 2012 IEEE MTT-S International”. June 2012, pp. 1–3.

[231] L. Varani et al. “A model noise temperature for nonlinear transport in semiconductors”. In: *Journal of Applied Physics* **80.9** (Nov. 1996), pp. 5067–5075.

[232] L. Reggiani et al. “Modelling of small-signal response and electronic noise in semiconductor high-field transport”. In: *Semiconductor Science and Technology* **12.2** (Feb. 1997), pp. 141–156.

[233] E. Starikov et al. “Monte Carlo calculations of static and dynamic electron transport in nitrides”. In: *Journal of Applied Physics* **98.8** (Oct. 2005), p. 083701.

[234] C. Jacoboni and P. Lugli. “The Monte Carlo Method for Semiconductor Device Simulation (Computational Microelectronics)”. Springer, 2002. ISBN: 3211821104.

[235] K. van Vliet and A. van der Ziel. “The quantum correction of the Einstein relation for high frequencies”. In: *Solid-State Electronics* **20.11** (Nov. 1977), pp. 931–933.

[236] L. D. Landau and E. M. Lifshitz. “Statistical Physics: Volume 5”. Butterworth-Heinemann, 2013. ISBN: 9780080570464.

[237] J.-P. Nougier. "Fluctuations and noise of hot carriers in semiconductor materials and devices". In: *IEEE Transactions on Electron Devices* **41.11** (1994), pp. 2034–2049.

[238] J. L. Thobel, A. Sleiman, and R. Fauquembergue. "Determination of diffusion coefficients in degenerate electron gas using Monte Carlo simulation". In: *Journal of Applied Physics* **82.3** (Aug. 1997), pp. 1220–1226.

[239] P. Borowik and J. L. Thobel. "Monte Carlo method for the investigation of electron diffusion in degenerate semiconductors". In: *Journal of Applied Physics* **87.1** (Jan. 2000), pp. 329–333.

[240] R. Rengel and M. J. Martín. "Diffusion coefficient, correlation function, and power spectral density of velocity fluctuations in monolayer graphene". In: *Journal of Applied Physics* **114.14** (Oct. 2013), p. 143702.

[241] P. J. Price. "On the calculation of differential mobility". In: *Journal of Applied Physics* **54.6** (June 1983), pp. 3616–3617.

[242] J. D. Buron et al. "Graphene mobility mapping". In: *Scientific Reports* **5.1** (July 2015).

[243] P. Shiktorov et al. "Noise temperature of $n+$ $nn+$ GaAs structures". In: *Physical Review B* **54.12** (Sept. 1996), pp. 8821–8832.

[244] R. Brunetti and C. Jacoboni. "Analysis of the stationary and transient autocorrelation function in semiconductors". In: *Physical Review B* **29.10** (May 1984), pp. 5739–5748.

[245] R. Brunetti and C. Jacoboni. "Diagonal and Off-Diagonal Contributions to Autocorrelation of Velocity Fluctuations in Semiconductors". In: *Physical Review Letters* **50.15** (Apr. 1983), pp. 1164–1167.

[246] T. G. Sánchez, J. E. V. Pérez, P. M. G. Conde, and D. P. Collantes. "Monte Carlo analysis of the transient spectral density of velocity fluctuations in semiconductors". In: *Applied Physics Letters* **60.5** (Feb. 1992), pp. 613–615.

[247] M. Tonouchi. "Cutting-edge terahertz technology". In: *Nature Photonics* **1.2** (Feb. 2007), pp. 97–105.

[248] P. Jepsen, D. Cooke, and M. Koch. "Terahertz spectroscopy and imaging - Modern techniques and applications". In: *Laser & Photonics Reviews* **5.1** (Oct. 2010), pp. 124–166.

[249] K. Tanaka, H. Hirori, and M. Nagai. "THz Nonlinear Spectroscopy of Solids". In: *IEEE Transactions on Terahertz Science and Technology* **1.1** (Sept. 2011), pp. 301–312.

[250] B. Sensale-Rodriguez et al. "Broadband graphene terahertz modulators enabled by intraband transitions". In: *Nature Communications* **3.1** (Jan. 2012).

[251] N. Orihashi, S. Suzuki, and M. Asada. "One THz harmonic oscillation of resonant tunneling diodes". In: *Applied Physics Letters* **87.23** (Dec. 2005), p. 233501.

[252] K. Y. Xu, X. F. Lu, A. M. Song, and G. Wang. "Terahertz harmonic generation using a planar nanoscale unipolar diode at zero bias". In: *Applied Physics Letters* **92.16** (Apr. 2008), p. 163503.

[253] M. F. Pereira et al. "Theory and measurements of harmonic generation in semiconductor superlattices with applications in the 100 GHz to 1 THz range". In: *Physical Review B* **96**.**4** (July 2017), p. 045306.

[254] N. Yoshikawa, T. Tamaya, and K. Tanaka. "High-harmonic generation in graphene enhanced by elliptically polarized light excitation". In: *Science* **356**.**6339** (2017), pp. 736–738.

[255] M. J. Paul et al. "High-field terahertz response of graphene". In: *New Journal of Physics* **15**.**8** (Aug. 2013), p. 085019.

[256] J. D. Cox, A. Marini, and F. J. G. de Abajo. "Plasmon-assisted high-harmonic generation in graphene". In: *Nature Communications* **8** (Feb. 2017), p. 14380.

[257] P. Shiktorov et al. "Monte Carlo calculation of electronic noise under high-order harmonic generation". In: *Applied Physics Letters* **80**.**25** (June 2002), pp. 4759–4761.

[258] P. Shiktorov et al. "Monte carlo simulation of threshold bandwidth for high-order harmonic extraction". In: *IEEE Transactions on Electron Devices* **50**.**5** (May 2003), pp. 1171–1178.

[259] R. R. Nair et al. "Fine Structure Constant Defines Visual Transparency of Graphene". In: *Science* **320**.**5881** (June 2008), pp. 1308–1308.

[260] F. Wang. "Intraband Optical Transitions in Graphene". In: "CLEO:2011 - Laser Applications to Photonic Applications". OSA, 2011.

[261] A. Marini, J. D. Cox, and F. J. G. de Abajo. "Theory of graphene saturable absorption". In: *Physical Review B* **95**.**12** (Mar. 2017), p. 125408.

[262] V. Ryzhii et al. "Terahertz lasers based on optically pumped multiple graphene structures with slot-line and dielectric waveguides". In: *Journal of Applied Physics* **107**.**5** (Mar. 2010), p. 054505.

[263] X. Cai et al. "Sensitive room-temperature terahertz detection via the photothermoelectric effect in graphene". In: *Nature Nanotechnology* **9**.**10** (Sept. 2014), pp. 814–819.

[264] P. A. George et al. "Ultrafast Optical-Pump Terahertz-Probe Spectroscopy of the Carrier Relaxation and Recombination Dynamics in Epitaxial Graphene". In: *Nano Letters* **8**.**12** (Dec. 2008), pp. 4248–4251.

[265] E. Malic, T. Winzer, E. Bobkin, and A. Knorr. "Microscopic theory of absorption and ultrafast many-particle kinetics in graphene". In: *Physical Review B* **84**.**20** (Nov. 2011), p. 205406.

[266] K.-C. Lin et al. "Ultrafast dynamics of hot electrons and phonons in chemical vapor deposited graphene". In: *Journal of Applied Physics* **113**.**13** (Apr. 2013), p. 133511.

[267] S. Winnerl et al. "Time-resolved spectroscopy on epitaxial graphene in the infrared spectral range: relaxation dynamics and saturation behavior". In: *Journal of Physics: Condensed Matter* **25**.**5** (Jan. 2013), p. 054202.

[268] M. Breusing et al. "Ultrafast nonequilibrium carrier dynamics in a single graphene layer". In: *Physical Review B* **83.15** (Apr. 2011), p. 153410.

[269] S. Butscher et al. "Hot electron relaxation and phonon dynamics in graphene". In: *Applied Physics Letters* **91.20** (Nov. 2007), p. 203103.

[270] E. Sano. "Monte Carlo Simulation of Ultrafast Electron Relaxation in Graphene". In: *Applied Physics Express* **4.8** (July 2011), p. 085101.

[271] B. Y. Sun, Y. Zhou, and M. W. Wu. "Dynamics of photoexcited carriers in graphene". In: *Physical Review B* **85.12** (Mar. 2012), p. 125413.

[272] T. Winzer and E. Malic. "The impact of pump fluence on carrier relaxation dynamics in optically excited graphene". In: *Journal of Physics: Condensed Matter* **25.5** (Jan. 2013), p. 054201.

[273] T. Low et al. "Cooling of photoexcited carriers in graphene by internal and substrate phonons". In: *Physical Review B* **86.4** (July 2012), p. 045413.

[274] I. Gierz et al. "Snapshots of non-equilibrium Dirac carrier distributions in graphene". In: *Nature Materials* **12.12** (Oct. 2013), pp. 1119–1124.

[275] M. Breusing, C. Ropers, and T. Elsaesser. "Ultrafast Carrier Dynamics in Graphite". In: *Physical Review Letters* **102.8** (Feb. 2009), p. 086809.

[276] B. Gao et al. "Studies of Intrinsic Hot Phonon Dynamics in Suspended Graphene by Transient Absorption Microscopy". In: *Nano Letters* **11.8** (Aug. 2011), pp. 3184–3189.

[277] L. Huang et al. "Ultrafast Transient Absorption Microscopy Studies of Carrier Dynamics in Epitaxial Graphene". In: *Nano Letters* **10.4** (Apr. 2010), pp. 1308–1313.

[278] A. Grüneis et al. "Inhomogeneous optical absorption around the K point in graphite and carbon nanotubes". In: *Physical Review B* **67.16** (Apr. 2003), p. 165402.

[279] Ó. Zurrón, A. Picón, and L. Plaja. "Theory of high-order harmonic generation for gapless graphene". In: *New Journal of Physics* **20.5** (May 2018), p. 053033.

[280] Ó. Zurrón-Cifuentes et al. "Optical anisotropy of non-perturbative high-order harmonic generation in gapless graphene". In: *Optics Express* **27.5** (Mar. 2019), p. 7776.

[281] R. D. Schaller, J. M. Pietryga, and V. I. Klimov. "Carrier Multiplication in InAs Nanocrystal Quantum Dots with an Onset Defined by the Energy Conservation Limit". In: *Nano Letters* **7.11** (Nov. 2007), pp. 3469–3476.

[282] J.-J. Chen et al. "Photovoltaic Effect and Evidence of Carrier Multiplication in Graphene Vertical Homojunctions with Asymmetrical Metal Contacts". In: *ACS Nano* **9.9** (Aug. 2015), pp. 8851–8858.

[283] F. E. Lytle, R. M. Parrish, and W. T. Barnes. "An Introduction to Time-Resolved Pump/Probe Spectroscopy". In: *Applied Spectroscopy* **39.3** (May 1985), pp. 444–451.

[284] O. Kühn and S. Lochbrunner. "Ultrafast Spectroscopy". In: *digital Encyclopedia of Applied Physics*. American Cancer Society, 2009, pp. 769–815. ISBN: 9783527600434. eprint: `https://onlinelibrary.wiley.com/doi/pdf/10.1002/3527600434.eap545.pub3`.

[285] L. M. Malard et al. "Observation of intra- and inter-band transitions in the transient optical response of graphene". In: *New Journal of Physics* **15**.**1** (Jan. 2013), p. 015009.

[286] K. F. Mak, L. Ju, F. Wang, and T. F. Heinz. "Optical spectroscopy of graphene: From the far infrared to the ultraviolet". In: *Solid State Communications* **152**.**15** (Aug. 2012), pp. 1341–1349.

[287] J. Horng et al. "Drude conductivity of Dirac fermions in graphene". In: *Physical Review B* **83**.**16** (Apr. 2011), p. 165113.

[288] J. H. Scofield. "Frequency-domain description of a lock-in amplifier". In: *American Journal of Physics* **62**.**2** (Feb. 1994), pp. 129–133.

[289] J. Bolger et al. "Nondegenerate two-photon absorption spectra of ZnSe, ZnS and ZnO". In: *Optics Communications* **97**.**3-4** (Mar. 1993), pp. 203–209.

[290] J. M. Dawlaty et al. "Measurement of ultrafast carrier dynamics in epitaxial graphene". In: *Applied Physics Letters* **92**.**4** (Jan. 2008), p. 042116.

[291] S. A. Thiele, J. A. Schaefer, and F. Schwierz. "Modeling of graphene metal-oxide-semiconductor field-effect transistors with gapless large-area graphene channels". In: *Journal of Applied Physics* **107**.**9** (May 2010), p. 094505.

[292] S. Thiele and F. Schwierz. "Modeling of the steady state characteristics of large-area graphene field-effect transistors". In: *Journal of Applied Physics* **110**.**3** (Aug. 2011), p. 034506.

[293] I. Meric et al. "Current saturation in zero-bandgap, top-gated graphene field-effect transistors". In: *Nature Nanotechnology* **3**.**11** (Sept. 2008), pp. 654–659.

[294] G. I. Zebrev, A. A. Tselykovskiy, and V. O. Turin. "Physics-based compact modeling of double-gate graphene field-effect transistor operation". In: "2012 28th International Conference on Microelectronics Proceedings". IEEE, May 2012.

[295] I. Meric, N. Baklitskaya, P. Kim, and K. L. Shepard. "RF performance of top-gated, zero-bandgap graphene field-effect transistors". In: "2008 IEEE International Electron Devices Meeting". IEEE, Dec. 2008.

[296] J. G. Champlain. "A first principles theoretical examination of graphene-based field effect transistors". In: *Journal of Applied Physics* **109**.**8** (Apr. 2011), p. 084515.

[297] Y. Wu et al. "Three-Terminal Graphene Negative Differential Resistance Devices". In: *ACS Nano* **6**.**3** (Feb. 2012), pp. 2610–2616.

[298] M. Lemme et al. "Mobility in graphene double gate field effect transistors". In: *Solid-State Electronics* **52**.**4** (Apr. 2008), pp. 514–518.

[299] N. Lu, L. Wang, L. Li, and M. Liu. "A review for compact model of graphene field-effect transistors". In: *Chinese Physics B* **26**.**3** (Mar. 2017), p. 036804.

[300] T. Fang, A. Konar, H. Xing, and D. Jena. "Carrier statistics and quantum capacitance of graphene sheets and ribbons". In: *Applied Physics Letters* **91**.**9** (Aug. 2007), p. 092109.

Appendices

Appendix A

Details on the implementation of carrier scattering interactions in the EMC simulator

In this appendix the implementation of carrier-carrier interactions in monolayer graphene for the ensemble Monte Carlo simulator will be covered in order to offer a complete understanding of such topics introduced in section 2.4.

A.1 Physical parameters

A.1.1 General MLG parameters

Quantity	**Description**	**Value**
ρ_{m}	Mass sheet density	$7.6\,\mathrm{kg/m^2}$
v_F	Fermi velocity	$10^6\,\mathrm{m/s}$
d_{VdW}	Van der Waals separation with the substrates	$4\,\text{Å}$

Table A.1: General physical parameters of monolayer graphene.

A.1.2 Intrinsic phonons

Phonon interaction	Type	$D_{type,\nu}$ (see caption)	$\hbar\omega_\nu(\mathbf{q}_0)$ (meV)	v_ν (10^4 m/s)	τ_ν (ps)	Refs.
TA/LA-Γ	D_1	6.8		2		[128]
TA/LA-K	D_0	35	124		5	[121, 132]
TO-K/LO-Γ	D_0	100	164.5		2.5	[121, 131]

Table A.2: Parameters for the intrinsic phonon scattering in monolayer graphene in the deformation potential approximation. The deformation potential in the third column can refer to the first-order deformation potential (D_1, for elastic phonon collisions) whose units are eV, or to the zeroth-order deformation potential (D_0, for inelastic phonon interactions), which units are given in eV/nm.

A.1.3 Dielectric substrates

In the following table we summarize the relevant physical parameters for the model.

Dielectric	ϵ_0	ϵ_∞	$\hbar\omega_{\mathrm{SPP}_1}$ (meV)	$\hbar\omega_{\mathrm{SPP}_2}$ (meV)
SiO$_2$	3.9	2.5	59.98	146.51
h-BN	5.09	4.1	101.7	195.7
SiC	9.7	6.5	116.0	–
HfO$_2$	22.0	5.03	19.42	52.87
Al$_2$O$_3$	12.53	3.2	55.01	94.29

Table A.3: Relevant parameters for the definition of surface polar optical phonons of a dielectric substrate as seen in section 2.4.6. Data taken from [147].

A.2 EMC treatment of carrier-carrier interactions

Dealing with two-particle interactions supposes a complex task to deal with in an ensemble Monte Carlo model. In this section the approach employed to implement these effects is explained with detail from the final equations presented in section 2.4.3.

A.2.1 Intraband scattering

We are interested in obtaining an expression for carrier-carrier scattering based on the energy of the particle. With such purpose we take equation (2.63) as an starting point. Computing an accurate scattering rate is a computational power and time-demanding task, so some simplifications are made. First, it is observed that maximum probabilities $\int_0^{2\pi} \Xi(s, \mathbf{k}, s_2, \mathbf{k}'_2, \theta')\, d\theta'$ are achieved when the angle between $\mathbf{k}$ and $\mathbf{k_2}$ is $(1 - ss_2)\pi/2$. Also, for a particular magnitude of $\mathbf{k}$, the scattering probability increases with the modulus of $\mathbf{k_2}$. We, then, select a $k_2 \sim k_{\mathrm{MAX}}$ magnitude sufficiently large (usually at the edge of the simulated energies $k_{\mathrm{MAX}} = \varepsilon_{\mathrm{MAX}}/\hbar v_F$) and, instead of performing the calculation of the scattering rate weighted over each state occupation, we calculate a magnified probability as:

$$\tilde{\Gamma}^{(\mathrm{MLG})}_{\text{c-c}}(\varepsilon) = \frac{\Omega^2}{(2\pi)^2} N P(\pm s > 0)\xi \int_0^{2\pi} \Xi\left[\mathrm{sign}(\varepsilon); \left(\frac{|\varepsilon|}{\hbar v_F}, 0\right), \pm\mathrm{sign}(\varepsilon), (\mp k_{\mathrm{MAX}}, 0), \theta'\right] d\theta', \tag{A.1}$$

where with $NP(\pm s > 0)\xi$ we are counting for the total electron $(+s > 0)$ or hole $(-s > 0)$ densities according to the sub-band, s where they are, $+(-)\text{sign}(\varepsilon)$ stands for intraband (interband) interactions, and the vector $(\mp k_{\text{MAX}}, 0)$ is the maximum length of the wavevector under consideration with the opposite (for intraband) and same (for interband) interactions. This way it is assumed that all the particles are occupying the same (*overoccupied*) state and therefore that all would interact with such maximum probability.

This way, we have avoided performing the integral over all the reciprocal space, saving calculation time. On the other hand, this is done at the expense of obtaining a larger scattering probability. This involves more frequent selection of interband carrier-carrier interactions, some of which should not take place. Therefore, when a carrier-carrier scattering event is selected, a random particle from the congruent ensemble (electrons or holes) is randomly chosen, being its sub-band s_2 and wavevector $\mathbf{k}_2$. Then, the total probability $\int_0^{2\pi} \Xi(s, \mathbf{k}, s_2, \mathbf{k}_2, \theta')\, d\theta'$ is compared against the maximized probability from equation (A.1) in a Monte Carlo rejection procedure. Finally, the final states for the two particles are set by selecting the appropriate final angle of the triggering particle, θ', according to the probability distribution of $\Xi(s, \mathbf{k}, s_2, \mathbf{k}_2, \theta')$.

A.2.2 Auger processes

The inclusion of collinear events in the EMC simulator is a complex task. We part from equation (2.66), which gives the probability of a triggering particle of energy ε to interact in the collinear limit with all possible mating particles at energies ε_2, regardless on the type of interaction (impact ionization or Auger recombination). However, we are interesting in separating the different contributions, differentiating between all the mechanisms depicted in 2.7. Moreover, in the EMC simulator it is neccesary to distinguish between the triggering and mating particle. Consequently all the cases depicted in figure 2.7 particle splint into the eight cases shown in figure A.1 (a) to (h). In the first row –figures A.1 (a) to (d)– we have the impact ionization collisions, while on the second row –figures A.1 (e) to (h)–, there are the Auger processes. In the first two columns, the two interacting carriers initially lie in the same band, while on the third and fourth, the two carriers belong to initial states in conduction and valence band. The final distinction in the EMC regards which particle (the one that triggers the mechanisms or the one that is selected) is doing the interband transition, being the triggering particle the one switching band in the first and third column, and the mating particle in the second and fourth.

A simulation framework dealing with an electron and hole description for carriers in the conduction and valence bands respectively implies that the only-electron view of the

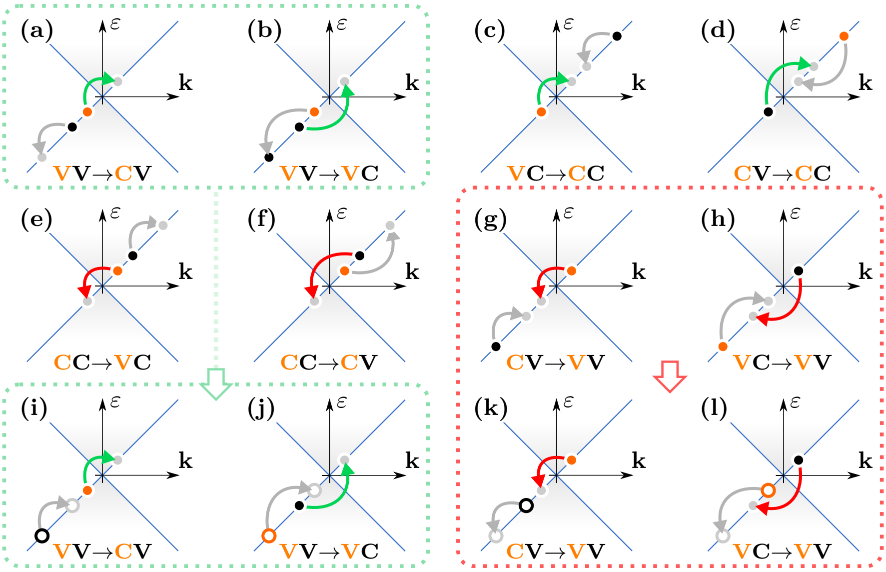

Figure A.1: (a) to (h) Different collinear events as seen from an *"only-electrons"* perspective: (a) to (d) represent impact ionization transititions, and (e) to (h) impact Aguer recombination mechanisms. The cases on the left –(a), (b), (e) and (f)– involve two electrons that lie in the same band, while those on the right –(c), (d), (g) and (h)– involve two electrons in different bands. Equivalent transitions –for example, (a) and (b)– are considered distinctly from the EMC perspective according to the particle which is triggering the event, which is depicted in orange, while the mating electron is black. The four cases on the bottom row represent the EMC treatment of the particles considering a system of electrons and holes in the simulator, corresponding (i) to (a), (j) to (b), (k) to (g), and (l) to (h).

Auger interactions presented can not be carried out as depicted in figures A.1 (a) to (h). Instead, electron-hole collinear interactions should be considered in the cases (a), (b), (g), and (h). In these cases, instead of the electron in the valence band, we consider a hole that performs the complementary (opposite) transition, as depicted in figures A.1 (i), (j), (k), and (l). According to this, the probabilities for each case are computed as in (2.66) and the occupation function $f(\varepsilon_2)$ is that of the kind of particle that must be chosen for the interaction. On the cases where an electron on the valence band travels to the conduction band, like in figures A.1 (g) and (h), these electrons are created upon the assumption of the absence of a hole, and $f(\varepsilon_2)$ is always taken as 1.

Equation (2.66) supposes a isotropic carrier distribution. However, in this PhD thesis, out-of-equilibrium phenomena has been in the spotlight. In order to correctly deal with this circumstance, the collinear scattering probabilities are updated every time step according to the updated distribution function. However, this can change even along a

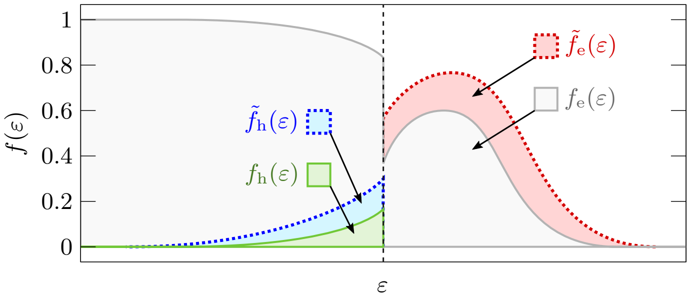

Figure A.2: Illustration of the enhanced carrier occupation for the calculation of collinear scattering rate. Electron and hole distribution functions are computed separately in order to be included in equation (2.66) according to the type of transition.

single time step.

To let the model correctly capture the out-of-equilibrium state of the system, instead of $f(\varepsilon_2)$, an enhanced occupation is considered. We achieve this by a convolution of the instantaneous distribution:

$$\tilde{f}_{\mathrm{e,h}}(\varepsilon, t') = \min\left\{1, \int_{-\infty}^{\infty} f_{\mathrm{e,h}}(\varepsilon, t-\Delta t) C_{\tilde{f}} \exp\left[\frac{(\varepsilon-\varepsilon')^2}{2\sigma_{\tilde{f}}}\right] d\varepsilon'\right\}, \tag{A.2}$$

where $\sigma_{\tilde{f}}$ and $C_{\tilde{f}}$ are parameters set so that $\tilde{f}$ is somewhat greater than f, as illustrated in figure A.2. Considering this enhanced occupation function, a scattering probability higher than that corresponding to the real distribution function is obtained. Therefore, when a collinear scattering event is selected a rejection step must be added in order to correct this overestimation. When a collinear event is selected in the standard Monte Carlo work flow, the following succession of events takes place. First, the energy of the mating particle chosen according to the distribution $\int \tilde{f}(\varepsilon_2) P_{\mathrm{coll}}(\varepsilon, \varepsilon_2, \varepsilon') d\varepsilon'$, which was stored in memory at the moment of calculating the probabilities. Then, the rejection step considering the real $f_{s_2}(\mathbf{k}_2)$ occupation and $\tilde{f}(\varepsilon_2)$ is performed. If the later did not overestimate the former, a particle is chosen around $\mathbf{k_2}$. Then, the final energy of the triggering particle is selected according to the distribution of $P_{\mathrm{coll}}(\varepsilon, \varepsilon_2, \varepsilon')$ given the boundaries of ε' where the selected type of transition is fulfilled. Finally, the Pauli exclusion principle is evaluated for both particles. In the case that the transitions are accepted, electron-hole pairs are created or annihilated depending on the interaction type.

Appendix B

Research accomplishments relative to this thesis

In this appendix, the works realized along the PhD that has fructified into research articles and conference contributions are listed and categorized according to the chapter they are related to.

B.1 Publications

Chapter 3
Carrier transport phenomena in Graphene

- J. M. Iglesias, R. Rengel, E. M. Hamham, E. Pascual, and M. J. Martín. "Interplay of out-of-equilibrium phonons and self-heating under high field transport conditions in graphene". In: *Journal of Physics D: Applied Physics* **50.30** (July 2017), p. 305101
- J. M. Iglesias, E. Pascual, E. M. Hamham, M. J. Martín, and R. Rengel. "Interband scattering-induced ambipolar transport in graphene". In: *Semiconductor Science and Technology* (Apr. 2019)
- P. C. Feijoo, F. Pasadas, J. M. Iglesias, E. M. Hamham, R. Rengel, and D. Jimenez. "Radio Frequency Performance Projection and Stability Tradeoff of h-BN Encapsulated Graphene Field-Effect Transistors". In: *IEEE Transactions on Electron Devices* **66.3** (Mar. 2019), pp. 1567–1573
- P. C. Feijoo, F. Pasadas, J. M. Iglesias, M. J. Martín, R. Rengel, C. Li, W. Kim, J. Riikonen, H. Lipsanen, and D. Jiménez. "Scaling of graphene field-effect transistors supported on hexagonal boron nitride: radio-frequency stability as a limiting factor". In: *Nanotechnology* **28.48** (Nov. 2017), p. 485203

Chapter 4
Fluctuation phenomena in graphene

- R. Rengel, J. M. Iglesias, E. Pascual, and M. J. Martín. "Noise temperature in graphene at high frequencies". In: *Semiconductor Science and Technology* **31.7** (May 2016), p. 075001
- R. Rengel, J. M. Iglesias, E. Pascual, and M. J. Martín. "A balance equations approach for the study of the dynamic response and electronic noise in graphene". In: *Journal of Applied Physics* **121.18** (May 2017), p. 185705
- J. M. Iglesias, M. J. Martín, E. Pascual, and R. Rengel. "Spectral density of velocity fluctuations under switching field conditions in graphene". In: *Journal of Statistical Mechanics: Theory and Experiment* **2016.5** (May 2016), p. 054018

- J. M. Iglesias, E. M. Hamham, E. Pascual, and R. Rengel. "Monte Carlo investigation of noise and high-order harmonic extraction in graphene". In: *Semiconductor Science and Technology* **33.12** (Nov. 2018), p. 124012

Chapter 5
Ultrafast dynamics of photoexcited carriers

- J. M. Iglesias, M. J. Martín, E. Pascual, and R. Rengel. "Hot carrier and hot phonon coupling during ultrafast relaxation of photoexcited electrons in graphene". In: *Applied Physics Letters* **108.4** (Jan. 2016), p. 043105
- J. M. Iglesias, M. Martín, E. Pascual, and R. Rengel. "Substrate influence on the early relaxation stages of photoexcited carriers in monolayer graphene". In: *Applied Surface Science* **424** (Dec. 2017), pp. 52–57

Other related works

- R. Rengel, J. M. Iglesias, E. M. Hamham, and M. J. Martín. "Damping of acoustic flexural phonons in silicene: influence on high-field electronic transport". In: *Semiconductor Science and Technology* **33.6** (May 2018), p. 065011
- E. M. Hamham, J. M. Iglesias, E. Pascual, M. J. Martín, and R. Rengel. "Impact of the hot phonon effect on electronic transport in monolayer silicene". In: *Journal of Physics D: Applied Physics* **51.41** (Sept. 2018), p. 415102

B.2 Conference contributions

Chapter 3
Carrier transport phenomena in Graphene

- R. Rengel, J. M. Iglesias, E. Pascual, and M. J. Martín. "Monte Carlo modeling of mobility and microscopic charge transport in supported graphene". In *10th Spanish Conference on Electron Devices* (CDE 2015; Feb. 2015, Aranjuez, Spain). POSTER PRESENTATION
- J. M. Iglesias, R. Rengel, E. Pascual, and M. J. Martín. "High electric field transport in graphene: impact of screened coulomb interactions". In *ImagineNano 2015*(Mar. 2015, Bilbao, Spain). POSTER PRESENTATION
- R. Rengel, J. M. Iglesias, M. J. Martín, and E. Pascual. "Effect of charged impurity scattering on the electron diffusivity and mobility in graphene". In *19th International*

Conference on Electron Dynamics in Semiconductors, Optoelectronics and Nanostructures (EDISON'19; June 2015, Salamanca, Spain). POSTER PRESENTATION

- J. M. Iglesias, M. J. Martín, E. Pascual, and R. Rengel. "Impact of Self-heating and Hot Phonons on the Drift Velocity in Graphene". In *11th Spanish Conference on Electron Devices* (CDE 2017; Feb. 2017, Barcelona, Spain). POSTER PRESENTATION

- P. C. Feijoo(speaker), F. Pasadas, J. M. Iglesias, M. J. Martín, R. Rengel, and D. Jiménez. "Impact of scattering mechanisms and dimensions scaling in Graphene Field-Effect transistors". In *11th Spanish Conference on Electron Devices* (CDE 2017; Feb. 2017, Barcelona, Spain). ORAL PRESENTATION

- J. M. Iglesias, E. M. Hamham, M. J. Martín, E. Pascual, P. C. Feijoo, F. Pasadas, D. Jiménez, and R. Rengel. "Impact of scattering mechanisms and dimensions scaling in Graphene Field-Effect transistors". In *11th Spanish Conference on Electron Devices* (CDE 2017; July 2017, Buffalo, New York, USA). POSTER PRESENTATION

- J. M. Iglesias(speaker), E. Pascual, E. M. Hamham, M. J. Martín, and R. Rengel. "The role of interband processes on electronic transport in monolayer graphene". In *12th Spanish Conference on Electron Devices* (CDE 2018; Nov. 2018, Salamanca, Spain). ORAL PRESENTATION

Chapter 4
Fluctuation phenomena in graphene

- R. Rengel, J. M. Iglesias, E. Pascual, and M. J. Martín. "A combined Monte Carlo-balance equations investigation of the high frequency response of graphene". In *11th Spanish Conference on Electron Devices* (CDE 2017; Feb. 2017, Barcelona, Spain). POSTER PRESENTATION

- J. M. Iglesias, R. Rengel, E. Pascual, and M. J. Martín. "Monte Carlo study of velocity fluctuations during transient regimes in graphene". In *7th International Conference on Unsolved Problems on Noise* (UPON 2015; June 2015, Barcelona, Spain). ORAL PRESENTATION

- J. M. Iglesias, E. M. Hamham, E. Pascual, M. J. Martín, and R. Rengel. "Monte Carlo simulation of harmonic generation in graphene under AC applied fields". In *Graphene Week 2017*(Sept. 2017, Athens, Greece). POSTER PRESENTATION

Chapter 5
Ultrafast dynamics of photoexcited carriers

- J. M. Iglesias$^{(\text{speaker})}$, M. J. Martín, E. Pascual, and R. Rengel. "Carrier-carrier and carrier-phonon interactions in the dynamics of photoexcited electrons in graphene". In *19th International Conference on Electron Dynamics in Semiconductors, Optoelectronics and Nanostructures* (EDISON'19; June 2015, Salamanca, Spain). ORAL PRESENTATION

- J. M. Iglesias, M. J. Martín, E. Pascual, and R. Rengel. "Substrate-dependent Out-of-equilibrium Phonon and Electron Dynamics in Photoexcited Graphene". In *7th International Conference on Advanced Nanomaterials, 2nd International conference on Graphene Technolog, 1st International Conference on Spintronics Materials* (ANM 2016; July 2016, Aveiro, Portugal). POSTER PRESENTATION

- O. Zurrón, J. M. Iglesias, R. Rengel, M. J. Martín, and L. Plaja. "High order harmonic generation in graphene". In *2017 Conference on Lasers and Electro-Optics Europe* (CLEO Europe 2017; June 2017, Munich, Germany)

- O. Zurrón, J. M. Iglesias, M. J. Martín, R. Rengel, and L. Plaja. "Non perturbative high harmonic generation in graphene". In *X Spanish Optoelectronics Meeting* (OPTOEL 2017; June 2017, Santiago de Compostela, Spain)

Other related works

- J. M. Iglesias, M. J. Martín, E. Pascual, and R. Rengel. "Influence of systematic gate alignment variations on static characteristics in DG-SB-MOSFETs". In *10th Spanish Conference on Electron Devices* (CDE 2015; Feb. 2015, Aranjuez, Spain). POSTER PRESENTATION

- E. M. Hamham, J. M. Iglesias, M. J. Martín, and R. Rengel. "A Monte Carlo study of electronic transport in silicene: importance of out-of-equilibrium phonons". In *ImagineNano 2018*(Mar. 2018, Bilbao, Spain). POSTER PRESENTATION

- E. Pascual, J. M. Iglesias, E. M. Hamham, M. J. Martín, and R.Rengel. "Diffusive electronic transport in MoS2: a Monte Carlo study". In *12th Spanish Conference on Electron Devices* (CDE 2018; Nov. 2018, Salamanca, Spain). POSTER PRESENTATION